MODELLING FIBRIL FORMATION ON MEMBRANE SURFACES

Dissertation

zur Erlangung des Grades

„Doktor der Naturwissenschaften (Dr.-rer. nat.)“

am Fachbereich für Physik, Mathematik und Informatik

der Johannes Gutenberg-Universität Mainz

vorgelegt von

André Kesser

geboren in Mainz

Mainz, den 8. Mai 2017

JOHANNES GUTENBERG
UNIVERSITÄT MAINZ

Für meine Eltern.

ABSTRACT

Aggregates of highly ordered peptides, called fibrils, are in the focus of many scientific disciplines, as they play a major role in neurodegenerative diseases like Alzheimer's disease or Parkinson's disease. Despite many efforts, the origin of toxicity is not fully understood.

In this thesis two well established models for coarse-grained Monte Carlo simulations of lipids and peptides are combined to form a tool to investigate how membranes influence the process of peptide fibrillization. To combine both models, the peptide model is completely rewritten to fit into the lipid model framework. The interactions are ported from discrete to continuous potentials, and solvent interactions are added to replace the originally used implicit solvent. The original lipid model is only slightly modified to better represent the relative amount of hydrophobic and hydrophilic beads.

The behaviour of a single peptide for different parameters in the interaction potentials is explored to localise a set of values that is suited for simulations of fibril formation. The ability of the new peptide model to form fibrillar structures by means of the formation of hydrogen bonds is tested, and the possibilities to control the process of fibrillization by varying the applied hydrogen bond strength are explored. The results obtained from simulations of peptides in the bulk provide the basis for the study of peptide behaviour in the presence of a lipid membrane.

To estimate the behaviour of peptides in simulations with different values of the lipid-peptide interaction strength, the free energy of inserting a single peptide into the membrane is measured. In systems containing a lipid membrane, the process of fibrillization is faster than in the bulk. The peptides accumulate on the membrane surface, and thus the degree of freedom of the peptides is reduced. Subsequent simulations show that the sole presence of a membrane causes an increase in the fibrillization rate in the case of weak lipid-peptide interactions. The influence of strong lipid-peptide interactions depends on the strength of hydrogen bond energies. For strong hydrogen bonds, an increase in fibril size is observed, whereas weak hydrogen bonds lead to smaller fibrils compared to simulations with weaker lipid-peptide interactions. The comparison of fibril structures between simulations with and without a membrane shows that instead of forming multi-layered fibrils, the peptides tend to form single or double layered fibrils on membrane surfaces. From wet lab experiments it is known that oligomeric clusters possess the ability to destroy lipid membranes. This effect was not observed in the simulations that were run in the context of this thesis.

The model presented in this work is meant to enable further investigations of interactions between lipids and peptides as well as between membranes and fibrils. This thesis should therefore be used as a manual to understand the behaviour of the model under different values of interactions.

ZUSAMMENFASSUNG

Cluster geordneter Peptide, sogenannte Fibrillen, stehen im Fokus vieler wissenschaftlicher Arbeiten, da sie bei neurodegenerativen Erkrankungen, wie beispielsweise Alzheimer oder Parkinson, eine große Rolle spielen. Trotz der umfangreichen Bemühungen in der Wissenschaft ist es bisher nicht gelungen, den Ursprung der Toxizität in vollem Umfang zu erfassen.

In der vorliegenden Arbeit werden zwei etablierte Modelle für grobkörnige Monte-Carlo-Simulationen von Lipiden und Peptiden kombiniert, um ein Werkzeug zur Untersuchung des Einflusses von Membranen auf die Fibrillisation von Peptiden zur Verfügung zu stellen. Dazu musste ein existierender Simulationscode substantiell erweitert werden. Die Wechselwirkungen des Peptidmodells wurden von diskreten zu kontinuierlichen Potentialen überführt sowie Wechselwirkungen zwischen Peptiden und Lösungsmittel-Teilchen hinzugefügt. Das originale Lipid-Modell wurde nur geringfügig modifiziert, um den relativen Anteil hydrophober und hydrophiler Beads besser zu repräsentieren.

Das Verhalten eines einzelnen Peptids bei unterschiedlichen Parametern der Wechselwirkungspotentiale wird untersucht, um einen Satz passender Parameter für Simulationen zur Bildung von Fibrillen zur Verfügung zu haben. Die Fähigkeit des Modells, Fibrillen durch Bildung von Wasserstoff-Brücken aufzubauen, sowie die Möglichkeit, den Prozess der Fibrillenbildung mit Hilfe der eingestellten Stärke der Wasserstoff-Brücken zu kontrollieren, wird getestet. Um das Verhalten der Peptide in Systemen mit unterschiedlichen Lipid-Peptid-Wechselwirkungen zu untersuchen, wird zunächst die Freie Energie eines Peptides als Funktion des Abstandes zur Membran-Mitte bestimmt. In der Gegenwart von Membranen ist eine beschleunigte Bildung der Fibrillen an der Membran-Oberfläche zu beobachten. In Simulationen mit mehreren Peptiden wird gezeigt, dass die Eigenschaften der resultierenden Fibrillen sich für schwache Lipid-Peptid-Wechselwirkungen kaum unterscheiden, d.h. dass bereits die Anwesenheit einer Membran zu einem Anstieg der Fibrillisationsrate führt. In Systemen mit starken Wasserstoff-Brücken ist eine Zunahme der Fibrillengröße zu beobachten, schwache Wasserstoff-Brücken führen zu kleineren Fibrillen. Der Vergleich der Struktur von Peptiden, die in Simulationen mit bzw. ohne einer Membran entstehen, zeigt, dass die Zahl der Lagen der Fibrillen an Membran-Oberflächen reduziert ist. Im Gegensatz zur in Experimenten beobachteten Störung der Membran durch Oligomere konnte in den Simulationen für diese Arbeit keine Zerstörung der Membran durch Peptide oder daraus bestehender Aggregate beobachtet werden.

Das in der vorliegenden Arbeit beschriebene Modell ist dazu gedacht, weitergehende Untersuchungen der Wechselwirkungen zwischen Lipiden und Peptiden sowie zwischen Membranen und Fibrillen zu ermöglichen. Diese Arbeit sollte als Handbuch aufgefasst werden, das es ermöglicht, das Verhalten des Modells bei unterschiedlichen Wechselwirkungs-Parametern zu verstehen.

CONTENTS

ACRONYMS

COM centre of mass

PBC periodic boundary conditions

DPPC dipalmitoylphosphatidylcholine

FENE finite extensible nonlinear elastic

LJ Lennard-Jones

BA bond angle

MC Monte Carlo

MD molecular dynamics

CG coarse grained

Part I

INTRODUCTION AND THEORY

1 INTRODUCTION

1.1 MEMBRANE LIPIDS

Lipids are a vital component for all membranes. For most animals they constitute about half of the cell membrane mass [1]. Over one hundred different types of lipids can be found inside a single membrane. Despite the large diversity of membrane lipids, they share at least one property; all lipids observed in membranes are amphiphilic [2], that is they have a hydrophobic and a hydrophilic part. These parts are often called hydrophobic tail and hydrophilic head.

The most common membrane lipids are phospholipids, consisting of one hydrophilic head and two hydrophobic tails - usually fatty acids, consisting of 14 to 24 backbone atoms. Those fatty acids can be further distinguished by their saturation. If a fatty acid is not saturated, one or more double bonds exist, leading to a kink, in contrast to saturation where no double bonds are found. Phospholipids have often one saturated and one unsaturated tail. The lipid model used in the simulations corresponds to dipalmitoylphosphatidylcholine (DPPC), a lipid of the group of phosphatidylcholines, a subclass of phospholipids. It consists of two palmitic acids, which are saturated fatty acids, and a phosphatidylcholine head group. The chemical structure of a DPPC molecule is shown in Figure 1.1.

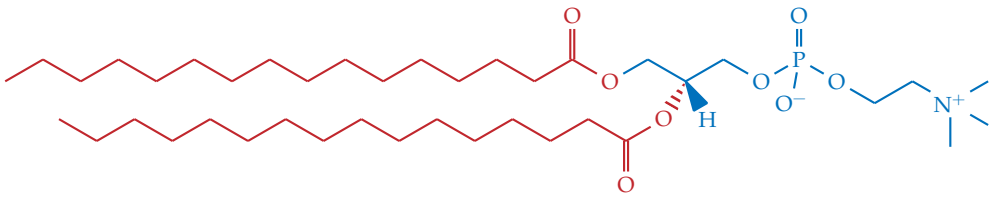

Figure 1.1: The chemical structure of dipalmitoylphosphatidylcholine (DPPC). The two palmitic acids (red) are attached to the phosphatidylcholine head group (blue). The chemical formula of DPPC is $C_{40}H_{80}NO_8P$.

Due to the amphiphilic structure and the shape of lipids, they tend to form different kinds of aggregates in aqueous solutions. Wedge-shaped lipids tend to form micelles as illustrated in Figure 1.2 (a), whereas cylindrical-shaped lipids tend to form vesicles or bilayers, as shown in Figure 1.2 (b) and 1.2 (c). Forming bilayers is, from an energetic point of view, most favourable for phospholipids. The hydrophilic heads get into contact with water on both sides of the membrane, thereby shielding the hydrophobic parts inside against the environment. Vesicles are formed to prevent hydrophobic parts to be exposed to water. Micelles are mono-layered structures bent to form a closed shield of hydrophilic heads towards the aqueous environment. In inverted micelles

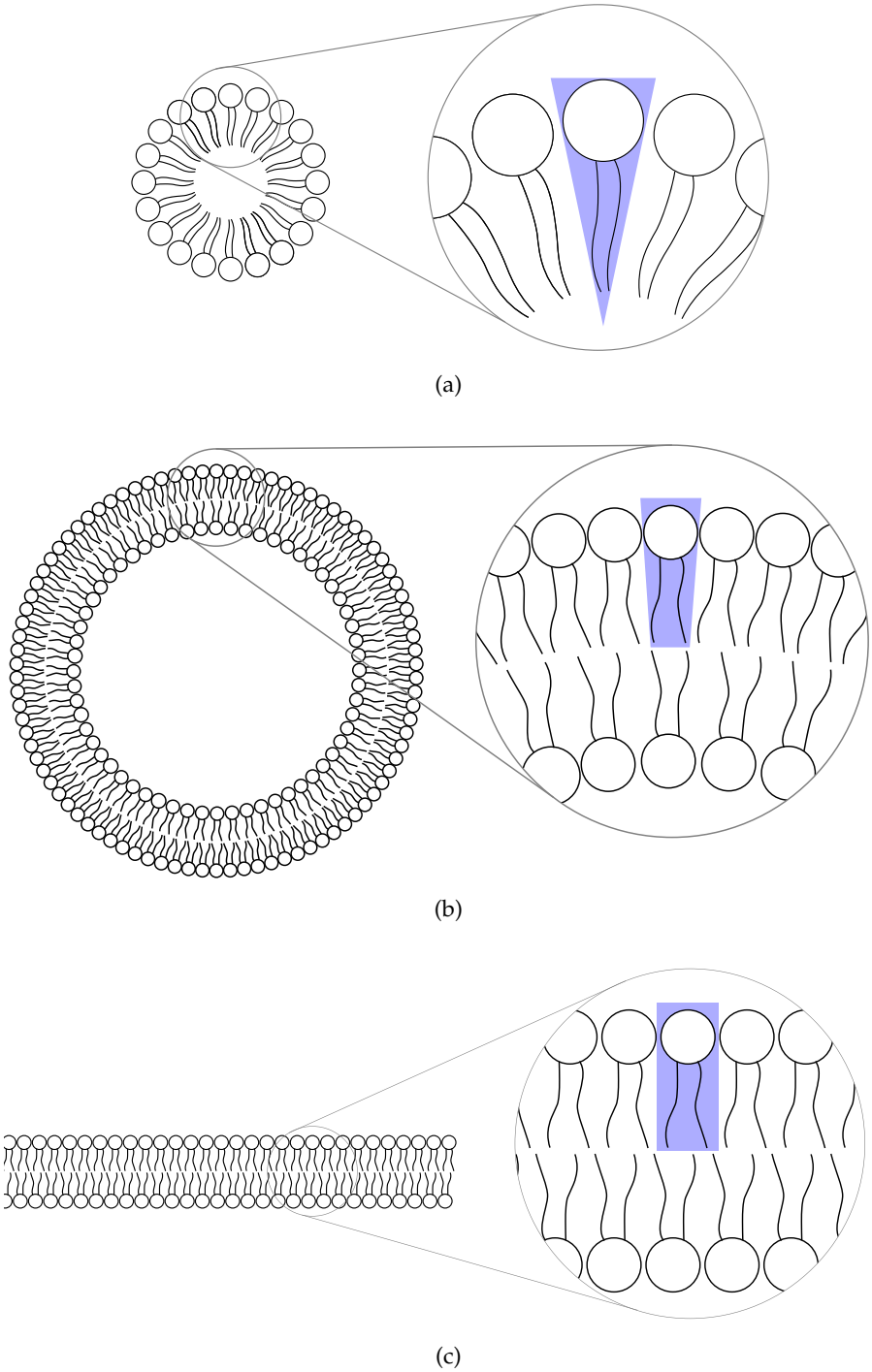

Figure 1.2: Two-dimensional illustration of (a) a micelle, (b) a vesicle, and c) a lipid bilayer. The enlarged views on the right show the shape of the lipids forming a triangle (a), trapezium (b), or a cylinder (c), highlighted in blue.

aqueous solution gets surrounded by hydrophilic parts to prevent contact of hydrophobic tails with the solution. Depending on the temperature of the system, lipid membranes show different phases [3, 4]. At low temperatures the lipids are in a crystalline phase L_c. At temperatures around 18.8°C a transition into a gel phase L_β or into the tilted gel phase $L_{\beta'}$ takes place. In these

phases the heads form a hexagonal or quasi-hexagonal lattice, the tail chains are well ordered. In the L_β phase the lipid tails are oriented parallel to the bilayer normal, in the $L_{\beta'}$ phase they are tilted with respect to the bilayer normal. Whether a L_β or a $L_{\beta'}$ phase is formed depends on the relation of the head surface area and the tail cross section. At about 34.4°C there is a second transition into a rippled gel phase $P_{\beta'}$. Characteristic for this phase is a ripple structure visible at the bilayer surface. A third transition can be observed at about 41.3°C, where the lipids form a lipid-crystalline phase L_α [5]. In this phase the lipids show a high in plane mobility and the tails become quite disordered; the lipids show a fluid-like behaviour. The transition $L_c - L_\beta$ is called sub-transition, the transition $L_\beta - P_{\beta'}$ pre-transition, and the transition from $P_{\beta'} - L_\alpha$ is called main-transition [6]. An illustration of the phases is given in Figure 1.3.

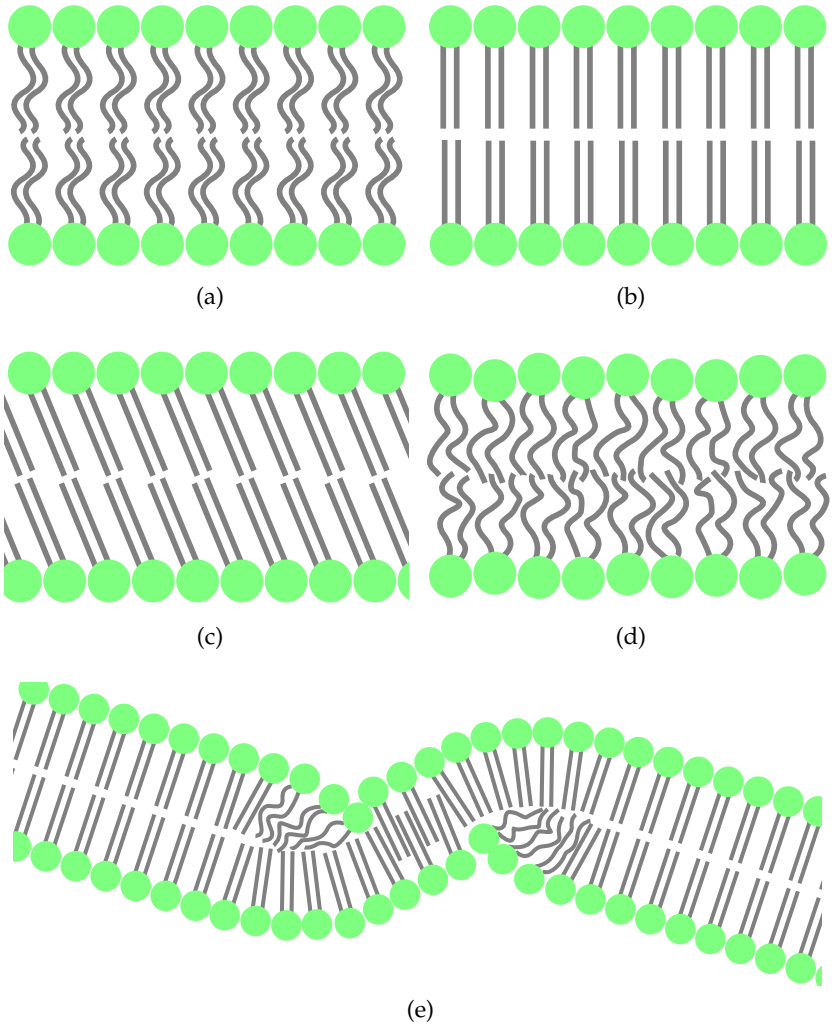

Figure 1.3: Illustration of the different phases of lipid membranes: (a) crystalline phase L_c, (b) non tilted gel phase L_β, (c) tilted gel phase $L_{\beta'}$, (d) liquid-crystalline phase L_α, and (e) ripple phase $P_{\beta'}$.

1.2 PEPTIDES

Peptides are composed of *amino acids*. Amino acids are structures that contain one core carbon atom to which several groups are attached. These are a carboxyl (-COOH) group, an amino ($-NH_2$) group, a hydrogen (-H) atom and a side chain (-R). The amino acids differ in side chain attached to the functional group and number of core carbon atoms. Several hundred different amino acids are known [7], but only 22 of them are found in peptides and proteins of eucaryotes [8], organisms with cells containing a nucleus and other cell organelles. Proteins are peptides which consist of more than 50 amino acids. These 22, so called *proteinogenic* amino acids have in common that the carboxyl group ($-COOH$) and the amino group ($-NH_2$) are attached to the same carbon atom, denoted by C_α. Hence the members of this group are also called α amino acids. Due to their chemical structure, α amino acids are isomeric molecules, and can as such appear in two spatial configurations. Figure 1.4 shows the basic structure of α amino acids as *L* (left handed) and *D* (right handed) amino acids. Although D amino acids are found in some organisms, including

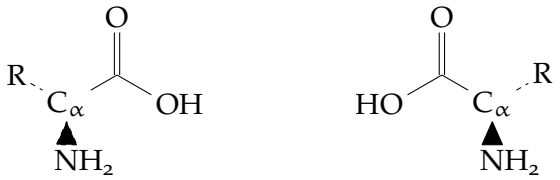

Figure 1.4: The basic structure of α amino acids with side chain R, the carboxyl group ($-COOH$) and the amino group ($-NH_2$) attached to the backbone atom C_α. L amino acid on the left, D amino acid on the right.

insects, earthworms, sharks and others [9–12], the vast majority of peptides of eucariots consist of L amino acids [8]. 20 of the 22 proteinogenic α amino acids are encoded in DNA. This subgroup is shown in Figure 1.5. As implied by the different colours, these amino acids can be sorted into two groups: hydrophobic and hydrophilic peptides, depending on the polarity of their side chain. Amino acids form peptide chains by forming *peptide bonds*. These are covalent bonds formed between the carboxyl group of one amino acid and the amino group of an other amino acid. Figure 1.6 shows the basic structure of a peptide consisting of $(n+2)$ amino acids.

Peptides and proteins are involved in many processes inside living organisms [8, 15]; they act as antibodies or toxins [16–18], they are used as enzymes for catalysing reactions [19–22], they act as hormones [23, 24], and they are involved in haemostasis [25, 26], to name a few. As collagenes, which make up to one third of the bodies protein mass, they act as structural proteins in the extracellular space.

The function of peptides and proteins is not only determined by their amino acid sequence, but also by their spatial configuration. The amino acid sequence is called the primary structure of the peptide or protein, the spatial arrangement of repeating sequences and stabilizing hydrogen bonds is called secondary structure. They can be further described by their tertiary structure which

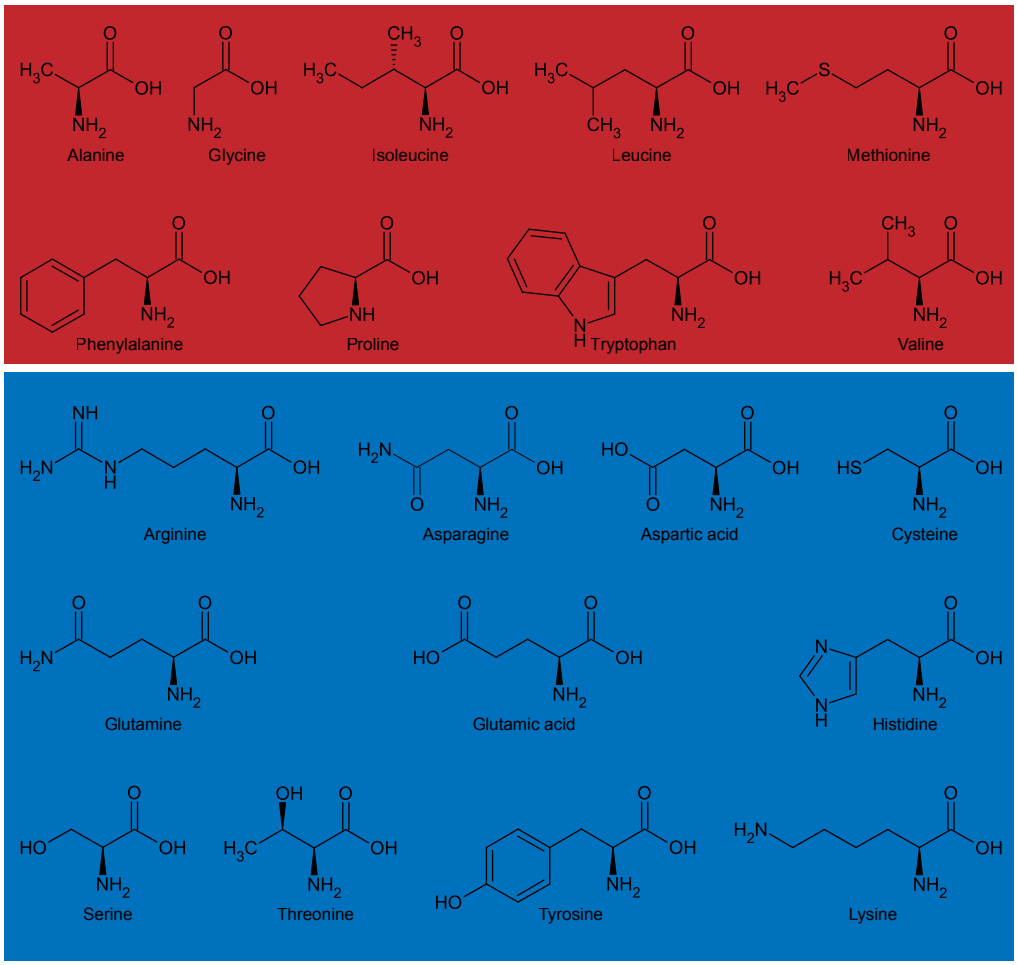

Figure 1.5: 20 of the 22 proteinogenic α amino acids, grouped by the polarity of the side chain. Red background indicates unpolar, blue polar amino acids. Ordered corresponding to [13]. Not shown are selenocysteine and pyrrolysine, as they are not encoded in DNA in most organisms [14].

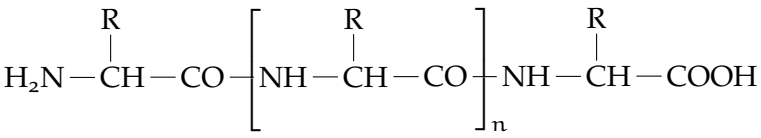

Figure 1.6: The basic structure of a peptide consisting of $(n+2)$ amino acids. The amino acid on the left end is called *N-terminus*, the amino acid on the right *C-terminus*.

gives information about the spatial configuration of the whole peptide. The tertiary structure is determined by the position of hydrophobic and hydrophilic amino acids in the sequence. If a protein consists of several peptide subunits, the number of subunits and their spatial configuration is called quaternary structure of the protein. It is influenced by the location of hydrophilic and

hydrophobic amino acids, whether they are inside or outside of the peptide surface.

1.2.1 *Diseases associated with peptides*

As peptides are involved in many processes in the body, there are several diseases associated with dysfunctional peptides and proteins. In the following some of the better known diseases are shortly described.

Amyloid β peptide, which is necessary for information exchange in the brain [27], is believed to act neurotoxic in pathological environments. In the brain of patients having *Alzheimer's disease* so called *plaques* are found. Plaques are extracellular aggregates of peptides with a diameter of about 50 µm [28]. Alzheimer's disease is the most frequent form of dementia, according to the World Health Organisation it is responsible for 60-70 percent of all dementia cases [29]. First scientific publications on Alzheimer's disease were written around the change from the nineteenth to twentieth century [30, 31]. Characteristics of this disease are the loss of short term memory and, with progress of the disease, an increasing inability to perform everyday tasks due to a loss of neurons in the brain [32, 33].

Parkinson's disease is an illness of the central nervous system. It is the second most common disease regarding neurodegenerative disorder [34]. Nervous cells inside the substantia nigra die, leading to a lack of dopamine. Dopamine is an important neurotransmitter inside the brain and the body, for example to control motor functions. It is also able to regulate the blood flow in organs. Through these functions, a loss of dopamine leads to the symptoms observed in people having Parkinson's disease [35, 36]: tremor at rest, rigidity (increased muscular tone), akinesia (slowed movements), and postural instability. Sometimes these are summarized as *TRAP* according to their first letters. The death of nervous cells in the substantia nigra is believed to be caused by a clustering of the protein α-synuclein inside the cells [37]. Such protein clusters are called Lewis Bodies [38]. First scientific descriptions of the disease date back to 1817 [39], but the symptoms were already mentioned earlier, for example in an Egyptian papyrus or the bible [40].

In the case of *Huntington's disease* a defect gene causes neurodegenerative disorder. The gene causing the disease was discovered in 1993, it encodes the protein *huntingtin* [41]. In its pathological form the produced protein consists of more amino acids compared to the protein encoded and produced in healthy bodies [42]. Inside neurons of people having Huntington's disease inclusions of huntingtin can be found [43]. These inclusions seem to cause a cellular dysfunction and, at a later stage of the disease, cell death [44]. People having Huntington's disease show at first a *hyperkinesis*, an increased muscular activity, in a later stage of the disease a *hypokinesis*, a decrease in muscular activity, is developed. Together with the aforementioned symptoms, the patients show changes in cognition and personality [45]. The disease was first academically discussed in the 19th century, the most noted description was from George Huntington in 1872 [46, 47].

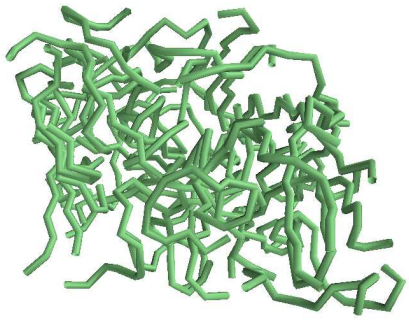

Figure 1.7: Illustration of an oligomer consisting of 50 peptides.

Despite the differences between these diseases, they share at least one similarity: Clusters of proteins, which are believed to cause the disease are found in the bodies of patients. These clusters, called *plaques* in the case of Alzheimer's disease, *Lewy bodies* in case of Parkinson's disease and *intranuclear inclusions* in the case of Huntington's disease, consist of highly ordered fibrillar structures and they lack the solubility of the single proteins. It is unclear, whether these *fibrils*, or there predecessors, soluble *oligomers* are causing cell death [48, 49]. An oligomer, as illustrated in Figure 1.7, is a complex of several, unordered peptide chains, the term refers to the quaternary structure [8]. When the oligomer consists of one type of peptide chains, it is called homopolymer, otherwise copolymer. In fibrils the peptides possess a higher order compared to those inside an oligomer. An illustration for a fibril is shown in Figure 1.8.

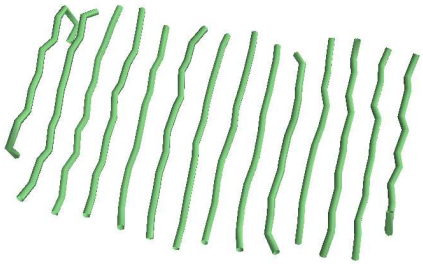

Figure 1.8: Illustration of a fibrillar structure consisting of 14 peptides. The fibril is part of a four layer fibril structure developed from the oligomer shown in Figure 1.7. The other three layers are not shown for clarity.

In this thesis the formation of oligomeric and fibrillar structures of peptides with and without a lipid bilayer present in the simulations is investigated. Both, the peptides which form clusters and the model lipids which form the bilayer membrane, are coarse grained models that have been used separately before [50–54] [55–58]. For the simulations in this thesis, both models were adapted as described in the following chapter. The simulation technique used is called Monte Carlo (MC) simulation and is described in Chapter 3.

1.3 THIS WORK IN THE CONTEXT OF OTHER COARSE GRAINED MODELS

Publications that include the phrase "all-atom" in their title, allow the reader to easily conceive the level of detail that is incorporated into a model used in such a study: All atoms of the system of interest can be found in the model used for simulations. In the case of coarse grained simulations, however, the degree of coarsening has to be explained. It reaches from models that use all-atom representations for main parts of the system combined with beads representing multiple atoms in areas of less interest, to models of single beads or rods to represent the complete system. According to [59], the wide range of coarse graining concerning peptide simulations can be divided into four groups, *simple models*, *phenomenological models*, *systematic coarse graining*, and *higher-resolution models*, sorted from a higher degree of coarsening towards more detailed models. Examples of each group will be discussed shortly in the following, an illustration for the mentioned models is given in Table 1.1.

The MARTINI Force Field, for example used by Monticelli et al [60] or Lee et al [61], normally uses a 4:1 mapping [62] for atoms to model beads. Water is also mapped using this relation. Non bonded interactions only consider the properties of the model beads, like polarity or charge. Bonded interactions, however use the original all-atom representation of the system. In the OPEP model, the peptide backbone uses an all-atom representation, whereas the chain beads are modelled using a single bead. OPEP is an abrevation for *Optimized Potential for Efficient protein structure Prediction*. This model is used for a wide range of simulations, reaching from single peptide simulations to studies of fibril formation [63]. Both, the MARTINI Force Field and the OPEP model belong to the group of higher-resolution models.

Carmichael and Shell [64] used a systematic coarse graining approach to simulate the aggregation of peptides. The parameters used by their model are obtained by comparing coarse grained simulations with all-atom simulations, according to a method developed by Shell [65]. Systematic coarse graining is characterised by the process of reducing degrees of freedom in a system to obtain a model. The resulting representation is tuned to reproduce the properties and behaviour of a single system or an only small range of systems. The process of model optimization has to be redone for different structures. A description of a systematic coarse graining approach can for example be found in [66].

Opposite to the process of reducing degrees of freedom in systematic coarse graining, simple models are set up by adding as few degrees of freedom to a system as possible to acquire the desired behaviour of the model. The resulting systems can consist of simple rods, like in the sphero-cylindrical model [67], or orientable sticks like in simulations run by Irbäck et al [68]. Different simple models have in common that they are generic.

The group of phenomenological models lies in between simple and systematic coarse grained models. The number of degrees of freedom in these systems is higher than in simple models, but they still follow the principle of being generic. The Shea model [69] for example uses three beads per residue, the

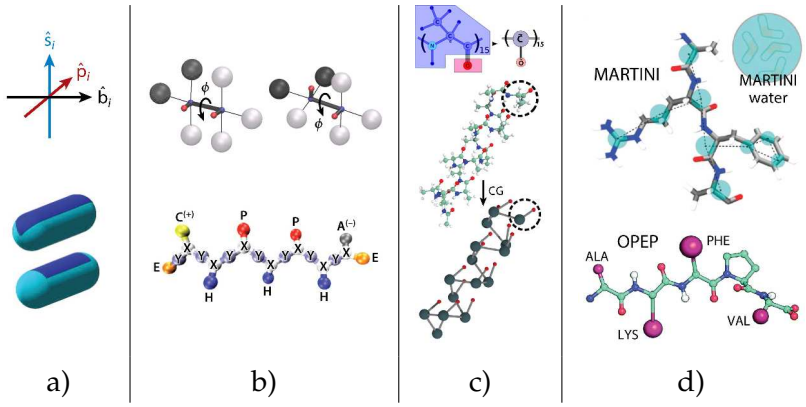

Table 1.1: Examples for models with different degrees of coarse graining: a) simple models: Orientable stick model [68] and sphero-cylindrical model [67], b) phenomenological models: Caflisch model [70] and Shea model [69], c) systematic coarse grained: Carmichael and Shell [64], d) higher-resolution models: MARTINI Force Field [60] and OPEP model [63]. The images are adapted from [59].

Caflisch model [70] two. Both models have in common that they incorporate a dihedral potential to control the peptide β-sheet propensity.

The model described in the following chapters and used for the simulations discussed in this thesis can be sorted into the group of simple models. Both the lipid and the peptide model are constructed as generic representations of their species. Although more complex as the examples given for simple models, the level of detail that would allow to call it phenomenological is not reached. By not modelling the backbone and side chains of a peptide, the model does not reproduce the primary structure. Nevertheless, by using multiple beads per peptide, the model is able to reproduce the secondary structure of peptides, controlled by the potentials applied. With even simpler models, like the mentioned sphero-cylindrical model [67], the secondary structure can not be reproduced. Compared to more detailed models, like the Shea model [69], or higher-resolution models like the MARTINI Force Field [60], the computational costs of the model presented in this thesis are lower, allowing the simulation of bigger systems with the same, or even less, amount of time. As the model is designed as a top-down system, that is by reproducing the peptide behaviour with as few degrees of freedom as possible, the system ensures a generic behaviour. Such a generic behaviour is often not given in more detailed models, which are constructed in a bottom-up approach, by reducing the degrees of freedom in an all-atom representation of the system, until the desired level of coarse-graining is reached. The model used for peptides has a similar degree of coarse-graining as the lipid-model, developed in the group of Friederike Schmid [71], that is adapted in this thesis. This allowed a combination of both systems to study the lipid-peptide interactions.

With an increasing degree of coarsening the ability of a model to reproduce the specific details of a system of interest decreases. At the same time the computational costs decrease, allowing bigger simulations to be run. Although

the computational power available to scientists is constantly increasing, coarse grained simulations will be the method of choice for many studies concerning lipid peptide interactions and fibril formation to come.

1.4 LIPID-PEPTIDE INTERACTIONS: EXPERIMENTAL RESULTS

In the literature, many experimental results regarding the interactions of lipids and peptides can be found. In the following, the results of three experiments are discussed. Those experiments were chosen, because they support the idea of generic coarse-grained simulations to study the formation of fibrils in the presence of a lipid membrane.

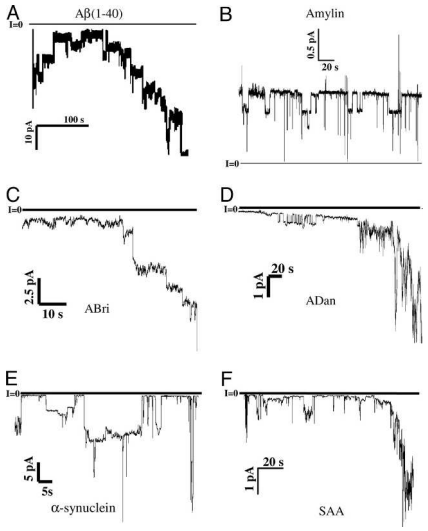

Figure 1.9: The measured current through a membrane as a function of time for oligomers of different peptides. The jumps in the curves correspond to the opening and closing of single ion-channel-like structures in the membrane. A) Aβ or amyloid β is associated with Alzheimer's disease, B) amylin or IAPP (islet amyloid polypeptide) can be found in the fibrillar deposits in the pancreatic islets of type-II diabetes patients, C) ABri is a peptide associated with familial British dementia, D) ADan is associated with familial Danish dementia, E) α-synuclein is associated with Parkinson's disease, F) SAA means serum amyloid A. All oligomers, with the exception of amylin, induce ion-channel-like structures in the membrane. Image taken from [49], Copyright 2005 National Academy of Sciences.

In 2005 Quist and coworkers [49] set up an experiment to explore the toxicity of oligomeric structures. They set up a bilayer membrane, connected to electrodes. With the help of the electrodes, they were able to measure the current through the membrane caused by ion-channels. Without the addition of oligomers, no ion-channels could be measured. After adding oligomers to one side of the membrane, curves like those shown in Figure 1.9 were recorded. The addition of oligomers of different peptides resulted in similar curves: All oligomers, with the exception of those consisting of amylin, induced ion-channel-like structures in the membrane. These channels could lead to leakage of the membrane and thus to the death of a living cell. The observation similar

ion-channel-like structures for different types of oligomers indicates a generic mechanism of toxicity.

Kayed et al. [48] reported an experiment, where they designed an antibody that recognises oligomers of Aβ. To test that the antibody recognises only oligomeric structures of Aβ, they ran an ELISA assay. ELISA is the abbreviation of enzyme-linked immunosorbent assay [72]. In this type of assay, the antigen, in this case the oligomeric form of Aβ, is attached to a surface, typically in a microtiter plate. The antibody, connected to an enzyme that causes a colour change in the following step, is added to the antigen. Unbound antibodies are removed with the help of a detergent. By adding an enzymatic substance, the colour of the antibodies changes. By measuring the optical density (OD) the relative amount of antibody-antigen reactions can be measured.

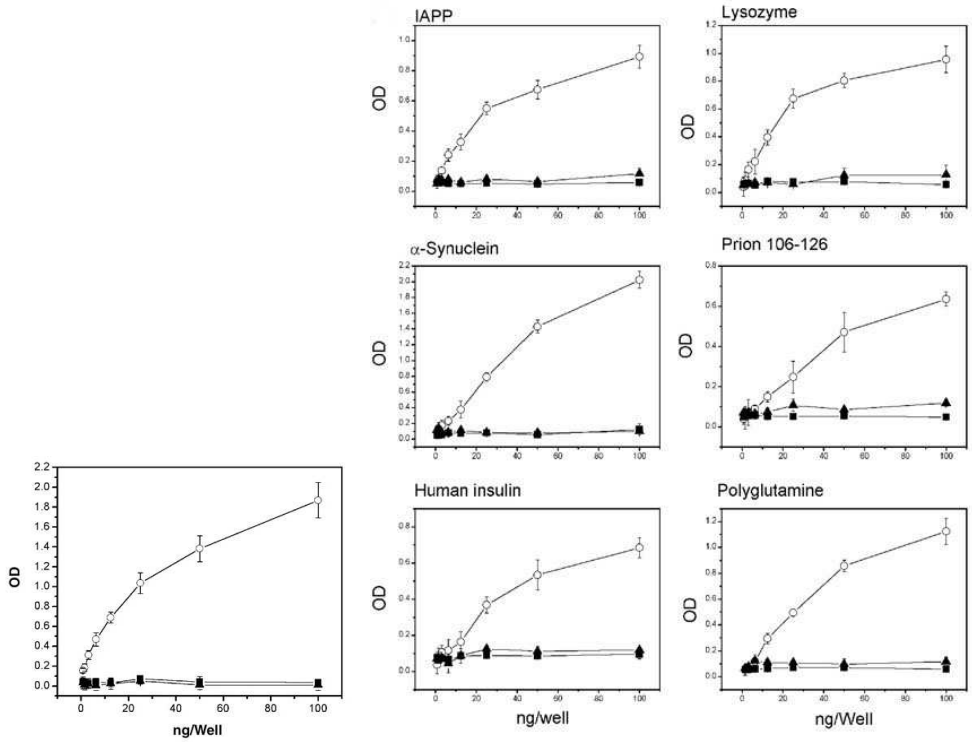

(a) (b)

Figure 1.10: ELISA assay to detect the interaction strength of a designed antibody with low molecular weight structures (solid triangles), fibrils (solid squares) and oligomers (open circles) of various peptides. The optical density (OD) is plotted against the concentration if antibodies per microtiter well. a) Aβ40 peptides b) IAPP, Lysozyme, α-synuclein, Prion106-126, human insulin and Polyglutamine. The antibody only detects oligomers, measurements with low molecular weight structures and fibrils only show background values. Image taken from [48].

The curves plotted in Figure 1.10 (a) show that the antibody ignores both low molecular weight Aβ and Aβ fibrils, but recognises Aβ oligomers. After successfully testing this ability of the antibody, they investigated the behaviour of the antibody in the presence of low molecular weight structures, oligomers and fibrils of other peptides. The measured values, shown in Figure 1.10 (b)

reveal that the antibody, although custom built to recognise Aβ oligomers, also recognises oligomers consisting of other peptides.

Furthermore they observed that the addition of their antibodies reduces the toxicity of oligomers. Again this works both with Aβ oligomers and oligomers of other peptides. This effect is shown in Figure 1.11. Kayed et al. concluded from their findings that oligomers have a structure, distinct from fibrils and low molecular weight systems of the same peptides. The universality of the designed antibody also suggests a common structure of oligomers [73], supporting the investigations of oligomers and there interactions with membrane by using generic coarse-grained models.

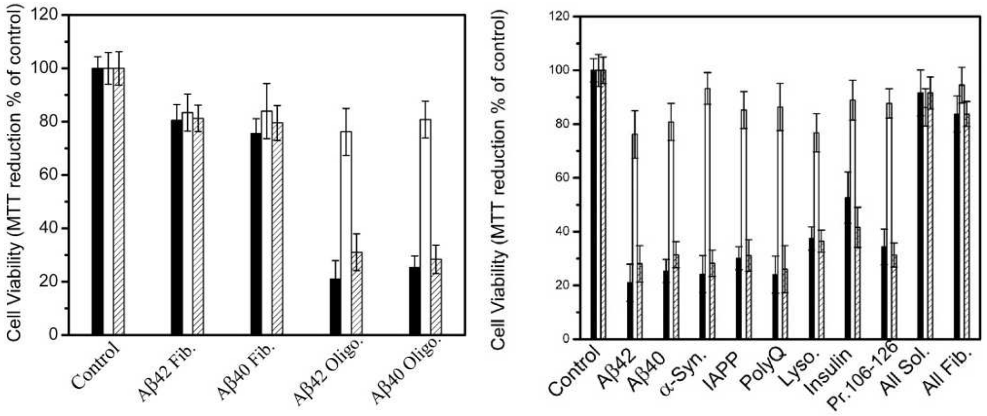

(a) (b)

Figure 1.11: a) Reduction of the cytotoxicity of Aβ fibrils and Aβ oligomers, with (open bars) and without (filled bars) the addition of the antibody. The hatched bars show the results obtained from experiments with the addition of non-immune rabbit IgG (immunoglobulin G). The y-axis shows the viability of the membrane. In systems of oligomers, where the antibody was added viability of the cell is clearly higher than in those systems without the antibody. In experiments with fibrils, the viability is not significantly reduced, both in systems with and without the antibody. b) Same measurements as in a), but with oligomers of different peptides. Image taken from [48].

Knight and Miranker [74] set up an experiment, where they investigated the fibril formation of IAPP with and without lipids present. Without the addition of lipids, the peptide did not form fibrillar structures in the time frame of their experiments ($\approx$ 700 minutes). After adding lipids, obtained from the pancreas of non-insulin-dependent diabetes mellitus patients, fibrils could be observed by fluorescence. By increasing the lipid concentration, the fibrils form faster. The same effect, with a different time frame, could be reproduced by adding chicken liver lipids. The resulting curves of this experiments are given in Figure 1.12. The accelerated fibril formation in the presence of one of two different types of lipids is another hint that the interactions of lipids and peptides are independent of the detailed atomic structure of the constituents. The accelerated formation of fibrils in the presence of a lipid membrane was also shown by other experiments [75], some of the suggesting electrostatic attraction, caused

by negative lipid head groups, to be the driving force [76]. Weakly stable α-helices are reported to preferably bind to membranes [76–78]. Several reasons for an accelerated formation of fibrils are also discussed in literature [79, 80]: Peptides on membrane surfaces possess a reduced degree of freedom and they have a reduced diffusion constant. Also the membrane structure might promote fibril formation.

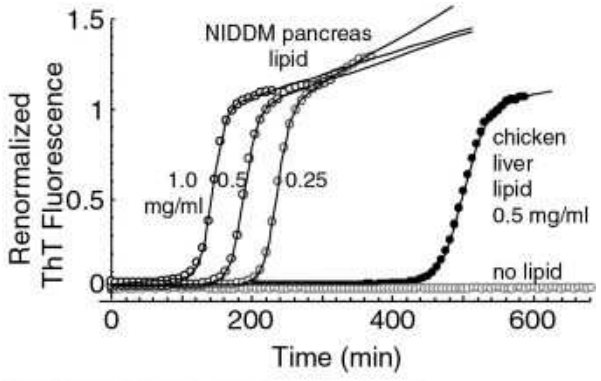

Figure 1.12: Acceleration of the formation of fibrils in the presence of membranes. Without the addition of lipids, the peptides do not form fibrils in the time frame of the experiment (open grey circles). The addition of lipids of the pancreas of people having non-insulin-dependent diabetes mellitus (NIDDM), the formation of fibrils can be observed. With higher concentration of lipids, the fibrils form faster. Also the addition of chicken liver lipids (black circles) promote the formation of fibrils. The y-axis shows the measured fluorescence of thioflavin T (ThT) that acts as a dye indicating the presence of amyloids. Image reprinted from [74] with permission from Elsevier.

The list above represent only a small amount of experiments that have been done to investigate the huge field of fibril formation and lipid-peptide interactions. Other experiments have shown that the fibrillization of peptides follows similar multi step pathways for different types of peptides [81, 82]. This process includes the formation of oligomers, protofibrils and fibrils, whereby oligomers are believed to be the source of toxicity in respect to membrane disruption. This disruption might be caused by different mechanisms [83–86]: The formation of a pore, the binding of peptides to single lipids, leading to the formation of holes in the membrane, called *detergent effect*, and *carpeting*, where peptides cover one double-layer leaflet leading to an asymmetric pressure and thus membrane disruption. Growing fibrils [87] are also able to disrupt lipid membranes, however, their toxicity is reduced, in experiments with faster growing fibrils [88, 89]. Mature fibrils seem to influence the structure of lipid membranes [90, 91], but to much less extent than oligomers and growing fibrils.

2 THE MODEL

The results presented in this thesis are obtained by doing MC simulations with a coarse grained (cg) model for lipids and for peptides. The properties and the structure of both cg models as well as the interactions between their constituents will be described in the following. The simulation technique and the implemented routines for different moves are described in Chapter 3.

2.1 UNITS

All values used in our simulations are based on two fundamental units: The unit of energy ϵ and the unit of length σ. By mapping the simulation units to standard units the relation $\sigma \approx 6\text{Å}$ can be shown [92]. The relation $\epsilon \approx 0.36 \cdot 10^{-20}\text{J}$ for the energy unit can be obtained by comparing the transition temperature of DPPC and the model membrane [57]. The values for temperature T in this simulation are given as a reduced temperature

$$T = \frac{k_B T^*}{\epsilon} \quad , \tag{2.1}$$

with the real temperature T^*. The pressure in all simulations is, if not otherwise stated fixed to $p = 2\epsilon\sigma^{-3}$.

2.2 LIPIDS

The model for lipids used in our simulations was designed to match the behaviour of the well studied lipid DPPC. The version we are using for our simulations is based on the lipid model described in [71]. A single lipid is modelled as linear spring bead chain, a popular model used both in MC [93] and molecular dynamics (MD) [94] simulations. The spring bead chains we use consist of one ore more head beads and a fixed number of tail beads, in all our simulations containing lipids we use two head beads and four tail beads. The head beads correspond to the phosphatidylcholine head group, the tail beads to the two palmitic acids of a single DPPC lipid. Although the model only contains a single tail, it is able to reproduce the main characteristics of lipid monolayers and membranes [56, 58, 71]. An illustration of an all-atom representation of DPPC and a lipid as it is used in our simulations is shown in Figure 2.1 for comparison.

2.2.1 *Lipid properties*

In this thesis the diameter of head beads is denoted as $\sigma_{h,l}$, the diameter of tail beads as $\sigma_{t,l}$. Throughout our simulations we use the relation $\sigma_{h,l} = \sigma_{t,l}$. The original implementation used one head bead per lipid and the relation

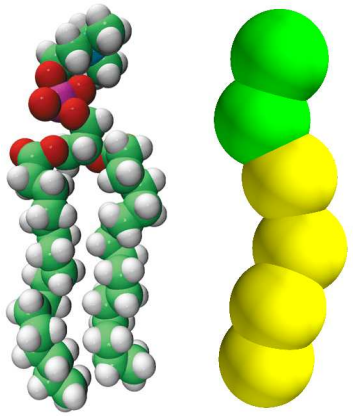

(a) (b)

Figure 2.1: (a) All-atom representation of DPPC. (b) A model lipid with two head beads, shown in green and four tail beads, shown in yellow, as used in our simulations. The image of the all-atom representation and of the CG lipid are both scaled to be at the same height for this illustration. The interaction parameters used for this lipids correspond to those described in this chapter. The image is obtained from a simulation with $T = 1.1$, $p = 2.0$. The chemical structure of DPPC is shown in Figure 1.1 on page 3.

$\sigma_{h,l} = 1.1\sigma_{t,l}$ [71]. The bond between adjacent lipid beads is modelled by a finite extensible nonlinear elastic (FENE) potential. The potential used in our simulation has the following form:

$$U_{FENE}(r) = \frac{1}{4}\epsilon_F (\Delta r_{max})^2 \left[\left\{ 1 - \left(\frac{r - r_0}{\Delta r_{max}} \right)^2 \right\}^{-2} - 1 \right] \quad , \tag{2.2}$$

with the spring constant ϵ_F, the cut-off radius Δr_{max} and the equilibrium length r_0. A plot of the potential is shown in Figure 2.2.

The interactions between two not adjacent beads are described by a shifted Lennard-Jones (LJ) potential:

$$U_{LJ}^{shifted}(r) = \begin{cases} U_{LJ}(r) - U_{LJ}(r_c) & \text{if } r < rc \\ 0 & \text{otherwise} \end{cases} \quad , \tag{2.3}$$

with the unshifted LJ potential U_{LJ}:

$$U_{LJ} = \epsilon_{LJ} \left(\left(\frac{\sigma_{LJ}}{r} \right)^{12} - 2 \left(\frac{\sigma_{LJ}}{r} \right)^{6} \right) \quad . \tag{2.4}$$

Here r_c is the cut-off radius, σ_{LJ} is the mean value of the diameter of the interacting beads, and ϵ_{LJ} controls the depth of the potential. The cut-off radius r_c is used for two different purposes. For values of $r_c < \sigma_{LJ}$ the potential loses its attractive part and can be used to model purely repulsive interactions. Using a cut-off radius of $r_c \geqslant 2\sigma_{LJ}$, the computation of the interaction can be speeded up, as the computation of the potential is avoided for values of $r \geqslant r_c$. For those high cut-off radii, the form of the potential is only slightly changed

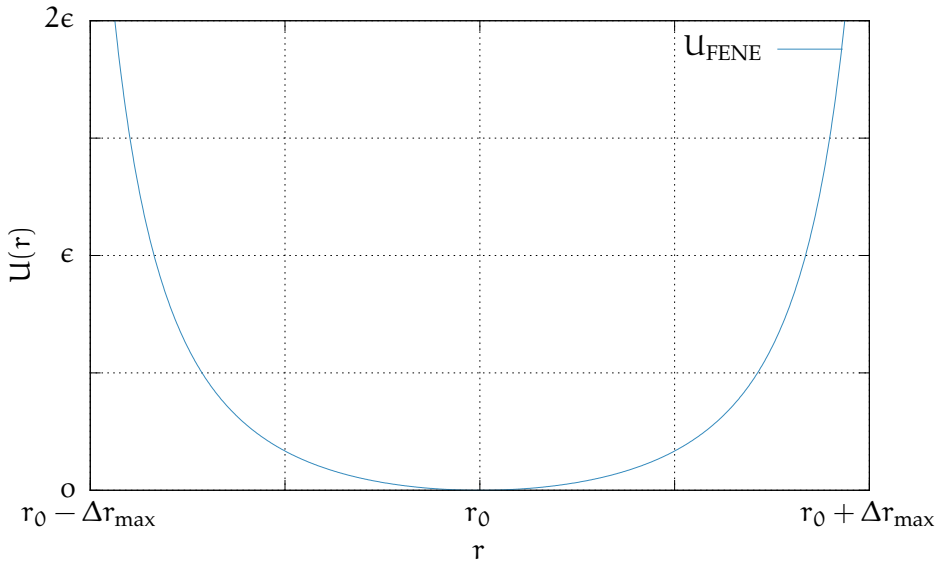

Figure 2.2: The FENE potential used in our simulations to model the interactions between adjacent lipid beads as defined in Equation 2.2.

ϵ_F/ϵ	r_0/σ	$\Delta r_{max}/\sigma$	ϵ_{BA}/ϵ
100	0.7	0.2	4.7

Table 2.1: The values of ϵ_F, r_0, and Δr_{max} used for the FENE potential between adjacent lipid beads and ϵ_{BA} for the bond angle potential of lipids used in our simulations.

compared to the unshifted version of the LJ potential. To illustrate this, both, the unshifted and the shifted potential for $r_c = 1.0$ and $r_c = 2.0$, are plotted in Figure 2.3.

The angle formed by three adjacent beads is controlled by a cosine bond angle (BA) potential:

$$U_{BA}(\theta) = \epsilon_{BA}(1 - \cos\theta) \quad . \tag{2.5}$$

Here ϵ_{BA} is the potential strength and θ is the angle between the three beads.

Table 2.1 lists the values of ϵ_F, r_0 and Δr_{max} used for the FENE potential and ϵ_{BA} for the bond-angle potential used for lipids in the simulations. The values for σ_{LJ} and ϵ_{LJ} used in the LJ potential are the same for head-head, head-tail, and tail-tail interactions. The cut-off radius is chosen to model a pure repulsive potential for head-head and head-tail interactions and an attractive potential for tail-tail interactions. The values used in the simulations are listed in table 2.2.

2.3 PEPTIDES

The peptide model used in the simulations is based on a model developed by Hoang and Auer [50, 52]. Use cases for their model can be found for example

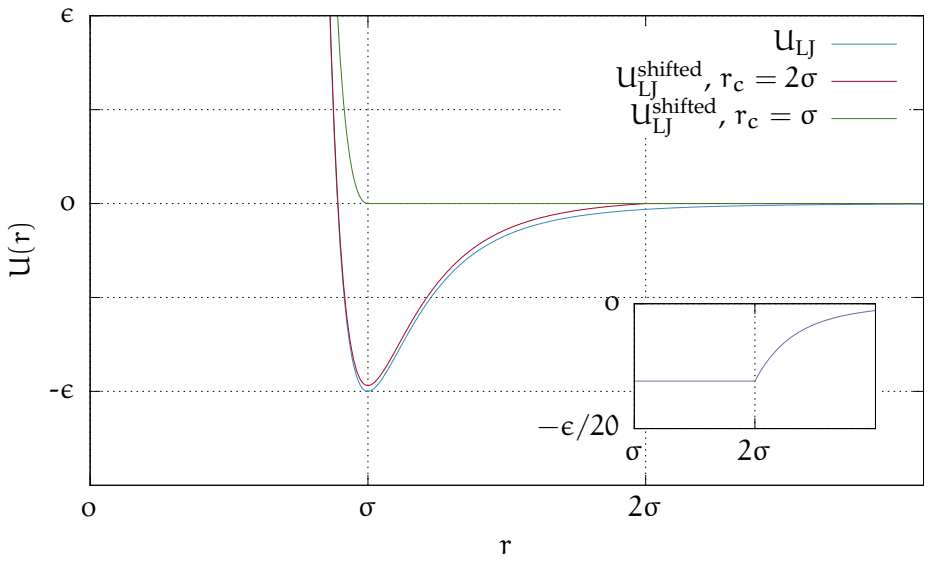

Figure 2.3: Plot of the shifted and unshifted LJ potential (blue). The shifted potential is plotted with $r_c = 2\sigma$ (red) and $r_c = \sigma$ (green). The inset shows the difference between U_{LJ} and $U_{LJ}^{shifted}$ with $r_c = 2\sigma$. The shifted LJ potential with $r_c = \sigma$ (green) is used in our simulations to model purely repulsive interactions.

interaction type	σ_{LJ}/σ	r_c / σ_{LJ}	ϵ_{LJ}/ϵ
head-head	1.0	1.0	1.0
head-tail	1.0	1.0	1.0
tail-tail	1.0	2.0	1.0

Table 2.2: The values of σ, r_c/σ, and ϵ_{LJ} used for head-head, head-tail, and tail-tail interactions used for lipids in our simulations.

in [51, 53, 54, 95, 96]. The original model is solvent free and uses discrete potentials. We adapted the model to use continuous potential and added interactions with the phantom solvent used in our simulations. The energies used in the original implementation are mapped to the basic units ϵ and σ for our simulations.

2.3.1 *Peptide properties*

A peptide is, like the lipids used in our simulations, constructed as a linear spring bead chain. If not stated otherwise, we use peptides consisting of twelve beads in our simulations. To favour the formation of fibrillar structures [97], the beads along the chain are alternating hydrophobic (H) and hydrophilic (P). The potential between adjacent beads is modelled using a FENE type potential as given in Equation 2.2. Interactions between non adjacent beads are modelled using shifted LJ potentials (Equation 2.3). The potential between two hydrophobic (H) beads has an attractive part, interactions between a hydrophobic

ϵ_F/ϵ	r_0/σ	$\Delta r_{max}/\sigma$
100	0.63333	0.2

Table 2.3: The values of ϵ_F, r_0 , and Δr_{max} used for the FENE potential between adjacent peptide beads used in our simulations.

interaction type	ϵ_{LJ}/ϵ	σ_{LJ}/σ	r_c/σ_{LJ}
hydrophobic-hydrophobic (HH)	0.6	0.75	2.0
hydrophilic-hydrophilic (PP)	1.0	0.75	1.0
hydrophobic-hydrophilic (HP)	1.0	0.75	1.0

Table 2.4: Values of the LJ potential used to model the interactions between the different types of peptide beads.

(H) and a hydrophilic (P) bead or two hydrophilic (P) beads are purely repulsive. The parameters used for the FENE potential are given in Table 2.3, those for the LJ potential in the three aforementioned cases are given in Table 2.4.

The angle between connected beads is controlled by a bond angle potential as used in the Martini model:

$$U_{BA,\,p}(\theta) = \frac{1}{2} k_0 \left[\cos\theta - \cos\theta_0\right]^2 \quad . \tag{2.6}$$

The average angle θ_0 is held fixed at $\theta_0 = 2.0255 \approx 120°$. The stiffness constant k_0 is varied with the strength of the hydrogen bonds. The value of k_0 is chosen to match the relation $0.3 \times E_{HB,\,local} = E_{BA}$ between hydrogen bonds and bending stiffness at an angle of 95°, used in [52].

2.3.2 *Hydrogen bonds*

The peptide model includes hydrogen bonds which can be formed between the beads of a single peptide, or between beads of different peptides. The first and last bead of a peptide be start- or endpoint of one hydrogen bond, all other beads can be involved in up to two hydrogen bonds. Situations, in which more than two hydrogen bonds for a bead would be possible are not allowed by the implemented algorithms. We distinguish between two types of hydrogen bonds, *local* and *non-local* bonds. A peptide forming an α-helix and the local hydrogen bonds which cause this helix, are illustrated in Figure 2.4. Several requirements must be fulfilled to form a hydrogen bond: The distance between two beads under consideration must be between 0.7833σ and 0.9333σ for local hydrogen bonds and between 0.6833σ and 0.8833σ for non-local hydrogen bonds. These values and the following constraints are based on values given in [50] and are obtained from an analysis of PDB structures. Local hydrogen bonds can only be formed between beads of the same peptide that are separated by two other beads. Non-local bonds can be formed between beads that are separated by at least four beads, if the beads are of the same peptide,

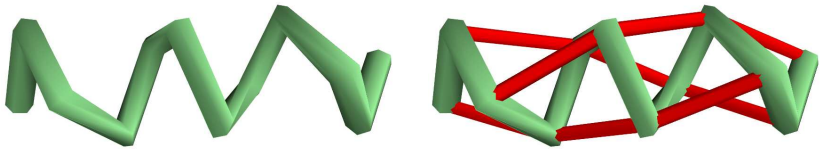

(a) (b)

Figure 2.4: Illustration of a single peptide consisting of twelve beads. a) shows the peptide forming an α-helical structure, b) highlights the local hydrogen bonds (red) that stabilise the helix.

or between beads of different peptides. The angle between the two binormal vectors of the beads must be less than 37°, the angle between each binormal vector and the vector connecting the two beads must be less than 20°. Local bonds are only formed when a positive chirality is maintained. If a hydrogen bond is formed, depending on the bond type, a fixed (negative) energy is added. If two local hydrogen bonds are formed in parallel, a *cooperative* hydrogen bond which lowers the energy further, is formed. Parallel refers to two hydrogen bonds formed between beads (i, j) and $(i \pm 1, j \pm 1)$ in this context, with i and j being beads of the same or of different peptides. If at least one of two parallel hydrogen bonds is non-local, it is additionally required that the angle between the binormal vectors of beads i and j and the angle between the binormal vectors of beads $i \pm 1$ and $j \pm 1$ is bigger than 90° to form a cooperative hydrogen bond. The first and last bead of a peptide can only form local hydrogen bonds. Table 2.5 summarizes the constraints described above.

2.4 PHANTOM SOLVENT

Our simulations use a special form of explicit solvent. One big advantage of explicit solvent models over implicit solvent models is the possibility to apply external pressure without constraining the flexibility of a membrane. Explicit solvent also introduces an attractive interaction between lipid head beads and peptide beads which is controlled by external pressure. One disadvantage of explicit over implicit solvent models are the higher computational costs of the former. To compensate for this, we use a *phantom solvent* environment. Like an explicit solvent, the phantom solvent is modelled as single beads that interact with lipid and peptide beads with a purely repulsive LJ potential. What distinguishes phantom solvent from explicit solvent is the fact that the phantom solvent beads do not interact with each other. The energy, calculated during solvent bead moves to decide whether to accept or to reject the move, takes only interactions with lipid and peptide beads into account and ignores neighbouring solvent beads. A second positive aspect of this type of solvent is that it circumvents the formation of structures inside the solvent bulk [55], an effect that is not prevented in classical explicit solvent models. The number of solvents N inside a simulation box is determined by the ideal

local hydrogen bonds	
distance in peptide sequence	$j = i + 3$
bead-bead distance	$4.7\,\text{Å} < r_i j < 5.6\,\text{Å}$
binormal-binormal-corelation	$\lvert\vec{b}_i \cdot \vec{b}_j\rvert > 0.8$
binormal-connecting vector	$\lvert\vec{b}_i \cdot \vec{c}_{ij}\rvert > 0.94$ and $\lvert\vec{b}_j \cdot \vec{c}_{ij}\rvert > 0.94$
chirality	$(\vec{r}_{i,i+1} \times \vec{r}_{i+1,i+2}) \cdot \vec{r}_{i+2,i+3} > 0$
non-local hydrogen bonds	
distance in peptide sequence	$j > i + 4$
bead-bead distance	$4.1\,\text{Å} < r_i j < 5.3\,\text{Å}$
binormal-binormal-corelation	$\lvert\vec{b}_i \cdot \vec{b}_j\rvert > 0.8$
binormal-connecting vector	$\lvert\vec{b}_i \cdot \vec{c}_{ij}\rvert > 0.94$ and $\lvert\vec{b}_j \cdot \vec{c}_{ij}\rvert > 0.94$
cooperative hydrogen bonds	
angle between successive beads	$\vec{b}_i \cdot \vec{b}_{i\pm1} < 0$ and $\vec{b}_j \cdot \vec{b}_{j\pm1} < 0$, applied only if at least one of the two hydrogen bonds is non-local

Table 2.5: Constraints used for local, non-local and cooperative hydrogen bonds. Reproduced from [50].

interaction type	ϵ_{LJ}/ϵ	σ_{LJ}/σ	r_c/σ
solvent-lipid head bead	1.0	1.05	1.0
solvent-lipid tail bead	1.0	1.0	1.0
solvent-peptide bead	1.0	0.8833	1.0

Table 2.6: Parameters for the LJ potential used to model the interaction between solvents and lipid beads and solvent and peptide beads.

gas law: $N = V \cdot p/T$ with the desired solvent volume V, the system pressure p, and temperature T. Table 2.6 lists the parameters used for the LJ potential to model the interaction between solvents and lipid beads and solvents and peptide beads.

2.5 LIPID-PEPTIDE INTERACTIONS

Both the model for lipids and the model for peptides were used independently from each other before. Therefore, neither of them defines an interaction between lipid beads and peptide beads. To define an interaction between those two groups of beads we followed a model proposed by Shea and coworkers [98–100], which is used to simulate interactions of peptides with lipid membranes in an implicit solvent environment using the MD simulation technique

interaction type	ϵ_{LJ}/ϵ	σ_{LJ}/σ	r_c/σ
lipid head bead-hydrophobic peptide bead	1.0	0.8333	1.0
lipid head bead-hydrophilic peptide bead	1.0	0.8333	1.0
lipid tail bead-hydrophobic peptide bead	0.6	0.8333	2.0
lipid tail bead-hydrophilic peptide bead	1.0	0.8333	1.0

Table 2.7: Parameters for the LJ potential used to model the interaction between lipid beads and peptide beads used in our simulations if not otherwise stated.

(see Section 3.1). The interactions between lipid and peptide beads in their model are calculated by using LJ potentials. Depending on the type of lipid and peptide bead under consideration, they use purely repulsive potentials, or potentials containing an attractive and a repulsive part.

Following their example, we decided to also use shifted LJ potentials. The interactions between hydrophobic peptide beads and lipid tail beads are modelled using a cut-of radius of 2σ, allowing attractive and repulsive interactions between those two types of beads. For interaction between the three other possible lipid-peptide combinations, polar peptide bead - lipid tail bead, hydrophobic peptide bead - lipid head bead, and polar peptide bead - lipid head bead, we use a cut-of radius of 1σ, leading to repulsive potentials. Table 2.7 shows the values used for simulations that include peptides and lipids. The value ϵ_{LJ} for interactions between hydrophobic peptide beads and lipid tail beads is set to a value of 0.6ϵ, corresponding to the value used for interactions between non adjacent hydrophobic peptide beads. In Section 6.1 and Section 6.5 we discuss simulations with different values for the interaction strength between hydrophobic peptide beads and lipid tail beads, to investigate the influence of this parameter on the process of fibril formation.

3

SIMULATION TECHNIQUE

Most simulations concerning biophysical, biological, or biochemical processes can be categorised into one of two groups: Monte Carlo (MC) and molecular dynamics (MD) simulations. The results presented in this work were obtained using MC simulations. The main characteristics of MC simulations will be described in Section 3.2, MD simulations will be only shortly described in the next section to illuminate the main differences between MD and MC simulations.

3.1 MAIN CHARACTERISTICS OF MOLECULAR DYNAMIC SIMULATIONS

In MD simulations the process of obtaining a new state of the system consists of two steps. To move the system forward in time, the forces acting on all particles are calculated and used to move the particles according the Newton's equations of motion. The obtained positions are used in a loop to re-calculate the forces and move the particles further. Several intelligent algorithms were developed which deal with the details of the calculation of force and new positions on one hand and, on the other hand, which guarantee reversibility in time, like the Velocity Verlet algorithm [101] and others [102].

As the main focus of this thesis lies on MC simulations we refer to the literature for an in-depth description of the theory behind MD simulations [103–107].

3.2 MONTE CARLO SIMULATIONS

MC simulations are used to calculate thermal averages of interacting many particle systems in equilibrium. A new state of a system is not obtained by solving the Newton's equations of motion as in MD simulations, but by (carefully thought out) picking a random number to determine a change in the configuration. The paths that lead to a new physical state can therefore be unphysical and many algorithms, some of which will be discussed in following sections, exist to drive a system from an old to a new state.

3.2.1 *Markov process, Markov chain and master equation*

The generation of a new state of the system follows the principle of a Markov chain. The principle of a Markov chain, and its more general form of a Markov process, will be describe shortly in this subsection, thereby following the more in detail derivation shown in [108]. A process is called Markovian, if for all successive times $t_1 < t_2 < \cdots < t_n$ the equation

$$P_{1|n-1}(y_n, t_n | y_1, t_1; \ldots; y_{n-1}, t_{n-1}) = P_{1|1}(y_n, t_n; y_{n-1}, t_{n-1}) \tag{3.1}$$

is fulfilled. $P_{1|1}(y_n, t_n; y_{n-1}, t_{n-1})$ is the probability of a transition from a state y_{n-1} at time t_{n-1} to a state y_n at time t_n. Equation 3.1 means that the probability to change into a state y_n at time t_n, given a history of states $y_1, y_2, \ldots, y_{n-2}, y_{n-1}$ at times $t_1, t_2, \ldots, t_{n-2}, t_{n-1}$ depends only on the state y_{n-1} at time t_{n-1}, preceding state y_n at time t_n; knowledge of the $n-2$ states before is not necessary. By knowing the probability of the system of being in a state y_1 at time t_1, $P_1(y_1, t_1)$ and the function $P_{1|1}(y_2, t_2|y_1, t_1)$ between those, all following states can be calculated, e.g.

$$\begin{aligned} P_3(y_1, t_1|y_2, t_2, y_3, t_3) &= P_2(y_1, t_1; y_2, t_2)\, P_{1|2}(y_3, t_3|y_1, t_1; y_2, t_2) \\ &= P_1(y_1, t_1)\, P_{1|1}(y_2, t_2|y_1, t_1)\, P_{1|1}(y_3, t_3|y_2, t_2)\,. \end{aligned} \tag{3.2}$$

For two functions P_1 and $P_{1|1}$ to form a Markov process, two conditions must be fulfilled:

$$P_{1|1}(y_3, t_3|y_1, t_1) = \int dy_2 P_{1|1}(y_3, t_3|y_2, t_2)\, P_{1|1}(y_2, t_2, |y_1, t_1) \tag{3.3}$$

$$P_1(y_2, t_2) = \int dy_1 P_{1|1}(y_2, t_2|y_1, t_1)\, P_1(y_1, t_1) \quad . \tag{3.4}$$

Most many-body systems in nature are Markov processes and in principle any closed isolated physical system can be described as a Markov process. Equation 3.3 is the *Chapman-Kolmogorov* equation and is obtained by integrating Equation 3.2 over y_2 and dividing by $P_1(y_1, t_1)$. In the case of a stationary Markovian process the transition probability $P_{1|1}$ no longer depends on two points in time, but on the time difference. In this case Equation 3.3 can be written as

$$T_{\tau+\tau'}(y_3|y_1) = \int dy_2 T_{\tau'}(y_3|y_2)\, T_\tau(y_2|y_1) \quad , \tag{3.5}$$

where $T_\tau(y_2|y_2)$ is defined as

$$T_\tau(y_2|y_1) = P_{1|1}(y_2, t_2|y_1, t_1) \quad \text{with} \quad \tau = t_2 - t_1 \quad . \tag{3.6}$$

For stationary Markovian processes, a more convenient form of the Chapman-Kolmogorov equation, the *master-equation* can be formulated by going to the limit of vanishing time intervals τ'. If we write the probability of a transition $T_{\tau'}(y_2|y_1)$ as

$$T_{\tau'}(y_2|y_1) = (1 - \alpha_0(y_1))\,\delta(y_2 - y_1) + \tau' W(y_2|y_1) + o(\tau') \quad , \tag{3.7}$$

where $(1 - \alpha_0(y_1))$, with $\alpha_0(y_1) = \int dy_2 W(y_2|y_1)$, is the probability that no transition takes place, $W(y_2|y_1)$ is the transition probability per time unit and $o(\tau')$ is an unspecified term with $o(\tau')/\tau' \to 0$ for $\tau' \to 0$, and insert this into Equation 3.3 we get:

$$T_{\tau+\tau'}(y_3|y_1) = \left[1 - \alpha_0(y3)\,\tau'\right] T_\tau(y_3|y_1) + \tau' \int dy_2 W(y_3|y_2)\, T_\tau(y_2|y_1) \quad . \tag{3.8}$$

By dividing this equation by τ' and going to the limit $\tau' \to 0$ this leads to the master equation

$$\frac{\partial T_\tau(y_3|y_1)}{\partial \tau} = \int dy_2 W(y_3|y_2)\, T_\tau(y_2|y_1) - \int dy_2 W(y_2|y_3)\, T_\tau(y_3|y_1) \quad . \tag{3.9}$$

If the range of a Markov Process Y is a discrete set of states, Equation 3.9 can be written as:

$$\frac{dp_n(t)}{dt} = \sum_n W_{nn'} p_{n'}(t) - \sum_n W_{n'n} p_n(t) \quad , \tag{3.10}$$

where $p_n(t)$ is the probability of finding the system in state n at time t and W_{ab} is the probability of a transition from state b to state a per time unit. If (i) the above mentioned condition holds true, (ii) the time variable of the process is discrete and takes only integer values, and (iii) the process is stationary or homogeneous, it is called a *Markov chain*. In this case

$$\frac{dp_n(t)}{dt} = 0 \quad , \tag{3.11}$$

an therefore

$$\sum_n W_{nn'} p_{n'}(t) = \sum_n W_{n'n} p_n(t) \quad , \tag{3.12}$$

as the process is stationary.

3.2.2 *Detailed balance*

One common way to fulfil Equation 3.12 in an equilibrium simulation, and our simulations are no exception, is to ensure an even stricter requirement. In the case of *detailed balance* all single terms of the sums have to be equal:

$$W_{nn'} p_{n'} = W_{n'n} p_n \quad \forall n, n' \in Y \quad . \tag{3.13}$$

It can easily be seen that Equation 3.13 fulfils Equation 3.12. Detailed balance is a sufficient but not a necessary condition. Successful simulations that break detailed balance but satisfy Equation 3.12 exist [109, 110].

3.2.3 *Metropolis algorithm*

Experiments using random sampling date back until 1777 [111], but until the late 1940's such experiments were carried out without the use of computers. The first results obtained using MC simulations were published by Metropolis and Ulam in 1949 [112].

As mentioned above, the choice of random numbers is crucial to the simulation. Random numbers picked without any thought can effect the efficiency of the simulation dramatically or can even bias the result. A good (figural) illustration of this problem is e.g. given in [105].

In 1953 Metropolis et al. published the Monte Carlo importance sampling algorithm [113], today better known as *Metropolis algorithm*. In this algorithm the probability of switching from a state n to a state n' is connected to the energy difference of these two steps. The following description of the algorithm is based on the scheme shown in [105] and [114]. First we show the special case for point-like particles in an NVT ensemble, in the following we will focus on NpT-ensembles that are used in our simulations.

The probability of being in a state n in a classical system is defined as

$$p_n = \frac{e^{-\frac{E_n}{k_B T}}}{Z} \quad , \tag{3.14}$$

with Z being the partion function. This equation can hardly be solved for interesting systems due to the difficulty of calculating Z. By generating a Markov chain we can calculate the ratio of two probabilities p_n and $p_{n'}$:

$$\frac{p_n}{p_{n'}} = e^{\frac{-\Delta E}{k_B T}} \quad \text{with} \quad \Delta E = E_{n'} - E_n \quad , \tag{3.15}$$

where the partition function Z cancels out. What Metropolis did was to define a transition probability $W_{n'n}$ based on this equation that fulfils detailed balance[113]:

$$W_{n'n} = \begin{cases} e^{\frac{-\Delta E}{k_B T}} & \Delta E > 0 \\ 1 & \Delta E < 0 \end{cases} \tag{3.16}$$

$$= \min\left(1, e^{\frac{-\Delta E}{k_B T}}\right) \quad . \tag{3.17}$$

A recipe for an implementation of such a Monte Carlo simulation using Metropolis' importance sampling could be:

1. Choose one bead at random
2. Calculate the energy (the part which can change in the following move) E_O
3. Move the bead randomly by a small distance and store the old positions
4. Calculate the new energy E_N and $\Delta E = E_N - E_O$
5. Pick a random number r from [0,1] and accept the move, if $r < e^{\frac{-\Delta E}{k_B T}}$
6. If the move is not accepted, restore the old coordinates of the bead
7. Repeat Steps 1-6 for every Monte Carlo Move

The transition probability Metropolis suggested is not the only way to fulfil detailed balance, other valid transition probabilities are e.g. given in [115] and [116].

3.2.4 *Isobaric-isothermal- (NpT) ensemble*

For simulating fluid-solid transitions or different phases in solids it is convenient to use isobaric-isothermal (NpT) ensembles. By applying a constant pressure instead of a constant volume the system is free to transform into the state of lowest possible free energy. By choosing the wrong value for the volume in a NVT ensemble a system may be captured in a state where finite size effects prohibit a transition.

The first MC simulations using constant pressure were published by W. W. Wood [117], describing the behaviour of hard disks, published in 1968. In 1972, McDonald [118] applied NpT ensemble MC simulations to systems with continuous potentials. Following the descriptions in Frenkel and Smith [105] and Landau and Binder [114], the method developed by McDonald is described next.

The partition function $Z(N,V,T)$ of a NVT ensemble in a box of the volume $V = L^3$ can be written as:

$$Z(N,V,T) = \frac{1}{\Lambda^{3N} N!} \int_0^L d\mathbf{r}^N \exp\left[-U\left(\mathbf{r}^N\right)/k_B T\right] \quad , \tag{3.18}$$

where Λ denotes the particle de Broglie wavelength and $U\left(\mathbf{r}^N\right)$ is the interaction energy for a set of N particles with positions $\mathbf{r}^N$. In the NpT ensemble the volume V and hence the length of the box L is not fixed. Therefore scaled coordinates $\mathbf{s}^N$ are used:

$$\mathbf{s}_i^N = \frac{\mathbf{r}_i^N}{L} \qquad \text{for } i = 1,2,\ldots,N \quad . \tag{3.19}$$

The Helmholtz free energy $F(N,V,T)$ is then:

$$\begin{aligned} F(N,V,T) &= -k_B T \ln Z(N,V,T) \\ &= -k_B T \ln\left\{\frac{V^N}{\lambda^{3N} N!}\right\} - k_B T \ln \int_0^1 d\mathbf{s}^N \exp\left[-\frac{U\left(\mathbf{s}^N;L\right)}{k_B T}\right] \\ &= F_{ig}(N,V,T) + \Delta F(N,V,T) \quad . \end{aligned} \tag{3.20}$$

Here $F_{ig}(N,V,T)$ is the free energy for an ideal gas and $\Delta F(N,V,T)$ contains all interactions.

If we now consider our system to be a subsystem of a box containing ideal gas with a volume $V_0 \gg V$ and a total number of $M \gg N$ atoms, the partition function of the whole system can be written as a product of partition functions of the two subsystems:

$$\begin{aligned} Z(N,M-N,V,V_0-V,T) &= Z(N,V,T)\cdot Z(M-N,V_0-V,T) \\ &= \frac{V^N (V_0-V)^{M-N}}{N!\,(M-N)!\,\Lambda^{3M}} \int_0^1 d\mathbf{s}'^{M-N} \int_0^1 d\mathbf{s}^N \exp\left[-\frac{U\left(\mathbf{s}^N;L\right)}{k_B T}\right] \end{aligned} \tag{3.21}$$

with

$$\int_0^1 d\mathbf{s}'^{M-N} = 1 \quad . \tag{3.22}$$

The probability density $p(V)$ to find a system with a volume V is then:

$$p(V) = \frac{V^N (V_0 - V)^{M-N} \int_0^1 d\mathbf{s}^N \exp\left[-U\left(\mathbf{s}^N; L\right)/k_B T\right]}{\int_0^{V_0} dV' V'^N (V_0 - V')^{M-N} \int_0^1 d\mathbf{s}^N \exp\left[-U\left(\mathbf{s}^N; L'\right)/k_B T\right]} \quad . \tag{3.23}$$

In the limit $V_0 \to \infty$ and $M \to \infty$ with constant $\rho = (M-N)/V_0$ we can write

$$\begin{aligned} (V_0 - V)^{M-N} &= V_0^{M-N} \left[1 - \frac{V}{V_0}\right]^{M-N} \\ &\approx V_0^{M-N} \exp\left[-(M-N)\frac{V}{V_0}\right] \\ &= V_0^{M-N} \exp\left[-\rho V\right] \quad . \end{aligned} \tag{3.24}$$

By using the ideal gas law $\rho = p/k_B T$ we can replace the factor $\exp[-\rho V]$ by $\exp[-pV/k_B T]$. By integrating over the volume V and extracting the partition function of the bigger system $V_0^{M-N}/\left[(M-N)!\Lambda^{3(M-N)}\right]$ we obtain the partition function $Y(N, p, T)$ of the smaller system as a function of the particle number N, the pressure p and the temperature T:

$$Y(N, p, T) = \frac{p/k_B T}{\lambda^{3N} N!} \int dV V^N \exp\left[-pV/k_B T\right] \int_0^1 d\mathbf{s}^N \exp\left[-U\left(\mathbf{s}^N; L\right)/k_B T\right] \quad . \tag{3.25}$$

The probability density $p(V)$ then becomes:

$$p(V) = \frac{V^N \exp\left[-pV/k_B T\right] \int_0^1 d\mathbf{s}^N \exp\left[-U\left(\mathbf{s}^N; L\right)/k_B T\right]}{\int_0^{V_0} dV' V'^N \exp\left[-pV'/k_B T\right] \int_0^1 d\mathbf{s}^N \exp\left[-U\left(\mathbf{s}^N; L\right)/k_B T\right]} \quad . \tag{3.26}$$

The probability to find a system in a specific configuration $\mathbf{s}^N$ is then:

$$\begin{aligned} P(\mathbf{s}^N; V) &\propto V^N \exp\left[-pV/k_B T\right] \cdot \exp\left[-U\left(\mathbf{s}^N; L\right)/k_B T\right] \\ &= \exp\left[-\left[U\left(\mathbf{s}^N; L\right) + pV - N k_B T \ln V\right]/k_B T\right] \quad . \end{aligned} \tag{3.27}$$

We now have to use volume changing moves to sample the system. The volume changing moves must satisfy the same rules single atom moves do. The transition probability for such a move from state n to state n' with volumes V and V' would be:

$$W_{n'n} = \min\left(1, \exp\left[-\frac{1}{k_B T}\left[\Delta E + p\left(V' - V\right) - k_B T N \ln\left(V'/V\right)\right]\right]\right) \quad , \tag{3.28}$$

where $\Delta E = U\left(\mathbf{s}^N; L'\right) - U\left(\mathbf{s}^N; L\right)$ is the difference in potential energy for the system with different volumes.

3.3 IMPLEMENTED MOVES

In many cases simulations including local and global moves are more effective compared to systems with only local moves [119, 120]. Several different types of moves for different types of simulations are discussed in the literature

[121–125], therefore we only briefly describe the moves implemented in our simulations.

In each simulation step we do m bead moves, where m is the sum of the lipid-, peptide- and solvent-beads. The decision whether we do a lipid-, a peptide- or a solvent-bead move is randomly chosen according to the proportion of each bead type count. On average one move for each bead is done during the simulation.

3.3.1 *Lipids*

Moving single lipid beads is the only move implemented for lipids. Adjacent beads inside a single lipid are connected by a FENE type potential. Therefore single beads can be moved altering the distance to the previous and the next bead in the lipid. The biggest possible distance a bead can travel during a single move is limited by a given move range that gets optimised during a pre-run previous to a production-run of a simulation. Identity-switch moves which are applied in other implementations of the lipid model [126], are not used in the simulations discussed in this thesis, due to the fact that the membranes in these simulations consist only of one type of lipids. In the simulations a lipid bead is randomly chosen and moved in a random direction. The maximum movement in each direction is limited by a given move-range.

3.3.2 *Peptides*

Two different types of moves to change the configuration of peptide beads are used: Single-bead moves and moves that alter the position of several beads. The single bead moves for peptides correspond to those implemented for lipids: A peptide is choosen randomly and displaced according to a random vector, whose elements are limited by a move-range. The move-range for peptide moves is different from the move-range used for lipid moves.

Several moves that change the position of more than one peptide bead at once are implemented. An illustration of the moves described in the following is given in Figure 3.1.

Rotation move

To do a rotation move the algorithm randomly picks a bead of a given peptide as a rotation centre and uses a random unit vector to rotate the whole peptide by a random angle. The maximum angle of such a rotation is given by a rotation-range. The illustration of this move in Figure 3.1 (a) shows a rotation of the peptide around the third peptide, counted from the bottom, by 30°.

Translation move

In a translation move, the whole peptide gets moved according to a random translation vector. The elements of this vector are limited by a move-range, like in the case of single bead moves. In Figure 3.1 (b) the vector $(1, 1, 2)$ is used to illustrate the effect.

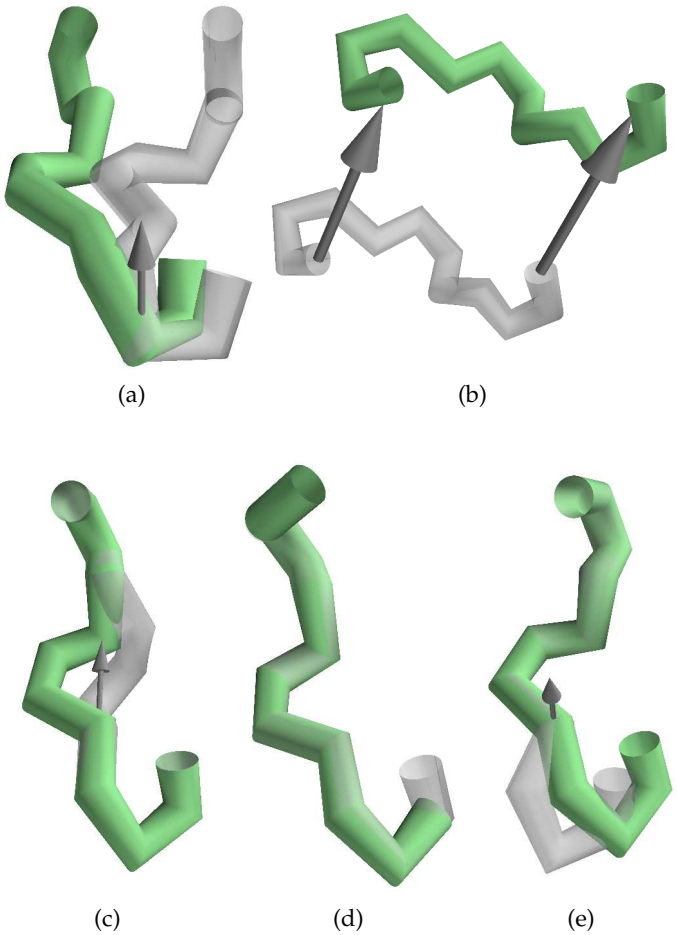

Figure 3.1: Illustration of the implemented peptide moves: (a) rotation move, (b) translation move, (c) crankshaft move, (d) reptation move, and (e) pivot move. The moves are explained in the text. The original position of the peptide is shown in transparent grey, the new positions in green. The arrows show a rotation axis or the path of a translation. The rotation angles in (a),(c), and (e) and the translation vector in (b) are bigger than the values used in our simulations to illustrate the effect of each move.

Crankshaft move

In a crankshaft move two beads of the same peptide get chosen randomly as start- and end-points. These two beads must be separated by one to five other beads. The connection vector of the two picked beads is normalised and the beads between the start- and end-point get rotated around this vector by a random angle. The angle is limited by a maximum value, like in the case of a rotation move. The crankshaft move in Figure 3.1 (c) uses the forth and eighth peptide, counted from the bottom, as the start- and end-beads and rotates the bead in between by 30°.

Reptation move

The algorithm for a reptation move selects the first or last bead of a given peptide at random. The selected bead is then moved to the opposite end of the peptide and connected to the last bead on that side of the peptide. The distance to the new neighbour is chosen according to the parameter r_0 of the FENE potential between peptide beads. The moved peptide is positioned in such a way that the angle that is formed between the last three peptides lies between 82° and 147°. In Figure 3.1 (d) the bead at the bottom is moved to the top of the peptide. The illustration for this and all following moves uses values for rotations and translations that are much bigger than those implemented to visualise the effect of each move.

Pivot move

A pivot move is comparable to a rotation move, but only some beads of a peptide get rotated. To do such a move, one bead of the peptide gets selected as a rotation centre randomly and either the beads preceding or following the chosen one get rotated around a random vector by a random angle. Again, this angle is limited by a rotation range. In the illustration of the move given in Figure 3.1 (e), the fifth bead from the bottom is chosen as the rotation centre and the preceding beads are rotated.

3.3.3 *Peptide move frequency*

The different moves for peptide beads are not carried out with equal frequency. Pivot and reptation moves are done in ten percent of all peptide moves, crankshaft moves in 30 percent, translation and rotation moves in 25 and 24 percent, respectively. Single peptide bead moves are done in one of hundred cases.

3.3.4 *Solvent beads*

To change the configuration of the solvent, only single bead moves are carried out. The move of a solvent is similar to the moves of a lipid and the single bead peptide moves: A solvent bead is selected at random and translated by a random vector. The elements of the vector are limited. The move range of solvent beads can be bigger than the move range of a lipid or peptide bead, due to the fact that solvent beads do not interact with each other. Therefore a solvent bead move can only be rejected if at least one peptide or lipid bead is in the interaction radius of the moved solvent bead.

3.3.5 *Volume and shear moves*

The volume changing moves in our simulations are illustrated in Figure 3.2 (a) for 2D, or as a top view on a 3D system, with a change in two directions simultaneously. By applying a volume move, one or more directions of the system change by Δl that can have a positive or negative value. All bead positions get

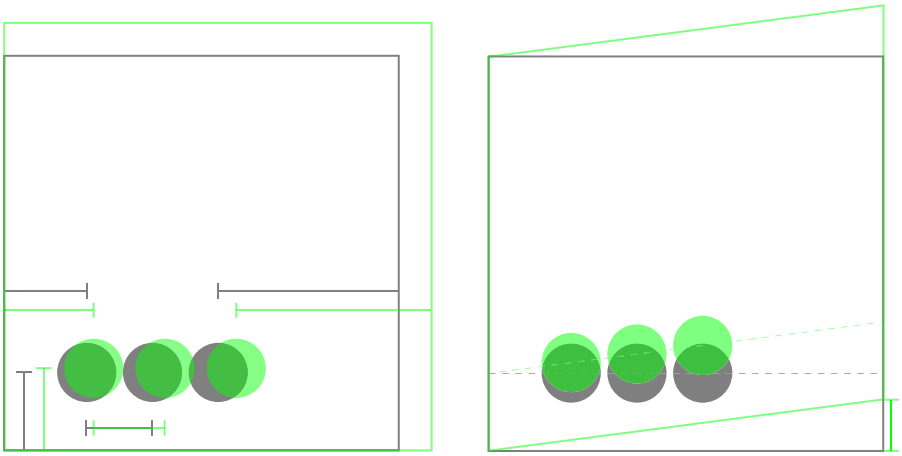

(a) (b)

Figure 3.2: Illustration of a volume move (a) and a shear move (b) in 2D, or as a top view on a 3D system. The systems in grey and green show the simulation before and after applying the move. Like in the illustrations for the different peptide moves, the move ranges shown here are much bigger than the values used in our simulation to visualise the effect of each move.

scaled according to the length change, the relative positions relative to the simulation box stay the same, e.g. a bead in the centre of the simulation box stays in the centre after a volume move. The distances to neighbour beads change, thereby changing the potential energy of the system. In our simulations we use two different ways to apply volume moves. When only peptide and solvent beads are simulated, the volume is changed in all three directions at the same time. This prevents the growth of the system in one direction by shrinking in another at the same time. In a system where one or two directions shrink to a very small value, peptides can interact with themselves, or fibrillar structures that percolate, can form. In simulations with lipid, peptide and solvent beads, the length of the system is changed in x and y direction at the same time, the length in z direction is changed individually. We change x and y directions at the same time, because they span the plain the lipid membrane lies in. The z direction can be changed separately, because the membrane normally prevents the shrinking or stretching of the system in the x and y direction.

Shear move

We adopted the shear moves from the original implementation of the lipid model. In a shear move, the position of the beads in one direction gets scaled based on the position in a second direction and a shear factor. Shear moves are implemented in our simulations to prevent shear stress of the membrane, caused by beads that do not fit to their periodic boundary neighbours[92]. In the illustration of this move in Figure 3.2 (b), the system (grey) gets shifted upwards (green). The vertical shift of each bead is in this example connected to its position on the horizontal axis.

In pre-runs both volume and shear move are applied at every MC step, that is, after one move was done for every bead in the simulation on average. In production-runs volume and shear moves are applied after every 50th MC step.

3.3.6 *Move ranges*

Each of the bead moves presented above is limited by a move range. In moves where beads get rotated, this is a maximum value for the rotation angle, in case of a translation a maximum value for each element of the translation vector. The only exception to this rule is the reptation move, as there is no translation or rotation involved. The move ranges and maximum angles for all other moves are set to an initial value at the start of a pre-run and adjusted during the pre-run according the *Loeding acceptance rate adaption* [127], to reach an acceptance rate of 30 percent.

Part II

MEASUREMENTS

4

PEPTIDE BEHAVIOUR

To investigate the behaviour of the peptide model, we start with simulations of a single peptide in solvent. All simulations run using one peptide consisting of twelve beads and 1818 solvents. Volume changing moves are only done in all three dimensions at once, to prevent the simulation box to shrink in one or more directions to very small sizes. In simulations with small dimensions in one or more directions, it can happen that the peptide interacts with a mirror image of itself, which would influence the measurement. The peptides are prepared in an α-helical conformation and placed in the centre of the simulation box. During the first 20 000 steps, the hydrophobic interactions between the peptide beads and the hydrogen bond energies are disabled to allow the peptide to organise into a stretched configuration. A pre-run of 100 000 steps is done for every simulation to adjust the move range of peptide and solvent moves. We strive for an acceptance rate of 30 percent for each type of move. Following this pre-run, a production-run consisting of 1 million steps is carried out for each simulation. The peptide bead positions, which are saved every thousandth step, are used to measure the peptide structure. The setup for the simulations discussed in this chapter is illustrated in Figure 4.1.

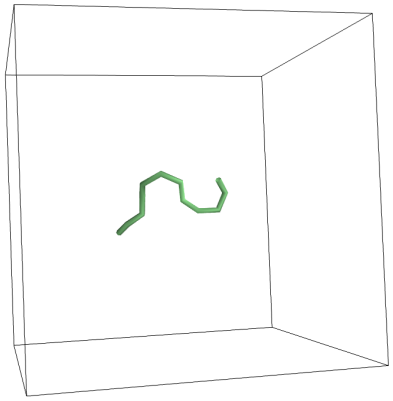

Figure 4.1: Setup for the simulations described in this chapter. The picture was taken from an early stage of a simulation with $\epsilon_{HH} = 0.1\epsilon$, $E_{HB,\text{ non-local}} = -2.0\epsilon$. For clarity the solvent beads inside the simulation box are not shown.

4.1 PEPTIDE STRUCTURE

We distinguish between four different peptide structures: α-helices, β-helices, β-sheets and random coil peptides. The following subsections describe how we detect each structure. The following equations are used to calculate a value between 0 and 1 for each structure:

$$N(p) = \text{Number of beads of peptide } p \tag{4.1}$$

$$N_{B,t}(p) = \text{Number of hydrogen bonds of type } t \text{ in peptide } p \tag{4.2}$$

$$P_{S,t}(p,i) = \text{Label of the bead where the } i\text{th hydrogen bond of type } t \text{ in peptide } p \text{ starts} \tag{4.3}$$

$$P_{E,t}(p,i) = \text{Label of the bead where the } i\text{th hydrogen bond of type } t \text{ in peptide } p \text{ ends} \tag{4.4}$$

$$D_{B,t}(p) = \frac{1}{N_{B,t}-1}\sum_i \{P_{S,t}(p,i+1) - P_{S,t}(p,i)\}$$ Mean "distance number" of hydrogen bonds of type t in peptide p. Here the term "distance number" refers to the number of bonds between two beads in a peptide. (4.5)

$$B_B(p,i) = P_{E,nl}(p,i) - P_{S,nl}(p,i)$$ bridge number of a non-local hydrogen bond in a peptide p (4.6)

$$M_B(p) = \frac{1}{N_{B,t}-1}\sum_i B_B(p,i)$$ Mean bridge number of non-local hydrogen bonds in peptide p (4.7)

$$S_\beta(p) = \frac{1}{N_{B,nl}(p)}\sum_i \begin{cases} 1 & \text{if} \quad P_{E,nl}(p,i+1) < P_{E,nl}(p,i) \\ 0 & \text{otherwise} \end{cases} \tag{4.8}$$

Calculates the fraction of hydrogen bonds pairs which fulfils the condition $P_{E,nl}(p,i+1) < P_{E,nl}(p,i)$

4.1.1 *α-helices*

To recognise an α-helical structure with our algorithm, two conditions must be fulfilled:

- Two or more local hydrogen bonds must be formed between beads of the peptide under consideration.
- The mean distance number of the hydrogen bonds $D_{B,t}(p)$ must be smaller than 1.5. The mean distance number is defined in Equation 4.5.

If both conditions are fulfilled, we calculate the value associated with the α-helicity as the number of local hydrogen bonds formed, divided by the maximal possible number of local hydrogen bonds for a peptide of the given length. The value of α-helicity can thus be calculated as:

$$f_{\alpha H}(p) = \begin{cases} 0 & \text{if} \quad N_{B,l}(p) \leqslant 1 \text{ or } D_{B,l}(p) > 1.5 \\ \dfrac{N_{B,l}(p)}{N(p)-3} & \text{otherwise} \end{cases} . \tag{4.9}$$

$N_{B,l}(p)$ and $D_{B,l}(p)$ are the number of local hydrogen bonds, and the mean distance of the local hydrogen bonds in peptide p, as given in Equation 4.2 and 4.5.

4.1.2 β-*helices*

The algorithm we use to recognise β-helices is very similar to the one used for α-helices:

- Three or more non-local hydrogen bonds must be formed between the beads of the given peptide.
- The bridge number $B_B(p,i)$ of each bond must not deviate from the mean bridge number of all non-local bonds by more than 1. The bridge number is defined in Equation 4.6.
- The mean distance number $D_{B,nl}(p)$ (Equation 4.5) between adjacent hydrogen bonds must be smaller that 1.5.

The total number of non-local hydrogen bonds in the given peptide is then divided by the maximal possible number of non-local hydrogen bonds with a length of $D_{B,nl}(p)$ for a peptide of the given length. The three conditions then lead to the formula

$$f_{\beta H}(p) = \begin{cases} 0 & \text{if} \quad N_{B,nl}(p) \leqslant 2 \\ \dfrac{N_{B,nl}(p)}{N(p) - 2 - D_{B,nl}(p)} & \text{if} \quad M_B(p) - B_B(p,i) < 1 \quad \forall i \\ 0 & \text{otherwise} \end{cases} . \tag{4.10}$$

Figure 4.2 illustrates two peptides, one forms an α- the other a β-helix.

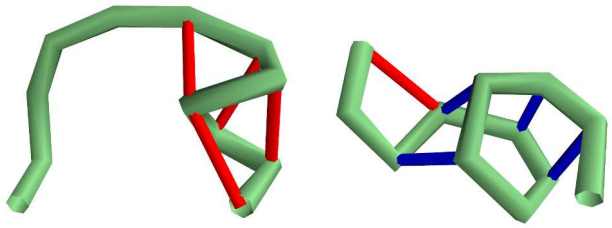

(a) (b)

Figure 4.2: a) Example of a peptide with a measured α-helicity $= 0.44$ (four of nine possible local hydrogen bonds (red) formed) and β-helicity $= 0$ (no non-local internal hydrogen bonds), b) Peptide with a measured α-helicity $= 0$ (only one local hydrogen bond) and β-helicity $= 0.8$ (four of five possible non-local internal hydrogen bonds with length 5 (blue) formed).

4.1.3 β-*sheet*

To calculate the β-sheet property, the algorithm stores for all non local hydrogen bonds i in a peptide the start point $P_{S,nl}(p,i)$ and the end point $P_{E,nl}(p,i)$ of the bond. The following conditions must be fulfilled to recognize a β-sheet:

- More than one non-local hydrogen bond has to be formed.
- In at least 60% of the pairs of adjacent hydrogen bonds (i, i+1), the position of the end of the later bond $P_{E,nl}(p,i+1)$ must be smaller than or equal the position of the end of the first hydrogen bond $P_{E,nl}(p,i)$.

If both conditions are met, the number of non-local hydrogen bonds is divided by the number of maximal possible non-local hydrogen bonds in a β-sheet. Figure 4.3 illustrates the conditions listed above.

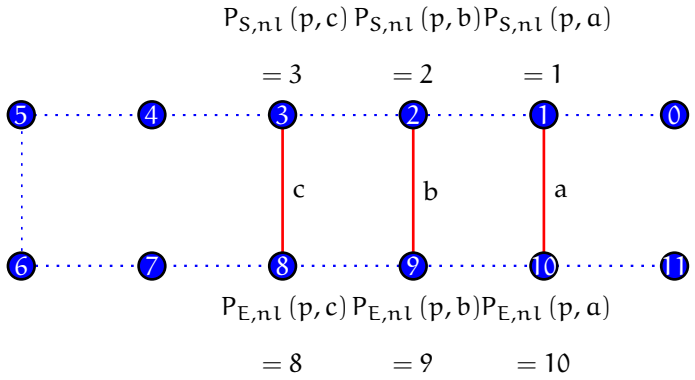

Figure 4.3: Illustration of a peptide with a β-sheet-property of 1.0: The illustrated peptide consists of twelve beads (blue). The dotted line marks the peptide backbone. All possible non-local hydrogen bonds (a - c) have formed: between beads 1, and 10 (a), between beads 2 and 9 (b), and between beads 3 and 8 (c). For both pairs of neighbouring hydrogen bonds (a,b) and (b,c) the end position of the bonds is smaller for later bonds: $P_{E,nl}(p,b) < P_{E,nl}(p,a)$ and $P_{E,nl}(p,c) < P_{E,nl}(p,b)$. Beads 4 and 5 can not be connected by a non-local hydrogen bond, because two beads must be separated by at least four other beads on the same peptide to form a non-local hydrogen bond. Bead 0 and 11 do not form a non-local hydrogen bond, as they are only allowed to form local bonds.

Using Equation 4.8, the formula to calculate the β-sheet-property can be written as

$$f_{\beta S}(p) = \begin{cases} 0 & \text{if} \quad N_{B,nl}(p) \leqslant 1 \\ 0 & \text{if} \quad S_\beta(p) < 0.6 \\ \dfrac{N_{B,nl}(p)}{\lfloor 0.5 \cdot (N(p) - 6) \rfloor} & \text{otherwise} \end{cases}, \tag{4.11}$$

where $\lfloor x \rfloor$ is the floor function.

	A	B	C
$E_{HB,\,local}$	-4.0	-5.5	-8.0
$E_{HB,\,non\text{-}local}$	-2.8	-3.85	-5.6
$E_{HB,\,cooperative}$	-1.2	-1.65	-2.4
k_0	14.1006	19.3883	28.2011

Table 4.1: The values used for the simulations described in this chapter. The values for the different hydrogen bond energies are given in units of ϵ.

4.1.4 *Random coil peptides*

If the peptide does not form an α-helix, β-helix, or a β-sheet, it is sorted into the group of random coil peptides. To plot the amount of random coil peptides, we can use the following function:

$$f_{rc}(p) = 1.0 - f_{\alpha H}(p) - f_{\beta H}(p) - f_{\beta S}(p) \quad . \tag{4.12}$$

An example for a β-sheet and a random coil peptide is shown in Figure 4.4.

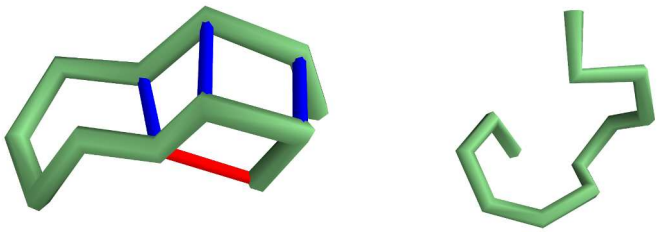

(a) (b)

Figure 4.4: a) Example of a peptide with a measured β-sheet-property of 1.0 (all possible non-local internal hydrogen bonds formed), b) a peptide in a random coil configuration.

In this chapter, systems with three different sets of hydrogen bond energies are simulated. The different values for local, non-local, and cooperative hydrogen bonds, together with the spring parameter k_0 used in each set, are given in Table 4.1. Here and in the following, each group is referred to by the energy associated with local hydrogen bonds $E_{HB,\,local}$. Here and in the following chapters, if not otherwise stated, the energies $E_{HB,\,local}$, $E_{HB,\,non\text{-}local}$, and $E_{HB,\,cooperative}$ have the following relations:

$$E_{HB,\,non\text{-}local} = 0.7 E_{HB,\,local} \quad , \quad E_{HB,\,cooperative} = 0.3 E_{HB,\,local} \quad .$$

For each column in Table 4.1, three types of simulations are discussed in the following, first with values of $E_{HB,\,local}$ varied between -2.0ϵ and -12.0ϵ with a step size of 0.2ϵ and fixed values of $E_{HB,\,non\text{-}local}$ and $E_{HB,\,cooperative}$, second

with values of $E_{HB,\,\text{non-local}}$ varied in the region between -2.0ϵ and -12.0ϵ with a step size of 0.2ϵ and fixed values of $E_{HB,\,\text{local}}$ and $E_{HB,\,\text{cooperative}}$, and third with values of $E_{HB,\,\text{cooperative}}$ varied between -0.2ϵ and -4.0ϵ with a step size of 0.2ϵ and fixed values of $E_{HB,\,\text{local}}$ and $E_{HB,\,\text{non-local}}$. In all simulations, k_0 is fixed to the value given in Table 4.1 in the corresponding column. The value for the interaction between hydrophobic peptide beads is varied in all simulations between $\epsilon_{HH} = 0.1\epsilon$ and $\epsilon_{HH} = 2.0\epsilon$ in steps of 0.1ϵ. For each set of E_{HB} and ϵ_{HH} we averaged over all steps in the production-run of 32 independent simulations. Examples of peptide structures which occurred in the simulations, are marked and shown underneath the plots of the different structure measurements.

4.2 WEAK HYDROGEN BONDS ($E_{HB,\,\text{LOCAL}} = -4.0\epsilon$)

For simulations with weak hydrogen bonds we use the parameters shown in Table 4.1, column A. Figure 4.5 shows the measured structures for all three types of simulations with this set of hydrogen bonds (variation of the value of either $E_{HB,\,\text{non-local}}$, $E_{HB,\,\text{local}}$, or $E_{HB,\,\text{cooperative}}$).

In the first set of simulations, with varied $E_{HB,\,\text{non-local}}$, shown in the first row of Figure 4.5, no α-helices are observed. The majority of peptides adopts either a random coil or a β-helical structure. In simulations with small (absolute) values of $E_{HB,\,\text{non-local}}$ the peptides adopt a random coil conformation, for stronger hydrogen bonds β-helices are observed. β-sheets are observed in the transition zone of random coil to β-helical peptides which is between $E_{HB,\,\text{non-local}} = -4.0\epsilon$ and -6.0ϵ. Additionally, they are observed for cooperative hydrogen bond energies stronger than -10ϵ. In both cases the maximum values for β-sheets are much smaller than those measured for random coil and β-helical peptides in their preferred regions. The transition zone from random coil peptides to peptides forming β-helices shows a shift towards smaller (absolute) values of $E_{HB,\,\text{non-local}}$ for higher values of ϵ_{HH}. This shift is also visible in the values obtained for the measurements of β-sheets. For non-local hydrogen bond energies below -10.0ϵ, the amount of β-sheets rises because the non-local hydrogen bonds are strong enough in this area to trap a peptide in its position, once a hydrogen bond is formed. A peptide that would normally bend to form a helix, gets trapped by the first possible non-local hydrogen bond that develops. If the bending happens between the beads placed in the peptide centre, more hydrogen bonds can form between the peptide beads towards both ends of the peptide and form a β-sheet like structure.

α-helices do not play a role in simulations for these hydrogen bond energies, because the value for local hydrogen bonds $E_{HB,\,\text{local}}$ is fixed at a value, which is to small compared to the other interaction energies applied on the peptide, to form stable local hydrogen bonds. The transition from random coil to β-helical peptides shows the rising importance of the non-local hydrogen bond energy compared to the other interaction energies. For low values of $E_{HB,\,\text{non-local}}$ the energies are not strong enough to form stable bonds, the interactions with solvent beads prevent those structures to be formed. With the non-local energies rising, the relative influence of interactions with solvents

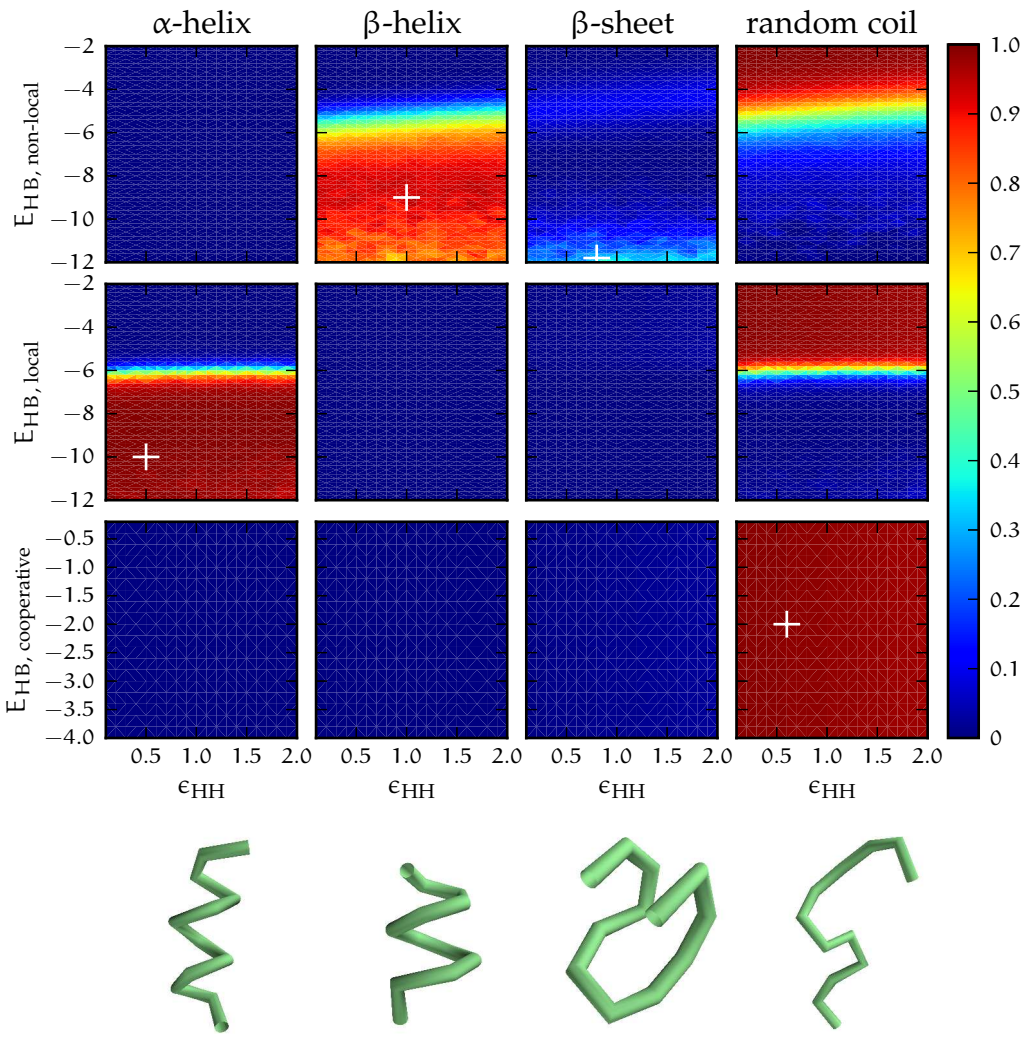

Figure 4.5: Measured structure of a single peptide average over all steps in production-run for 32 simulations per value. The columns show the structure which is measured according to Equation 4.9 for α-helices, 4.10 for β-helices, 4.11 for β-sheets, and 4.12 for random coils. The rows show the hydrogen bond energy (non-local, local, or cooperative) which is altered in the simulations, while the other two are held constant at the value given in Table 4.1, column A. The last row shows one example of each structure, the simulation the image is taken from is marked by white crosses in the column above.

decreases, allowing the peptides to form β-helices and β-sheets. By forming those structures, the peptides gain extra energy due to the cooperative energy accounted for hydrogen bonds formed between adjacent peptide beads.

In simulations with varied local hydrogen bond energies, shown in the second row of Figure 4.5, no β-helices or β-sheets are observed. Like in simulations with varied $E_{HB,\,non\text{-}local}$, the peptides adopt a random coil conformation in simulations with small hydrogen bond energies. For values of $E_{HB,\,local}$ between -5.0ϵ and -7.0ϵ, the fraction of random coil peptides decreases, to-

gether with an increase of the measured fraction of α-helical peptides. No β-helices or β-sheets are formed, independent of both $E_{HB,\,local}$ and ϵ_{HH}, as the non-local hydrogen bond values are fixed to a value, small compared to the other interactions applied, comparable to the situation of α-helices in simulations discussed above.

In contrast to the simulations with varied non-local hydrogen bond energies, the starting point of the transition from random coil to helical structures is only increasing slightly with higher values of ϵ_{HH}; between $\epsilon_{HH} = 0.1\epsilon$ and $\epsilon_{HH} = 2.0\epsilon$ the transition from random coil peptides to α-helices is shifted only by 0.2ϵ towards higher values of $E_{HB,\,local}$. In the model discussed in this thesis, each turn of an α-helix consists of four beads, the turns in β-helices, observed in the simulations, consist of six beads. The number of hydrogen bonds between beads in a peptide forming an α-helix is thus higher than in a peptide forming a β-helix. This is illustrated in Figure 4.6. In Figure 4.7 (a) the

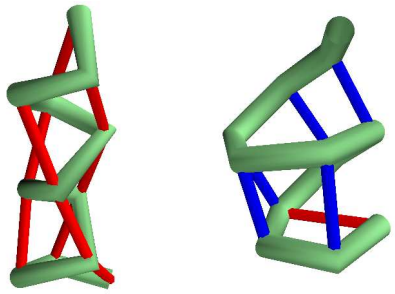

(a) (b)

Figure 4.6: Illustration of a) an α-helix, with four beads per turn and b) a β-helix, with six beads per turn. The α-helix is formed by nine local hydrogen bonds (red), whereas the only five non-local hydrogen bonds (blue) form the structure of the β-helix.

average hydrogen bond energies per peptide for α-helices and β-helices, taken from simulations with $E_{HB,\,local} = -8.0\epsilon$, $E_{HB,\,non\text{-}local} = -2.8\epsilon$ for α-helices and $E_{HB,\,local} = -4.0\epsilon$, $E_{HB,\,non\text{-}local} = -8.0\epsilon$ for β-helices are plotted. The values are obtained from simulations with $E_{HB,\,local} = -8.0\epsilon$ and $E_{HB,\,non\text{-}local} = -3.85\epsilon$ for α-helices and $E_{HB,\,local} = -5.5\epsilon$ and $E_{HB,\,non\text{-}local} = -8.0\epsilon$ for β-helices. In both cases, the values for cooperative hydrogen bonds is set to -1.2ϵ. The different sets of $E_{HB,\,non\text{-}local}$ and $E_{HB,\,local}$ were chosen, to show the influence of the interaction energies applied to non adjacent peptide beads which are connected by hydrogen bonds of the same strength.

Figure 4.7 (a) shows that ϵ_{HH} influences the hydrogen bond energy only slightly in the case of β-helices; E_{HB} decreases from $-42.01 \pm 0.02\epsilon$ for $E_{HH} = 0.1\epsilon$ to $-43.15 \pm 0.02\epsilon$ for $E_{HH} = 2.0\epsilon$. In the case of α-helices, E_{HB} does not change with changing E_{HH}.

The total energy of hydrophobic interactions E_{nA} varies with the value of ϵ_{HH}, as the strength of the LJ potential, used to calculate the interaction, is determined by ϵ_{HH}. This is shown in Figure 4.7 (b). For β-helices the influence of ϵ_{HH} is stronger. This is caused by the fact that the average distance between beads, connected by non-local hydrogen bonds, is smaller than between those

connected by local hydrogen bonds. Dividing E_{nA} by E_{HB} reveals the increasing influence of hydrophobic interactions on the peptide energy for higher values of ϵ_{HH}, see Figure 4.7 (c). In peptides forming β-helices, this influence increases faster, leading to a bigger shift of the start- and end-points of the transition zone from random coil peptides to β-helices for higher values of ϵ_{HH} (first row of Figure 4.5), compared to the shift of the transition zone from random coil peptides to α-helices (second row of Figure 4.5).

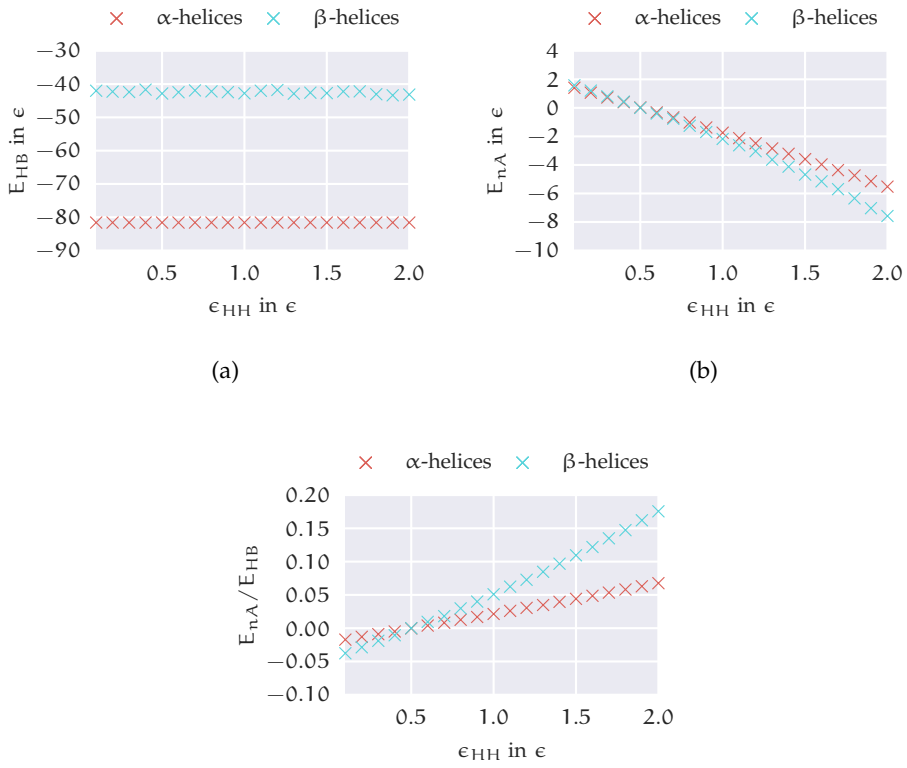

Figure 4.7: The three images show the influence of ϵ_{HH} on peptides forming α-helices or β-helices. a) average value of the total hydrogen bond energy E_{HB}, b) average value of the total energy of hydrophobic interactions in a peptide E_{nA} c) E_{nA} divided by E_{HB}. The values for α-helices were taken from simulations with $E_{HB,\,local} = -8.0\epsilon$, $E_{HB,\,non\text{-}local} = -2.8\epsilon$, those for β-helices from simulations with $E_{HB,\,local} = -8.0\epsilon$,$E_{HB,\,non\text{-}local} = -4.0\epsilon$. In both cases the energy for cooperative hydrogen bonds was set to -1.2ϵ, according to Table 4.1, column A. The total hydrogen bond energy stays constant, whereas the value of E_{nA} decreases. This decrease is faster in peptides forming β-helices. See text for details.

The results for varied values of $E_{HB,\,cooperative}$ are shown in the third row of Figure 4.5. As the energies of local and non-local hydrogen bonds are too weak to form stable hydrogen bonds in these simulations, neither α-helices nor β-helices form in these simulations, independent of the cooperative hydrogen bond energy $E_{HB,\,cooperative}$ and the interaction energy between hydrophobic peptide beads ϵ_{HH}. This is similar to the observations in the simulations with

varied non-local hydrogen bonds, where no α-helices formed independent of $E_{HB,\,\text{non-local}}$ and ϵ_{HH} and the simulations with varied local hydrogen bonds, where no β-helices were found. Also almost no β-sheets are measured. Towards high values of ϵ_{HH} only up to three percent of the measured peptides form β-sheets. The majority of the peptides adopt a random coil configuration. The portion of random coil peptides depends on the strength of the interactions between hydrophobic peptide beads, but is independent from the cooperative hydrogen bond energy. For low values of ϵ_{HH}, up to 97 percent of the peptides adopt a random coil configuration, towards $\epsilon_{HH} = 2.0\epsilon$ this value decreases towards 89 percent.

To form either α-helices, β-helices, or β-sheets, two or more hydrogen bonds have to be formed. Cooperative hydrogen bond energies only apply if at least two hydrogen bonds are formed in parallel. As our measurements show, no α- and β-helices are formed and only a small fraction of peptides form β-sheets, so the difference in cooperative hydrogen bond strength plays no active role in the simulations, and both the fraction of β-sheets and random coil peptides does not change with varying $E_{HB,\,\text{cooperative}}$. Although no β-helices are observed, we do observe β-sheets, as the peptides need only to bend once to form the latter, leading to a lower bending energy for a β-sheet, compared to a β-helix. In simulations with stronger non-local hydrogen bonds, the increase in bending stiffness energy E_{BA} can be compensated by the hydrogen bonds. This is not the case for the simulations discussed in this section.

4.3 NORMAL HYDROGEN BOND STRENGTH ($E_{HB,\,\text{local}} = -5.5\epsilon$)

The term *normal hydrogen bond* was chosen to refer to hydrogen bonds with a value of $E_{HB,\,\text{local}} = -5.5\epsilon$, because this value is used for simulations of hydrogen bonds with lipids that are presented in the following chapters. Like for weak hydrogen bonds, the behaviour for a single peptide with varied energies for non-local, local and cooperative hydrogen bonds as a function of the interaction energy between hydrophobic peptide beads ϵ_{HH} is investigated. The values for hydrogen bond energies and the bending stiffness used in these simulations are given in Table 4.1, column B. The results discussed in the following are shown in Figure 4.8.

In simulations with varied non-local hydrogen bond energy, the peptides prefer again β-helical and random coil conformations, depending on the hydrogen bond strength. β-sheets occur for values of $E_{HB,\,\text{non-local}}$ between the two regions of β-sheets and random coil peptides, and for strong hydrogen bonds. The reason for the formation of β-sheet like peptides in systems with strong hydrogen bonds is the same as described in the previous section. Opposite to the simulations with weaker hydrogen bonds, α-helices can be observed in these simulations. For $E_{HB,\,\text{non-local}}$ weaker than -5ϵ, up to ten percent of the measured peptides form α-helical structures.

The variation of local hydrogen bond strength leads to a majority of random coil peptides and α-helical structures. Random coil peptides again occur for weaker hydrogen bond energies, α-helical structures in simulations with val-

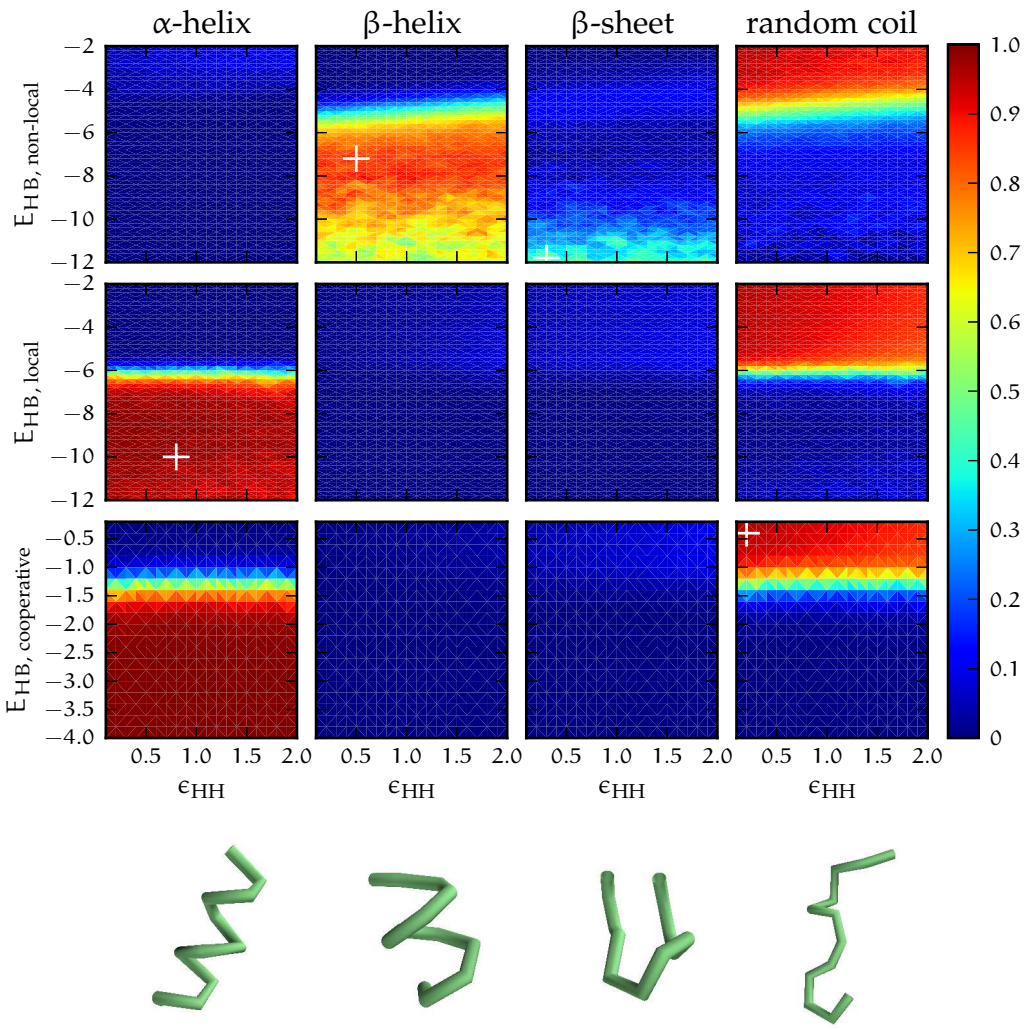

Figure 4.8: Same as Figure 4.5, with the values of hydrogen bond energies according to Table 4.1, column B.

ues of $E_{HB,\,local} < -5.6\epsilon$. In simulations with weak hydrogen bonds, up to ten percent of peptides form β-helices or β-sheets.

Both in simulations with varied local and non-local hydrogen bond strength, the peptides behave similar to those in simulations discussed in the previous section: helical structures develop in simulations with stronger hydrogen bonds, in simulations with weak hydrogen bonds, the peptides prefer random coil configurations. In simulations with varied cooperative hydrogen bond strength, the peptide behaviour changes. Changing the strength of cooperative hydrogen bonds leads to random coil peptides in the case of weak hydrogen bond simulations, shown in Figure 4.5. With the current set of hydrogen bond energies, the formation of random coil peptides and α-helices can be observed, as shown in the third row of Figure 4.8. For high values of ϵ_{HH} and weak cooperative hydrogen bond energies weaker than -6ϵ, also up to ten percent of β-sheets occur.

The slope in the amount of β-helices in simulations with varied non-local hydrogen bond energies, is comparable to the slope observed in the simulations discussed in Section 4.2. For all three types of simulations (varied $E_{HB,\text{ non-local}}$, $E_{HB,\text{ local}}$, or $E_{HB,\text{ cooperative}}$) the amount of random coil peptides shows a dependence on the value of ϵ_{HH}, opposite to the observations in the previous section. The decrease of the fraction of random coil peptides towards higher values of ϵ_{HH} is caused by the increase of helical structures, α-helices in the case of varied non-local hydrogen bonds, β-helices and β-sheets in simulations with varied local and varied cooperative bonds, in the same direction.

α-helical structures and β-sheets can be observed in simulations with varied cooperative hydrogen bonds, because the energies for $E_{HB,\text{ non-local}}$, $E_{HB,\text{ local}}$ and k_0 are fixed to values that allow the formation of those structures. Because the value for local hydrogen bonds is the strongest hydrogen bond energy in the system, the peptides adopt an α-helical structure for strong cooperative hydrogen bonds.

4.4 STRONG HYDROGEN BONDS ($E_{HB,\text{ LOCAL}} = -8.0\epsilon$)

The results for these simulations are shown in Figure 4.9. In simulations with varied non-local hydrogen bond energies, all three structures that are formed by hydrogen bonds can be measured. For low values of $E_{HB,\text{ non-local}}$ nearly all peptides adopt an α-helical structure. With increasing hydrogen bond strength, β-helices and β-sheets occur. As the peptides in the simulations tend to build many hydrogen bonds, due to the high hydrogen bond energies in the simulations, almost no peptide adopts a random coil configuration.

In the simulations described before the transition between different structures took place for simulations with hydrogen bond values between -4.0ϵ and -7.0ϵ, this transition zone is shifted towards stronger hydrogen bonds in simulations with varied local hydrogen bonds and energies for non-local and cooperative hydrogen bonds as given in Table 4.1, column C.

Towards stronger hydrogen bonds the fraction of β-helices decreases, like in the previous simulations parallel to an increase of β-sheets.

In simulations with varied local hydrogen bonds, shown in the second row of the Figure 4.9, the peptide behaviour, in regard to the formation of α- and β-helices, seems like a mirrored image of the first row: For weak non-local hydrogen bonds, the majority of peptides adopt a β-helical conformation, α-helices occur only for strong non-local hydrogen bonds. The slope of the transition area also shows this mirrored behaviour, towards higher values of ϵ_{HH}, the transition from β-helices to α-helices happens in simulations with stronger hydrogen bonds. In simulations with varied non-local hydrogen bonds, the transition from α- to β-helices is shifted towards weaker hydrogen bonds for higher values of ϵ_{HH}.

The fraction of β-sheets has its maximum in the area between the transition from β-helices to α-helices. As it lies between the areas of β- and α-helices it is also tilted towards stronger hydrogen bond energies for higher values of ϵ_{HH}.

In simulations with varied cooperative hydrogen bond energies, show in the third row, the fraction of both α- and β-helices is independent of the co-

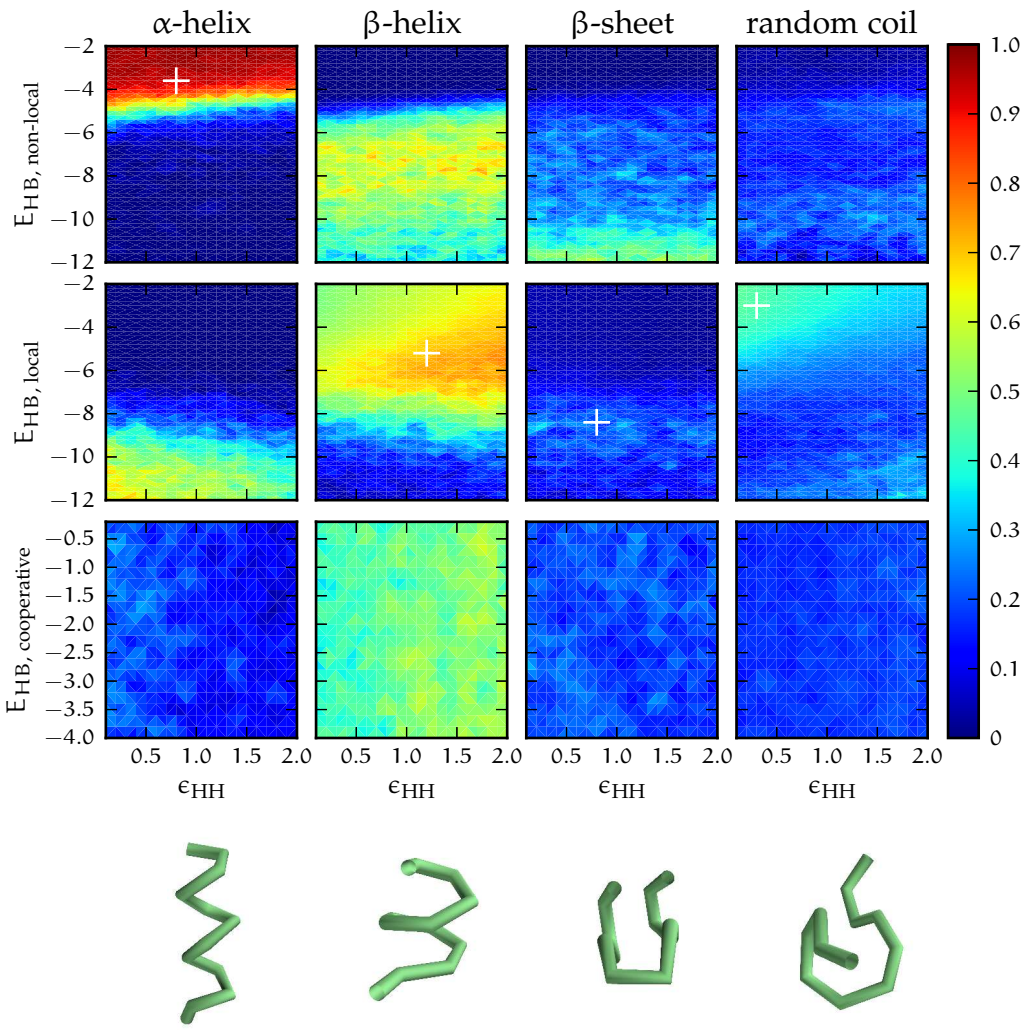

Figure 4.9: Same as Figure 4.5, with the values of hydrogen bond energies according to Table 4.1, column C

operative hydrogen bond energy applied to the peptides in the simulations. However, they both depend on the interaction energy between hydrophobic peptide beads ϵ_{HH}: The amount of α-helices decreases towards higher values of ϵ_{HH}, the amount of β-helices increases in this direction. As seen in the simulations with varied local and non-local hydrogen bonds, described before in this section, the energies applied for local and non-local hydrogen bonds are strong enough to form both, α- and β-helices. In the simulations described in the sections before - with hydrogen bond energies as given in Table 4.1 column A and B - only a transition between one of these structures and random coil peptides happens. Therefore the simulations with varied cooperative hydrogen bond energies described in this section show completely different results to those with weak and normal hydrogen bonds. The transition between α- and β-helices is not driven by the cooperative hydrogen bond energy, because in both structures parallel hydrogen bonds, which are the basis to apply the co-

operative hydrogen bond energy, are formed. However, the transition depends on ϵ_{HH}, as the distance between hydrophobic beads is smaller in β-sheets than in α-helices, leading to a bigger influence of ϵ_{HH} on β-helices, as described in Section 4.2.

4.5 CONCLUSION

The simulations discussed in the three sections before highlight the behaviour of a single peptide for different sets of hydrogen bond energies. For weak hydrogen bonds, the majority of peptides adopt a random coil conformation, unless one hydrogen bond energy, either local or non-local, is strong enough to stabilise α- or β-helices. With all energies associated with hydrogen bonds getting stronger, more and more peptides adopt an α- or β-helical structure, if the varied hydrogen bond energies are weak. The simulations with strong hydrogen bonds, described in the previous section, show that here a transition between α- or β-helical peptides is driven by the varied local and non-local hydrogen bond energy. The majority is shifted from random coil peptides in simulations with weak hydrogen bonds to peptides in a structure stabilised by hydrogen bonds. At the same time the region, in which the transition happens is shifted towards lower values of the varied energy for stronger hydrogen bonds. In simulations with varied non-local hydrogen bonds the transition zone between β-helices and random coil peptides, β-helices and α-helices respectively, overlaps with a local maximum of β-sheets, independent of the values for the fixed hydrogen bonds. The influence of ϵ_{HH} is not as strong as the varied hydrogen bond energy, but we can see differences in how much it influences structures based on local, and such based on non-local hydrogen bonds. The results of the simulations presented in this chapter help us to understand and interpret simulations with multiple peptides discussed in the following chapters.

Helical peptides and β-sheets in nature belong to the class of *marginally compact* [50, 128] peptide structures. These structures are characterized among others by an efficient space filling and the ability to squeeze water out of the hydrophobic core. Additionally these structures show a high flexibility, as they can adjust their conformation in response to interactions [129]. Experimental results additionally show that the propensity of peptides to form weakly stable α-helices plays a role in the process of fibril formation in the presence of a lipid membrane [76, 77]. The parameter set used for simulations in the following chapters should lead to the formation of helical structures and sheets which reproduce this flexibility and versatility. Therefore, neither those parameters used in Section 4.2, to simulate peptides with weak hydrogen bonds, nor those used in Section 4.4, to simulate strong hydrogen bonds, are suitable. Instead, the hydrogen bond energies that will be used in the following correspond to those used in Section 4.3, in all following simulations, local hydrogen bonds with a strength around -5.0ϵ will be used. As the simulations showed only a small dependence on the value of ϵ_{HH}, this value will be fixed to 0.6ϵ.

5 FIBRIL FORMATION

The peptide model described in Chapter 2 is designed to mimic fibril forming peptides. In this chapter, the ability of the model to mimic the formation of fibrils is proved. Additionally the differences in the process and the resulting structures in simulations with varied hydrogen bond energies are shown. After discussing the obtained structures and their different paths of formation, parameter sets that will be used to investigate the influence of lipid membranes in the following chapter, are explored.

5.1 SIMULATION SETUP

To investigate the formation of fibrils, systems consisting of 50 peptides, each composed of twelve beads, are simulated. All peptides are prepared in an α-helical conformation and placed randomly in a cubic simulation box. The box is filled with 14544 solvent beads. Because NpT ensembles are used for the simulations, the volume and therefore also the peptide concentrations vary. By using the approach described in [92], a conversion factor of $1\sigma \approx 6.9$Å can be calculated. Using this relation, the concentration of peptides in simulations that have run for several million steps and show only small volume changes can be determined to be in the range of 30 mMol per liter. Volume changing moves, applied as described in Section 3.3.5 to retain constant pressure, are carried out in all three directions simultaneously to keep the simulation box cubic. Without this requirement there is the possibility that the simulation box contracts in one ore more directions, leading to interactions of structures (single peptides, clusters, fibrils) in the simulation with mirrored images of itself. For each set of parameters 128 distinct simulations are run. An example of a setup is shown in Figure 5.1.

At the beginning of each simulation a pre-run is carried out that allows the parameters of peptide and volume moves to be adjusted in such a way that the acceptance rate for each type of move is about 30 percent. This pre-run consists of 100 000 steps, volume and shear moves are carried out every single step, the move ranges are adapted every two hundredth step. Measurements are also carried out every two hundredth step.

The pre-run is followed by a production-run consisting of at least 5 million steps. In the production-runs, volume and shear moves are carried out every fiftieth step, measurements every thousandth step. In both pre-run and production-run, whenever measurements are carried out also the positions of the peptide beads are saved in a file to be able to further investigate the interactions between and the structure of the peptides. For the reasons of performance and memory size, the positions of solvent beads are not saved in these files.

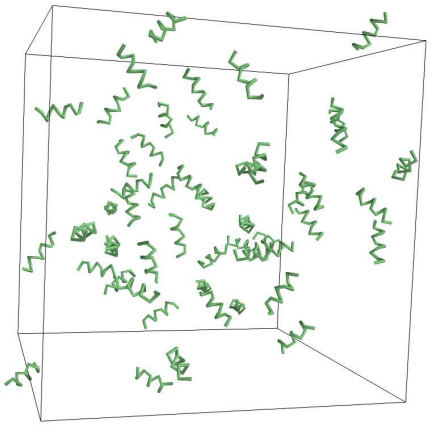

Figure 5.1: Setup for the simulation of fibril formation. 50 peptides in an α-helical conformation are placed randomly inside a cubic box. The 14544 solvent beads, which fill up the simulation box, are not shown for clarity. Peptides that seem to cross the boundaries of the simulation box in this illustration, enter the simulation box at the opposite side due to PBC.

5.2 MEASUREMENTS

A Python script is used to analyse the structure of the peptides that are saved during the simulations. Several methods are implemented in this script to detect different peptide structures. Two of them, which are needed for the simulations discussed in this chapter, are presented in the following.

5.2.1 *Fibril detection*

Two adjacent peptides belong to a fibril, when more than n_f hydrogen bonds are formed between beads of both peptides. If not stated otherwise, at least $n_f = 4$ hydrogen bonds must be formed between two peptides to count them as part of a fibril. The implemented algorithm calculates the number of peptides that are part of a fibril, the number of fibrils in the simulation, and the size (in number of peptides) of each fibril.

5.2.2 *Cluster detection*

To detect clusters the DBSCAN algorithm described in [130] was implemented. DBSCAN means *Density Based Spatial Clustering of Applications with Noise*. The algorithm distinguishes between three types of points: points inside a cluster, points outside a cluster, and points at the border of a cluster. A point p is taken to be inside a cluster, when at least N_{min} points can be found around point p which have a distance of d_ϵ or less to p. A point p is at the border of a cluster, when less than N_{min} points have a distance of d_ϵ from p, but p itself is positioned less than d_ϵ away from a core point. All points that are neither core nor border points are outside a cluster. The algorithm automatically detects the greatest possible cluster in a given set of points. In the implementation

used for this thesis the DBSCAN algorithm works on the set of peptide bead positions. If not otherwise stated, $d_\epsilon = 2.0$ and $N_{min} = 3$ is chosen.

As the Python scripts, used to detect clusters, use the same C++ classes the simulations use to handle cell lists, the algorithms presented before are able to detect structures that cross the boundaries of the simulation box. An illustration for the structures detected with both algorithms is given in Figure 5.2.

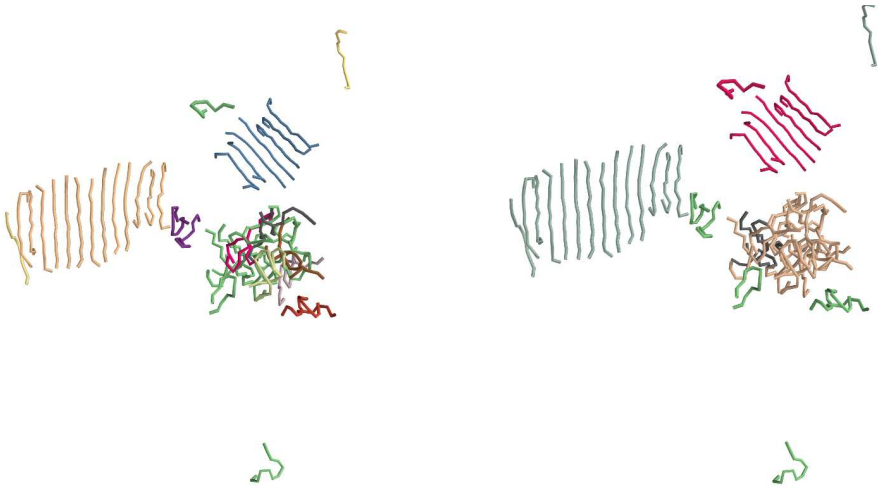

(a) (b)

Figure 5.2: Illustration of the different structures found in a simulation, peptides with the same color belong to the same structure. Green peptides could not be sorted to the structures under consideration. a) The algorithm implemented to find fibrillar structures found ten different fibrils, one consisting of thirteen, one of seven peptides. The other fibrils consist of two peptides. The peptide in the upper right corner, shown in yellow is connected to the yellow fibril on the left side due to PBC conditions. b) The cluster algorithm found four clusters, consisting of eighteen, fifteen, eight, and three peptides. Six peptides are not clustered. The grey peptide in the upper right corner belongs to the grey cluster on the left side. The parameters used here are $n_f = 4$, $d_\epsilon = 2.0$ and $N_{min} = 3$.

5.3 SIMULATIONS WITH HYDROGEN BOND ENERGIES BETWEEN -4.0ϵ AND -4.8ϵ

The parameters used for the simulations described in this section are shown in Table 5.1. The tables in Appendix E list all parameters used in the simulations discussed in this chapter for a complete overview. The different sets of simulations are referred to by the value used for $E_{HB,\,local}$. For all given hydrogen bond energies the number of peptides that are part of a fibril N_{PiF}, shown in Figure 5.3, quickly rises at the beginning of the pre-runs. In simulations with hydrogen bond energies between -4.0ϵ and -4.7ϵ, N_{PiF} stays constant at a low level during the production-runs. The value of N_{PiF} depends on the hydrogen bond energies in the simulation, it rises with stronger hydrogen bonds.

$E_{HB,\,local}$	k_0
-4.00ϵ	14.1006
-4.10ϵ	14.4531
-4.20ϵ	14.8056
-4.30ϵ	15.1581
-4.40ϵ	15.5106
-4.50ϵ	15.8631
-4.60ϵ	16.2157
-4.70ϵ	16.5682
-4.80ϵ	17.2732

Table 5.1: The values for the hydrogen bond energies and the peptide bending stiffness used for simulations with local hydrogen bond energies between -4.0ϵ and -4.8ϵ. The relations $E_{HB,\,non\text{-}local} = 0.7 \times E_{HB,\,local}$ and $E_{HB,\,cooperative} = 0.3 \times E_{HB,\,local}$ are used for the energies of non-local and cooperative hydrogen bonds.

For $E_{HB,\,local} = -4.8\epsilon$, N_{PiF} is no longer constant, but rises during the simulation.

The number of peptides per fibril N_{PpF} behaves accordingly; for hydrogen bond energies between -4.7ϵ and -4.0ϵ the value of N_{PpF} stays at a constant low level, simulations with stronger hydrogen bonds lead to more peptides per fibril. For $E_{HB,\,local} = -4.8$, N_{PpF} rises, but stays below 3.0. The plotted curves of N_{PpF} can be found in Figure 5.4.

At the beginning of the pre-runs, several peptide clusters form quickly, as shown in Figure 5.5, independent of the hydrogen bond strength in the simulation. The number of clusters N_C decreases after about twelve thousand steps. This decrease continues at the beginning of the production-runs and ends after about half a million steps at a level of 1.2 to 1.4 clusters per simulation on average. The number of clusters increases at the beginning of the simulations, because the simulations start with randomly distributed peptides. The algorithm described in Section 5.2.2 finds a cluster when at least three peptides meet, therefore it is expected that several clusters form at the beginning.

For the values of $E_{HB,\,local}$, described in this section, attempts of the formation of fibrils are observed, but the average size of those structures that form is small. For $E_{HB,\,local} \geqslant -4.7$, these structures do not grow during the simulations. Only for $E_{HB,\,local} = -4.8$, the fibrils that form during the simulations grow in size, but the growth rate is far too small, to measure a majority of peptides to be part of a fibril within reasonable simulation times.

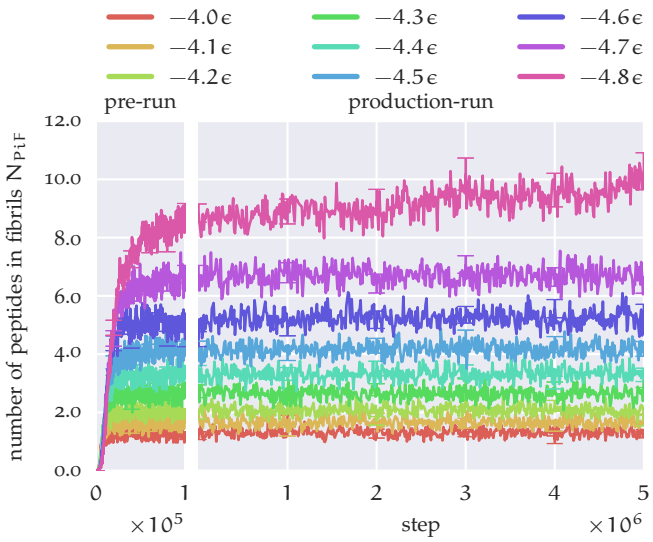

Figure 5.3: The total number of peptides in fibrils N_{PiF} for simulations with hydrogen bond energies between −4.0ϵ to −4.8ϵ. The number of peptides in fibrils during the pre-runs are shown on the left side, those during the production-runs are shown on the right side. The step number on the x-axis is separated for pre-runs and production-runs, both start at zero. The data for the pre-runs was obtained every two hundredth step, the data for the production-runs every ten thousandth step. Please note the different scaling of the x-axis of pre-runs and production-runs.

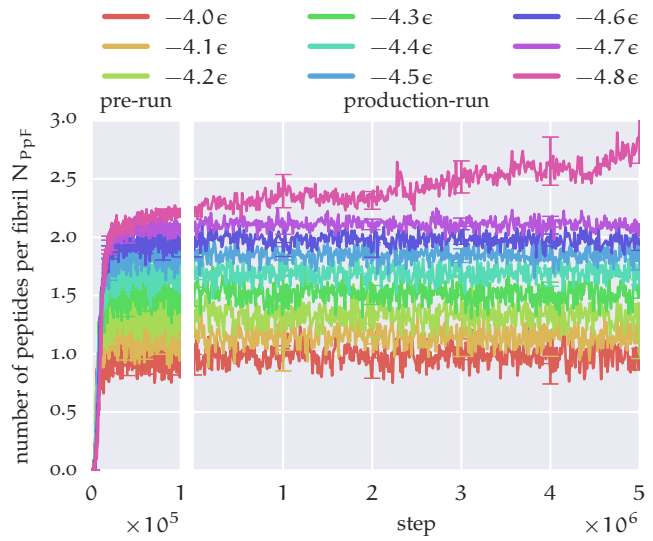

Figure 5.4: The number of peptides per fibrils N_{PpF} for simulations with hydrogen bond energies between −4.0ϵ and −4.8ϵ. The structure of the plot is as described in Figure 5.3.

5.4 SIMULATIONS WITH HYDROGEN BOND ENERGIES BETWEEN −4.9ϵ AND −5.5ϵ

The parameters used in the simulations are given in Table 5.2, a complete overview of the used parameters can again be found in Appendix E. In simulations

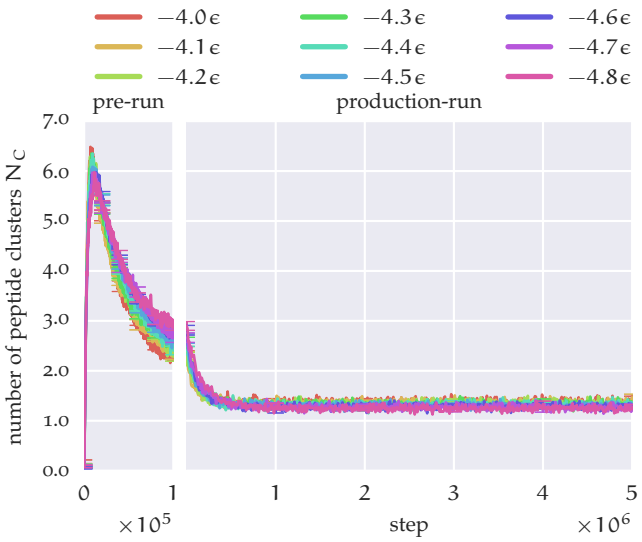

Figure 5.5: The number of clusters N_C for simulations with hydrogen bond energies between -4.0ϵ and -4.8ϵ. The structure of the plot is as described in Figure 5.3.

with local hydrogen bond energies lower than -4.9ϵ, fibrils consisting of more than three peptides exist, in contrast to the simulations with local hydrogen bonds of -4.8ϵ or weaker. As shown in Figure 5.6, N_{PiF} quickly rises in the pre-runs and the increase continues in the production-runs. How quick all peptides get part of a fibril also depends on the strength of the hydrogen bonds, the stronger the bonds, the quicker all peptides get incorporated. In simulations with $E_{HB,\,local} = -5.5\epsilon$ all peptides are part of a fibril after 3.5×10^5 steps, for $E_{HB,\,local} = -5.0\epsilon$, this state is reached after about 2.2×10^6 steps; for $E_{HB,\,local} = -4.9\epsilon$, it takes more than 8×10^6 steps, until the average number of peptides in fibrils reaches values around 50.

The number of peptides per fibril N_{PpF} in Figure 5.7, behaves completely different compared to the simulations with $E_{HB,\,local} \leqslant -4.8$. During the pre-runs, the N_{PpF} starts to increase. In the production-runs the value of N_{PpF} continues to rise, independent of $E_{HB,\,local}$. In simulations with stronger hydrogen bonds the number of peptides per fibril rises quickly. As described in the previous paragraph and shown in Figure 5.6, all peptides in the simulation are part of a fibril after 3.5×10^5 to 2×10^6 steps, depending on $E_{HB,\,local}$. Therefore the curves of N_{PpF} show a kink as soon as almost all peptides are part of a fibril. After 5×10^6 steps, the fibrils in simulations with stronger hydrogen bonds are on average smaller than those in simulations with weaker hydrogen bonds. The only exceptions from this rule are the simulations with $E_{HB,\,local} = -4.9\epsilon$, the fibrils there are about 0.8 peptides smaller than the fibrils observed in simulations with $E_{HB,\,local} = -5.0\epsilon$. This is caused by the slow growth of fibrils in those simulations: After 5×10^6 million steps, not all peptides are part of a fibril in those simulations. However, after 8×10^6 steps, when all peptides are part of a fibril, these fibrils are bigger than those observed in simulations with stronger hydrogen bonds.

$E_{HB,\,local}$	k_0
-4.90ϵ	17.2732
-5.00ϵ	17.6257
-5.10ϵ	17.9782
-5.20ϵ	18.3307
-5.30ϵ	18.6833
-5.40ϵ	19.0358
-5.50ϵ	19.3883

Table 5.2: The values for the hydrogen bond energies and the peptide bending stiffness used for simulations with local hydrogen bond energies between -4.9ϵ and -5.5ϵ. Like for the simulations discussed in the previous section, the relations $E_{HB,\,non\text{-}local} = 0.7 \times E_{HB,\,local}$ and $E_{HB,\,cooperative} = 0.3 \times E_{HB,\,local}$ are used for the energies of non-local and cooperative hydrogen bonds.

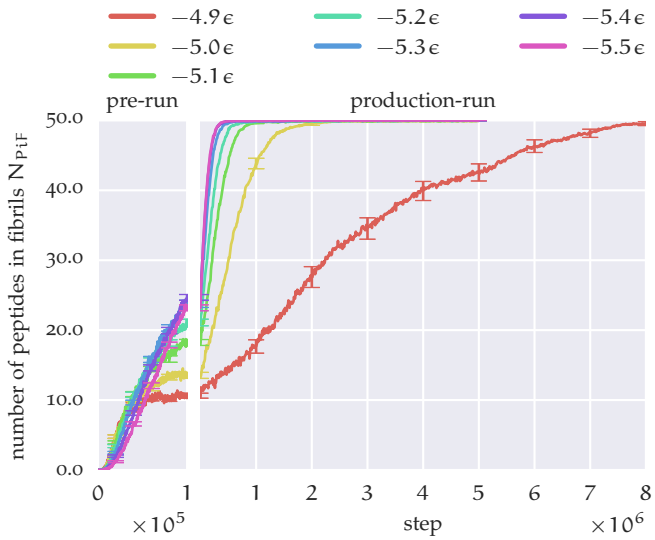

Figure 5.6: The number of peptides in fibrils N_{PiF} for simulations with hydrogen bond energies from -4.9ϵ to -5.5ϵ. The number of peptides in fibrils during the pre-runs are shown on the left side, those during the production-runs are shown on the right side. The step number on the x-axis is separated for pre-runs and production-runs, both start at zero. The data for the pre-runs was obtained every two hundredth step, the data for the production-runs every ten thousandth step. Please note the different scaling of the x-axis of pre-runs and production-runs. The simulations with local hydrogen bond energies of -4.9ϵ ran for eight million steps, the others for five million steps.

When all peptides are part of a fibril, N_{PpF} increases only slowly. This increase is stronger for stronger hydrogen bonds, in simulations with $E_{HB,\,local} = -5.0\epsilon$ there is almost no increase after 2.2×10^6 steps.

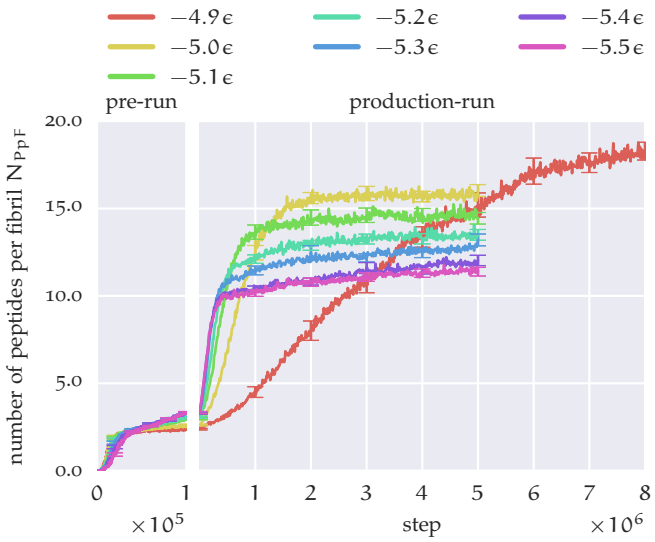

Figure 5.7: The number of peptides per fibril N_{PpF} for simulations with hydrogen bond energies between −4.9ϵ and −5.5ϵ. The structure of the plot is as described in Figure 5.6.

This slow growth of the fibrils can be understood in connection with the graphs shown in Figure 5.8. The number of peptide clusters N_C rises in the pre-runs quickly, similar to the simulations with hydrogen bond energies weaker than −4.9ϵ. After reaching a maximum of 5.0 to 5.8 clusters per simulation, depending on the hydrogen bond strength, N_C decreases again. At the beginning of production-runs about 3 clusters are found in each simulation. This number decreases further and reaches 1.0 to 1.1 at the end of the production-runs. The lower limit is reached faster in simulations with weaker hydrogen bonds.

The slow growth of the number of peptides per fibril in simulations with hydrogen bond energies between −5.0ϵ and −5.5ϵ after the initial phase of quick growth is therefore caused by connections of fibrils, rather than by incorporating single unbound peptides.

The different mechanisms that are responsible for the formation of fibrils are discussed in Section 5.6.

5.5 SIMULATIONS WITH HYDROGEN BOND ENERGIES BETWEEN −5.6ϵ AND −6.5ϵ

The values for local, non-local and cooperative hydrogen bonds as well as the bending stiffness parameter used in the simulations described in this section are given in Table 5.3, like before the complete list of parameters is given in Appendix E. Similar to peptides in simulations with hydrogen bond energies between −4.9ϵ and −5.5ϵ, the peptides in the simulations described in this section do form fibrils. However, the measurements of the number of fibrils N_{PiF} (Figure 5.9), the number of peptides per fibril N_{PpF} (Figure 5.10), and the number of peptide clusters N_C (Figure 5.11) reveal a different behaviour of the simulated peptides.

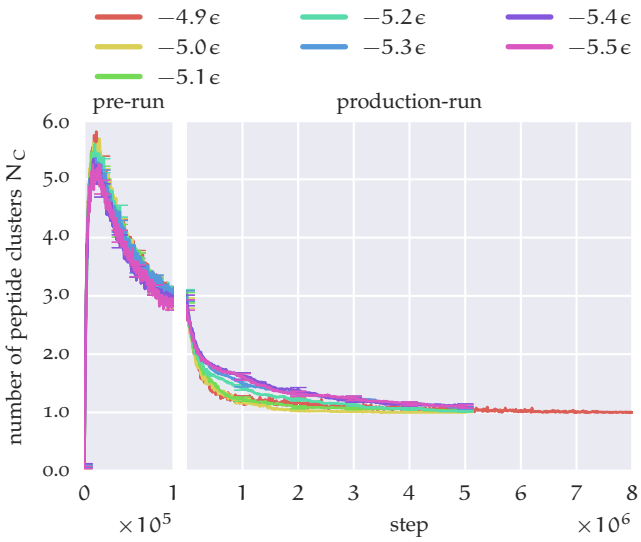

Figure 5.8: The number of peptide clusters N_C for simulations with hydrogen bond energies between −4.9ϵ and −5.5ϵ. The structure of the plot is as described in Figure 5.6.

N_{PiF} increases quickly during the whole pre-run, depending on the hydrogen bond strength: Opposed to the results in simulations with hydrogen bond energies between −4.9ϵ and −5.5ϵ, here simulations with weaker hydrogen bonds lead to higher values of N_{PiF}, compared to simulations with stronger hydrogen bonds. This process resumes in production-runs; in simulations with $E_{HB,\,local} = -5.6\epsilon$ all peptides are part of a fibril after about 4×10^5 steps. Simulations with $E_{HB,\,local} = -6.1\epsilon$ reach this state after about 2.4×10^6 steps. After 8×10^6 steps on average 45.6 ± 0.3 peptides are part of a fibril in simulations with $E_{HB,\,local} = -6.5\epsilon$.

This inversion in the relation between the number of peptides in fibrils and the hydrogen bond strength compared to the simulations described in the previous section can also be seen in the number of peptides per fibril N_{PpF}.

In simulations with $E_{HB,\,local} = -5.6\epsilon$ the quick growth of fibrils stops in the production-runs after about 5×10^5 steps. It continues with reduced rate. The simulations with hydrogen bond energies of −5.7ϵ to −6.1ϵ show the same behaviour, however, the quick growth of the fibrils stops at later points with bigger fibrils. The increase of the fibril size after the kink gets smaller in simulations with stronger hydrogen bonds.

In simulations with hydrogen bond energies between −6.2ϵ and −6.3ϵ, the kink in the curve becomes smoother, but the value of N_{PpF} also stays almost constant till the end of the simulations. For even stronger hydrogen bonds the peptides behave differently. The kink in the growth rate that can be observed in simulations with hydrogen bond energies between −5.0ϵ and −6.3ϵ, vanishes. Instead the number of peptides per fibril grows smoothly with decreasing rate during the whole simulations.

The number of peptide clusters N_C behaves like in the simulations described in the previous sections during the pre-runs: At first several clusters, which

$E_{HB,\,local}$	k_0
-5.60ϵ	19.7408
-5.70ϵ	20.0933
-5.80ϵ	20.4458
-5.90ϵ	20.7983
-6.00ϵ	21.1509
-6.10ϵ	21.5034
-6.20ϵ	21.8559
-6.30ϵ	22.2084
-6.40ϵ	22.5609
-6.50ϵ	22.9134

Table 5.3: The values for the hydrogen bond energies and the peptide bending stiffness used for the simulations with local hydrogen bond energies between -5.6ϵ and -6.5ϵ. Again, the relation $E_{HB,\,non\text{-}local} = 0.7 \times E_{HB,\,local}$ and $E_{HB,\,cooperative} = 0.3 \times E_{HB,\,local}$ are used for the energies of non-local and cooperative hydrogen bonds.

merge during the simulation, form. In the pre-runs the number of clusters decreases faster in simulations with stronger hydrogen bonds. During the production-runs the number of peptide clusters behaves differently for different hydrogen bond strengths. In simulations with strong hydrogen bonds the number of clusters decreases quickly and shows a kink after about 2×10^5 steps. After this kink the number of clusters continues to decrease slowly towards one cluster per simulation. This behaviour holds true for simulations with $E_{HB,\,local} = -6.5\epsilon$ and $E_{HB,\,local} = -6.4\epsilon$. In the other simulations with weaker hydrogen bonds the curve of N_C shows no kink, but also decreases and reaches 1.0 to 1.2 cluster per simulation.

The different mechanisms that are involved in the formation of fibrils, and, as a consequence, influence the behaviour of the measured number of fibrils, the number of peptides per fibril, and the number of clusters, are discussed in the following sections.

5.6 DIFFERENT MECHANISMS OF FIBRIL FORMATION

The formation of fibrils is driven by at least two different mechanisms. Both will be presented in the following.

5.6.1 *Fibril growth in clusters of random coil peptides*

Fibrils can grow in clusters of random coil peptides that form inter-peptide hydrogen bonds. For hydrogen bond energies stronger than -4.8ϵ these bonds get strong enough, compared to the other interaction energies applied to the system, to form permanently. Due to random movement of the peptides fur-

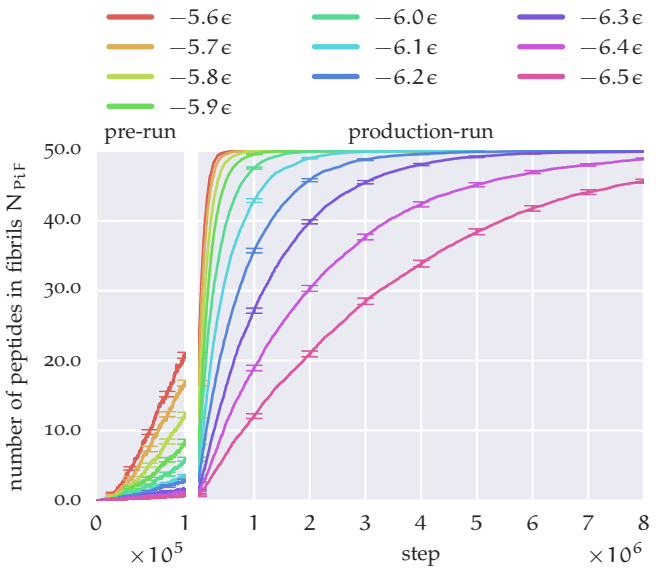

Figure 5.9: The number of peptides in fibrils N_{PiF} for simulations with hydrogen bond energies between −5.6ϵ and −6.5ϵ. The number of peptides in fibrils during the pre-runs are shown on the left side, those during the production-runs are shown on the right side. The step number on the x-axis is separated for pre-runs and production-runs, both start at zero. The data for the pre-runs was obtained every two hundredth step, the data for the production-runs every ten thousandth step. Please note the different scaling of the x-axis of pre-runs and production-runs. The simulations with local hydrogen bond energies between −5.6ϵ and −6.1ϵ were carried out for five million steps, those with local hydrogen bond energies between −6.2ϵ and −6.5ϵ for eight million steps.

ther hydrogen bonds and cooperative bonds can form. From such a seed point, fibrils can grow inside the cluster as long as random coil peptides are accessible to the fibril. Most of the time, not one, but several starting points occur in a cluster and two or more fibrils form as parallel layers. Sometimes fibrils start to grow perpendicular to already existing layers of fibrils. Those fibrils stay shorter, their length is comparable with the width of mature fibrils. During the simulations such perpendicular fibrils tend to rotate in the plane of the fibrils to also adopt a parallel orientation.

The process of fibril formation from a single cluster of random coil peptides is illustrated in Figure 5.12. If the formation of fibrils starts before all peptides are gathered in a single cluster, layers of shorter fibrils in several clusters can form. This is shown in Figure 5.13 and 5.14. The two figures show the different ways in which multiple clusters can merge to form a single fibril cluster. In the simulation shown in Figure 5.13, the clusters connect in such a way that in the end several layers of short fibrils, consisting of less than fifteen peptides, exist. Figure 5.14 shows the behaviour if two clusters connect with fibrils aligned to each other. In this case, the fibrils can connect to form long fibrils in only a few layers. Due to the geometry of the process, the latter happens less often than the formation of short multi-layered clusters. The aforementioned process of

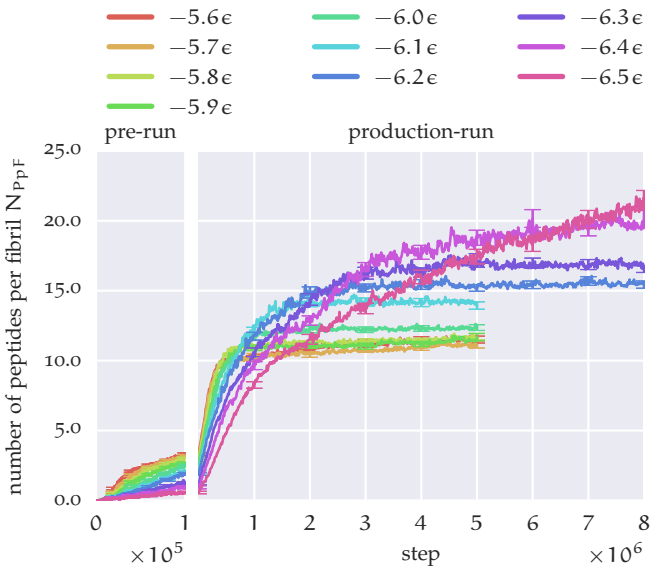

Figure 5.10: The number of peptides per fibril N_{PpF} for simulations with hydrogen bond energies between −5.6ϵ and −6.5ϵ. The structure of the plot is as described in Figure 5.9.

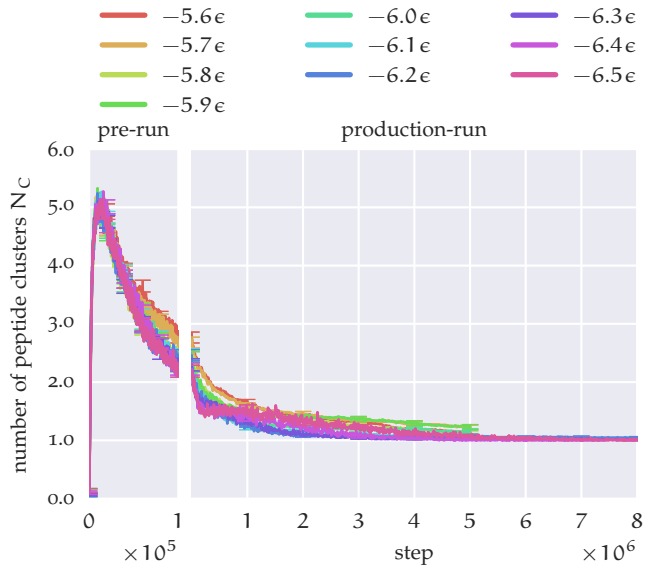

Figure 5.11: The number of clusters for simulations with hydrogen bond energies from −5.6ϵ to −6.5ϵ. The structure of the plot is as described in Figure 5.9.

a fibrillar structure that grows perpendicular to an existing layer and rotates during the simulation to adopt a parallel alignment can be seen in Figure 5.12 (g), 5.12 (h) and 5.12 (i).

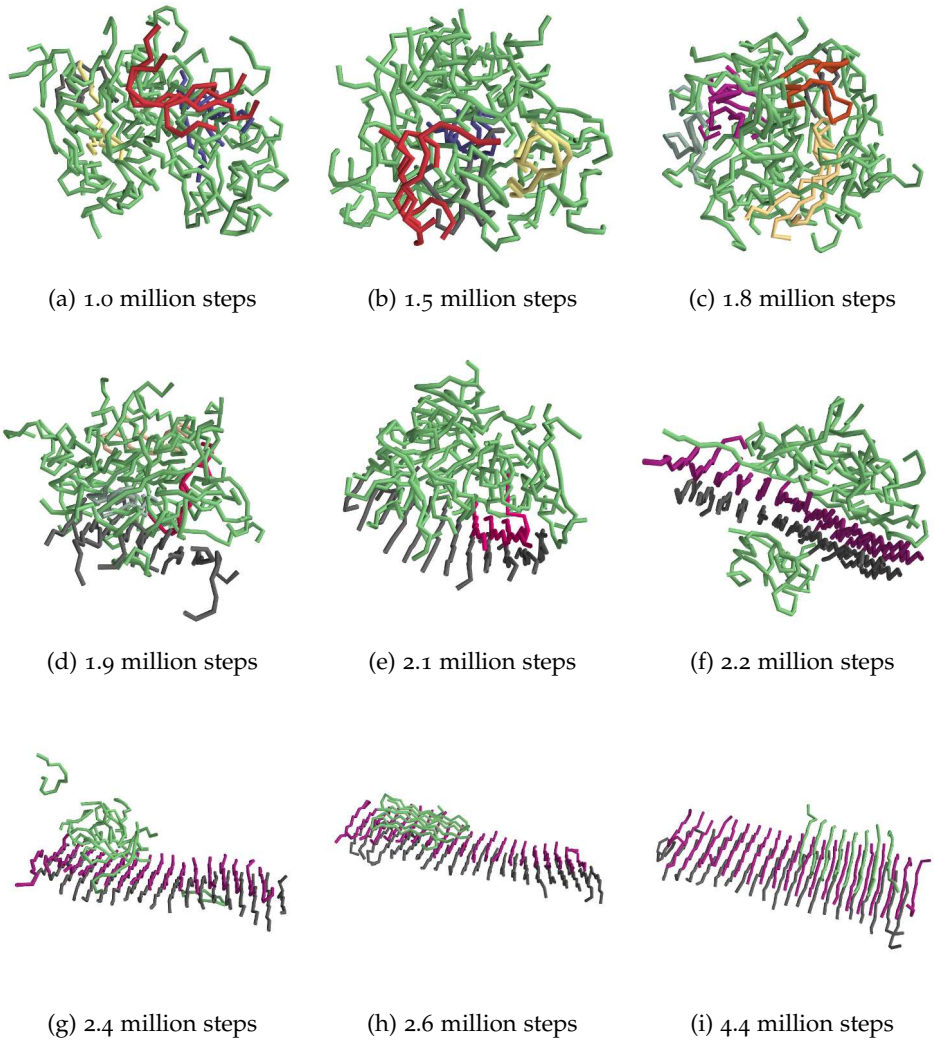

(a) 1.0 million steps (b) 1.5 million steps (c) 1.8 million steps

(d) 1.9 million steps (e) 2.1 million steps (f) 2.2 million steps

(g) 2.4 million steps (h) 2.6 million steps (i) 4.4 million steps

Figure 5.12: Fibril formation from random coil peptides. The snapshots are taken from a simulation with $E_{HB,\,local} = -4.9\epsilon$ (compare Table 5.2). In (a) to (d) all fibrils that exist inside the cluster are highlighted, beginning with (e) only the main fibrils are highlighted. During the first 1.8 million steps only small fibrils consisting of two or three peptides develop. After 1.9 million steps (d) a fibril consisting of nine peptides is formed inside the cluster. 2×10^5 thousand steps later (e), this fibril is grown to twelve peptides and a second fibril consisting of four peptides has developed parallel to the first one. After 2.2 million steps (f), the fibrils contain twelve and thirteen peptides. (g) shows the situation after 2.4 million steps, both fibrils have grown further and now contain nineteen and eighteen peptides. After 2.6 million steps (h) a third layer of seven peptides has formed with the peptides perpendicular to those in the bigger layer. The two parallel layers incorporate 22 and 21 peptides. (i) It takes 1.8 million further steps for the smallest fibril to rotate about 90 degrees to place itself parallel to the two other fibrils.

5.6.2 *Fibril growth in clusters of α-helical peptides*

In simulations with sufficiently high hydrogen bond energies, the peptides stay in their initial set α-helical structure. Like in simulations with weaker

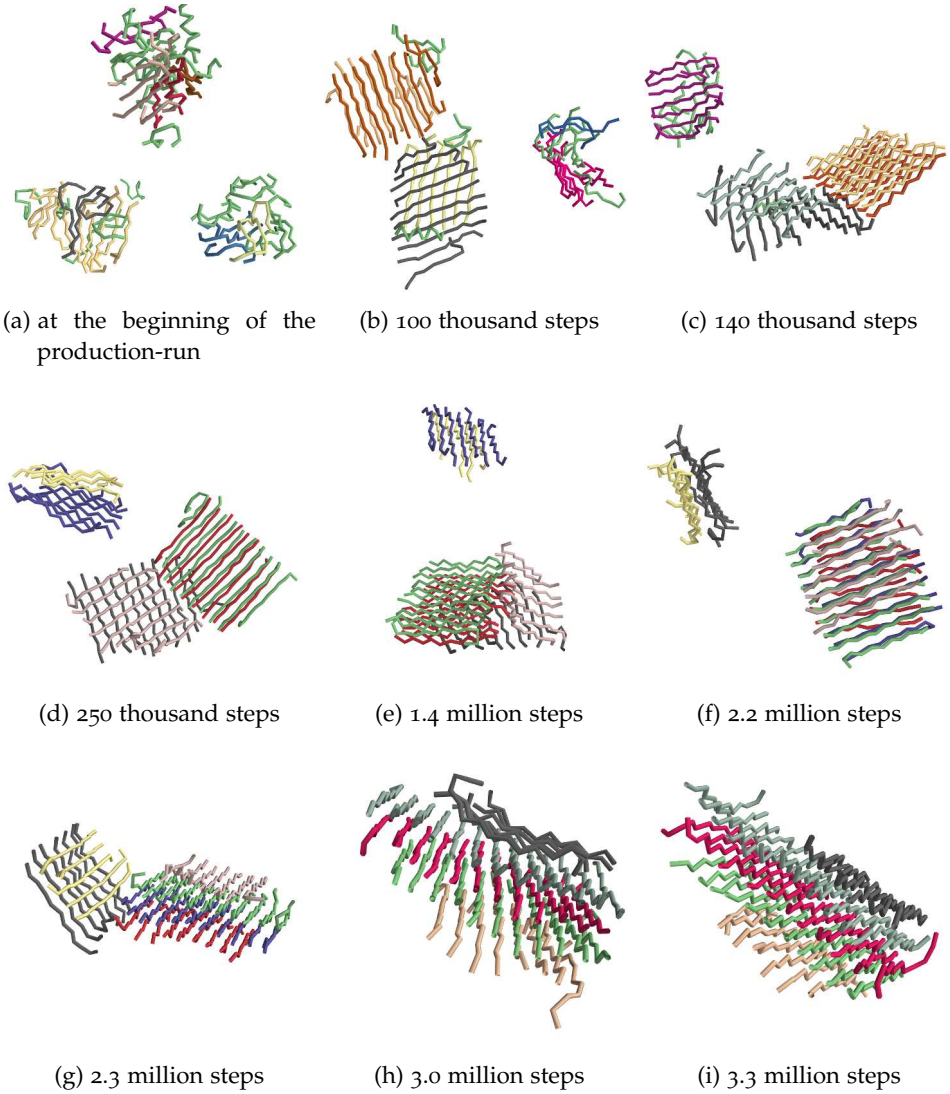

(a) at the beginning of the production-run

(b) 100 thousand steps

(c) 140 thousand steps

(d) 250 thousand steps

(e) 1.4 million steps

(f) 2.2 million steps

(g) 2.3 million steps

(h) 3.0 million steps

(i) 3.3 million steps

Figure 5.13: Fibril formation from random coil peptides in several clusters. The snapshots are taken from a simulation with $E_{HB,\,local} = -5.4\epsilon$ (compare Table 5.2). They show the formation of a cluster consisting of five parallel aligned fibrils. The formation of fibrils starts before all peptides are gathered in one cluster (a). Therefore three clusters of fibrils are formed during the first 100 thousand steps (b). After 140 thousand steps two clusters begin to merge (c). During the next 2.06 million steps this merge is complete and all fibrils in the new cluster are parallel aligned (d) - (f). After 2.3 million steps the last two clusters begin to connect themselves (g). Another 7×10^5 steps later the two clusters are fully connected, with one misaligned fibril (h). After 3.3 million steps all five fibrils are aligned in parallel (i).

hydrogen bonds, the peptides begin to form clusters. The number of inter-peptide hydrogen bonds stays at a low level, compared to clusters of random coil peptides. The clustering is driven by the attraction of hydrophobic peptide beads. Although local hydrogen bonds are stronger than non-local hydrogen bonds, fibrillar structures can form. In contrast to the formation of fibrillar

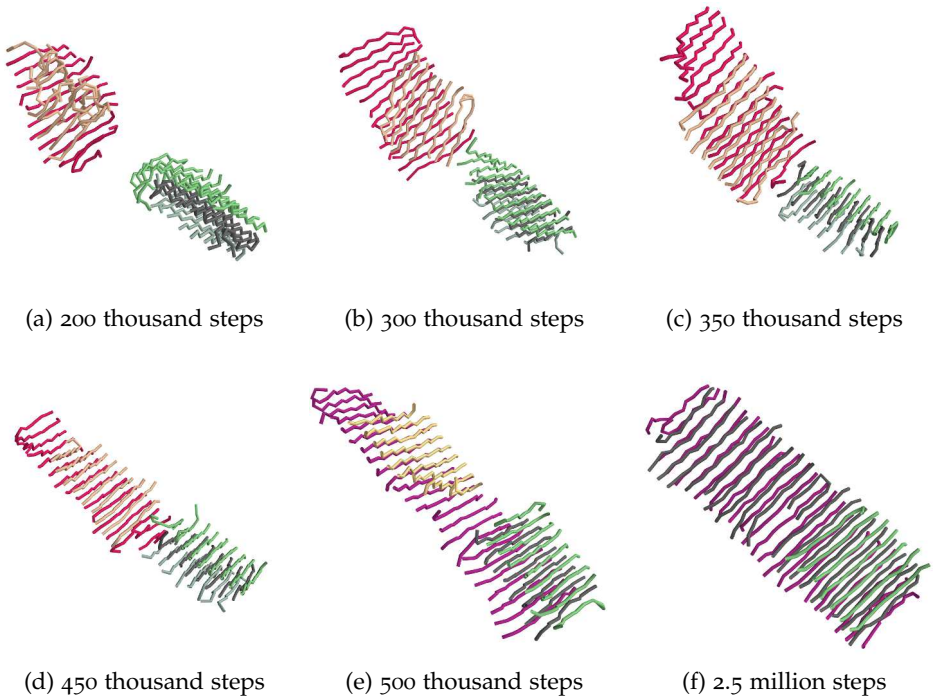

(a) 200 thousand steps (b) 300 thousand steps (c) 350 thousand steps

(d) 450 thousand steps (e) 500 thousand steps (f) 2.5 million steps

Figure 5.14: Fibril formation from random coil peptides in several clusters. The snapshots are taken from a simulation with $E_{HB,\,local} = -5.4\epsilon$ (compare Table 5.2). They show the formation of a cluster of three fibrils by the merging of two independent clusters. (a) - (e) Compared to Figure 5.13 the fibrils in the different clusters do not overlap and rearrange to be parallel, but are able to just connect two fibrils to form a longer one. The process of merging for the first layer is fast compared to the rearrangement in Figure 5.13, as less spatial rotation is needed. (f) On top of the first layer two other fibrils merge by movement in the direction of the fibrils. This process again is one order slower that the merging by connecting two fibrils.

structures from random coil peptides, the driving force behind the formation of fibrils in the case of α-helical formed peptides is the energy associated with the angle between three adjacent peptide beads. The angles are smaller in a peptide that forms an α-helix compared to a stretched peptide that is found in a fibril. Therefore the process of peptide stretching in combination with the formation of non-local and cooperative hydrogen bonds between different peptides leads to stable fibrillar structures. An illustration of the process of fibril formation from a cluster of α-helical peptides is given in Figure 5.15.

The number of steps it takes for all peptides to become part of a fibril, varies, as already mentioned before, with different values of hydrogen bond energies. As shown in Figure 5.6, for $E_{HB,\,local}$ between -4.9ϵ and -5.5ϵ, in those simulations with stronger hydrogen bonds, the transition from clusters of random coil peptides to fibrils takes fewer steps than in such with weaker bonds. In the case of hydrogen bond energies between -5.6ϵ and -6.5ϵ, the systems behave

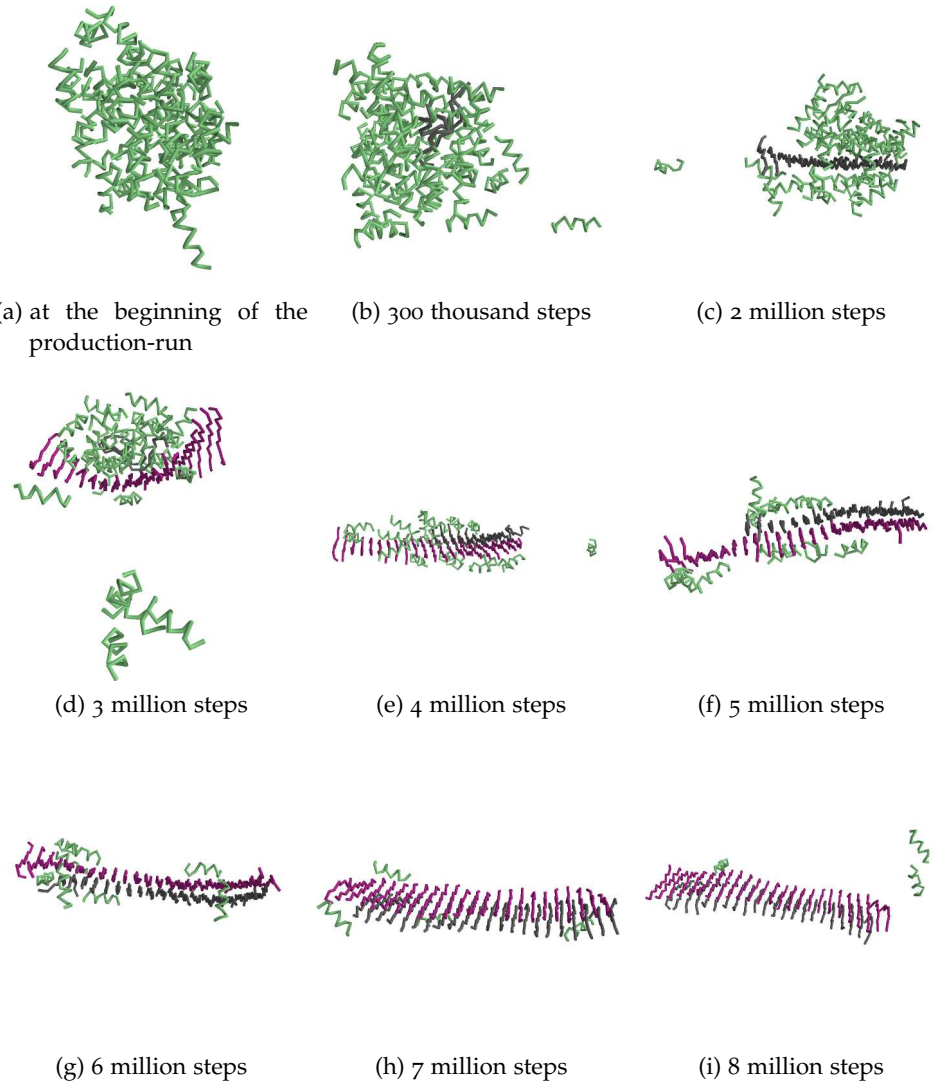

(a) at the beginning of the production-run
(b) 300 thousand steps
(c) 2 million steps
(d) 3 million steps
(e) 4 million steps
(f) 5 million steps
(g) 6 million steps
(h) 7 million steps
(i) 8 million steps

Figure 5.15: Fibril formation from α-helical peptides. The snapshots are taken from a simulation with $E_{HB,\,local} = -6.5\epsilon$ (compare Table 5.3). They show the formation of a cluster consisting of two parallel aligned fibrils. (a) During the pre-run, all peptides have formed a single cluster and stayed in an α-helical configuration. (b) After 300 thousand steps, the first fibril consisting of three peptides has formed. (c) After two million steps the fibril has grown to a size of thirteen peptides. (d) 1×10^6 steps later, the first fibril contains eighteen peptides and a second fibril consisting of three peptides starts to grow. Both fibrils grow further and reach a size of 22 and 10 (e), 23 and 15 (f), 23 and 19 (g), 24 and 22 (h), 25 and 22 (i) peptides after four, five, six seven and eight million steps respectively.

the other way round: In simulations with stronger hydrogen bonds, it takes more steps for the transition to complete. To visualize this effect, the function

$$a \cdot (1 - \exp(-\tau [x - c])) \tag{5.1}$$

is fitted to the values of N_{PiF} in the production-runs, shown in Figure 5.6 and Figure 5.9. The parameter a is the maximum value of the function and is

reached for $x \to \infty$. Because 50 peptides are used in the simulations, a is expected to be around this value. c is a shift on the x-axis. This shift is necessary, as $N_{PiF} \neq 0$ at step 0 in production-runs. The main focus lies on parameter τ, as it describes how many steps it takes until all peptides are part of a fibril. For high values of τ the function gets quicker close to its maximum, than with low values. A plot showing the fit parameter τ versus the local hydrogen bond energy $E_{HB,\,local}$ is given in Figure 5.16. The resulting fit parameters and plots, showing both the fitted function and N_{PiF} are given in Appendix C.

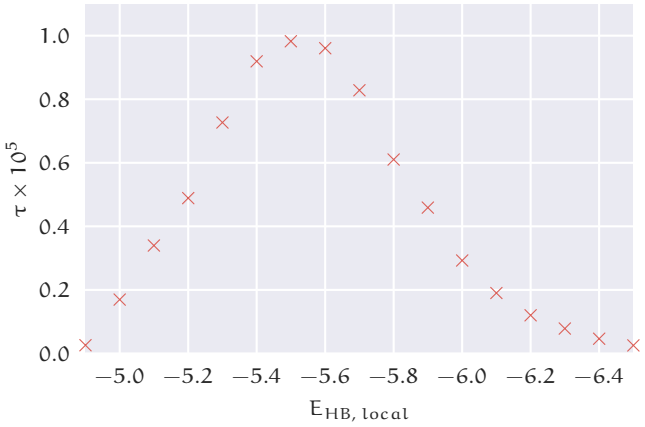

Figure 5.16: Fit parameter τ plotted versus the local hydrogen bond energy $E_{HB,\,local}$. Higher values of τ correspond to a quicker increase of the number of peptides in fibrils N_{PiF}. The errors for the fit parameter τ, are not shown here, as they would be to small to be visible.

The maximum of τ is reached in simulations with $E_{HB,\,local} = -5.5\epsilon$. Both for weaker and stronger hydrogen bonds, τ decreases. This is caused by the two different types of clusters fibrils grow in: Clusters of random coil and of α-helical peptides. In the following the differences in the two mechanisms from an energetic point of view are discussed.

5.6.3 *Different paths of fibril formation*

The differences in the energies associated with the formation of fibrils for simulations with weak ($E_{HB,\,local} = -4.9\epsilon$) and strong ($E_{HB,\,local} = -6.5\epsilon$) hydrogen bonds are illustrated in Figure 5.17 and 5.18. The peptide bending stiffness energy $E_{BA,\,peptide}$, plotted in Figure 5.17, quickly drops in simulations with weak hydrogen bonds during the pre-runs and shows only a small further decrease during the production-runs.This corresponds to the quick unwinding of α-helices observable during the pre-runs. As the peptides enter the production-runs in a random coil configuration, the small decrease of the bending energy also fits into the picture, as the angles between adjacent beads decrease slightly during the transition from a random coil peptide to a peptide that is bound in a fibril.

In simulations with strong hydrogen bonds the progress of the curves is completely different. At the beginning of pre-runs the bending stiffness energy

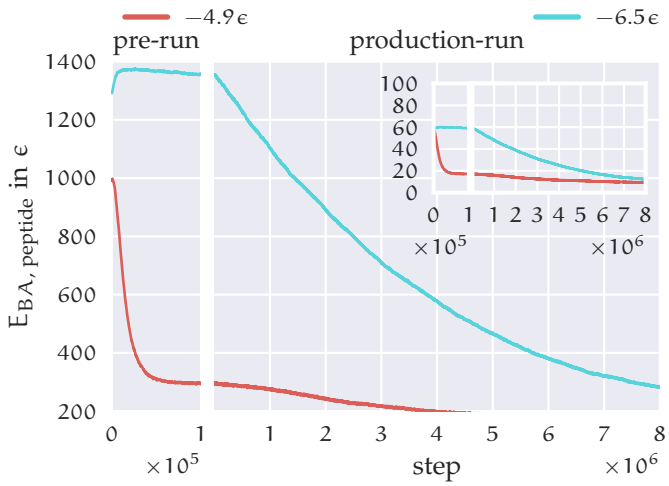

Figure 5.17: The plot illustrates the differences in the peptide bending stiffness energy $E_{BA,\,peptide}$ for simulations with $E_{HB,\,local} = -4.9\epsilon$ (red) and $E_{HB,\,local} = -6.5\epsilon$ (blue). Each curve is obtained as an average of 128 single measurements. The inset shows the values divided by the spring parameter k_0 used for the angle potential $U_{BA,\,peptide}$ (see Section 2.3.1), to ease the comparison of both curves. See text for details.

rises quickly and reaches a maximum after about 2.5×10^4 steps. During the further steps of the pre-runs, the value of $E_{BA,\,peptide}$ decreases slightly. The average bending stiffness energy decreases exponentially during the production-runs. The initial rising of the bending energy can be explained with the algorithm used to set up α-helical peptides: As the algorithm uses only average values to construct a helical structure, the number of local hydrogen bonds per peptide is slightly smaller than the possible number of hydrogen bonds in perfect α-helical peptides. Due to the high value of $E_{HB,\,local}$, and the small derivations from (perfect) helical structures, these hydrogen bonds form quickly during the first 1×10^4 steps, which leads to the small but observable increase of bending stiffness energy. By looking at $E_{BA,\,peptide}$ divided by the spring parameter k_0 used for the bending potential, shown in the inset of Figure 5.17, the energies of simulations with weak and strong hydrogen bonds can be compared directly. In this representation it is obvious that both curves start and end at almost the same values. The matching of the start values results from the comparable configuration of both simulations, the matching of the endpoints of both curves corresponds to the observation that the fibrillar structures obtained from both simulations have similar properties.

The total hydrogen bond energy E_{HB}, shown in Figure 5.18, increases in the case of weak hydrogen bonds during the pre-runs.

At the end of the pre-runs, this value drops again slightly. This corresponds to the disruption of local hydrogen bonds in the initially α-helical shaped peptides and formation of clusters of random coil peptides. During the production-runs the energy decreases further. In the case of simulations with strong hydrogen bonds, the hydrogen bond energy decreases during the first 4×10^4 simulation steps of the pre-runs, followed by a slow increase. The initial de-

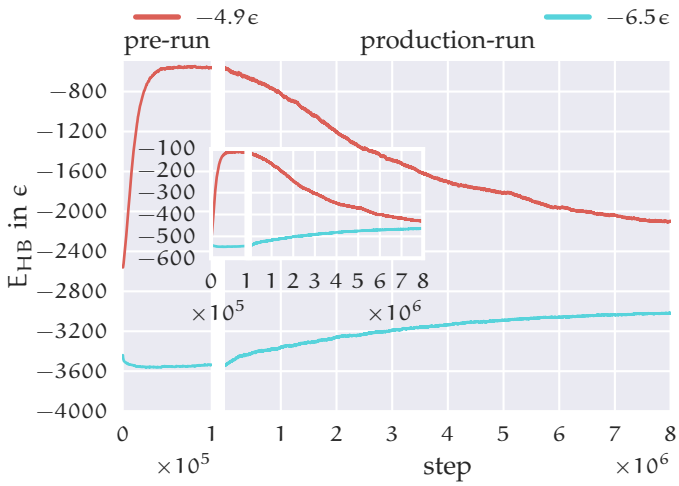

Figure 5.18: Illustration of the different values of the total hydrogen bond energy E_{HB} for simulations with $E_{HB,\,local} = -4.9\epsilon$ (red) and $E_{HB,\,local} = -6.5\epsilon$ (blue). Each curve is an average of 128 single simulations. The inset shows the averaged energies divided by the absolute value of $E_{HB,\,local}$ used in the according simulation to ease the comparison. The error bars for the simulation with $E_{HB,\,local} = -6.5$ are not visible due to their small size. See text for a description of the curves.

crease is again connected to the stabilisation of (perfect) helices. During the production-runs E_{HB} rises again slowly. The inset in Figure 5.18 shows the hydrogen bond energy divided by the absolute value of the local hydrogen bond energy $E_{HB,\,local}$. By dividing E_{HB} by $E_{HB,\,local}$ both curves get comparable. At the beginning of the pre-runs, both curves start at about $-525\epsilon/E_{HB,\,local}$. After eight million steps in production-runs, the curves reach $-429\epsilon/E_{HB,\,local}$ and $-461\epsilon/E_{HB,\,local}$, for simulations with $E_{HB,\,local} = -4.9\epsilon$, $E_{HB,\,local} = -6.5\epsilon$ respectively. The comparison shows that the values for simulations with stronger hydrogen bonds result in lower values for $E_{HB}/E_{HB,\,local}$, and therefore in a higher number of hydrogen bonds. This originates from two different sources: Firstly, peptides that get not bound in a fibril, stay in their initial α-helical configuration with its high number of local hydrogen bonds in simulations with $E_{HB,\,local} = -6.5\epsilon$, whereas such peptides adopt a random coil configuration in the case of weak local hydrogen bonds. Secondly, fibrils that grow in simulations with strong hydrogen bonds have fewer *hydrogen bond vacancies* and fewer *misaligned peptides*. This effect is shown in Figure 5.19. Hydrogen bond vacancies mean in this context that one or more hydrogen bonds between two adjacent peptides in a fibril are not formed, leading to a defect in the hydrogen bond pattern. Misaligned means that one end of a peptide in a fibril is shifted perpendicular to the axis of fibril growth, thereby reducing the number of possible hydrogen bonds.

By looking at Figure 5.18 and the curves for $E_{HB,\,local} = -4.9\epsilon$ and $E_{HB,\,local} = -6.5\epsilon$ in Figure 5.6 and Figure 5.9, it is obvious to see that these three plots share at least one characteristic: The error bars for simulations with $E_{HB,\,local} = -4.9\epsilon$ are bigger compared to those in simulations with $E_{HB,\,local} = -6.5\epsilon$. To

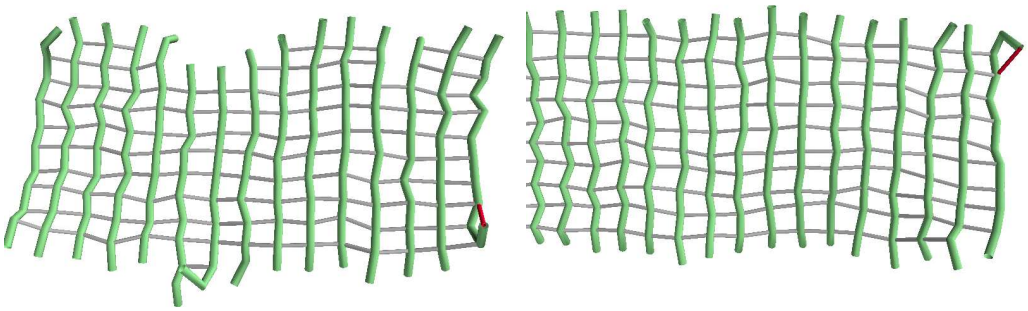

(a) (b)

Figure 5.19: Comparison of (a) a fibril from a simulation with $E_{HB,\,local} = -4.9\epsilon$ and (b) a part of a fibril from a simulation with $E_{HB,\,local} = -6.5\epsilon$. Both pictures were taken from two simulations that ran for 8×10^6 steps. The non-local external hydrogen bonds that form the fibrils are shown in grey, the local hydrogen bonds are shown in red. The fibril on the left shows more hydrogen bond vacancies and more misaligned peptides than the one shown on the right.

elucidate the reason for this, first the measured number of non-local hydrogen bonds for a single simulation for different values of $E_{HB,\,local}$, as given in Figure 5.20, is compared. The number of non-local hydrogen bonds is directly connected to the formation of fibrils, in consequence of the algorithm to calculate the number and size of fibrils in a simulation, see Section 5.2.1. The number of non-local hydrogen bonds increases slowly during the whole production-run in simulations with $E_{HB,\,local} = -6.5\epsilon$, starting from less than twenty bonds. This corresponds to a slow and continuous growth of the fibrils in the simulation that can also be observed in the snapshots that are taken from this simulation, given in Figure 5.15.

The curve for a simulation with $E_{HB,\,local} = -4.9\epsilon$, taken from the simulation shown in Figure 5.12, exposes a different behaviour: The number of non-local hydrogen bonds increases quickly during the pre-runs and stays more or less constant during the first 1.7×10^6 steps of the production-runs, apart from a short attempt to form a fibril after 0.8×10^6 steps. The fibrils are formed very quickly between steps 1.7×10^6 and 2.5×10^6, leading to a, again constant, number of non-local hydrogen bonds. The averaged values shown in Figure 5.6, 5.7, 5.8, and 5.18, reveal that the starting point of this quick process of fibril formation in a single simulation with $E_{HB,\,local} = -4.9\epsilon$ varies over the whole (x-)range of steps. This variation of the position of this process leads to big error bars compared to simulations with $E_{HB,\,local} = -6.5\epsilon$, where the process itself takes several million simulation steps. Figure 5.21 and Figure 5.22 show a more in-detail treatment of this effect. To estimate the duration of the process of fibril formation, the following procedure was applied: At first all curves of the measured number of non-local external hydrogen bonds are shifted along the x-axis, in such a way that the first occurrence of 300 or more non-local external hydrogen bonds is shifted to step 2.5×10^6. After shifting

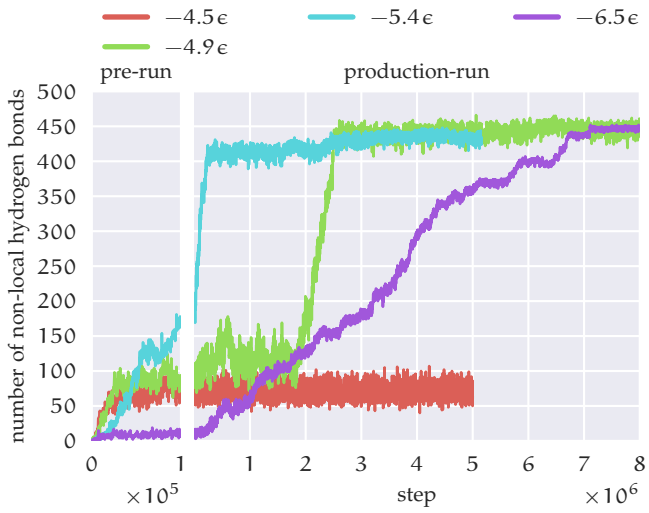

Figure 5.20: Comparison of the hydrogen bond numbers for three different mechanisms of fibril formation. Each curve shows the number of non-local external hydrogen bonds directly taken from the measurements during a single simulation. The curves shown for $E_{HB,local} = -4.9\epsilon$ (green), $E_{HB,local} = -5.4\epsilon$ (blue), and $E_{HB,local} = -6.5\epsilon$ (purple) correspond to the formation of fibrils shown in Figure 5.12, and 5.13, and 5.15. In the simulation with $E_{HB,local} = -4.0\epsilon$ the number of non-local external hydrogen bonds rises quickly during the first half of the pre-run and stays than constant at about 60 during the complete simulation. This behaviour corresponds to the observed formation of a cluster of random coil peptides, in which no fibrils grow. The simulation with $E_{HB,local} = -5.4\epsilon$ shows a quick growth of, as 5.13 shows, several fibrils. The merging of the independent fibril clusters can be observed between step 2.0×10^6 and 3.0×10^6 in the shift of the plateau of the measured number towards higher values. See the text for a description of the curves for simulations with $E_{HB,local} = -4.9\epsilon$, $E_{HB,local} = -6.5\epsilon$ respectively.

the values, the average of these shifted curves is calculated. As a third step the function

$$(a + b)/2 + (b - a)/2 \cdot \tanh(c\,(x - d)) \tag{5.2}$$

is fitted to the averaged value. The parameter a is the minimum value of the function, b the maximum value, d determines the position of the transition from the lowest to the highest value on the x-axis, and c is responsible for the width of the transition-zone. Higher values of c lead to sharper transitions. The optimized values for a, b, c, and d are given in Table 5.4. The plot in Figure 5.21 and the optimized values in the first row of Table 5.4 show that the function is well suited to describe the increase of the number of non-local hydrogen bonds for simulations with weak hydrogen bonds. The values in the second row of the table and the plot in Figure 5.22 reveal that this is not the case for simulations with strong hydrogen bonds. The negative value -9.8 ± 0.3 for a implies a non physical negative number of non-local hydrogen bonds. The fact that the function is better suited to describe the increase of the non-

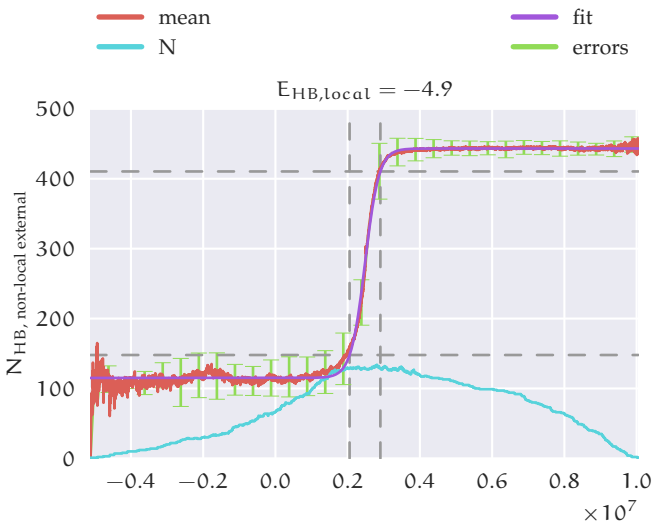

Figure 5.21: Comparison of the number of non-local external hydrogen bonds $N_{HB,\text{non-local external}}$ for simulations with $E_{HB,\text{local}} = -4.9\epsilon$. The error bars, shown in green are obtained from averaging the number of hydrogen bonds. The blue curves show how many simulations take part in the calculation of the average value.

E_{HB}	a	b	c	d
-4.9ϵ	115.1 ± 0.1	443.3 ± 0.1	$(2.577 \pm 0.006) \times 10^{-6}$	$(24791 \pm 5) \times 10^2$
-6.5ϵ	-9.8 ± 0.3	448.9 ± 0.2	$(3.108 \pm 0.005) \times 10^{-7}$	$(1482 \pm 3) \times 10^3$

Table 5.4: Values for the parameters used to fit Equation 5.2 to the averaged number of non-local hydrogen bonds for simulations with $E_{HB,\text{local}} = -4.9\epsilon$ and $E_{HB,\text{local}} = -6.5\epsilon$. The fitted functions are plotted in Figure 5.21 and Figure 5.22.

local hydrogen bond number for simulations with $E_{HB,\text{local}} = -4.9\epsilon$ can be explained by the width of the transition zone; this zone is much more narrow for simulations with $E_{HB,\text{local}} = -4.9\epsilon$ than for those with strong hydrogen bonds, where it is stretched almost across the whole x-range. As the results are obtained by using MC simulations, including non-physical bead moves, the measurements obtained do not show real dynamics, therefore the result can be interpreted only qualitatively. For a quantitative analysis of the process of fibril formation, MD simulations are necessary. Is it nevertheless possible to use the fitted function to explain the source of the different sized error bars in Figure 5.18.

The two vertical grey dashed lines in Figure 5.21 and 5.22 show the positions, where the fitted function reaches 10% and 90% of its maximum, both values denoted by dashed horizontal lines. If the steps between 10% and 90% are used to estimate roughly how many steps it takes on average to increase the number of non-local external hydrogen bonds, and hence to form fibrils, the start- and end-point of this process can be read directly from the shown plots.

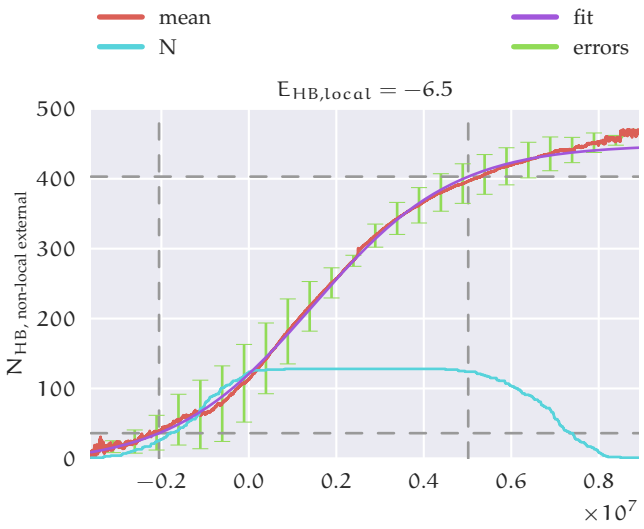

Figure 5.22: Comparison of the number of non-local external hydrogen bonds $N_{HB,\text{non-local external}}$ for simulations with $E_{HB,\text{local}} = -6.5\epsilon$. See Figure 5.21 and text for details.

In the case of simulations with weak hydrogen bonds, start- and endpoint are separated by about 1×10^6 steps, whereas about 7×10^6 steps lie between these two points in the case of simulations with strong hydrogen bonds. It is not possible, as already mentioned before, to translate this number of steps into something like time, due to the character of the simulation.

The number of simulations that enter the averaged measurement for both types of simulations is plotted in blue in Figure 5.21 and Figure 5.22. It shows a plateau between 0.0×10^7 and 0.5×10^7 for simulations with strong hydrogen bonds. That means that the curves for the number of non-local external hydrogen bonds for all simulations overlap in this relative broad region and that the shift of a single measurement relative to all other measurements on the x-axis is small. For simulations with weak hydrogen bonds, the situation is totally different. The number of simulations that enter the average does not show a plateau. This means that the position of the transition zone varies strongly on the x-axis between different simulations. This explains the different sizes of the error bars in Figure 5.18: The values for E_{HB} differ only slightly between single simulations with strong hydrogen bonds, due to the slow increase of the number of non-local external hydrogen bonds, that is distributed over the whole simulation. The values for E_{HB} and E_{total} of simulations with weak hydrogen bonds result from averaging over values that oscillate either around the minimum or the maximum value of the fitted function, the variation of the values is therefore bigger than in the case of strong hydrogen bonds, leading to bigger error bars.

Figure 5.23 shows a histogram obtained by fitting Equation 5.2 to the measured number of non-local external hydrogen bonds of each simulation with $E_{HB,\text{local}} = -4.9\epsilon$ followed by sorting the resulting parameter d for each fit into bins. Together with the histogram, an exponential distribution function

$A \exp[-\lambda x]$ is plotted. As the peptides need to form clusters before the formation of fibrils happens, the first bin of the histogram is not considered during the fit. The number of bins (11) is chosen according to the square-root rule. The fit yields $A = 0.38 \pm 0.03$ and $\lambda = 0.29 \pm 0.02$ per million steps in the exponential distribution function. Histogram and curve together show that the position of fibril formation process during the simulations is exponentially distributed for systems with $E_{HB,\,local} = -4.9\epsilon$. The height of bins 6 and 7, for events roughly between step 3.5×10^6 and 5×10^6 underestimates the fitted curve, but thus might be a statistical effect.

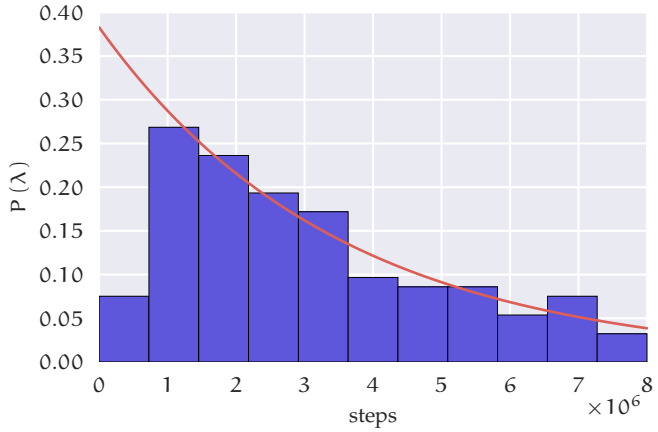

Figure 5.23: Shifted exponential distribution function, fitted to the histogram showing the formation of fibrils in simulations with $E_{HB,\,local} = -4.9\epsilon$. See text for details.

Fibril formation from a single or several clusters

The number of steps it takes to form fibrils also influences the process of fibril formation and hence the resulting fibrils, as shown in several images. In systems with slowly growing fibrils, either because the hydrogen bonds are too weak to stabilize fibrils quickly, or because the hydrogen bonds are strong enough to keep the peptides in their initial α-helical structure, the formation of a single peptide cluster (of random coil or α-helical peptides) takes place before the fibrils grow. In these systems, the observed structures at the end of the simulations mainly consist of two or three layers of fibrils, each consisting of many peptides. Examples for this path of fibril formation are shown in Figure 5.12 and Figure 5.15. In systems with hydrogen bond energies between these two extrema, the formation of a single cluster is slower than the formation of fibrils. In these simulations, the formation of layered structures of short fibrils in several clusters is observed during the runs. Towards the end of the simulations, these clusters of fibril layers often merge to form multiple layers of short fibrils, as illustrated in Figure 5.13. A situation like in Figure 5.14, where two clusters of fibrils merge in such a way that the fibrils inside the clusters can just connect to form longer fibrils, happens rarely.

To characterise the shape of the clusters of fibrils that form, the *gyration tensor* S [131] for the centre of mass of each peptide can be calculated:

$$S_{mn} = \frac{1}{N} \sum_{i=1}^{N} c_m^{(i)} c_n^{(i)} \quad , \tag{5.3}$$

with $c_m^{(i)}$ the mth cartesian coordinate of the centre of mass of a peptide i in a cluster consisting of N particles. The origin of the cartesian coordinates is set to be the centre of mass of the cluster. The resulting matrix can be diagonalised to

$$\mathbf{S} = \mathrm{diag}\left(\overline{X^2}, \overline{Y^2}, \overline{Z^2}\right) \quad , \tag{5.4}$$

so that the eigenvalues of $\mathbf{S}$, $\overline{X^2}$, $\overline{Y^2}$, and $\overline{Z^2}$ are ordered: $\overline{X^2} \geqslant \overline{Y^2} \geqslant \overline{Z^2}$. The squared *radius of gyration* R_g^2 can than be calculated as the trajectory of $\mathbf{S}$:

$$R_g^2 = \mathrm{tr}\,(\mathbf{S}) = \overline{X^2} + \overline{Y^2} + \overline{Z^2} \quad . \tag{5.5}$$

The *asphericity* b and the *acylindricity* c can be calculated as:

$$b = \overline{X^2} - \frac{1}{2}\left(\overline{Y^2} + \overline{Z^2}\right) \quad , b \geqslant 0 \tag{5.6}$$

and

$$c = \overline{Y^2} - \overline{Z^2} \quad , c \geqslant 0 \quad . \tag{5.7}$$

The asphericity b and the acylindricity c give us information about the symmetry of the cluster. If the cluster has tetrahedral or higher symmetry, $b = c = 0$, for cylindrical symmetry $c = 0$.

In the following images, the normalized asphericity b_N is plotted against R_g^2, and the normalized acylindricity c_N against b_N. Those two values are calculated as:

$$b_N = \frac{b}{R_g^2} \quad , \quad c_N = \frac{c}{R_g^2} \quad . \tag{5.8}$$

Figure 5.24 shows the normalized asphericity b_N plotted against R_g^2 for simulations with three different values of $E_{HB,\,local}$: -4.9ϵ, -5.4ϵ, and -6.5ϵ. The curves showing values for simulations with $E_{HB,\,local} = -4.9\epsilon$, marked by circles, and for simulations with $E_{HB,\,local} = -6.5\epsilon$, marked by squares, show a similar behaviour. During the whole simulations, the value of R_g^2 is growing and reaches values around 21 at the end of the simulations. The normalised asphericity b_N shows a two step behaviour. Till a value for R_g^2 around 8 is reached, b_N decreases from an initial value of 0.79 to values around 0.3. For higher values of R_g^2, b_N increases again, reaching values around 0.95. The decreases of b_N for structures with small values of R_g^2 is connected to the formation of clusters of either random coil ($E_{HB,\,local} = -4.9\epsilon$) or α-helical

($E_{HB,\,local} = -6.5\epsilon$) peptides. These clusters possess a higher symmetric structure than the fibrillar structures that aggregate towards the end of the simulations, therefore a minimum in the curve of b_N can be observed. The initial behaviour of b_N and R_g^2 is the same in simulations with $E_{HB,\,local} = -5.4\epsilon$, marked by triangles. Opposite to the two other curves, the increase of b_N already starts for values of R_g^2 around 5.0. In these simulations, both the maximum values of b_N and R_g^2 that are reached, are smaller than in simulations with $E_{HB,\,local} = -4.9\epsilon$ and $E_{HB,\,local} = -6.5\epsilon$. The majority of measured clusters reaches values of $b_N = 0.8$ for $R_g^2 = 10$, only a small number of clusters exceeds these values.

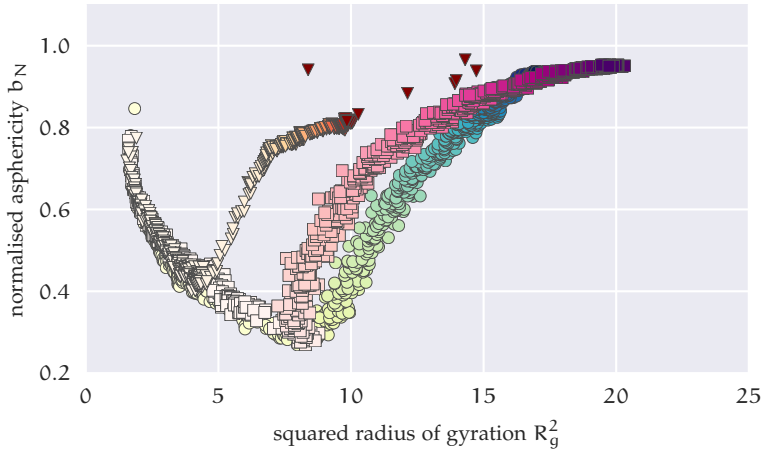

Figure 5.24: Normalized asphericity b_N plotted against the squared radius of gyration R_g^2, averaged over 128 independent runs. The values are calculated from the centre of mass of peptides inside the same cluster. The quadratic markers show values from simulations with $E_{HB,\,local} = -4.9\epsilon$, circles those for simulations with $E_{HB,\,local} = -6.5\epsilon$ and triangular markers those with $E_{HB,\,local} = -5.4\epsilon$. The brightness of the colour corresponds to the simulation step the value is taken from; darker colours correspond to later steps in the simulation. The values are obtained from both pre-runs and production-runs. The change from decreasing to increasing b_N happens roughly after 8×10^5, 1×10^5, and 1×10^6 steps for simulations with $E_{HB,\,local} = -4.9\epsilon$, -5.4ϵ, and -6.5ϵ.

The shift of the starting point of the increase of b_N and the values of R_g^2 that stay smaller than those values measured in the two other sets of simulations, are caused by the formation of several independent clusters of random coil peptides that is observed in the simulations. As the formation of fibrillar layers inside the independent clusters prevent the formation of a single symmetric cluster, the increase of b_N starts for smaller values of R_g^2. The growth of several small fibrils both leads to smaller values of R_g^2 and b_N, because the relation of width to length of a short fibril is smaller, compared to fibrils consisting of many peptides that form in simulations with weaker or stronger hydrogen bonds. Only towards the end of the simulations (dark red triangles), structures with values of $R_g^2 > 10$ and $b_N > 0.9$ form caused by the connection of single fibril clusters.

The occurrence of different structures can also be observed in Figure 5.25, where the normalised acylindricity c_N is plotted versus b_N. Additionaly three points, labelled with a), b), and c) are plotted. These points mark the values of b_N and c_N for three typical types of clusters that occur, shown in Figure 5.26.

Initially both c_N and b_N decrease in all three types of simulations. For $E_{HB,\,local} = -4.9\epsilon$ and -6.5ϵ, the clusters develop towards point c), in the case of simulations with $E_{HB,\,local} = -5.4\epsilon$ towards point b).

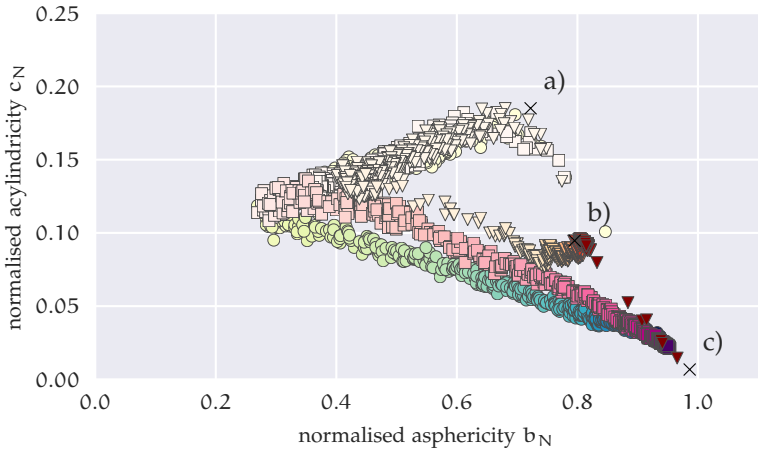

Figure 5.25: Normalized acylindricity c_N plotted against the normalized asphericity b_N. The colouring is the same as in Figure 5.24. The three points a), b), and c), corresponding to the clusters shown in Figure 5.26, illustrate the different structures that occur in the simulations.

5.7 CONTROLLING THE FIBRIL FORMATION PROCESS

To prepare the peptide model for simulations in the presence of lipid membranes, both fibrils that form slowly and that are formed by hydrogen bonds, which are neither too weak, nor too strong are needed. To fulfil the second condition, the value -5.5ϵ for $E_{HB,\,local}$ is chosen. Several simulations are set up as described in Section 5.1. To control how quickly the fibrils form, the value of the cooperative hydrogen bond energy $E_{HB,\,cooperative}$ is lowered. Instead of the original value -1.65ϵ, systems with values for $E_{HB,\,cooperative}$ between -0.5ϵ and -1.5ϵ are used. The results for this simulations are shown in Figure 5.27 - Figure 5.29. The number of peptides in fibrils N_{PiF} increases quickly at the beginning of the pre-runs, for simulations with $E_{HB,\,cooperative} \geqslant -0.9\epsilon$ there is no further increase during the rest of the pre-runs and the production-runs. In simulations with $E_{HB,\,cooperative} = -0.5\epsilon$ about 10 peptides are part of a fibril, in simulations with $E_{HB,\,cooperative} = -0.9\epsilon$ about 15.0, for simulations with $E_{HB,\,cooperative} = -0.6\epsilon$, -0.7ϵ, and -0.8ϵ, this value lies in between.

In simulations with $E_{HB,\,cooperative}$ between -1.5ϵ and -1.2ϵ, all peptides become part of a fibril almost as fast as in simulations with the original value $E_{HB,\,cooperative} = -1.65\epsilon$. The simulations with $E_{HB,\,cooperative} = -1.1\epsilon$ and $E_{HB,\,cooperative} = -1.0\epsilon$ are different from both other groups. For both values

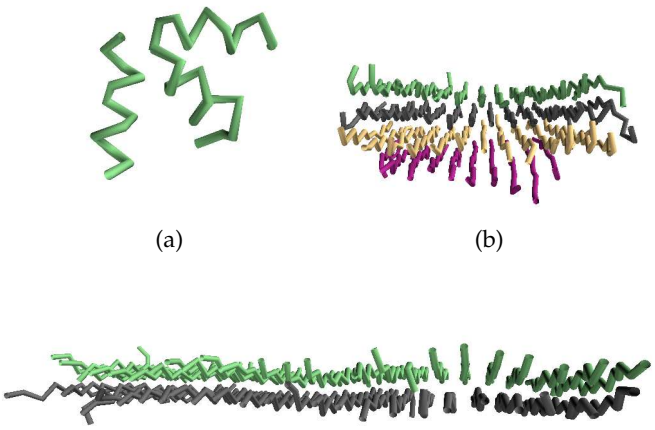

(a) (b)

(c)

Figure 5.26: Different types of clusters that occur during the simulations. a) shows a small cluster consisting of three peptides after 20 thousand steps of a pre-run in a simulation with $E_{HB,\,local} = -6.5\epsilon$, b) shows a cluster of four layered fibrils after five million steps in a simulation with $E_{HB,\,local} = -5.4\epsilon$, and c) illustrates the resulting fibril double layer in a simulation with $E_{HB,\,local} = -4.9\epsilon$ after eight million steps. The values of b_N and c_N are marked in Figure 5.25.

of $E_{HB,\,cooperative}$ there is a slow increase of N_{PiF} during the whole production-runs.

The number of peptides per fibril N_{PpF}, plotted in Figure 5.28, shows the same behaviour as in the simulations discussed before: The slower a fibril growths, the bigger it gets. This holds true for all plotted curves, except for simulations with $E_{HB,\,cooperative} = -1.0\epsilon$. The growth of the fibril in the latter case is too slow to form big fibrils during the 8×10^6 steps of the simulations.

In simulations with $E_{HB,\,cooperative} \geqslant -0.9\epsilon$ the maximum size of fibrils does not exceed 2.5, in full agreement to the observations of the number of peptides in fibrils.

N_{PpF}, shown in Figure 5.28, rises quickly in simulations with $E_{HB,\,cooperative}$ between -1.5ϵ and -1.3ϵ. This increase begins during the pre-runs and continues at the beginning of the production-runs. After less that 1×10^6 steps in the production-runs, this growth rate is damped and only a small increase in the size of fibrils during the rest of the simulation happens. This change happens earlier and at smaller fibril sizes, the stronger the cooperative hydrogen bond energy is. The curve looks similar for simulations with $E_{HB,\,cooperative} = -1.2\epsilon$, with the only distinction that the change in the growth rate happens later in the simulations, between step 1.5×10^6 and 2×10^6.

The number of fibril clusters N_C, shown in Figure 5.29, also shows the desired behaviour: For all values of $E_{HB,\,cooperative}$ it drops from an initially high value towards 1. The number of clusters at the beginning of pre-runs is higher in simulations with weak cooperative hydrogen bonds. Within the first 1×10^6 steps of the production-runs, the values fall below those for simulations with

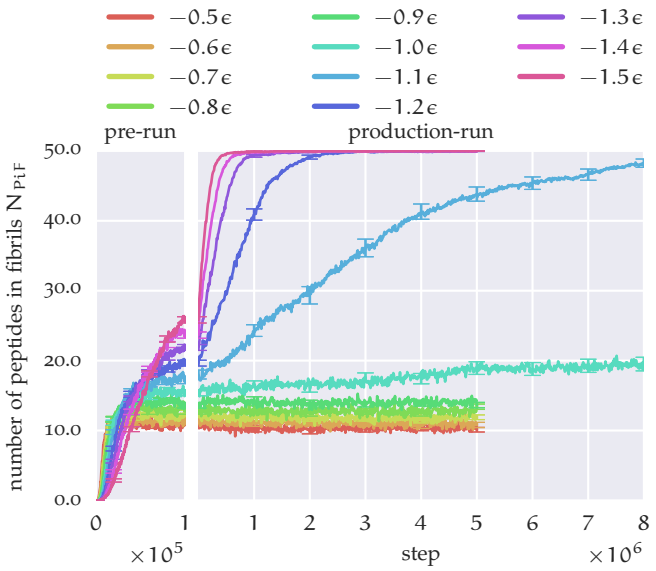

Figure 5.27: The number of peptides in fibrils N_{PiF} for simulations with cooperative hydrogen bond energies between −0.5ϵ and −1.5ϵ. The values of N_{PiF} during the pre-runs are shown on the left side, those during the production-runs are shown on the right side. The step number on the x-axis is separated for pre-runs and production-runs, both start at zero. The data for the pre-runs was obtained every two hundredth step, the data for the production-runs every ten thousandth step. Please note the different scaling of the x-axis of pre-runs and production-runs.

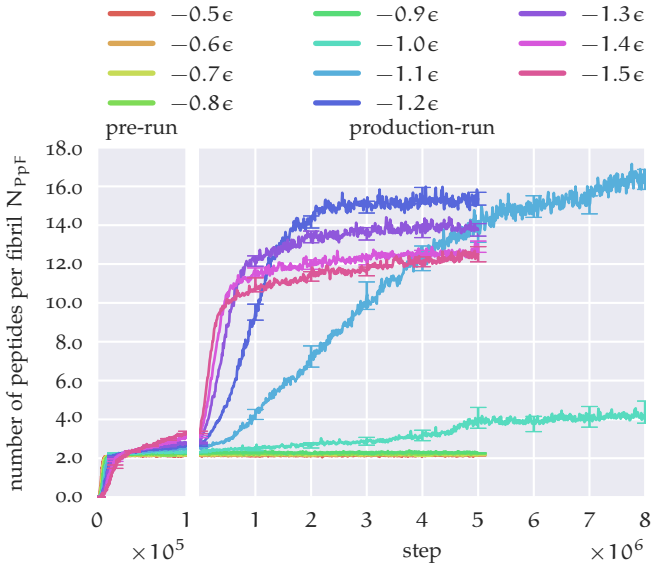

Figure 5.28: The number of peptides per fibril N_{PpF} for simulations with cooperative hydrogen bond energies between −0.5ϵ and −1.5ϵ. Structure of the plot like in Figure 5.27.

strong cooperative hydrogen bonds. After 2×10^6 additional steps the number of clusters drops in simulations with strong cooperative hydrogen bonds below the values of simulations with small absolute values of $E_{HB,\,cooperative}$. In the simulations with $E_{HB,\,cooperative} = -1.0\epsilon$ and $E_{HB,\,cooperative} = -1.1\epsilon$, that run for 8×10^6 steps, 1.15 ± 0.03 and 1.008 ± 0.008 clusters are present in each simulation on average at the end of the simulations.

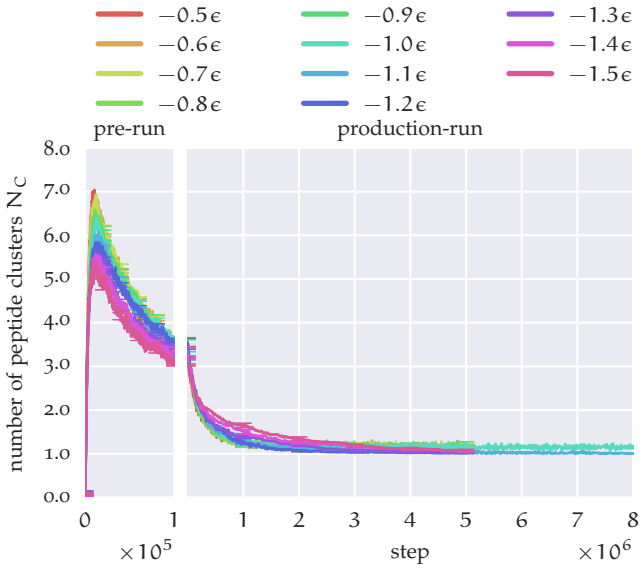

Figure 5.29: The number of peptide clusters N_C for simulations with cooperative hydrogen bond energies between -0.5ϵ and -1.5ϵ. Structure of the plot like in Figure 5.27.

5.8 CONCLUSION

In this chapter simulations with different values of the hydrogen bond energy were presented, to investigate the behaviour of the system in respect to fibril formation. The use of MC simulation techniques enables investigation of the process of fibrillization qualitatively, but not quantitatively. As already mentioned earlier, the un-physical moves implemented in this model do lead to un-physical dynamics. The model can nevertheless be used to investigate the different paths of fibril formation and to understand the differences of the resulting fibrils. To investigate the formation of fibrils more quantitatively, MD simulations are needed that lead to more realistic dynamics. The model presented in this thesis is designed with this in mind and is prepared to be used in a molecular dynamics environment.

The values for the hydrogen bond energies were chosen to enable simulations of the formation of fibrils in the presence of lipid membranes and to compare the results of both types of simulations. Therefore two conditions need to be fulfilled at the same time: Firstly, the strength of hydrogen bonds has to be neither too weak, so that no fibrils form at all, nor too strong, so that the presence of lipid membranes does not prohibit the formation of fib-

rils. Secondly, the formation should not be too quick, to enable us to measure the influence of a membrane present, and to enable interaction of the membrane with peptides in all different states of the simulation, e.g. single peptides, clustered peptides and fibrils. Simulations with local hydrogen bond energies of $E_{HB,\,local} = -5.5\epsilon$ and cooperative hydrogen bond energies of $E_{HB,\,cooperative} = -1.0$ and $E_{HB,\,cooperative} = -1.1$ fulfil all these requirements and are used for the simulations presented in the following chapter.

6 FIBRIL FORMATION IN THE PRESENCE OF MEMBRANES

The simulations discussed in the previous chapter showed that the peptide model is able to reproduce the formation of fibrillar structures in the bulk. By changing the parameters of the applied interactions, the process of fibril formation can be controlled.

Many experiments, some of them listed in Section 1.4, have shown that the influence of a membrane on the process of fibril formation can be investigated by generic simulations. Peptides and aggregates, which appear in the fibrillization process, influence the membrane, possibly resulting in membrane disruption. The interactions of fibrils and of structures which can be observed during the process of fibrillization with membranes play a major role in many diseases like Alzheimer's disease or Huntington's disease. Insight into the process of fibrillization in the presence and investigation of differences to the formation of fibrils in the bulk is therefore crucial.

The results presented in this chapter are obtained from simulations of peptides in the presence of a lipid bilayer. In the following, the influence of the membrane on the fibrillization process and the resulting fibrillar structures will be discussed. The interaction between peptide and lipid beads is modelled using a LJ-potential, as described in Chapter 2. In Section 6.1 the free energy for the insertion of a single peptide into the membrane is calculated. This is done to estimate a parameter range for attractive interactions between hydrophobic peptide beads and lipid tail beads. The setup of the following simulations of fibril formation in the presence of a membrane is described in Section 6.2. First systems with varied cooperative hydrogen bond strength are simulated (Section 6.3). The differences between fibrils that grow in the presence of a membrane and such that grow without are highlighted in Section 6.4. In the simulations in Section 6.3, the parameter ϵ_{lpi} used to determine the strength of the interaction between lipids and peptides is chosen to have the same value as for peptide-peptide interactions. In Section 6.5 systems with varied peptide-lipid interactions are simulated.

6.1 FREE ENERGY OF INSERTION FOR A SINGLE PEPTIDE

To assess the behaviour of peptides for different values of the interaction strength ϵ_{lpi} the free energy of inserting a single peptide into the membrane is calculated. To do so, umbrella sampling is used. Calculating the free energy can provide information about the sources of the apposition of peptides on the membrane surface, whether it is driven by entropy or by interaction energies.

For the umbrella sampling, simulations consisting of a single peptide, 3636 solvent beads, and a lipid membrane consisting of $2 \times 10 \times 10$ lipids are prepared. The variable d is defined as the distance between the centre of mass (COM) of the peptide and the COM of the membrane, with a positive value, if

the peptide is above the COM of the membrane and a negative value if it is underneath. To calculate the free energy of insertion, the density distribution function f as a function of the distance d is needed. $f(d)$ can be obtained by calculating a histogram for all possible distances.

The metropolis algorithm favours configurations of low energy by design. Therefore states of high energy get only scarcely sampled or stay even unreached during a simulation. To overcome this limitation, the successive umbrella sampling [132–134] is used, dividing the calculation of $f(d)$ into sub simulations. In those sub simulations, the distance d is only allowed to fluctuate in a given range $[d_{i,\,min}, d_{i,\,max}]$. Moves that would lead d outside of this range get rejected. Initially, the peptide is placed above the membrane with a distance from the COM of the membrane d between 8.0σ and 9.0σ. This setup is illustrated in Figure 6.1 (a). Inside the given range, the peptide is free to move. For the first simulations, the range for d is set to $[d_{i,\,min} = 8.0\sigma, d_{i,\,max} = 9.0\sigma]$. Following simulations are constructed by randomly picking a configuration with d in the range $[d_{i,\,min}, d_{i,\,min} + \Delta d]$. In the simulations discussed here, an overlap Δd of 0.2σ is used, together with a width of the range $[d_{i,\,min}, d_{i,\,max}]$ of 1σ. The following results are obtained from fourteen generations of simulations, meaning that the d is varied between 9σ (peptide above the COM of the membrane) and -2.4σ (peptide underneath the membrane), some figures only show positive values of d, as the results are symmetric in d around 0. Figure 6.1 (b) and 6.1 (c) show two snapshots from different generations of the umbrella sampling simulations.

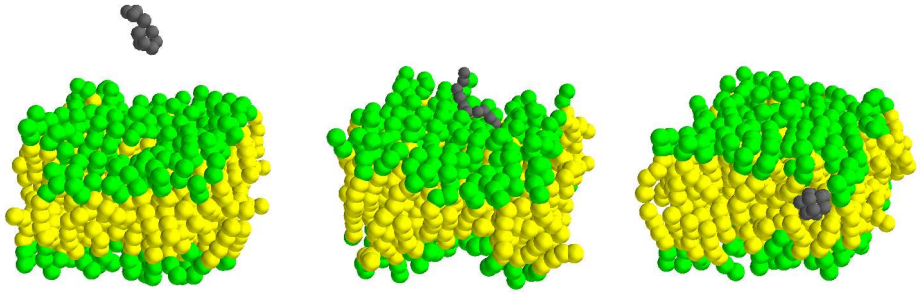

(a) (b) (c)

Figure 6.1: Different stages of the umbrella sampling simulations: a) Initial setup, b) Snapshot from a simulation with the distance d between centre of mass (COM) of the peptide and the COM of the membrane in a range between 3.4σ and 2.4σ, c) Snapshot from a simulation with d between 1.0σ and 0.0σ.

Each simulation in each generation, consists of a pre-run with 100 000 steps, followed by a production-run with 5×10^6 steps. The umbrella sampling procedure is applied for values of ϵ_{lpi} between 0.3ϵ and 1.1ϵ, with 128 independent simulations for each value of the interaction strength.

During the production-run, the values of d are stored and a histogram with twenty bins for all 128 simulations is calculated after the simulation in each generation. The histograms get connected, starting with the values obtained for the first generation ($9.0\sigma < d < 8.0\sigma$). To connect the values obtained for the next generation, the histogram of the new generation is scaled by a factor a, which is obtained by minimising the function

$$f(a) = \sum_{i=0}^{n} h_1^{(i)} - a \cdot h_2^{(i)} \quad , \tag{6.1}$$

where n is the number of overlapping bins, $h_1^{(i)}$ is the value of the ith overlapping bin of the older generation and $h_2^{(i)}$ is the value of the ith overlapping bin of the newer generation. By normalizing the obtained histogram for values of $d \geqslant 0$, the probability density distribution $P(d)$ can be obtained. This process is visualised in Figure 6.2 for the umbrella sampling simulations with $\epsilon_{lpi} = 0.6\sigma$.

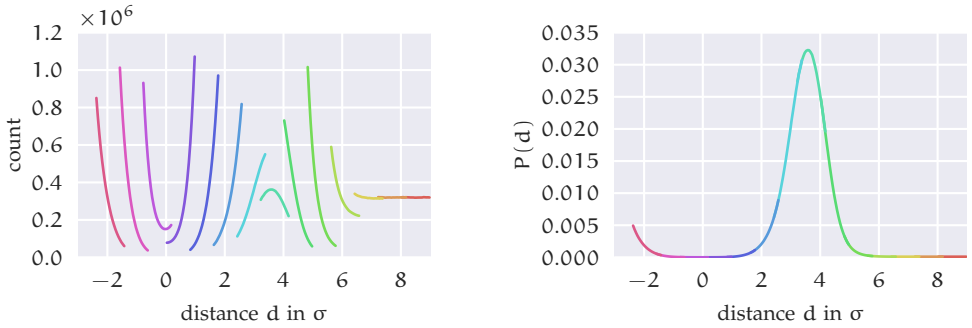

(a) (b)

Figure 6.2: Illustration of the process of connecting the histograms of the fourteen generations of simulations. For the sake of simplicity, the histogram values are plotted as lines, allowing to see the overlap of adjacent simulation generations on the x-axis. a) values for the single generations before connecting, b) values after connecting and normalizing.

$P(d)$ for each value of ϵ_{lpi} is plotted in Figure 6.3. For high values of d, $P(d)$ tends towards zero, independently of ϵ_{lpi}. In simulations with $\epsilon_{lpi} < 0.9$, $P(d)$ also tends towards zero for small values of d; for $\epsilon_{lpi} \geqslant 0.9$ $P(0) > 0$ is obtained. The position of the maximum of $P(d)$ is shifted towards lower values of d for higher values of ϵ_{lpi}. The positions and values of the maximum of $P(d)$ are given in Table 6.1. Those values are obtained by fitting a parabola to the maximum of each curve.

The position of the maximum of $P(d)$ is illustrated in Figure 6.4. To draw this illustration, the average distance in z of the first and second head bead from the COM of the membrane for all lipids in the simulations was calculated. These values, listed in Table 6.2, are shown as blue and green points for each value of ϵ_{lpi} in Figure 6.4. The calculated value d_{max} is marked with a red point. The semi-transparent areas around the blue, green and red points show the σ value used for interactions between lipid and peptide beads. The image

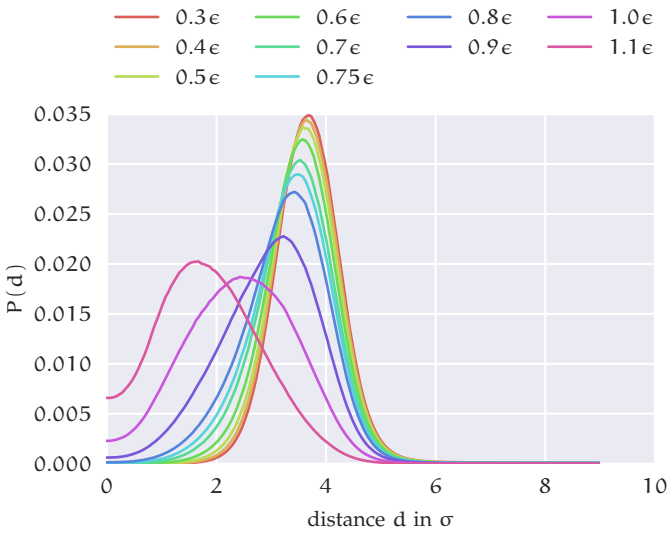

Figure 6.3: Probability density distribution $P(d)$ for values of $d \geqslant 0$. The errors are smaller than the lines and therefore not visible in this plot. A plot showing the size of the errors is given in Figure F.1.

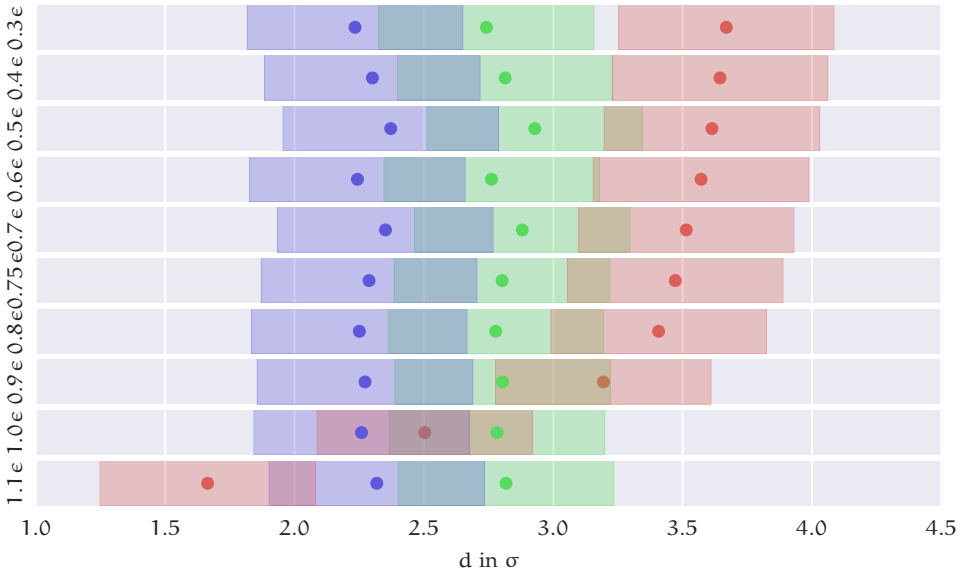

Figure 6.4: Illustration of the average position of the first and second lipid head bead (green and blue), and the position of the maximum of $P(d)$ (red). The semi-transparent backgrounds denote the maximum interaction range for interactions between lipid and peptide beads. The density distribution function is computed using the COM, therefore the semi-transparent background is only shown to guide the eye, rather than to give an information on the energies and interactions applied on the peptide. See text for more details.

shows that the peptides get closer to the COM of the membrane for higher values of ϵ_{lpi}.

ϵ_{lpi}	d_{max}	$P(d_{max})$
0.3ϵ	3.669 ± 0.001	$(3.476 \pm 0.005) \times 10^{-2}$
0.4ϵ	3.644 ± 0.001	$(3.422 \pm 0.001) \times 10^{-2}$
0.5ϵ	3.613 ± 0.001	$(3.353 \pm 0.001) \times 10^{-2}$
0.6ϵ	3.571 ± 0.001	$(3.235 \pm 0.003) \times 10^{-2}$
0.7ϵ	3.514 ± 0.001	$(3.025 \pm 0.003) \times 10^{-2}$
0.75ϵ	3.471 ± 0.001	$(2.894 \pm 0.003) \times 10^{-2}$
0.8ϵ	3.407 ± 0.001	$(2.716 \pm 0.003) \times 10^{-2}$
0.9ϵ	3.194 ± 0.002	$(2.263 \pm 0.003) \times 10^{-2}$
1.0ϵ	2.503 ± 0.004	$(1.865 \pm 0.004) \times 10^{-2}$
1.1ϵ	1.664 ± 0.004	$(2.019 \pm 0.003) \times 10^{-2}$

Table 6.1: Position and value of the maximum of $P(d)$ for different values of ϵ_{lpi}.

ϵ_{lpi}	z_1	z_2
0.3ϵ	2.74 ± 0.04	2.23 ± 0.04
0.4ϵ	2.81 ± 0.04	2.30 ± 0.04
0.5ϵ	2.93 ± 0.04	2.37 ± 0.04
0.6ϵ	2.76 ± 0.04	2.24 ± 0.04
0.7ϵ	2.88 ± 0.05	2.35 ± 0.04
0.75ϵ	2.80 ± 0.05	2.29 ± 0.05
0.8ϵ	2.78 ± 0.04	2.25 ± 0.04
0.9ϵ	2.80 ± 0.05	2.27 ± 0.04
1.0ϵ	2.78 ± 0.04	2.26 ± 0.04
1.1ϵ	2.82 ± 0.05	2.32 ± 0.05

Table 6.2: Average distance of the first (z_1) and second (z_2) lipid head in z-direction for different values of ϵ_{lpi}. For each value of ϵ_{lpi}, the values for z_1 and z_2 were obtained from membranes in simulations, in which the corresponding probability density distribution $P(d)$ has its maximum, eg. for $\epsilon_{lpi} = 0.6\epsilon$ the values are obtained from simulations with $3.2 < d < 4.2$.

For ϵ_{lpi} between 0.3ϵ and 0.8ϵ, the preferred position of the peptides is on top of the membrane, only for higher values of ϵ_{lpi}, the peptides begin to percolate the membrane surface deeper. For $\epsilon_{lpi} = 1.0\epsilon$, the peptides prefer positions between the first and the second head beads of the lipids, for $\epsilon_{lpi} = 1.1\epsilon$ the peptides reside inside the membrane. The reason for this behaviour will be discussed in the following, using the free energy of the system.

The free energy of the system G can be calculated, using the probability density distribution $P(d)$, by

$$G(d) = -\frac{1}{\beta} \log(P(d)) \quad , \tag{6.2}$$

because the ensemble average becomes equal to the time average in ergodic systems [134]. The curves for G are shown in Figure 6.5 (a).

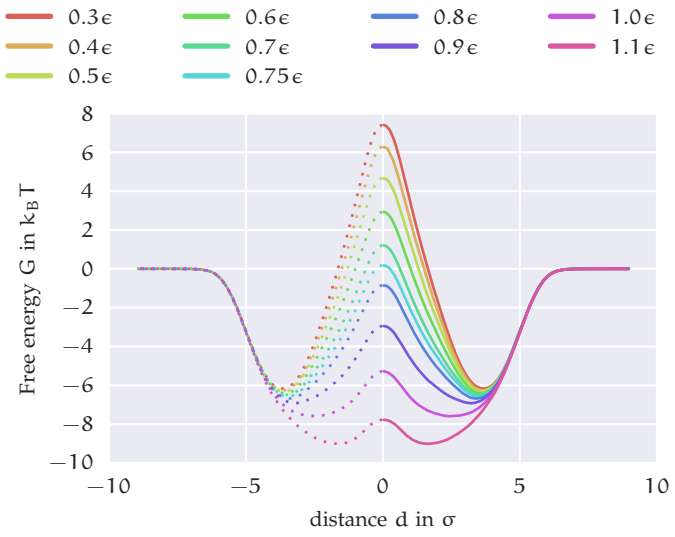

(a)

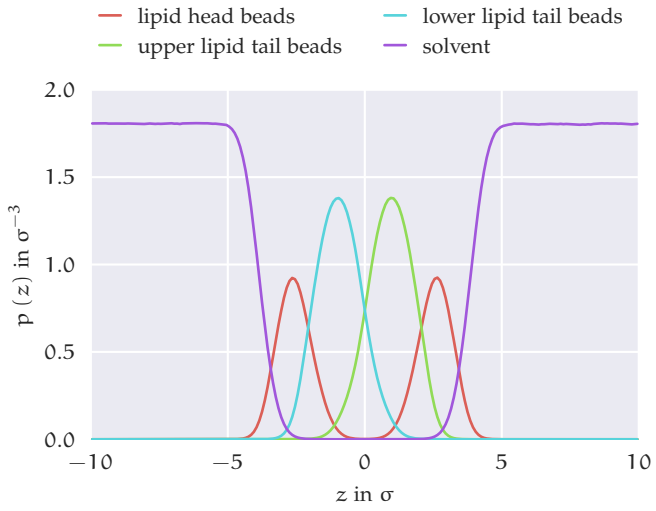

(b)

Figure 6.5: a) Free energy as a function of the distance d for different interaction energies between lipid head-beads and hydrophobic peptide beads ϵ_{lpi}. The errors are smaller than the lines and therefore not visible in this plot. A plot showing the size of the errors is given in Figure F.2. b) Density profile of a membrane without interactions between lipid and peptide beads. The COM of the membrane is shifted to 0 to simplify the comparison of the membrane position with the calculated free energy G, shown in a). Upper and lower lipid tail beads correspond to the lipid tail beads in the two leaflets.

To highlight the symmetry of the free energy, values of G for negative distances were added by simply mirroring G at $d = 0$. These values are plotted

ϵ_{lpi}/ϵ	d_{min}/σ	$G(d_{min})/k_BT$	d_{max}/σ	$G(d_{max})/k_BT$
0.3	3.669 ± 0.001	-6.168 ± 0.001	$(1.4 \pm 0.1) \times 10^{-2}$	7.406 ± 0.002
0.4	3.646 ± 0.001	-6.252 ± 0.001	$(2.7 \pm 0.1) \times 10^{-2}$	6.254 ± 0.006
0.5	3.615 ± 0.001	-6.311 ± 0.001	$(2.5 \pm 0.1) \times 10^{-2}$	4.650 ± 0.004
0.6	3.571 ± 0.001	-6.414 ± 0.001	$(8.7 \pm 0.6) \times 10^{-3}$	2.927 ± 0.002
0.7	3.513 ± 0.001	-6.494 ± 0.001	$(5.3 \pm 0.9) \times 10^{-3}$	1.219 ± 0.002
0.75	3.472 ± 0.001	-6.567 ± 0.001	$(1.4 \pm 0.06) \times 10^{-2}$	0.180 ± 0.001
0.8	3.406 ± 0.001	-6.678 ± 0.001	$(1.8 \pm 0.08) \times 10^{-2}$	-0.848 ± 0.001
0.9	3.193 ± 0.002	-6.918 ± 0.001	$(1.7 \pm 0.07) \times 10^{-2}$	-2.943 ± 0.001
1.0	2.505 ± 0.004	-7.587 ± 0.001	$(6.1 \pm 0.09) \times 10^{-3}$	-5.276 ± 0.001
1.1	1.665 ± 0.004	-9.008 ± 0.002	$(4.0 \pm 0.07) \times 10^{-3}$	-7.776 ± 0.001

Table 6.3: Position and value of the extremal points of the free energy G for different values of ϵ_{lpi}. See text for details.

with dotted lines. Both $P(d)$ and G were calculated using a *Jackknife* method [135]. Because the errors both for $P(d)$ and G are too small to be seen in the plots, they are shown in Figure F.1 and Figure F.2 in Appendix F, together with a short explanation of the Jackknife algorithm. The density profile of a membrane that is not interacting with peptide beads, plotted in Figure 6.5 (b), shows that the minimum of G is at the surface of the membrane.

Due to the symmetry of G, the following description for positive values of d is also valid for negative counterparts. For values of $d \gg 0$, G is set to 0. Towards lower values of d, G decreases. This decrease starts around values of $d = 6\sigma$, independent of ϵ_{lpi}. For values of $d < 4\sigma$ differences of G for different values of ϵ_{lpi} become visible. The minimum in G that is reached differs both in d and $G(d)$ for different values of ϵ_{lpi}; for higher interaction values, the minimum is shifted towards lower values of d and G. The free energy increases again for values of d smaller than d_{min}. A local maximum is reached for $d = 0$. In simulations with $\epsilon_{lpi} \leqslant 0.7\epsilon$ the value of G at this local maximum is positive, in simulation with $\epsilon_{lpi} \geqslant 0.8\epsilon$, the value is negative. For $\epsilon_{lpi} \leqslant 0.75\epsilon$, the value of G at $d = 0$ is close to the value outside the membrane. The minimum and maximum values of G and their positions are listed in Table 6.3. These values were obtained by fitting a parabolic function to the curve around the minimum and maximum position. The minimum of G corresponds to the position of the maximum of the probability density distribution $P(d)$. For higher values of ϵ_{lpi}, $G(0) - G(d \geqslant 6\sigma)$ becomes negative, meaning that a configuration with $d = 0$ is favoured over a configuration of $d \geqslant 7\sigma$. Nevertheless, both regions are connected by a minimum of G, and therefore neither configurations with peptides in the COM of the membrane nor configurations with peptides far away the bilayer are sampled often in the (non umbrella) simulations, described in the previous sections.

In Figure 6.6 the total energy E_{tot} of the system as a function of the distance d for systems with $\epsilon_{lpi} = 0.3$ is plotted. The values were obtained by connect-

ing the measured values of d and E_{tot} for each step in each simulations, and were then sorted into bins of d. For each bin, the average value of E_{tot}, shifted on the y-axis in such a way that $E_{tot}(d = 9) = 0$, is shown.

For values of d higher than 6σ, E_{tot} stays almost constant, because there are no lipid-peptide interactions in configurations with these distances. For smaller values of d, the total energy decreases and reaches its global minimum around $d = 4.7\sigma$ with a value of around $-4.5 k_B T$. Towards smaller values of d, E_{tot} increases again, showing a kink around $d = 1.0$ and reaches values of $20 k_B T$ for $d = 0$.

The plots for other values of ϵ_{lpi} are shown in Appendix F. For all values of ϵ_{lpi}, the position of the global minimum is roughly around $d = 5\sigma$. Both the probability density distribution and the free energy G shows that the peptides prefer positions closer to the membrane surface. The different positions of the minima lead to the conclusion that the preferred peptide position is driven by entropy rather than energy in the simulations. This also explains, why only small differences in the position of the maximum of $P(d)$ for small values of ϵ_{lpi} can be observed.

Figure 6.7 illustrates the preferred position of the peptides in the simulations. The figure shows two snapshots taken from simulations with $\epsilon_{lpi} = 0.3$ with d close to the value d_{min}.

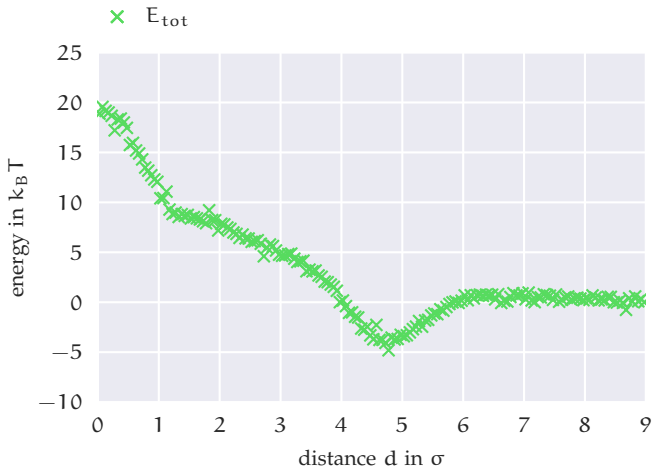

Figure 6.6: Total energy of the system as a function of distance d, averaged over all 128 simulations for $\epsilon_{lpi} = 0.3\epsilon$.

The location of the maximum of $P(d)$ and of the minimum of G in simulations with $\epsilon_{lpi} = 1.1\epsilon$ differs from the values obtained for simulations with weaker interactions. As illustrated in Figure 6.4, the position of the maximum of $P(d)$ is above the membrane or between the two lipid head beads for $\epsilon_{lpi} \leqslant 1.0\epsilon$. Only for $\epsilon_{lpi} = 1.1\epsilon$ a different situation can be observed: The highest probability for the position of the COM of the peptide is closer to the COM of the membrane, than both head beads of the lipids. Therefore a different behaviour, with respect to fibril formation, is expected in simulations with $\epsilon_{lpi} = 1.1\epsilon$. For simulations with ϵ_{lpi} between 0.3ϵ and 0.8ϵ, only

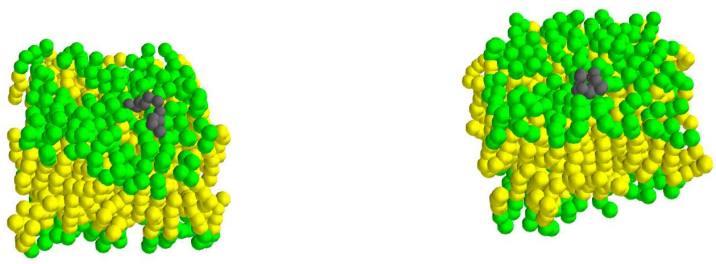

(a) (b)

Figure 6.7: Two snapshots from simulations with $\epsilon_{lpi} = 0.6\sigma$. Both snapshots show configurations of the system with d close to the minimum of the free energy G.

small differences in the peptide forming behaviour and the resulting peptides are expected, as the apposition of peptides is driven by entropy rather than interaction energy.

In the following section it will be tested whether the expectations which result from the calculation of the free energy G and the total energy E_{tot} as a function of the peptide lipid distance d for a single peptide, hold true for simulations with multiple peptides.

6.2 SETUP OF FIBRIL FORMATION SIMULATIONS

In the previous section, the free energy G of a single peptide was calculated. It was shown that the probability density function $P(d)$ has a maximum value at the surface of the membrane, leading to a minimum of G. In this and the following sections, it is tested if the model is able to form fibrils and whether the entropy-driven apposition of peptides on the membrane surface accelerates the process of fibril formation.

The simulation box contains a membrane consisting of $2 \times 20 \times 30$ lipids, oriented in the x-y-plane. Each lipid consists of two head and four tail beads, as described in Section 2.2. Like for the simulations of peptides in the bulk, 50 peptides in an α-helical configuration, randomly placed inside the simulation box, are used in the simulations. The algorithm used to distribute the peptides in the box during the system setup, prevents overlapping of peptide beads with the membrane. To simulate the solvent, 13 000 solvent beads are used. Like for the simulations described in the previous chapter, it is not possible to calculate a precise value for the peptide concentration, due to the variable value of the volume. Using the relation $1\sigma \approx 6.9$Å, the concentration of peptides in simulations that have run for several million steps and show only small volume changes, can be estimated to be around 50 mMol per liter. Like before 128 independent simulations for every varied parameter are carried out,

each one beginning with a pre-run consisting of 100 000 steps, followed by a production-run with five or eight million steps. To prevent a shrinking of the simulation box in one or more directions, volume changing moves in the x and y direction are applied with at once. The moves in z direction can be applied independently from those in x and y direction, as the membrane prevents a huge shrinking or growth in those two directions at the same time. Preventing small values for the length of the simulation box reduces the probability that structures emerge, which are connected through the periodic boundary conditions on both sides of the simulation box at the same time. Also the occurence of peptides that interact with images of themselves is prevented in this case. A typical setup is shown in Figure 6.8. The algorithms used to detect clusters and fibrillar structures are described in Section 5.2.

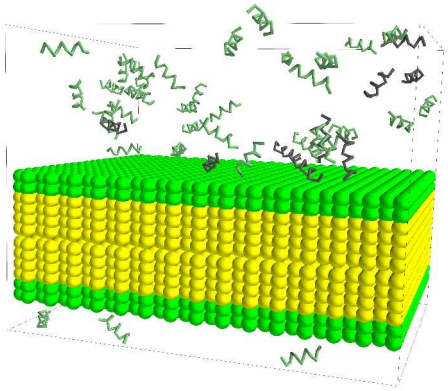

Figure 6.8: Setup for the simulation of fibril formation in the presence of membranes. 50 peptides in an α-helical conformation are placed randomly inside a cubic box. 13 000 solvent beads inside the simulation are not shown for clarity. The peptides shown in this illustration are ignoring the periodic boundary conditions for clarity. Peptide beads that appear to be outside the simulation box are folded back into the opposite site of the box.

6.3 VARIED COOPERATIVE HYDROGEN BOND STRENGTH

To investigate the influence of a lipid bilayer on the process of fibril formation, the same values for the local and non-local hydrogen bond energies as for the simulations described in Section 5.7 are used: The energies for local and non-local hydrogen bonds are fixed to values of -5.5ϵ and -3.85ϵ. The energy for cooperative hydrogen bonds is varied between -0.8ϵ and -1.1ϵ. The interactions between all lipid beads and peptide beads are purely repulsive, only between hydrophobic peptide beads and lipid tail beads an attractive LJ potential is used. The depth of the attractive potential is 0.6ϵ. See Table E.1 and Table E.16 for a complete list of parameters.

The number of peptides in fibrils, shown in Figure 6.9, behaves in the case of $E_{HB,\,\text{cooperative}} = -0.8\epsilon$ similar to the simulations without the presence of membranes. The number rises quickly at the beginning of the pre-run, reaching a value of 10.9 ± 0.4 after 35 600 steps. Towards the end of the pre-run the value decreases again slightly and reaches 9.2 ± 0.3 after 100 000 steps. During

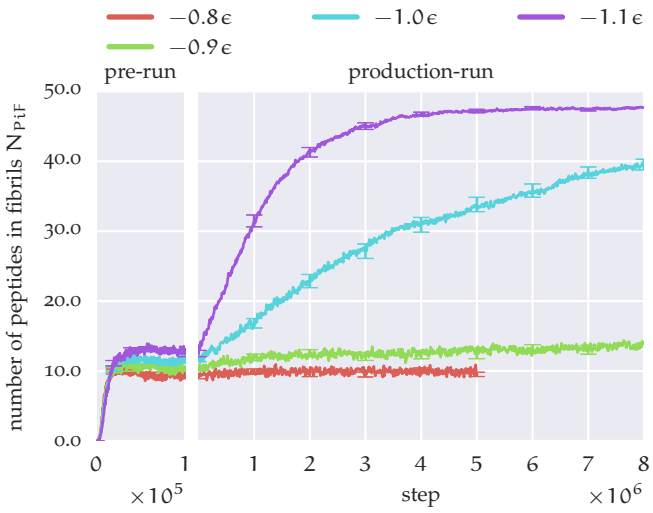

Figure 6.9: The number of peptides in fibrils for simulations with lipid membranes and peptides and cooperative hydrogen bond energies between -0.8ϵ and -1.1ϵ.

the production-runs the number of peptides in fibrils stays constant around a value of 10. The value behaves similar in simulations with $E_{HB,\,cooperative} = -0.9\epsilon$ during the pre-run, after a quick increase it reaches a maximum at 60 200 steps with 11.5 ± 0.3 peptides in fibrils. At the end of the pre-run on average 10.4 ± 0.4 peptides are part of a fibril. After about 1×10^6 steps in the production-runs the number of peptides in fibrils shows a small linear increase, reaching a value of 13.7 ± 0.7 after eight million steps. The curve for simulations with $E_{HB,\,cooperative} = -1.0\epsilon$ reaches values of 11.7 ± 0.4 at the end of the pre-runs. During the production-runs it increases and reaches values of 39.4 ± 0.8 after 8×10^6 steps. The number of peptides in fibrils for simulations with $E_{HB,\,cooperative} = -1.1\epsilon$ rises quickly at the beginning of the pre-runs and stays more or less constant at a value around 13 after 50 000 steps. During the production-runs, the number of peptides increases quickly at first, but the growth becomes weaker during the simulations. After eight million steps, 46.3 ± 2.3 peptides are part of a fibril on average.

Figure 6.10 shows the average number of peptides per fibril for each value of $E_{HB,\,cooperative}$. During the pre-runs, the value behaves similar for all values of $E_{HB,\,cooperative}$. The fibril size increases quickly at the beginning and stays constant afterwards at values between 2.0 and 2.5. During the production-runs, the number of peptides per fibril behaves differently depending on the value of $E_{HB,\,cooperative}$. In simulations with $E_{HB,\,cooperative} = -0.8\epsilon$, the fibril size stays constant at the level reached during the pre-runs, no increase in fibril size can be observed. The average fibril size in simulations with $E_{HB,\,cooperative} = -0.9\epsilon$ grows linearly during the production-runs, reaching fibril sizes of 3.4 ± 0.3 peptides on average after 8×10^6 steps. In simulations with $E_{HB,\,cooperative} = -1.0\epsilon$ the fibril size increases faster, leading to fibrils consisting of 18.3 ± 0.8 peptides on average at the end of the simulations. For values of $E_{HB,\,cooperative} = -1.1\epsilon$, the number of peptides per fibril grows fast at the beginning of the production-

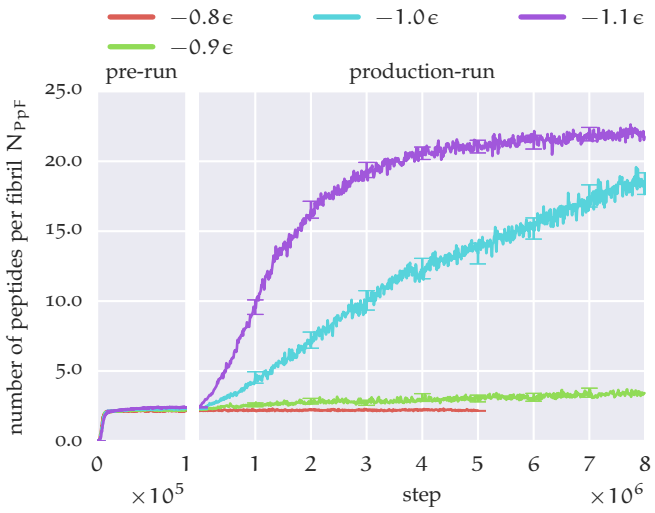

Figure 6.10: The number of peptides per fibril for simulations with lipid membranes and peptides and cooperative hydrogen bond energies between -0.8ϵ and -1.1ϵ.

runs, but the increase becomes smaller with the increasing number of simulation steps, in full agreement to the behaviour observed for the growth of the number of peptides in fibrils, shown in Figure 6.9. After 8×10^6 steps in production-runs, the average fibrils in simulations with $E_{HB,\,\text{cooperative}} = -1.1\epsilon$ have grown to 21.8 ± 0.5 peptides. During the pre-runs, the number of peptide

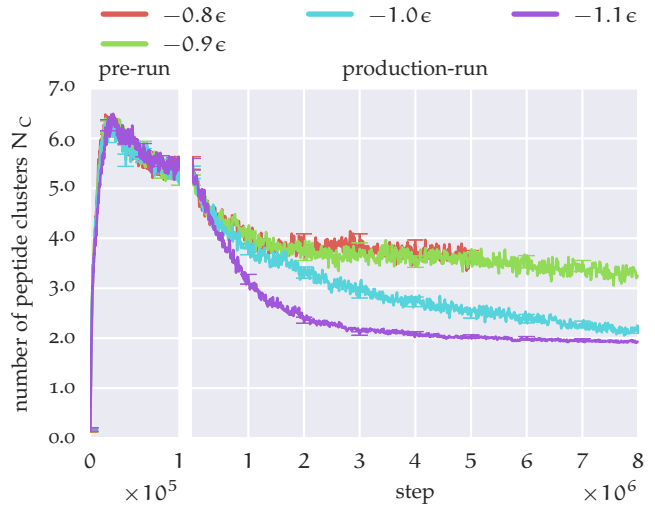

Figure 6.11: The number of peptide clusters N_C for simulations with lipid membranes and peptides and cooperative hydrogen bond energies between -0.8ϵ and -1.1ϵ.

clusters N_C, shown in Figure 6.11, behaves similar to the number of clusters in simulations without a lipid membrane; it increases rapidly during the first

20 000 steps and decreases then slowly towards the end of the pre-run. On average a maximum of 6.5 clusters exists in a simulation at the same time.

During the production-runs, the progress of the curves is different for different values of $E_{HB,\,cooperative}$, although for all cases the number of clusters seems to decrease exponentially, the level that is reached for each value of $E_{HB,\,cooperative}$ is different. For strong cooperative hydrogen bonds, the number of clusters develops towards two clusters, whereas 3.3 ± 0.1 and 3.8 ± 0.1 clusters exist at the end of the production-runs for $E_{HB,\,cooperative} = -0.9\epsilon$ and $E_{HB,\,cooperative} = -0.8\epsilon$, respectively.

The process of fibril formation is illustrated in Figure 6.12 and Figure 6.13 for the peptides on the top and the bottom side of the membrane of a simulation with $E_{HB,\,cooperative} = -1.0\epsilon$. The images show that preferred positions of the peptides are at the membrane surface. This is in agreement with the results obtained from single peptide simulations at the beginning of this chapter.

On the top layer of the membrane the growth of one fibrillar structure can be observed. During 500 000 steps, from step 1×10^6 to 1.5×10^6, the main increase in fibrils size takes place. In the following steps, the size increases only slowly, reaching its maximum value after two million steps (step 3×10^6 in the simulation). The fibril that forms on the bottom layer also takes about two million steps to reach its full size, but the process starts at a later step in the production-runs. Both figures show only the peptides that are on the top layer, and the bottom layer, respectively.

6.4 DIFFERENCES TO SIMULATIONS WITHOUT MEMBRANES

The graphs shown in this and the previous chapter reveal several differences between simulations with and without the presence of a lipid membrane. In simulations with a membrane, the number of peptide clusters reaches a value of 2 for simulations with $E_{HB,\,cooperative} = -1.0\epsilon$ and $E_{HB,\,cooperative} = -1.1\epsilon$. Without the presence of a membrane, on average only one cluster exists in each simulation after 8×10^6 steps. The membrane in the simulation acts as a barrier that prevents the clustering of all peptides in one cluster. Single peptides can and do change to the opposite side of the membrane through the solvent and the periodic boundaries. The two clusters form on the membrane surface mediated by attractive interactions between lipids and peptides. This attraction has two sources: The LJ potential, used to model the interactions between hydrophobic peptide beads and lipid tail beads, has an attractive part and entropic effects cause an apposition of peptides on the membrane surface in our model, as shown in Section 6.1.

The comparison of Figure 5.28 and Figure 6.10 reveals that the fibrils which form in the presence of membranes, are on average larger than their counterparts formed in simulations without membranes, although all peptides aggregate in one cluster in the latter case. Opposite to simulations without a membrane, peptides in simulations with a bilayer present do not form layers of parallel fibrils in the majority of simulations. A more detailed discussion on the occurrence of layered fibril clusters follows in Section 6.5.3.

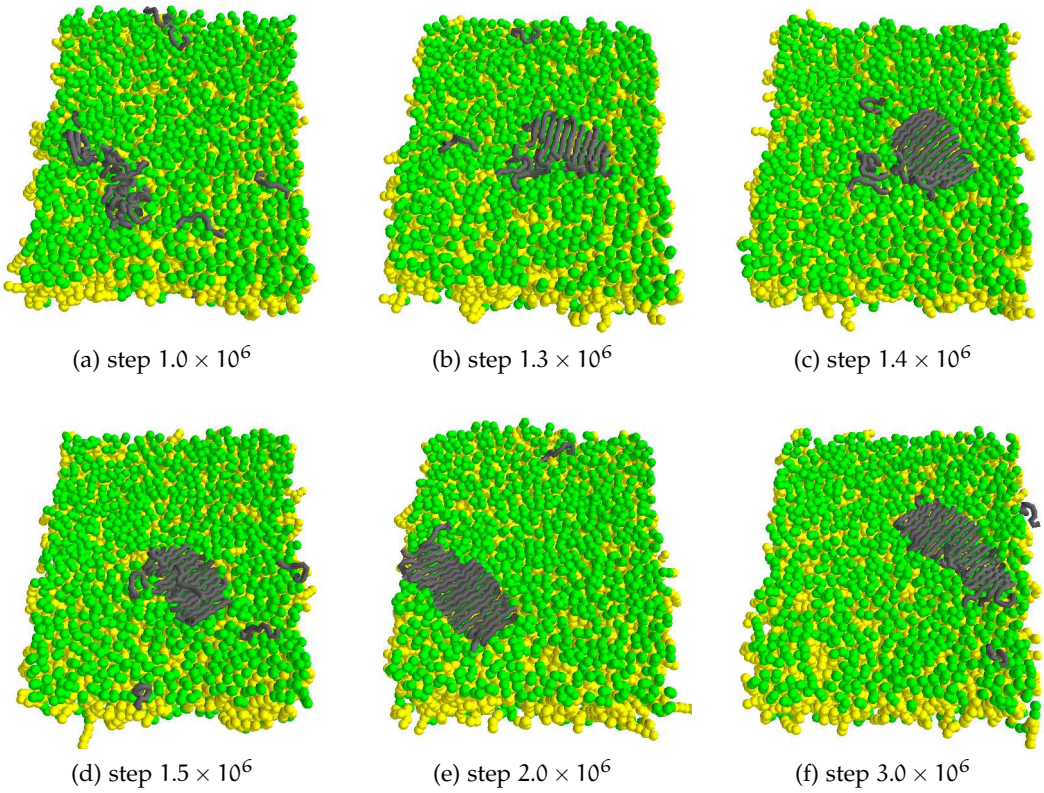

(a) step 1.0×10^6 (b) step 1.3×10^6 (c) step 1.4×10^6

(d) step 1.5×10^6 (e) step 2.0×10^6 (f) step 3.0×10^6

Figure 6.12: Formation of fibrils in the presence of a membrane: Top view of a simulation with $E_{HB,\,cooperative} = -1.0\epsilon$. The solvents are not shown for clarity. The bottom view is given in Figure 6.13. Images showing only the peptides with coloured fibrils are given in Figure D.1. See text for details.

Figure 6.14 shows the number of fibrils divided by the number of peptide clusters N_{FpC}. In simulations without a membrane N_{FpC} increases quickly at the beginning of the simulations and reaches values between 5.0 and 6.0, depending on $E_{HB,\,cooperative}$. In simulations with $E_{HB,\,cooperative} \geqslant -0.9\epsilon$, N_{FpC} stays roughly constant until the end of the simulations. For $E_{HB,\,cooperative} = -1.0\epsilon$, N_{FpC} decreases slowly, reaching values of 5.73 ± 0.05 after eight million steps, the decrease is faster in simulations with $E_{HB,\,cooperative} = -1.1\epsilon$, where N_{FpC} reaches values of 3.27 ± 0.2 after eight million steps.

In simulations with a lipid membrane, N_{FpC} behaves differently. During the first 6×10^5 ($E_{HB,\,cooperative} = -1.1\epsilon$) to 2×10^6 steps ($E_{HB,\,cooperative} = -0.8\epsilon$) N_{FpC} increases quickly and reaches values between 1.3 and 1.5. In simulations with $E_{HB,\,cooperative} \geqslant -0.9\epsilon$, N_{FpC} keeps increasing, but with a reduced rate. For $E_{HB,\,cooperative} = -1.0\epsilon$ and $E_{HB,\,cooperative} = -1.1\epsilon$, N_{FpC} decreases slowly, reaching values of 1.28 ± 0.05 and 1.22 ± 0.03, respectively.

In Figure 6.15, N_a, the number of peptides that are part of a fibril, divided by the number of peptides that are part of a cluster, is plotted. It is a measure, for how mature the fibrils in the simulations are. In simulations with $E_{HB,\,cooperative} = -0.8\epsilon$ and $E_{HB,\,cooperative} = -0.9\epsilon$, less than 40 percent of the peptides inside a cluster are also part of a fibril during the production-runs , both in simulations with and without a lipid membrane. For $E_{HB,\,cooperative} =$

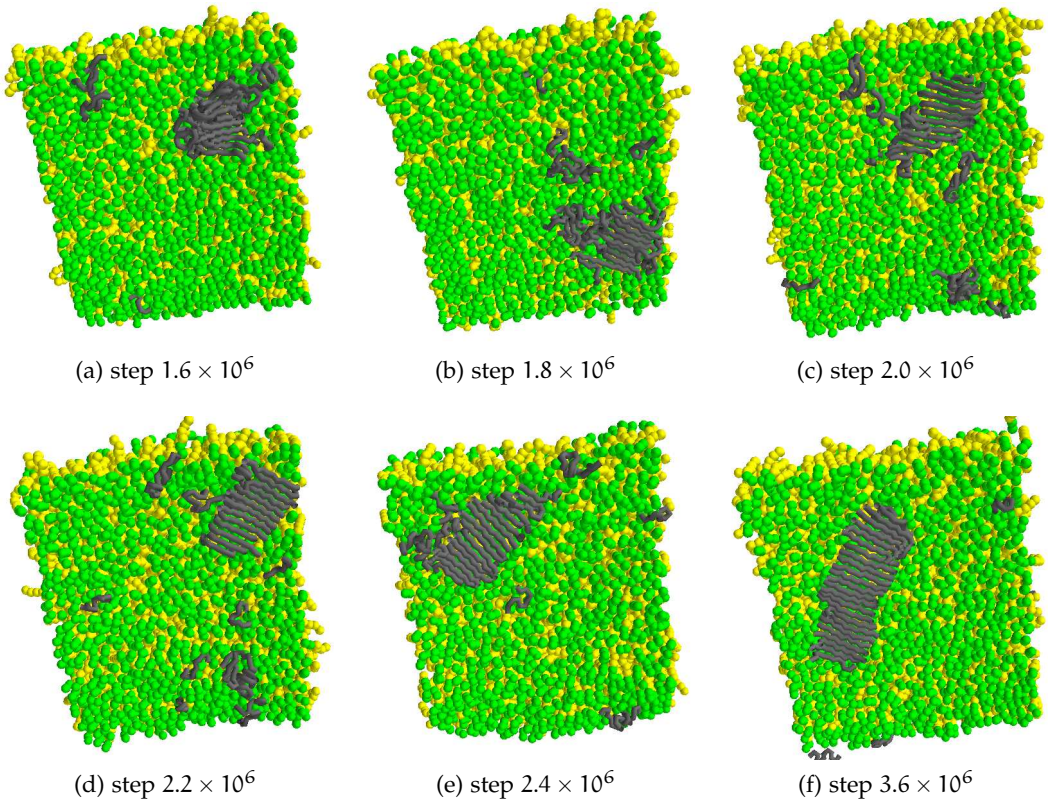

(a) step 1.6×10^6 (b) step 1.8×10^6 (c) step 2.0×10^6

(d) step 2.2×10^6 (e) step 2.4×10^6 (f) step 3.6×10^6

Figure 6.13: Formation of fibrils in the presence of a membrane: Bottom view of a simulation with $E_{HB,\,cooperative} = -1.0\epsilon$. The solvents are not shown for clarity. The top view is given in Figure 6.12. Images showing only the peptides with coloured fibrils are given in Figure D.2.

-1.0ϵ and $E_{HB,\,cooperative} = -1.1\epsilon$, N_a increases during the production-runs. In simulations without a membrane, N_a reaches values of 0.40 ± 0.02 for cooperative hydrogen bond energies of -1.0ϵ and 0.96 ± 0.01 for $E_{HB,\,cooperative} = -1.1\epsilon$. In the presence of a membrane, N_a reaches values of 0.90 ± 0.01 for $E_{HB,\,cooperative} = -1.0\epsilon$ and $1.0 \pm (0, 0.01)$ for $E_{HB,\,cooperative} = -1.1\epsilon$.

Combining the results from Figure 6.14 and Figure 6.15, it is obvious that in simulations without the presence of a lipid membrane several small fibrillar structures form in the case of cooperative hydrogen bonds weaker than -1.1ϵ. These fibrils incorporate only a fraction of the peptides inside the cluster. With $E_{HB,\,cooperative} = -1.1\epsilon$ the cooperative hydrogen bonds become strong enough to incorporate nearly all peptides inside the cluster. After eight million steps of the simulations, the clusters consist of three layers of fibrils and no peptides that are not part of a fibril, can be found inside the clusters. In the presence of a membrane, in simulations with $E_{HB,\,cooperative} = -0.8\epsilon$ and $E_{HB,\,cooperative} = -0.9\epsilon$ also only a small fraction of peptides inside a cluster gets part of a fibril, but the number of fibrils per cluster is smaller than in simulations without a membrane. From the curves for simulations with $E_{HB,\,cooperative} = -1.0\epsilon$ and $E_{HB,\,cooperative} = -1.1\epsilon$ it can be seen that after eight million steps the majority of clusters consists of a single fibril.

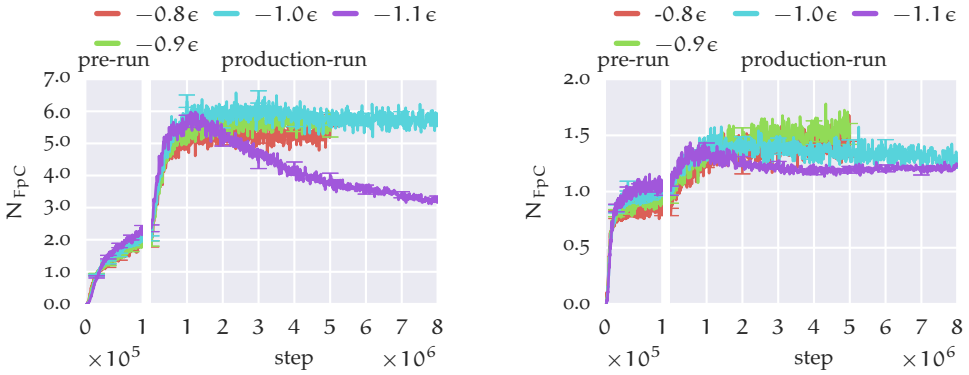

(a) (b)

Figure 6.14: The number of fibrils divided by the number of clusters N_{FpC}, plotted for simulations with values of $E_{HB,\,cooperative}$ between −0.8 and −1.1. (a) shows simulations without lipid membranes, (b) shows simulations with lipid membranes.

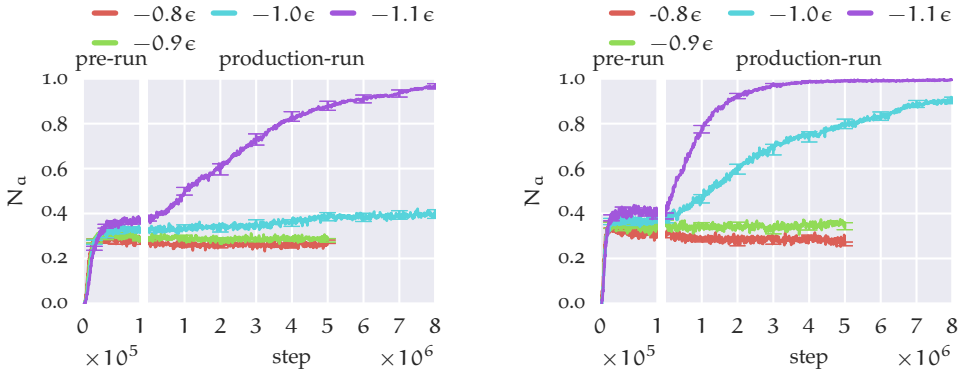

(a) (b)

Figure 6.15: The number of peptides in fibrils divided by the number of peptides in clusters N_a, plotted for simulations with values of $E_{HB,\,cooperative}$ between −0.8 and −1.1. (a) shows simulations without lipid membranes, (b) shows simulations with lipid membranes.

Like in Section 5.6.3, the normalized asphericity b_N, the normalized acylindricity c_N and the squared radius of gyration R_g^2, calculated by using the gyration tensor, as shown in Equation 5.3 - Equation 5.8, is used to characterise the shape of the peptide clusters that emerge in simulations with $E_{HB,\,cooperative} = -1.1\epsilon$. In Figure 6.16 and Figure 6.17 b_N and c_N, respectively, is plotted against R_g^2. Both graphs show a different behaviour for simulations with and without lipid membranes. The clusters and fibrils that form in simulations without the presence of a lipid membrane possess a smaller (squared) radius of gyration than those observed in simulations with a membrane. This is compatible to the observation that the fibrils which form on a

membrane surface grow bigger than those in the bulk. Despite the differences in the value of R_g^2, both types of simulations show a growth of the radius of gyration during the course of each run. The behaviour of the normalized asphericity b_N shows more differences between the two types of simulations. In systems without a membrane, b_N decreases initially, followed by a quick increase for values of $R_g^2 > 7$. This corresponds to the formation of clusters in the bulk, which initially develop towards a spherical shape. Together with the growth of fibrillar structures, the symmetry is reduced, mirrored by the increase of b_N. In simulations with a lipid membrane, the value of b_N increases during the whole simulation, reaching a value of 1.0 at the end of the runs. This behaviour corresponds to the observation that the peptides accumulate at the membrane surface without the formation of a spherical shape, and to the growth of fibrillar structures, longer than those observed in simulations without a membrane.

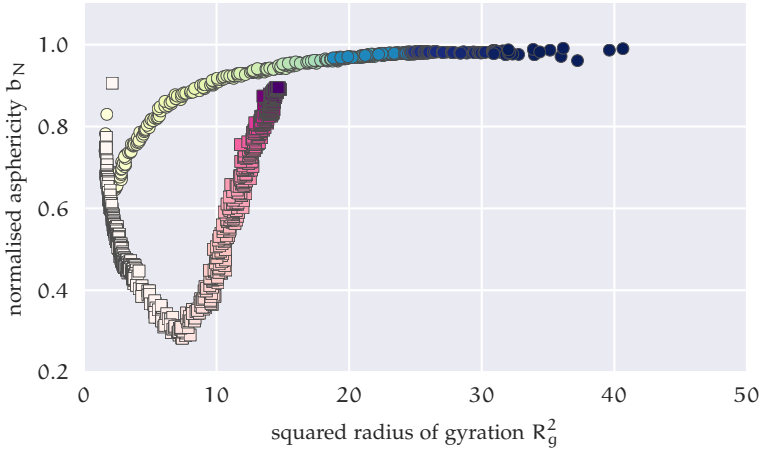

Figure 6.16: Normalized asphericity b_N plotted against the squared radius of gyration R_g^2, averaged over 128 independent runs with $E_{HB,\,\text{cooperative}} = -1.1\epsilon$. The values are calculated from the centre of mass of peptides inside the same cluster. The quadratic markers show values from simulations without a membrane, circles those for simulations with a membrane. The brightness of the colour corresponds to the simulation step the value is taken from; darker colours correspond to later steps in the simulation. The kink in the curve for simulations without a membrane is reached after about 7×10^5 steps. The values are obtained from both pre-runs and production-runs.

The normalized acylindricity c_N, plotted in Figure 6.17, decreases for clusters in simulations without a membrane, in two steps. In the first step c_N decreases exponentially for values of R_g^2 smaller than 7. Around $R_g^2 = 7$ a value of $c_N = 0.125$ is reached. Towards higher values of R_g^2, c_N decreases again faster. For $R_g^2 > 10$, the decrease of c_N becomes almost linear with R_g^2. The position of the step in c_N on the x-axis corresponds to the turning point in the curve of b_N shown in the previous figure. In simulations with a membrane, c_N decreases exponentially towards zero.

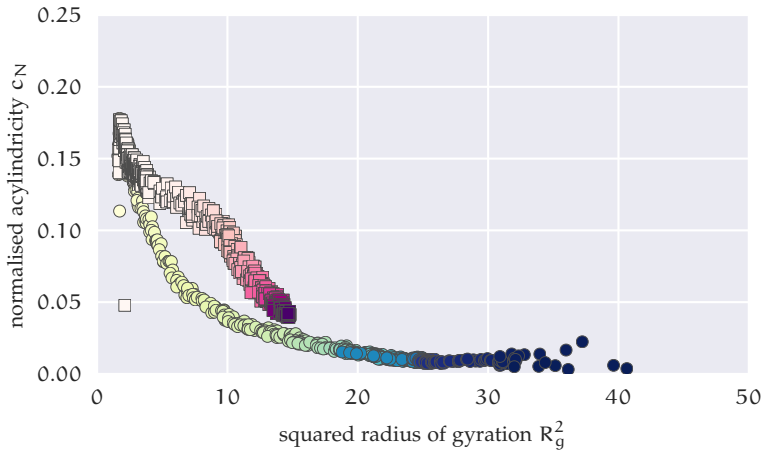

Figure 6.17: Normalized acylindricity c_N plotted against the squared radius of gyration R_g^2. The colouring is the same as in Figure 6.16.

By plotting the normalized acylindricity c_N against the normalized asphericity b_N, as in Figure 6.18, the differences in the process of fibril formation can be highlighted even more. Both the values obtained for simulations with and without a membrane tend towards high values of b_N and low values of c_N. In simulations with a lipid membrane, all (b_N,c_N) points lie on a line that connects a region of small clusters composed from three randomly placed points with a region of values of clusters in which all points lie on a line - marked as b) in the image. Without a membrane, the points for b_N and c_N form two lines. Again the values start in the region of clusters of three points. Initially the values of b_N and c_N decrease, what means that the clusters that form at the beginning of the simulations have a symmetric shape. After reaching values of 0.3 for b_N, the values for b_N begin to increase again. This kink is reached after about 7×10^5 steps. Opposite to the clusters and the majority of fibrils that develop on a membrane surface, the clusters in the bulk do not reach the point (1.0,0.0). As already stated before, this is due to the fact, that in the clusters that form in the bulk, layered fibrils develop. The missing kink in simulations with a membrane is caused by the apposition of peptides to the membrane surface: The formation of a (symmetric) cluster, which can be observed in simulations without a membrane, is not observed in the case of systems with a membrane. This formation of a cluster, and its following conversion from a cluster of random coil peptides to layers of fibrils, causes the value of b_N to decrease and increase again in simulations without a membrane. Three examples of typical structures, showing a cluster of four layers of fibrils grown in a simulation without a membrane, a single fibril, and a cluster of two parallel fibrils, which form in simulations with a membrane, are given in Figure 6.19. Their values of b_N and c_N marked in Figure 6.18. The normalized acylindricity c_N, the normalized asphericity b_N, and the squared radius of gyration R_g^2 for simulations with $E_{HB,\,\text{cooperative}} = -1.0\epsilon$ are not plotted here, but show a similar behaviour.

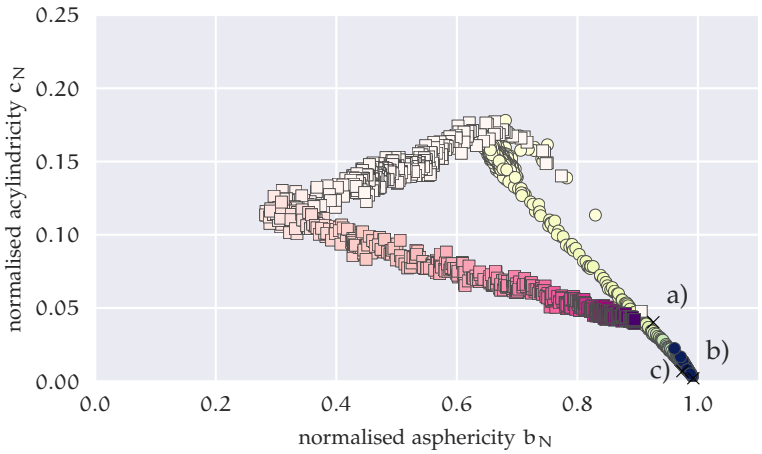

Figure 6.18: Normalized acylindricity c_N plotted against the normalized asphericity b_N. The colouring is the same as in Figure 6.16. The three labelled points denote the values of b_N and c_N three typical clusters, which formed during the simulations, shown in Figure 6.19.

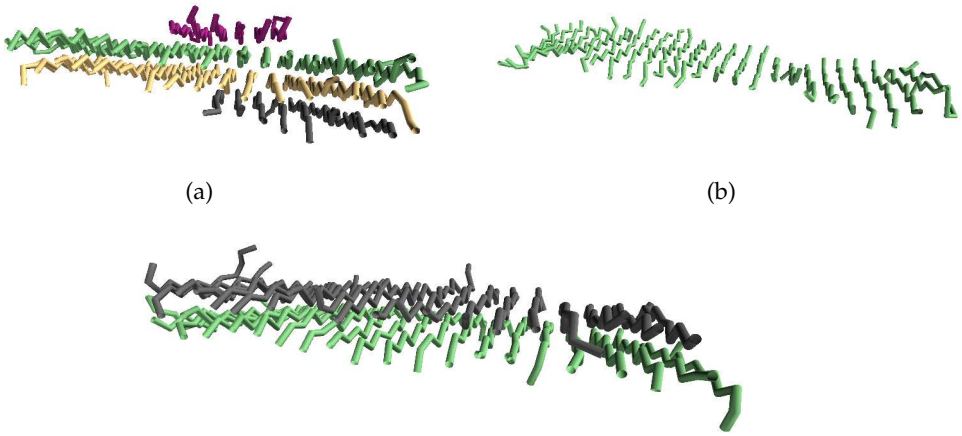

Figure 6.19: Three different structures that occur during the simulations. a) shows a cluster of four parallel fibrils which formed in a simulation without lipids, b) and c) show a single fibril and two parallel fibrils which formed at the surface of a lipid membrane. The values of b_N and c_N of these three clusters are marked in Figure 6.18.

6.5 VARYING LIPID-PEPTIDE INTERACTION STRENGTH

In Section 6.1 the free energy G and the total energy E_{tot} as a function of the distance of the COM of the peptide and the COM of the membrane was calculated for different values of the interaction strength between lipid tail beads and hydrophobic peptide beads. In Section 6.3 it was already shown that for cooperative hydrogen bond strength $\epsilon_{HB,\,\text{cooperative}} = -1.1\epsilon$ and -1.0ϵ and a

value of $\epsilon_{lpi} = 0.6\epsilon$ for interactions between lipids and peptides, the formation of fibrils can be observed, and that this process is accelerated compared to the formation of fibrils in simulations without a lipid membrane present. The curves obtained for the free energy G and the probability density distribution $P(d)$ showed that, at least for weak lipid-peptide interactions, the peptides tend to accumulate at the membrane surface. In this chapter, the results obtained from two sets of simulations are discussed, one with $\epsilon_{HB,\,cooperative} = -1.1\epsilon$, and one with $\epsilon_{HB,\,cooperative} = -1.0\epsilon$ which were set up similar to the simulations described in Section 6.2. In both sets of simulations the strength of cooperative hydrogen bonds is kept fixed and only the strength of the interactions between lipid tail beads and hydrophobic peptide beads ϵ_{lpi} is varied between 0.3ϵ and 1.0ϵ, for $\epsilon_{HB,\,cooperative} = -1.1\epsilon$, also the results obtained from simulations with $\epsilon_{lpi} = 1.1\epsilon$ are shown.

6.5.1 *Simulations with* $\epsilon_{HB,\,cooperative} = -1.1\epsilon$

The number of peptides in fibrils N_{PiF} rises at the beginning of the pre-runs quickly, as shown in Figure 6.20. After about 2×10^4 steps, about 12 to 13 peptides are part of a fibril on average. Towards the end of the pre-runs, N_{PiF} decreases again slightly, in simulations with stronger interaction parameters ϵ_{lpi}, the decrease is stronger than in those with weaker interactions: For $\epsilon_{lpi} = 0.3\epsilon$, 13.6 ± 0.4 peptides are part of a fibril after 1×10^5 steps, for $\epsilon_{lpi} = 1.1\epsilon$, N_{PiF} decreases to 7.0 ± 0.4. During the production-runs, the simulations with ϵ_{lpi}

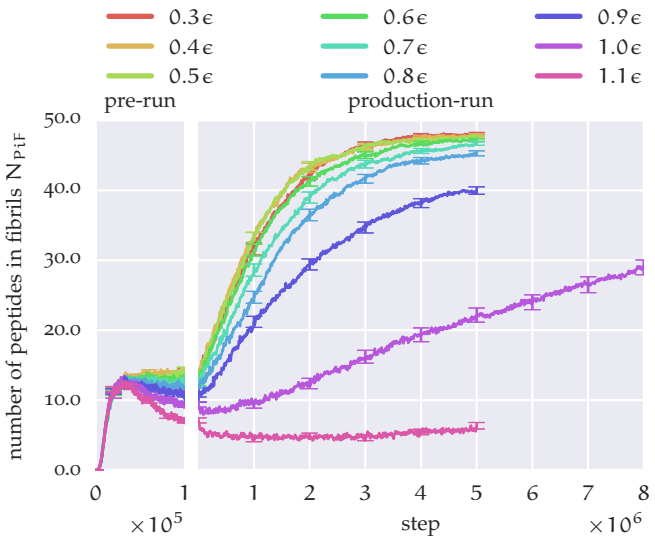

Figure 6.20: The number of peptides in fibrils N_{PiF} for simulations with lipid membranes and peptides, $\epsilon_{HB,\,cooperative} = -1.1\epsilon$. The strength of interactions between lipid tail beads and hydrophobic tail beads ϵ_{lpi} is varied between 0.3ϵ and 1.1ϵ.

between 0.3ϵ and 0.9ϵ behave similar. During the whole run, N_{PiF} increases, thereby the increase rate becomes smaller with every step. In simulations with $\epsilon_{lpi} = 1.0$, N_{PiF} initially continues to decrease. After about 150 thousand steps,

a minimum of 8.5 is reached, and N_{PiF} begins to increase again. Opposite to the concave curves for simulations with weaker interactions, the curve for N_{PiF} in simulations with $\epsilon_{lpi} = 1.0$ shows an almost constant increase during the simulations. For $\epsilon_{lpi} = 1.1$, N_{PiF} also continues to decrease at the beginning of the production-runs. In the second half, a small increase of N_{PiF} in these simulations can be observed. The values of N_{PiF} after five million steps are listed in Table 6.4.

ϵ_{lpi}	N_{PiF}
0.3ϵ	48.1 ± 0.2
0.4ϵ	47.8 ± 0.2
0.5ϵ	47.7 ± 0.2
0.6ϵ	47.7 ± 0.2
0.7ϵ	46.5 ± 0.3
0.8ϵ	45.2 ± 0.4
0.9ϵ	39.8 ± 0.5
1.0ϵ	22 ± 1
1.1ϵ	5.8 ± 0.4

Table 6.4: The number of peptides in fibrils N_{PiF} after 5×10^6 steps for different values of ϵ_{lpi}.

The decrease of N_{PiF} after 2×10^4 steps till the end of the pre-runs, in the case of $\epsilon_{lpi} = 1.0$ and 1.1 also during production-runs, is caused by the interactions between the peptides and the membrane. After the start of the simulations, small fibrils consisting of two to three peptides form in the bulk. The interactions between the peptides and the lipid membrane, that occur when those peptides attach to the membrane surface, lead to a reducing of the number of peptides in fibrils. The interaction energy E_{l-p} for the different values of ϵ_{lpi} are shown in Figure 6.21. For ϵ_{lpi} between 0.3ϵ and 0.6ϵ, E_{l-p} stays positive during the whole simulations. For stronger lipid peptide interactions, E_{l-p} attains negative values during both pre-runs and production-runs.

For $\epsilon_{lpi} \leqslant 1.0$, the lipid interaction energy increases during the production-runs again, in case of simulations with $\epsilon_{lpi} = 1.1$, the value stays constant. The increase of E_{l-p} is caused by the formation of fibillar structures, as will be shown later.

The number of peptides per fibril N_{PpF} is shown in Figure 6.22. During the first 2×10^6 steps of the pre-runs, N_{PpF} increases quickly and stays constant during the rest of the pre-runs. The behaviour of N_{PpF} during the pre-runs is independent from the value of ϵ_{lpi}, as the first fibrils, which consist of two or three peptides, form inside the solvent bulk, where the different values of ϵ_{lpi} have no influence on the otherwise identical peptides. With more and more peptides coming into contact with the membrane, a dependence of N_{PpF} on ϵ_{lpi} can be observed. In simulations with $\epsilon_{lpi} \leqslant 1.0$ the average fibril size increases.

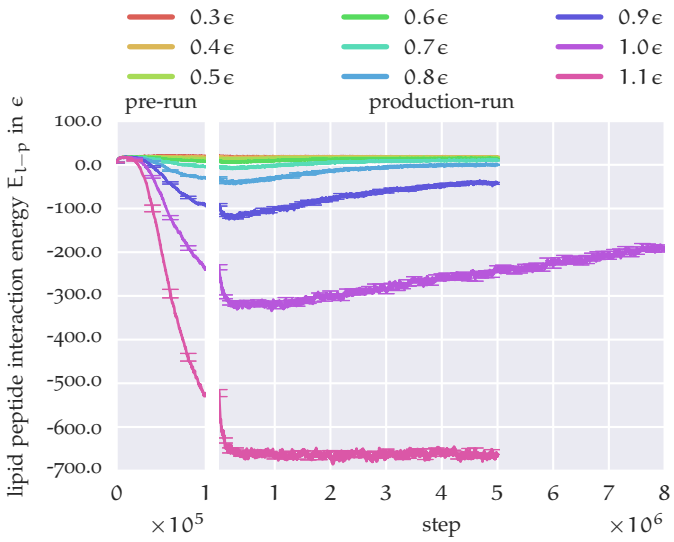

Figure 6.21: Interaction energy between lipid and peptide beads E_{l-p} for simulations with different values of ϵ_{lpi}. $\epsilon_{HB,\,cooperative} = -1.1\epsilon$.

For stronger values of ϵ_{lpi}, N_{PpF} stays almost constant at a low level during the whole production-runs.

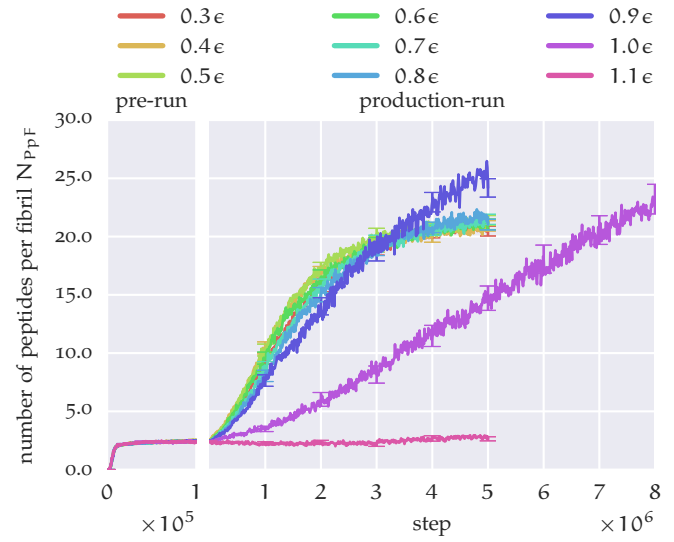

Figure 6.22: The number of peptides per fibril N_{PpF} for simulations with lipid membranes and peptides. ϵ_{lpi} is varied between 0.3ϵ and 1.1ϵ. $\epsilon_{HB,\,cooperative} = -1.1\epsilon$.

The number of fibril clusters N_C behaves similar to simulations with varied cooperative hydrogen bonds during the pre-runs, discussed at the beginning of this chapter. N_C increases quickly to values between six and seven peptides at the beginning of the pre-runs, as shown in Figure 6.23. After the quick increase, there is a slow reduction of the number of clusters in the case of

simulations with ϵ_{lpi} between 0.3ϵ and 0.8ϵ, leading to two clusters after five million steps. In simulations with $\epsilon_{lpi} = 0.9\epsilon$, the number of clusters reaches a value of 1.67 ± 0.06 at the end of the simulations.

For stronger values of ϵ_{lpi}, the number of clusters behaves differently. Instead of a slow decrease of the number of clusters during production-runs, a fast reduction of N_C at the beginning of the production-runs can be observed. For $\epsilon_{lpi} = 1.0\epsilon$, this is followed by a linear decrease towards two clusters, for $\epsilon_{lpi} = 1.1\epsilon$, a value of N_C below 2 is reached after 5×10^5 steps. During the course of the simulations N_C stays almost constant at this values. The origin of the different behaviour of N_C for different values of ϵ_{lpi} will be described shortly.

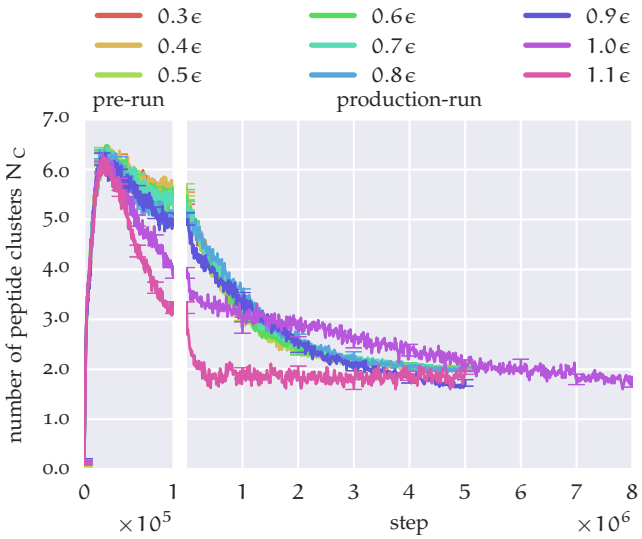

Figure 6.23: The number of peptide clusters N_C for simulations with lipid membranes and peptides. ϵ_{lpi} is varied between 0.3ϵ and 1.1ϵ. $\epsilon_{HB,\,cooperative} = -1.1\epsilon$.

The number of peptides per cluster N_{PpC}, shown in Figure 6.24, reveals that in the case of $\epsilon_{lpi} = 1.1\epsilon$, the fast decrease of the number of clusters N_C at the beginning of the production-runs does not show the formation of two big clusters, but rather the occurrence of single peptides, as the average cluster consists of 4.0 ± 0.3 peptides. For all other values of ϵ_{lpi}, the average cluster size grows. Values of ϵ_{lpi} between 0.3ϵ and 0.8ϵ lead to similar curves of N_{PpC} with average clusters of about 24 peptides. In simulations with $\epsilon_{lpi} = 1.0$, the clusters grow to sizes of 17 ± 1 peptides during the five million steps of the simulations, in those with $\epsilon_{lpi} = 0.9$, N_{PpC} reaches values of 28.1 ± 0.9.

In simulations with weak interactions between hydrophobic peptide beads and lipid tail beads, the formation of clusters and fibrils is primarily influenced by the entropy driven apposition of the peptides on the membrane surface. The surface leads to a faster formation of fibrils, in means of simulation steps, and fewer layers of fibrils compared to simulations without a membrane present. In simulations with $\epsilon_{lpi} = 1.1\epsilon$ the interactions between lipids and peptides become so strong that a formation of fibrils and clusters is prohibited. This

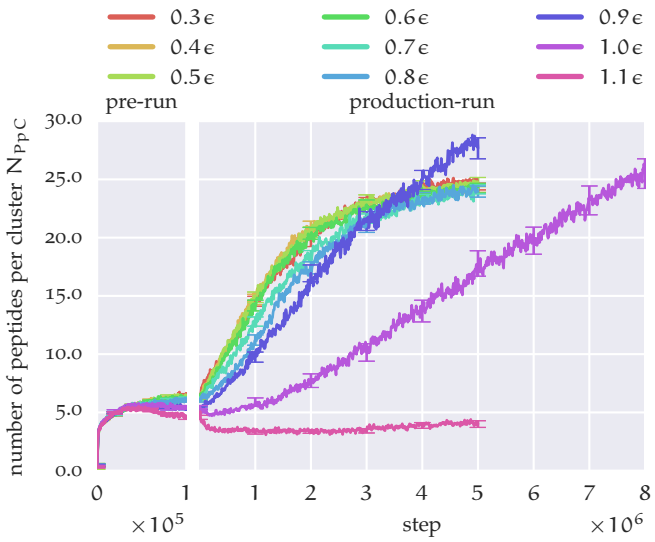

Figure 6.24: The number of peptides per cluster N_{PpC} for simulations with lipid membranes and peptides. ϵ_{lpi} is varied between 0.3ϵ and 1.1ϵ. $\epsilon_{HB,\,cooperative} = -1.1\epsilon$.

is illustrated in Figure 6.25, where a typical simulation with $\epsilon_{lpi} = 1.1\epsilon$ after 5×10^6 steps is shown. The majority of peptides is positioned inside the membrane, in agreement with the situation in simulations with a single peptide, discussed in Section 6.1. The interaction energies are too strong in this case to allow stable fibrils to be formed. The values of N_{PpC} are listed in Table 6.5, together with those values obtained for simulations with $\epsilon_{HB,\,cooperative} = -1.0\epsilon$, discussed in the following section.

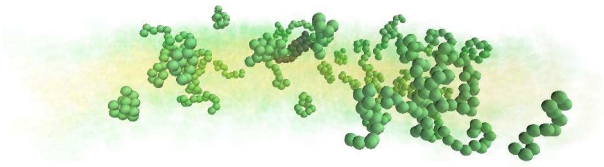

Figure 6.25: Snapshots of a simulation with $\epsilon_{lpi} = 1.1\epsilon$, taken from a simulation after five million steps. The lipids are shown with a reduced opacity, to allow the peptides inside the membrane to be seen. A fibril consisting of two peptides is shown in grey colour.

In the case of $\epsilon_{lpi} = 0.9\epsilon$, clusters and fibrils of more that 25 peptides can be found. Due to the two surfaces of the membrane, one would expect an evenly distribution of peptides on both sides of the membrane. This is indeed the case in simulations with weaker lipid-peptide interactions. For stronger interactions, an additional effect has to be considered: Due to the strong attraction between hydrophobic peptide beads and lipid tail beads, single peptides are able to switch through the membrane onto the other surface. However, a peptide, once part of a fibril, loses this ability. In situations, where a fibril forms quickly on one surface of the membrane (surface A), while the peptides on the opposite membrane surface (B) show random coil configurations, more

peptides change from surface B to A, than from A to B. The growth of the fibril acts as a peptide drain, reducing the number of peptides that are free to move through the membrane. The result of such a process is illustrated in Figure 6.26, where a snapshot from a simulation after five million steps in production-run with $\epsilon_{lpi} = 0.9\epsilon$ is shown. On one membrane surface, a fibril consisting of 40 peptides has formed. Six peptides reside on the same surface in a random coil configuration, one peptide is placed inside the membrane. On the opposite surface, only three random coil peptides can be found.

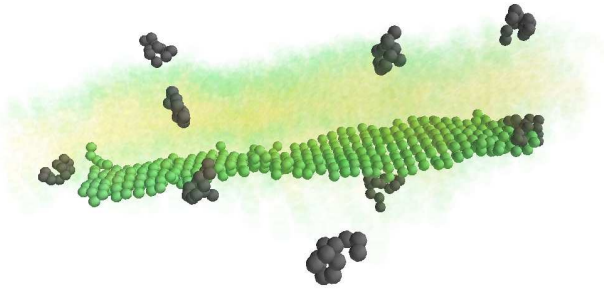

Figure 6.26: Snapshots of a simulation with $\epsilon_{lpi} = 0.9\epsilon$. The image shows a simulation after 5×10^6 steps. A fibril of 40 peptides has formed on one side of the membrane. Like in the previous image, the lipids are shown with a reduced opacity. See text for details.

6.5.2 *Simulations with* $\epsilon_{HB,\,cooperative} = -1.0\epsilon$

In simulations with $\epsilon_{HB,\,cooperative} = -1.0\epsilon$, the number of peptides in fibrils N_{PiF}, Figure 6.27, shows the same behaviour during the pre-runs, like in the simulations discussed before. During the production-runs, the value of N_{PiF} increases for all applied values of ϵ_{lpi}. In simulations with ϵ_{lpi} between 0.3ϵ and 0.7ϵ, roughly the same number of peptides is part of a fibril at the end of the simulations, the value of N_{PiF} lies between 35 ± 1 and 32 ± 1. For stronger interaction parameters, N_{PiF} still increases, but the values, reached after five million steps, get smaller; for 0.8ϵ, 0.9ϵ, and 1.0ϵ, 27 ± 1, 20 ± 1 and 7.8 ± 0.6 peptides are part of a fibril at the end of the simulations.

The number of peptides per fibril N_{PpF}, shown in Figure 6.28, increases to values around 2 during the pre-runs. During the production-runs, the fibril size behaves similar in simulations with ϵ_{lpi} between 0.3ϵ and 0.8ϵ, leading to fibrils consisting on average of 13.1 ± 0.9 to 14.4 ± 0.8 peptides. In simulations with $\epsilon_{lpi} = 0.9\epsilon$, N_{PpF} reaches a value of 10.1 ± 0.9 peptides after 5×10^6 steps. For $\epsilon_{lpi} = 1.0\epsilon$, the number of peptides per fibril increases only slightly, reaching a value of 3.3 ± 0.4.

The number of clusters N_C increases during the pre-runs to values between 6 and 7, followed by a decrease, as shown in Figure 6.29. This pattern was already observed in previous simulations. Simulations with ϵ_{lpi} between 0.3ϵ and 0.7ϵ show again a similar behaviour; the number of clusters decreases exponentially, reaching values between 2.46 ± 0.08 and 2.67 ± 0.09. In simu-

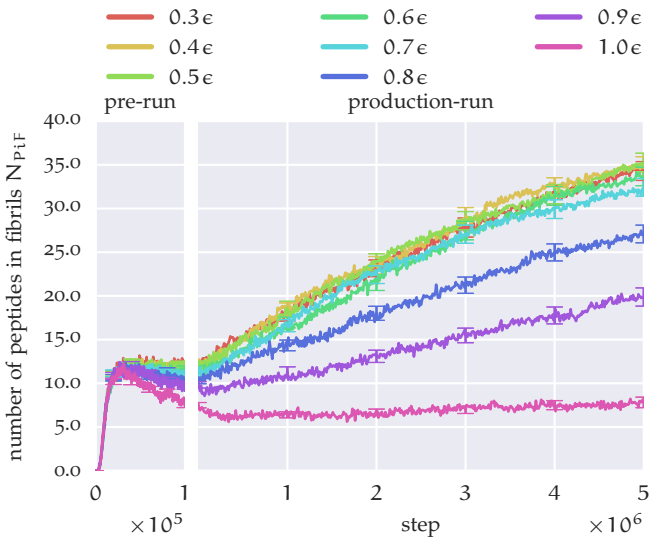

Figure 6.27: The number of peptides in fibrils N_{PiF} for simulations with lipid membranes and peptides, $\epsilon_{HB,\,cooperative} = -1.0\epsilon$. ϵ_{lpi} is varied between 0.3ϵ and 1.0ϵ.

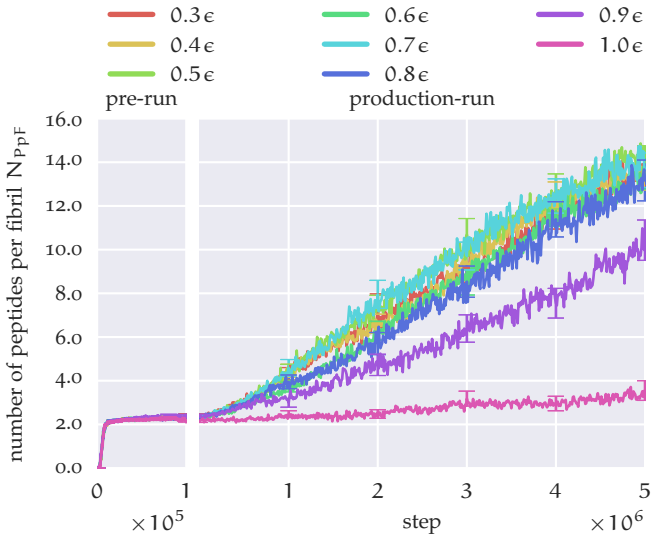

Figure 6.28: The number of peptides per fibril N_{PpF} for simulations with lipid membranes and peptides. ϵ_{lpi} is varied between 0.3ϵ and 1.0ϵ. $\epsilon_{HB,\,cooperative} = -1.0\epsilon$.

lations with $\epsilon_{lpi} = 0.8\epsilon$ and 0.9ϵ, N_C reaches values of 2.7 ± 0.1 and 3.0 ± 0.1, but the decrease is faster during the pre-runs and the beginning of the production-runs than in simulations with weaker lipid-peptide interactions. For even stronger interactions, N_C decreases quickly during the second half of the pre-runs and the first 5×10^5 steps of the production-runs. During the course of the runs, N_C stays about constant in these simulations, reaching 3.1 ± 0.1 clusters per simulation on average after five million steps. The

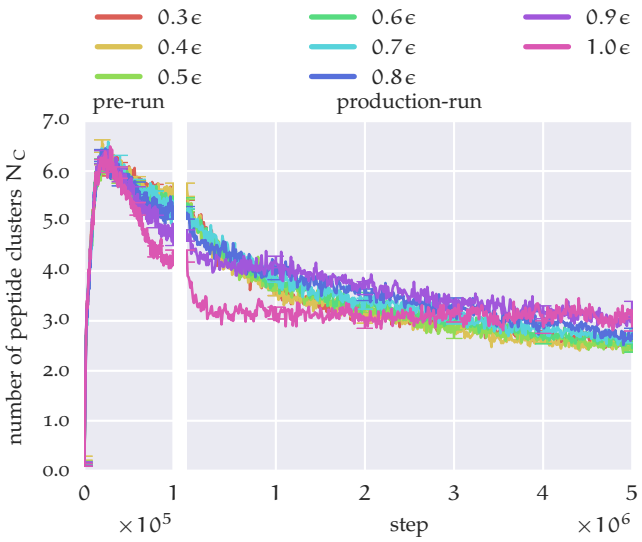

Figure 6.29: The number of peptide clusters N_C for simulations with lipid membranes and peptides. ϵ_{lpi} is varied between 0.3ϵ and 1.0ϵ. $\epsilon_{HB,\,cooperative} = -1.0\epsilon$.

number of peptides per cluster N_{PpC} in Figure 6.30 reveals, as already observed for strong interactions between lipids and peptides in simulations with $\epsilon_{HB,\,cooperative} = -1.1\epsilon$ that in simulations with $\epsilon_{lpi} = 1.0\epsilon$, only small clusters form. The decrease of N_C, shown in Figure 6.29, in these simulations is not caused by the formation of bigger clusters. The curves of N_{PpC} for simulations with ϵ_{lpi} between 0.3ϵ and 0.9ϵ show that the clusters grow in size. The reduction of the number of clusters is therefore connected with clusters that grow at the expense of others. The average number of peptides per cluster for the different values of ϵ_{lpi} are given in Table 6.5. The values show that the behaviour of simulations with weak lipid-peptide interactions is again similar. The third column of Table 6.5 lists the values for N_{PpC} obtained from simulations with $\epsilon_{HB,\,cooperative} = -1.1\epsilon$. The differences and their reasons are discussed in the following section.

6.5.3 *Differences in fibril formation*

As mentioned previously, the clusters and fibrils that form in simulations with different values of $\epsilon_{HB,\,cooperative}$ have different properties. The values listed in Table 6.5 reveal at least two differences. The average clusters in simulations with $\epsilon_{HB,\,cooperative} = -1.0\epsilon$ are smaller than clusters in simulations with the same interaction strength between lipid tail beads and hydrophobic peptide beads but stronger cooperative hydrogen bonds. Longer simulations could resolve this issue, but were not feasible due to the lack of time.

The second column of Table 6.5 shows that the average cluster size decreases for increasing lipid-peptide interaction strength in the case of $\epsilon_{HB,\,cooperative} = -1.0\epsilon$. For $\epsilon_{HB,\,cooperative} = 1.1$, N_{PpC} is almost constant for values of $\epsilon_{lpi} \leqslant 0.8\epsilon$; for $\epsilon_{lpi} \leqslant 0.9\epsilon$, the value of N_{PpC} increases before it drops again in simu-

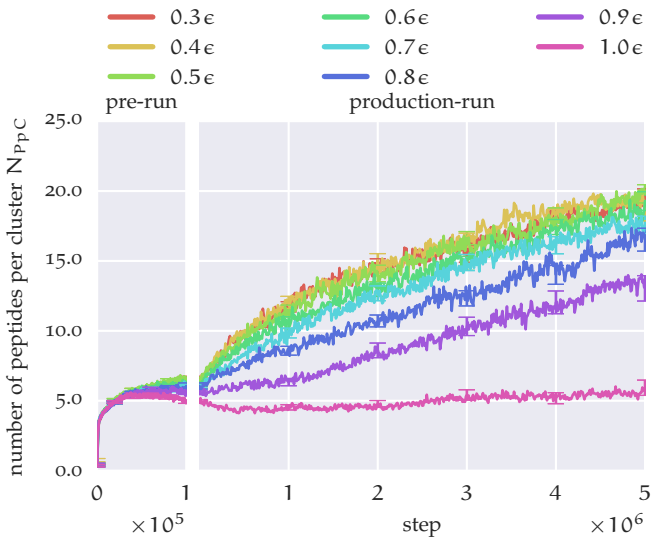

Figure 6.30: The number of peptides per cluster N_{PpC} for simulations with lipid membranes and peptides. ϵ_{lpi} is varied between 0.3ϵ and 1.0ϵ. $\epsilon_{HB,\,cooperative} = -1.0\epsilon$.

ϵ_{lpi}/ϵ	$\epsilon_{HB,\,cooperative} = -1.0\epsilon$	$\epsilon_{HB,\,cooperative} = -1.1\epsilon$
0.3	19.2 ± 0.6	24.8 ± 0.3
0.4	19.2 ± 0.6	24.1 ± 0.3
0.5	19.8 ± 0.6	24.7 ± 0.4
0.6	18.4 ± 0.6	25.8 ± 0.5
0.7	17.5 ± 0.6	23.9 ± 0.4
0.8	16.8 ± 0.8	24.2 ± 0.5
0.9	13.4 ± 0.9	28.1 ± 0.9
1.0	5.6 ± 0.5	17 ± 1 (25 ± 1)
1.1	-	4.0 ± 0.3

Table 6.5: Average number of peptides per cluster N_{PpC} for different values of ϵ_{lpi} in simulations with $\epsilon_{HB,\,cooperative} = -1.0\epsilon$ and -1.1ϵ after five million steps. The value in braces for $\epsilon_{HB,\,cooperative} = -1.1\epsilon$ and $\epsilon_{lpi} = 1.0\epsilon$ gives the value after eight million steps.

lations with $\epsilon_{lpi} = 1.0\epsilon$ and -1.1ϵ. The decrease in the case of $\epsilon_{HB,\,cooperative} = 1.0$ towards higher interaction strength can be explained by looking again at the results discussed in the previous sections of this chapter: The presence of a membrane promotes the formation of fibrils due to entropic effects, without a membrane present, the fibrils that develop during the simulations incorporate much less peptides. The energies associated with the formation of a hydrogen bond are only just strong enough to allow the formation of fibrils under the influence of interactions with solvents. The apposition on a membrane surface leads to a reduced degree of freedom, and therefore fibrils consisting of a

higher number of peptides develop. The increase of interactions between lipid tail beads and hydrophobic peptide beads counteracts this effect; the probability for an once formed hydrogen bond to be a seed for a fibril decreases, as its relative amount on the total energy associated with the peptides is reduced. In the case of $\epsilon_{\mathrm{HB,\,cooperative}} = -1.1\epsilon$, almost all peptides become part of a fibril, independent of the presence of a lipid membrane. Together with the growth of fibrils, in both cases, the formation of clusters, bigger than their counterparts in simulations with $\epsilon_{\mathrm{HB,\,cooperative}} = -1.0\epsilon$, can be observed. For strong lipid-peptide interactions, the influence of the effect described in Section 6.5.1 increases: The growth of fibrils hinders peptides to move through the membrane, leading to fibrils consisting of more than 25 peptides. In the discussed simulations, this effect has the biggest influence in simulations with $\epsilon_{\mathrm{lpi}} = 0.9\epsilon$ and 1.0ϵ. For even higher values of ϵ_{lpi}, the cluster and fibril size decrease again, as the benefit from forming hydrogen bonds is minimal compared to the energies associated with interactions between lipid and peptide beads.

This effect can also be seen in Figure 6.21, where the interaction energy increases (gets weaker) due to the formation of hydrogen bonds, and hence fibrils, in the case of simulations with $\epsilon_{\mathrm{lpi}} \leqslant 1.0\epsilon$. In simulations with $\epsilon_{\mathrm{lpi}} = 1.1\epsilon$ the interaction energy stays almost constant after reaching a minimum value. The absolute value of the interaction energy is twice as high as the value measured in simulations with $\epsilon_{\mathrm{lpi}} = 1.0\epsilon$. The interactions between lipid and peptide beads possess an attractive part only for interactions between hydrophobic peptide beads and lipid tail beads. Therefore the peptides favour positions closer to the COM of the membrane for higher values of ϵ_{lpi}, as shown in Section 6.1. The majority of peptides grows on the membrane surface. Only in simulations with $\epsilon_{\mathrm{HB,\,cooperative}} = -1.1\epsilon$, exceptions to this rule could be observed. In 17 of 128 simulations fibrils consisting of more than six peptides formed. In 12 of those simulations, the fibrils grew perpendicular to the membrane surface into the membrane. An illustration of this effect is given in Figure 6.31, where the only double layered fibril that was observed in the 128 simulations with $\epsilon_{\mathrm{HB,\,cooperative}} = -1.1\epsilon$ is shown. In simulations with weak lipid peptide interactions, the preferred peptide position and the fibril distance from the membrane COM match, therefore the change in lipid peptide interaction energy is small during the simulations. In simulations with stronger interactions, the peptides have to leave their preferred position, associated with an increase of the lipid peptide interaction energy.

Table 6.6 lists the average distance of fibrils from the COM of the lipid membrane and the average distance of the COM of peptides from the COM of the lipid, obtained from umbrella sampling simulations discussed previously. To measure the average distance of fibrils, the biggest fibril in each simulation was located and the average distance of the COM of each peptide in the fibril from the COM of the membrane was calculated. In the case of the umbrella sampling simulations, the average distance can be calculated using $P(d)$:

$$\langle d \rangle = \int dx\, P(x) \cdot x \qquad . \tag{6.3}$$

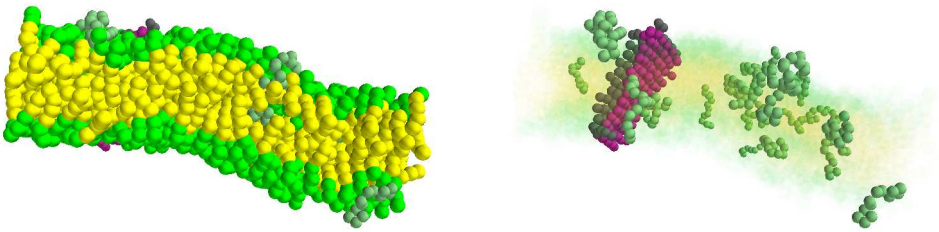

Figure 6.31: Fibrils that formed inside a membrane in a simulation with $\epsilon_{lpi} = 1.1\epsilon$ and $\epsilon_{HB,\,\text{cooperative}} = -1.1\epsilon$. Both fibrils consist of 13 peptides. Image b) is identical to a), only the opacity of lipids is reduced to allow the fibrils to be seen. The majority of the 24 peptides, which are not part of a fibril, is positioned inside the membrane.

For values of $\epsilon_{lpi} \leqslant 0.8\epsilon$, the average values of d for both types of simulations are quite similar. It seems therefore only natural that the formation of fibrils in these simulations is accelerated by the presence of a membrane for these interaction parameters. Despite the bigger difference in the two average values for simulations with $\epsilon_{lpi} = 0.9\epsilon$ and 1.0ϵ, fibrils still grow. In simulations with $\epsilon_{lpi} = 1.1\epsilon$, in the vast majority of simulations only small fibrils form. Only in 16 of 128 simulations, fibrils consisting of seven or more peptides form, only in a single simulation, the formation of two layered fibrils can be observed. The latter case is shown in Figure 6.31. In this simulation two parallel fibrils form inside the membrane, perpendicular to the membrane surface. In 14 of the 16 simulations with a developed fibril, the fibrils grow perpendicular to the bilayer surface into the membrane, or dip into the membrane at one end of the fibril. A fibril dipping into the membrane surface at one end is shown in Figure 6.32.

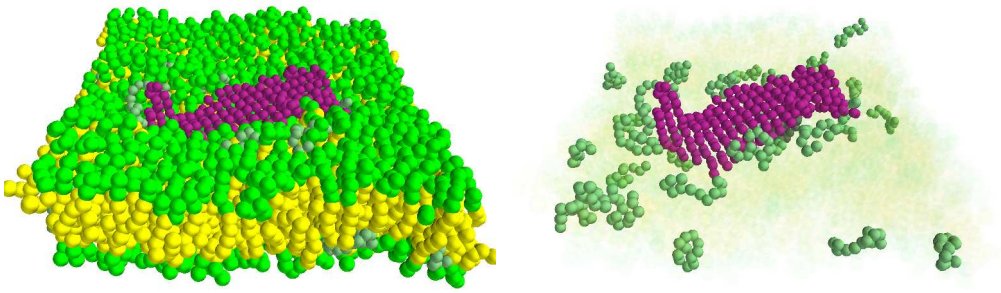

Figure 6.32: Illustration of a fibril consisting of 19 peptides that dips into the membrane at one end. See text for details.

ϵ_{lpi}/ϵ	A	B	C
0.3	3.70	3.56 ± 0.01	3.661 ± 0.009
0.4	3.67	3.57 ± 0.01	3.636 ± 0.009
0.5	3.62	3.62 ± 0.01	3.635 ± 0.009
0.6	3.55	3.55 ± 0.01	3.640 ± 0.009
0.7	3.44	3.59 ± 0.01	3.563 ± 0.009
0.8	3.26	3.53 ± 0.01	3.598 ± 0.009
0.9	2.94	3.42 ± 0.01	3.536 ± 0.009
1.0	2.44	3.00 ± 0.03	3.31 ± 0.01
1.1	1.87	-	2.34 ± 0.04

Table 6.6: Average distance of single peptides and fibrils from the COM of the lipid membrane. Column A $\langle d_{umbrella} \rangle / \sigma$ obtained from umbrella sampling simulations with $\epsilon_{HB,\,cooperative} = -1.1\epsilon$, column B $\langle d_{fibril} \rangle / \sigma$, $\epsilon_{HB,\,cooperative} = -1.0\epsilon$, and column C $\langle d_{fibril} \rangle / \sigma$, $\epsilon_{HB,\,cooperative} = -1.1\epsilon$. See text for details.

Parallel fibrils

In the majority of simulations, single layers of fibrils form at the membrane surface, the formation of two or more fibrils layered at each other is less prominent. With increasing ϵ_{lpi}, the percentage of simulations, in which two fibrils stacked onto each other develop, decreases. This is shown in Figure 6.33, where the percentage of stacked fibrils for different values of ϵ_{lpi} and $\epsilon_{HB,\,cooperative}$ is shown. In simulations with $\epsilon_{lpi} = 0.3\epsilon$, 0.4ϵ, and 0.5ϵ, in roughly one third of the runs, stacked fibrils develop. Between $\epsilon_{lpi} = 0.6\epsilon$ and $\epsilon_{lpi} = 1.0\epsilon$, this amount decreases almost linear towards 0. Due to the formation of two parallel fibrils in one of 128 simulations with $\epsilon_{lpi} = 1.1\epsilon$, the value reaches 0.78 percent.

In a single simulation, with $\epsilon_{lpi} = 0.4\epsilon$ and $\epsilon_{HB,\,cooperative} = -1.1\epsilon$, three peptides, stacked onto each other formed. A snapshot from the end of this simulation is given in Figure 6.34.

A snapshot of a simulation with $\epsilon_{lpi} = 0.3\epsilon$ and $\epsilon_{HB,\,cooperative} = -1.1\epsilon$, in which two fibrils stacked onto each other developed, is shown in Figure 6.35. Images showing parallel layers of fibrils for different values of ϵ_{lpi} and cooperative hydrogen bond energies are given in Appendix G.

6.6 CONCLUSION

The simulations in this chapter showed that the model is able to simulate the formation of fibrils on membrane surfaces. The comparison of results obtained in simulations with and without a membrane, with the same set of parameters, except for interactions between lipid and peptides beads, showed that fibrils on membrane surfaces need fewer simulation steps to grow. The majority of fibrils attached to a surface develops as single layers, opposite to simulations of fibril

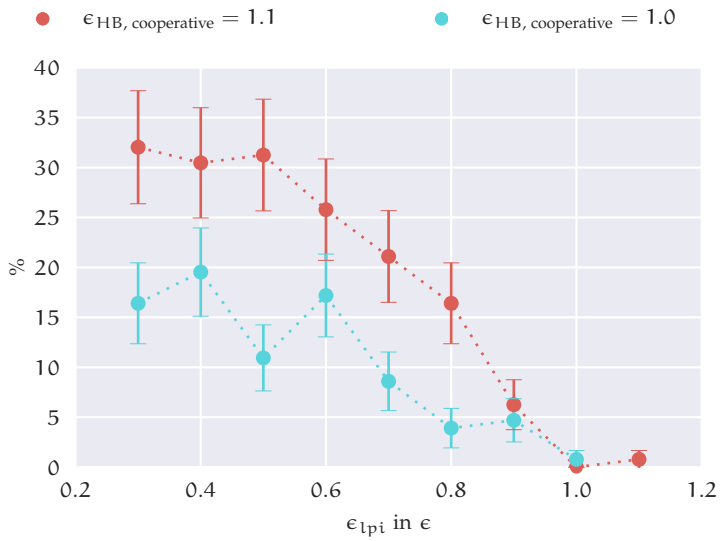

Figure 6.33: The percentage of simulations, in which two layered fibrils form for different values of ϵ_{lpi} and $\epsilon_{HB,\,cooperative}$. The errors are estimated with $\sqrt{n}$. See text for details.

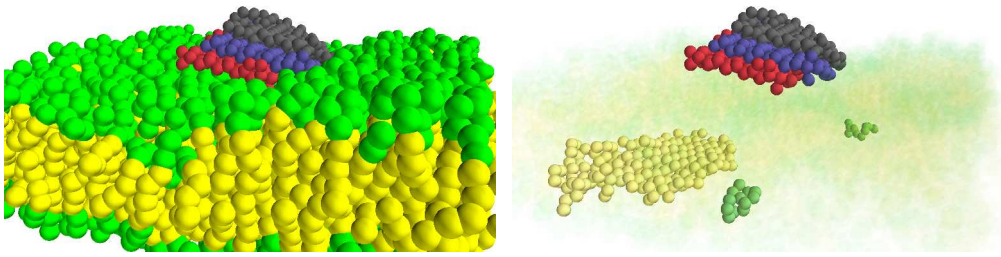

(a) (b)

Figure 6.34: Three peptides stacked onto each other observed in a simulation with $\epsilon_{lpi} = 0.4\epsilon$ and $\epsilon_{HB,\,cooperative} = -1.1\epsilon$. The snapshots were taken after five million steps. The stacked fibrils consist of 10 (red), 13 (blue), and 9 (dark gray) peptides. The fibril on the opposite side of the membrane, visible in image b), consists of 16 peptides.

development in the bulk, where parallel layers of at least two fibrils can be observed. The simulation of the free energy of inserting a single peptide into the lipid bilayer revealed entropy as the source for the apposition of peptides onto the membrane surface in our model. The following simulations with varied lipid-peptide interaction strength proved the results obtained in the umbrella sampling simulations: For weak interaction strength, the fibrils developing on membrane surfaces show only small differences. With increasing interactions, the fibril properties begin to change. The percentage of fibrils that form layers on the membrane surface decreases. Compared to simulations with weak interactions, the size of fibrils in simulations with strong interactions behaves differently for different values of $\epsilon_{HB,\,cooperative}$. In simulations with weak cooperative hydrogen bonds, where only small fibrils develop in the bulk, the

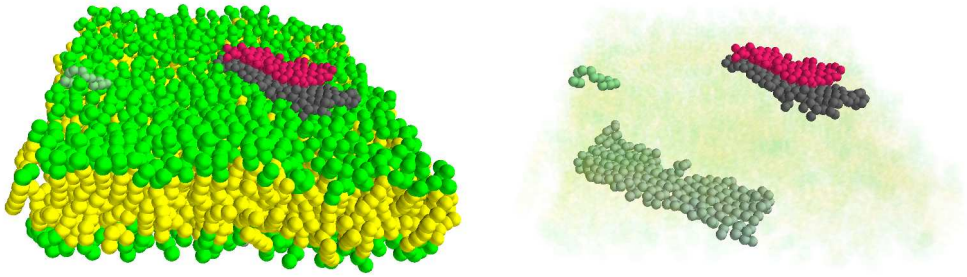

(a) (b)

Figure 6.35: Snapshots taken from a simulation with $\epsilon_{lpi} = 0.3\epsilon$ and $\epsilon_{HB,\,cooperative} = -1.1\epsilon$, showing the layered fibrils on the membrane surface after five million steps. b) shows the same image with increased transparency of the lipid to allow the fibril that formed on the opposite membrane surface to be visible. The red fibril consists of 10, the black of 16 peptides. The grey fibril on the opposite surface of the membrane consists of 23 peptides.

fibril size decreases in simulations with a membrane present towards higher values of lipid-peptide interactions. In simulations with stronger cooperative hydrogen bonds, a fibril acts as a peptide drain with increasing lipid-peptide interactions. The propensity of a peptide to move through the membrane increases with stronger attractions between lipid tail beads and hydrophobic peptide beads. A peptide which is part of a fibril is prevented from entering the membrane. In those simulations, the probability for peptides to move onto a surface with a fibril present is therefore higher than the probability to move the other way round. This effect explains the occurrence of average fibril sizes higher than the expected value of 25. Umbrella sampling simulations indicated a changed behaviour for lipid-peptide interactions with $\epsilon_{lpi} = 1.1\epsilon$. The maximum of the probability density distribution revealed that the preferred position of a peptide in these simulations lies underneath the two lipid head beads. Simulations with $\epsilon_{lpi} = 1.1\epsilon$ and $\epsilon_{HB,\,cooperative} = -1.1\epsilon$ of 50 peptides indeed showed that the majority of peptides places itself inside the membrane under these conditions and thereby loses its ability to form fibrillar structures.

7

CONCLUSION

In this thesis, the results obtained from a coarse-grained model for simulations of lipid-peptide interactions in a phantom solvent environment were discussed. Both, the peptide and the lipid model are based on coarse-grained models which were used before (Section 2.2 and Section 2.3). Both models had to be developed further in order to fit to each other. The results discussed in this thesis were obtained by using MC simulations in a NpT-ensemble (Chapter 3). In Chapter 4, the behaviour of a single peptide for different values of hydrogen bond strength and hydrophobicity was explored, to test the implementation of the model and to pick suitable parameters for the following simulations that involved multiple peptides. In Chapter 5, the ability of the peptide model to reproduce the fibril formation was tested, and it was demonstrated that the process of fibrilization can be controlled by varying the strength of the hydrogen bonds in the model. By changing the hydrogen bond energies on a wide range, different mechanisms of fibril formation could be detected in the model in Section 5.6, leading to two different structures of the fibril clusters observed and to differences in the amount of steps it takes for fibrils to form. Fibrils grown inside clusters either of random coil, or α-helical peptides, can be observed, depending on the value of hydrogen bond strength.

In simulations, where the growth of fibrils took more steps, the resulting structures consisted of only a few (two to three) layers of long fibrils, compared to short fibrils packed in several layers of multiple clusters, in simulations, where the fibrilization was quick.

Peptides and proteins form fibrils with different structural features, when growing in systems with different conditions [136–138]. The s-shaped progression of the fibril formation, shown in Figure 5.21, matches the discussed kinetics of fibrilization, e.g. see [139], Figure 2.

Simulations of peptides in the presence of lipid bilayers (Chapter 6), showed on one hand that the structure of the resulting fibrils differs from the structure of fibrils that form in simulations without a membrane (Figure 6.14), and on the other hand that membranes seem to catalyse the formation of fibrils (Figure 6.15). The attraction of membranes to peptides and the catalysing effect have both been reported by experimentalists [138, 140]. Calculations of the gyration tensor showed that the presence of a membrane changes the way in which fibrils form (Figure 6.18). The majority of fibrils that form at a membrane surface consists of a single layer. The percentage of simulations in which double layers of fibrils could be observed depends on the strength of interactions between lipid and peptide beads. In simulations with weak interactions, up to one third of simulations showed double layers of fibrils, for stronger interactions, this amount decreases down to zero. In a single simulation, layers of three fibrils were observed.

The investigation of the free energy landscape for the insertion of a single peptide into the membrane (Section 6.1) revealed that the apposition of peptides on the membrane surface is driven by entropy, rather than energy, in our model. Further investigation of the free energy could include the interactions of multiple peptides, both with and without the presence of a membrane to highlight differences in the fibril formation process [53].

Experiments with lipids and membranes showed that oligomers seem to be the source of cytotoxicity. This is e.g. shown in the experiments by Quist et al [49] and Kayed et al [48], shortly discussed in Chapter 1 of this thesis. In the simulations obtained with the model presented in this work, no such observations could be made. Both the lipid and the peptide model is coarse-grained and generic. The mechanisms of toxicity, that real oligomers seem to follow, may have been neglected in the model due to the simplifications coarse-graining entails. Recent publications [141] suggest that the ability to induce leakage is connected to the charge of the membrane lipids; with uncharged lipids the ability is reduced. Charge is not explicitly incorporated in the model used in this thesis. Other experiments showed that the ability of oligomers to cause membrane leakage is reduced in more complex model membranes [142].

Nevertheless the model was able reproduce the accelerated formation of fibrils in the presence of a membrane, which was observed experimentally and reported by Kayed and coworkers [48].

The change of properties of lipid rafts [143, 144] and the amount of cholesterol in these rafts [145, 146] as a starting point for fibril formation is discussed in literature. Depending on the amount of cholesterol and the environment, it is reported that cholesterol can both accelerate and inhibit the speed of fibril formation [141]. As the original lipid model is able to reproduce lipid rafts and was studied with addition of cholesterol [126], simulations investigating the influence of rafts and cholesterol to peptides and the fibril formation, would easily be set up with the system presented in this thesis.

Another interesting field for simulations with the model would be to investigate the interactions of membranes and peptides further, e.g. to measure the influence of lipid bilayers on fibrillar structures, that initially developed in the solvent bulk, or to measure the influence of peptides and fibrils on membrane properties. In experiments, membrane disruption through interactions of oligomers can be observed. This effect was not observed in the simulations for this thesis. It would be interesting, to investigate this further; is the missing disruption of membranes in the simulations caused by the construction of the model itself, or is it caused by the parameters applied to the used potentials?

The simulations discussed in this thesis showed that the model is able to reproduce the process of fibril formation, both with and without the presence of a lipid bilayer in a phantom solvent environment. The measurements shown in the thesis are meant to give a guidance to understand the behaviour of the model for further investigations regarding lipid-peptide and membrane-fibrils interactions.

Part III

APPENDIX

A

CALCULATING CENTRE OF MASS

It is often necessary to calculate the COM for a given set of coordinates. In this study, these coordinates can for example represent the position of peptide beads. However, for systems with PBC and for systems with PBC and shear the formulas used for systems without PBC cannot be used. The following chapter shows the methods we are using to circumvent this problem.

SYSTEMS WITHOUT PERIODIC BOUNDARY CONDITIONS

In systems without PBC the COM $\vec{x}_{com}$ is easily calculated using

$$\vec{x}_{com} = \frac{\sum_i m_i \vec{x}_i}{M} \quad , \tag{A.1}$$

where $\vec{x}_i$ is the position of the i-th particle, m_i is the mass for the i-th particle and $M = \sum_i m_i$ is the total mass. If all particles have the same mass $m = m_i \forall i$, Equation A.1 can be simplified to

$$\vec{x}_{com} = \frac{\sum_i \vec{x}_i}{N} \quad , \tag{A.2}$$

a simple example for calculating the COM for a two dimensional system without PBC is shown in Figure A.1.

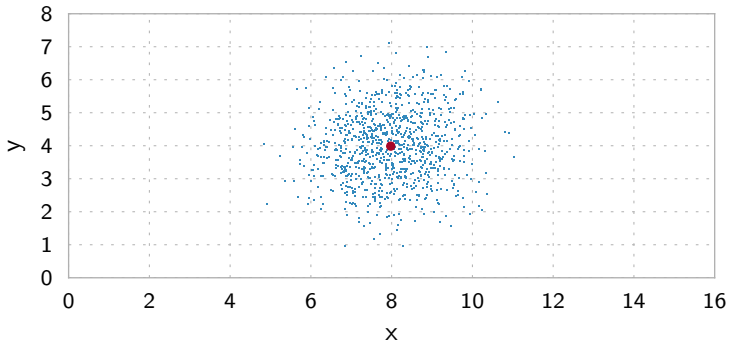

Figure A.1: Example for calculating the COM for a two dimensional system without PBC. The blue points are normal distributed random values in two directions, the centre of both normal distributions is placed in the centre of the simulation box. The COM is calculated using Equation A.2 and is shown in red.

SYSTEMS WITH PERIODIC BOUNDARY CONDITIONS

Equation A.2 is useful to calculate the COM in simple systems. However, if the system possesses Periodic Boundary Conditions, the location of the COM

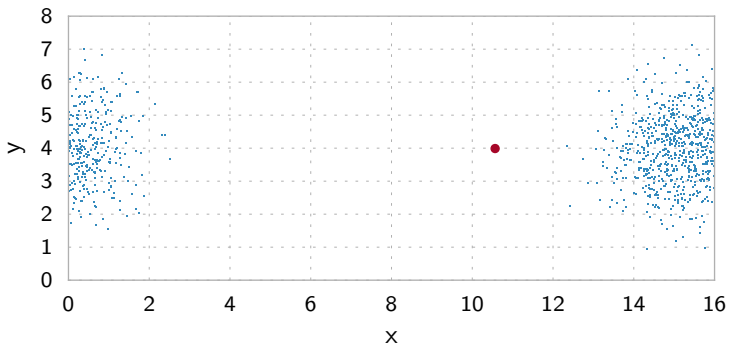

Figure A.2: A wrong result for the COM obtained by using Equation A.2 for a system *with* PBC. The positions of the blue points correspond to the positions in Figure A.1, shifted in x direction by 7.5. Values that leave the simulation enter it on the opposite side again. The calculated position of the COM (red) should be shifted in the same way. Because Equation A.2 cannot handle PBC, it assumes two distinct regions and locates the COM outside the particle cloud.

predicted by this equation is not correct, because clusters of positions overlapping the boundaries of the simulation box, as shown in Figure A.2, are not treated as connected regions, but as separate ones. To calculate the COM for systems with PBC we use an approach introduced by Lai and Breen [147]. For convenience we present the algorithm in one dimension for particles with the same mass m here. The steps of the algorithm listed below are illustrated in Figure A.3.

1. Map the positions into the interval $[-\pi, \pi)$,

$$x_{mapped} = \frac{x}{x_{len}} \cdot 2\pi - \pi \quad , \tag{A.3}$$

   with x_{len} being the size of the simulation box.

2. Calculate the sin and cos value for all mapped positions,

$$x_c = \sin\left(x_{mapped}\right) \quad , \quad y_c = \cos\left(x_{mapped}\right) \quad , \tag{A.4}$$

   x_c and y_c represent the positions on a unit circle.

3. Calculate the two dimensional mean value for the positions on the circle using Equation A.2,

$$x_m = \frac{\sum_i x_{c,i}}{N} \quad , \quad y_m = \frac{\sum_i y_{c,i}}{N} \quad . \tag{A.5}$$

4. Calculate the angle ϕ for the point (x_m, y_m),

$$\phi = atan2\left(x_m, y_m\right) \quad . \tag{A.6}$$

5. Map the point back to the coordinates of the simulation box,

$$x_{mean} = \frac{\phi + \pi}{2\pi} \cdot x_{len} \quad . \tag{A.7}$$

A simple python implementation of this algorithm is shown in Listing A.1. The correct COM for the system in Figure A.2 calculated with this algorithm is shown in Figure A.4.

SYSTEMS WITH PERIODIC BOUNDARY CONDITIONS AND SHEAR

When a particle moves outside the simulation box in a system with PBC and shear, not only the coordinate in the direction the particle left the box gets folded back, but also the coordinates in one or more other directions change. A schematic drawing of this adjustments for a three dimensional system with shear in y-x, z-x, and z-y direction, as used in our simulation, is shown in Figure A.6. The algorithm shown in the previous section does not compensate this shift. To calculate the correct COM for these systems, we have to adjust the coordinates used with the algorithm. To calculate the COM in a direction x_i, the unfolded coordinates have to be projected onto the x_i axis and mapped back into the system afterwards. By using these coordinates the algorithm is able to compute the position of the COM correctly. Figure A.5 shows both the incorrect and the correct value for the COM.

```
import numpy as np

pos = # np.array
pmax = # size of the simulation box
def comPBC(pxb, bmax):
        pmap = pxb/bmax * 2* np.pi - np.pi
        pmeanmap = np.arctan2(np.sin(pmap).mean(), np.cos(pmap).mean())
        pmean = (pmeanmap + np.pi) / (2*np.pi) * bmax

        return pmean
```

Listing A.1: A short python implementation of the algorithm in Figure A

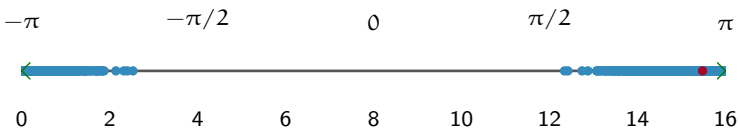

(a)

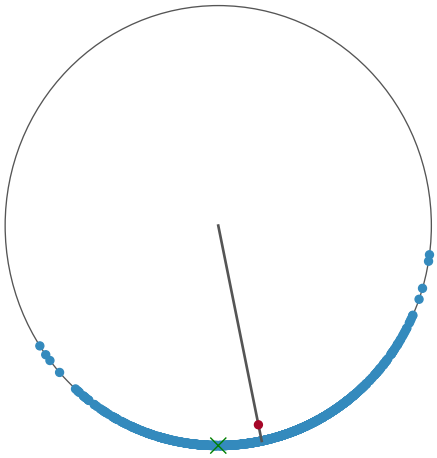

(b)

Figure A.3: Illustration of the algorithm explained in Figure A for the x direction of the system shown in Figure A.2. (a) The x-values of the points get mapped into the interval $[-\pi, \pi)$ (blue). The red point shows the COM for this system that gets calculated by the algorithm. (b) By calculating the sine and cosine values of the x-positions a unit circle gets formed. The blue points correspond to the x-values in (a). The centre of mass for this two-dimensional system is calculated using Equation A.2 and projected back onto the unit circle (black line). The green cross next to the calculated COM in (b) and at $x = 0 \mathrel{\widehat{=}} -\pi$ and $x = 16 \mathrel{\widehat{=}} \pi$ in (a) corresponds to the start- and end-point of the simulation box in x-direction. The COM for the system in x- and y-direction is shown in Figure A.4.

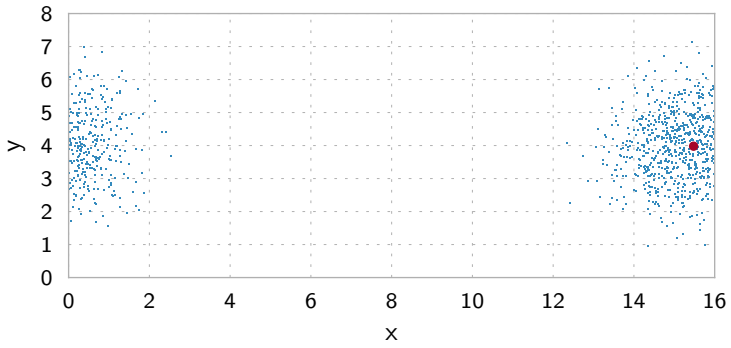

Figure A.4: A correct result for the COM for a system *with* PBC. The COM (red) is calculated using the algorithm shown in Figure A, both for the x and y direction.

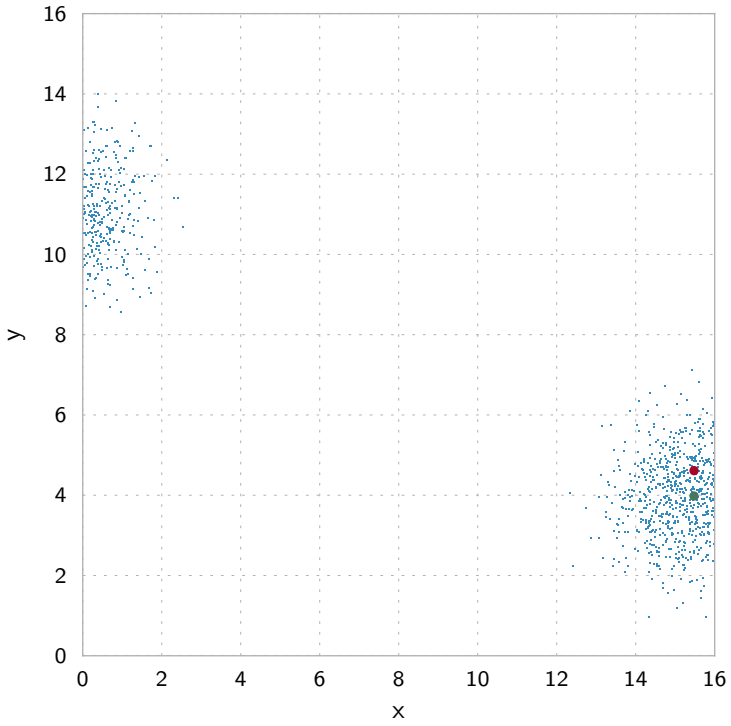

Figure A.5: A system with PBC and shear in x-y direction. The particles leaving the simulation box in x-direction get folded back into the system at a higher y-coordinate. The COM calculated with the algorithm presented in Figure A (red) therefore yields an incorrect result. By mapping coordinates onto the axes, and folding them back into the system, as discussed in Equation A, the algorithm calculates the correct position for the COM (green).

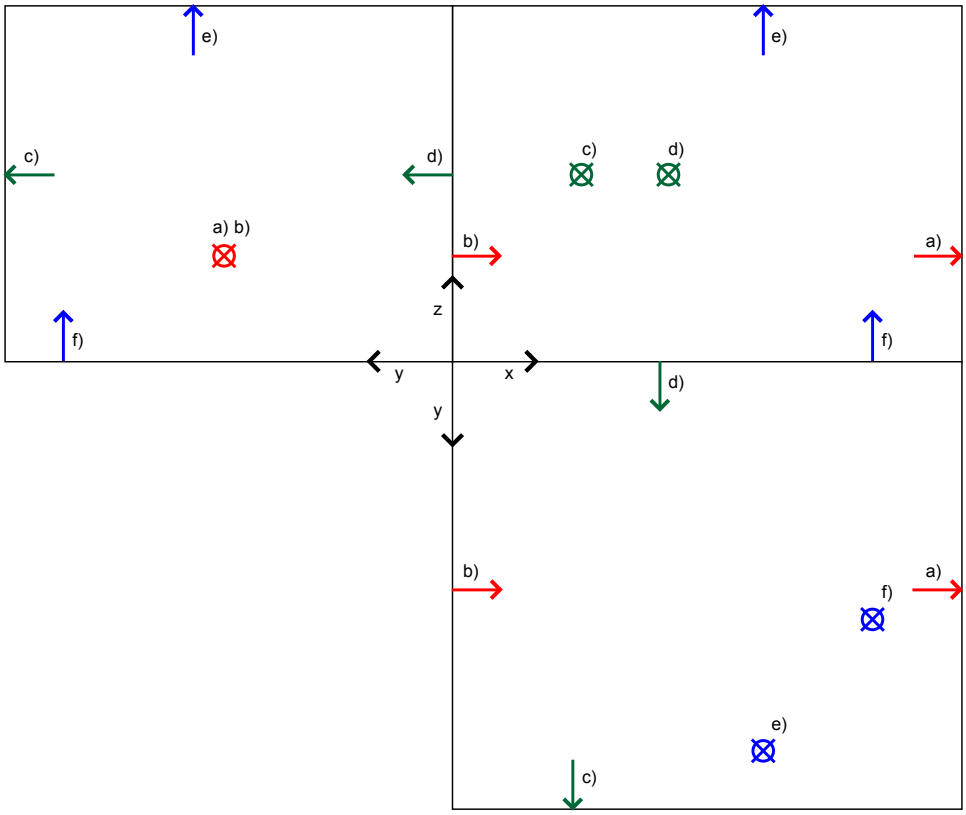

Figure A.6: Illustration of a 3D-system with shear in y-x, z-x and z-y direction. The three rectangles represent the xy, xz and yz planes of the simulation box. The three colors red, green, and blue denote particles moving outside the simulation box in x-, y-, and z-direction and their new position on the opposite side of the simulation box, where they enter the box again due to PBC. When a particle leaves the simulation box in x-direction (a), both the y- and z-coordinates stay unchanged (b). If a particle moves in y-direction out of the box (c), the z-position stays the same, whereas the x-position changes (d) according to the y-x shear value. For a particle leaving the simulation box in z-direction (e) both the x- and y-position get adjusted (f).

B

STRUCTURE OF SINGLE PEPTIDE SIMULATIONS WITH COMPARABLE COLOUR RANGE

The figures shown in this chapter correspond to the images shown in Chapter 4. In contrast to them, the colour rages used for α-helices, β-helices, β-sheets, and random coil peptides are different, to allow more detailed view on small differences.

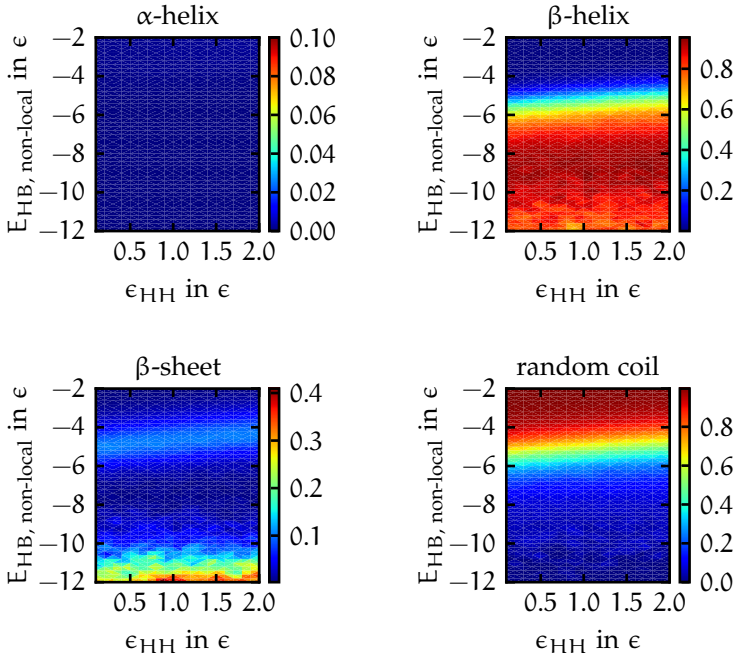

Figure B.1: Measured structure of a single peptide for different values of $E_{HB,\,non\text{-}local}$ and ϵ_{HH} according to Equation 4.9 for α-helices, 4.10 for β-helices, 4.11 for β-sheets, and 4.12 for random coils. Note the different scaling of the colour-bars. The values for $E_{HB,\,local}$, $E_{HB,\,cooperative}$ and k_0 correspond to weak hydrogen bonds, shown in Table 4.1, column A.

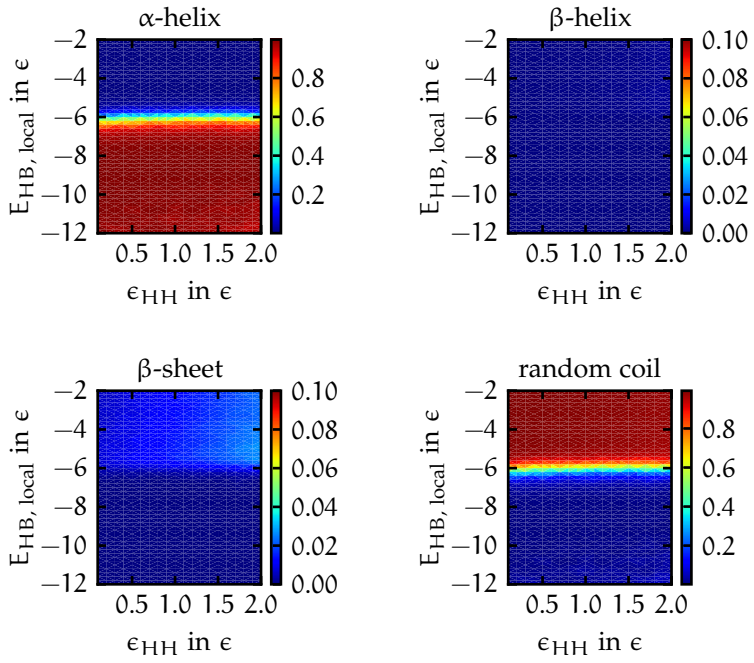

Figure B.2: Same as Figure B.1, with varied values of $E_{HB,\,local}$ and ϵ_{HH} for weak hydrogen bonds.

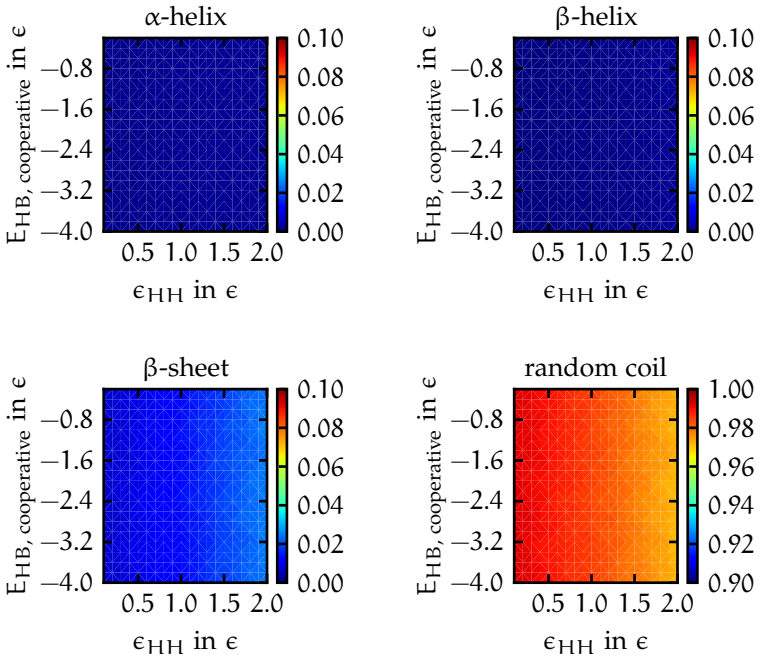

Figure B.3: Same as Figure B.1, with varied values of $E_{HB,\,cooperative}$ and ϵ_{HH} for weak hydrogen bonds.

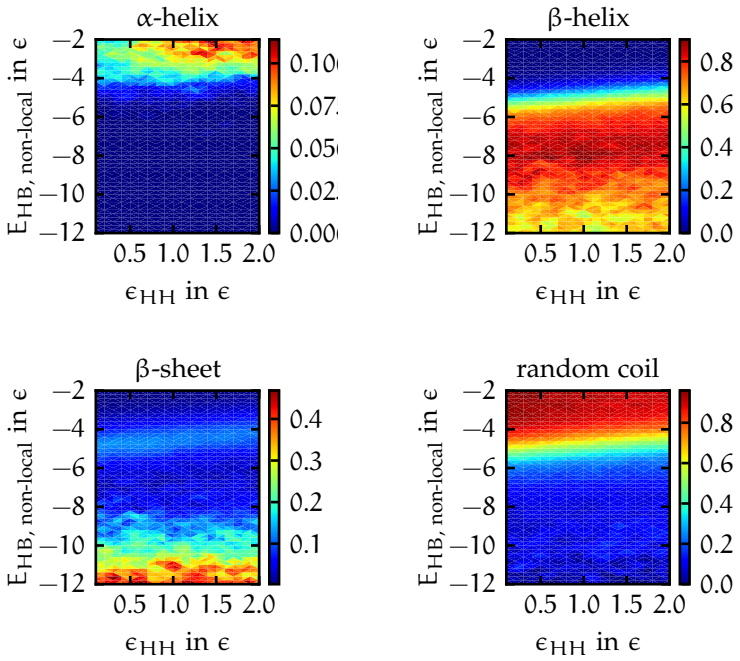

Figure B.4: Measured structure of a single peptide for different values of $E_{HB,\,non\text{-}local}$ and ϵ_{HH} according to Equation 4.9 for α-helices, 4.10 for β-helices, 4.11 for β-sheets, and 4.12 for random coils. Note the different scaling of the colour-bars. The values for $E_{HB,\,local}$, $E_{HB,\,cooperative}$ and k_0 correspond to normal hydrogen bonds, shown in Table 4.1, column B.

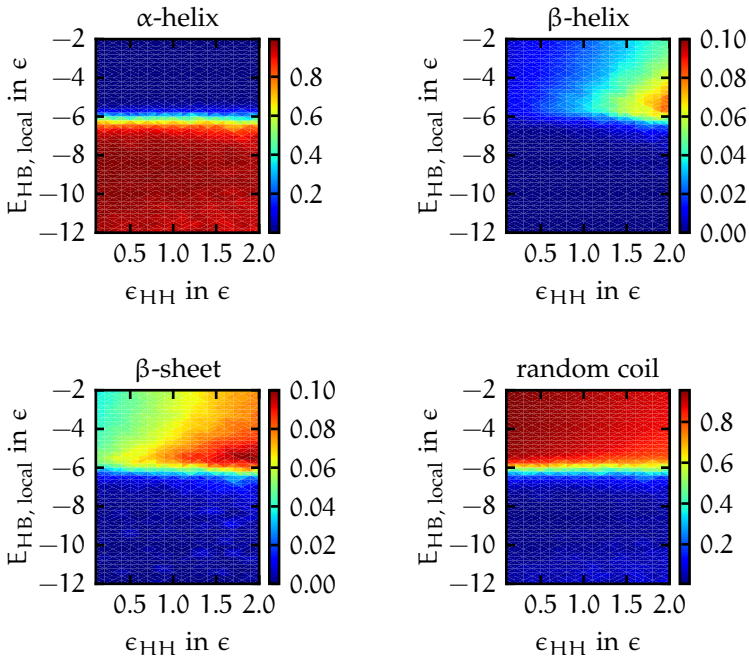

Figure B.5: Same as Figure B.4, with varied values of $E_{HB,\,local}$ and ϵ_{HH} for normal hydrogen bonds.

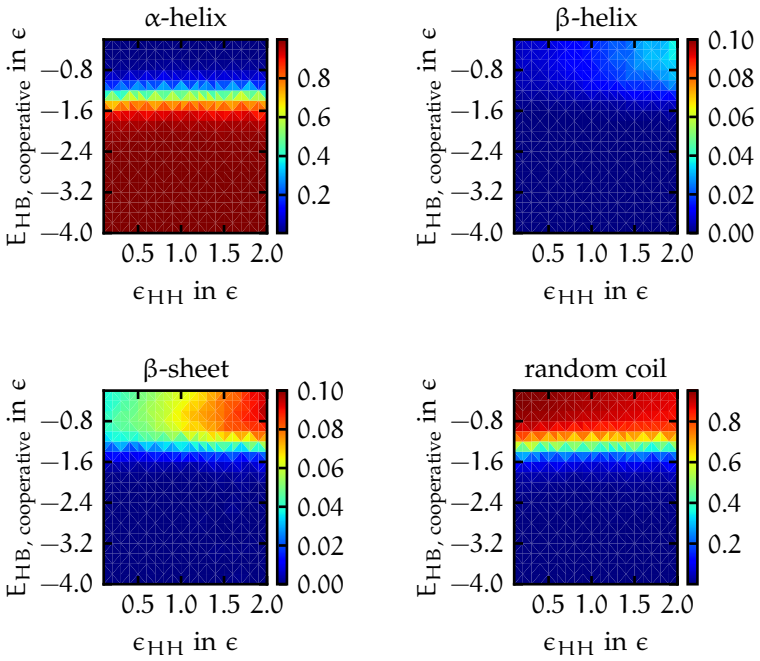

Figure B.6: Same as Figure B.4, with varied values of $E_{HB,\,cooperative}$ and ϵ_{HH} for normal hydrogen bonds.

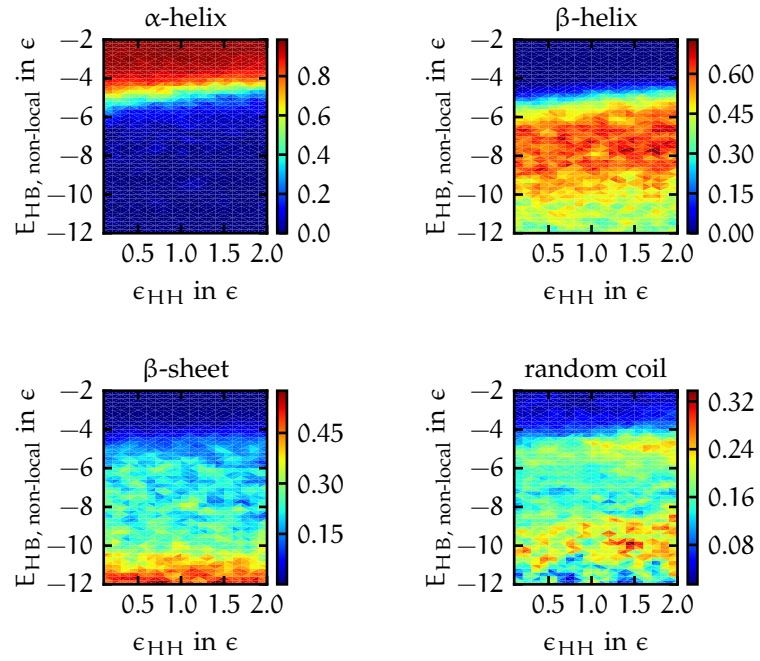

Figure B.7: Measured structure of a single peptide for different values of $E_{HB,\,non\text{-}local}$ and ϵ_{HH} according to Equation 4.9 for α-helices, 4.10 for β-helices, 4.11 for β-sheets, and 4.12 for random coils. Note the different scaling of the colour-bars. The values for $E_{HB,\,local}$, $E_{HB,\,cooperative}$ and k_0 correspond to strong hydrogen bonds, shown in Table 4.1, column C.

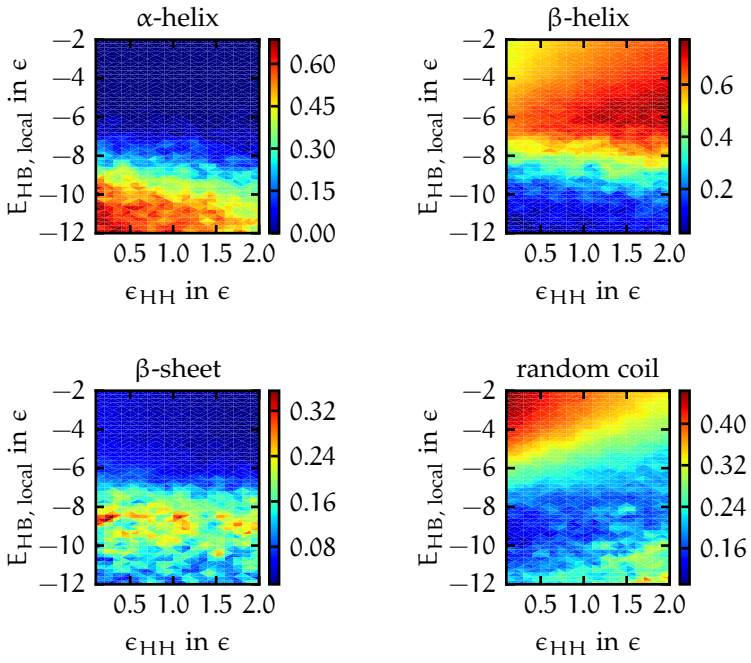

Figure B.8: Same as Figure B.7, with varied values of $E_{HB,\,local}$ and ϵ_{HH} for strong hydrogen bonds.

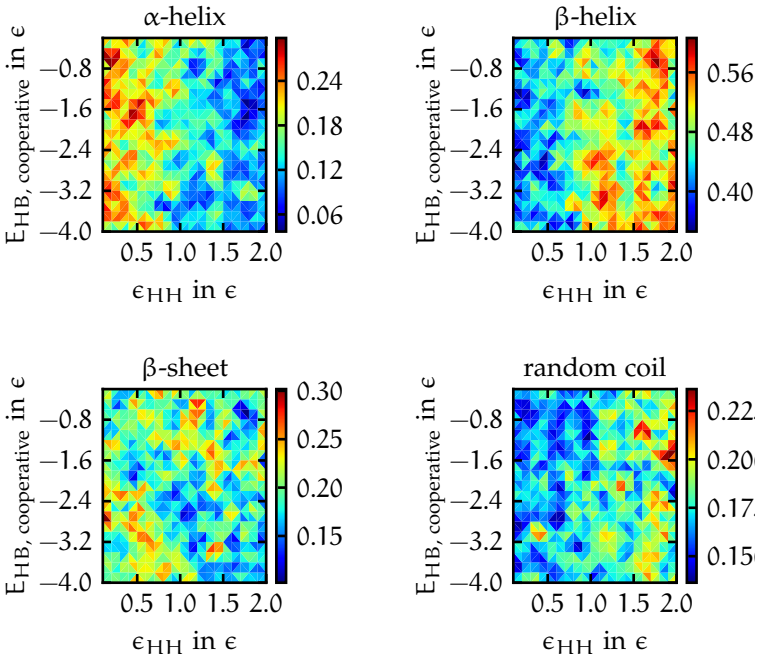

Figure B.9: Same as Figure B.7, with varied values of $E_{HB,\,cooperative}$ and ϵ_{HH} for strong hydrogen bonds.

C

FITTED NUMBER OF PEPTIDES IN FIBRILS

In this appendix, we list the values that resulted from fitting Equation 5.1 to the number of peptides in fibrils (N_{PiF}) for simulations with hydrogen bond energies between -4.9ϵ and -6.5ϵ in Table C.1, together with plots showing both the fitted functions and N_{PiF} in Figure C.1, C.2, and C.3.

$E_{HB,\,local}$	a	τ	c
-4.9ϵ	56.0 ± 0.2	$2.61 \pm 0.02 \times 10^{-7}$	$-6.4 \pm 0.1 \times 10^{5}$
-5.0ϵ	50.35 ± 0.06	$1.70 \pm 0.02 \times 10^{-6}$	$-1.09 \pm 0.05 \times 10^{5}$
-5.1ϵ	50.06 ± 0.03	$3.40 \pm 0.04 \times 10^{-6}$	$-9.5 \pm 0.3 \times 10^{4}$
-5.2ϵ	50.01 ± 0.23	$4.89 \pm 0.04 \times 10^{-6}$	$-9.1 \pm 0.1 \times 10^{4}$
-5.3ϵ	49.98 ± 0.01	$7.27 \pm 0.05 \times 10^{-6}$	$-7.8 \pm 0.1 \times 10^{4}$
-5.4ϵ	49.98 ± 0.01	$9.19 \pm 0.05 \times 10^{-6}$	$-6.83 \pm 0.07 \times 10^{4}$
-5.5ϵ	49.996 ± 0.006	$9.83 \pm 0.05 \times 10^{-6}$	$-6.07 \pm 0.05 \times 10^{4}$
-5.6ϵ	50.000 ± 0.006	$9.60 \pm 0.03 \times 10^{-6}$	$-5.27 \pm 0.04 \times 10^{4}$
-5.7ϵ	50.004 ± 0.005	$8.28 \pm 0.02 \times 10^{-6}$	$-4.65 \pm 0.03 \times 10^{4}$
-5.8ϵ	50.011 ± 0.006	$6.10 \pm 0.02 \times 10^{-6}$	$-3.96 \pm 0.04 \times 10^{4}$
-5.9ϵ	49.999 ± 0.006	$4.589 \pm 0.008 \times 10^{-6}$	$-3.17 \pm 0.03 \times 10^{4}$
-6.0ϵ	49.996 ± 0.005	$2.925 \pm 0.003 \times 10^{-6}$	$-4.08 \pm 0.03 \times 10^{4}$
-6.1ϵ	49.991 ± 0.006	$1.902 \pm 0.002 \times 10^{-6}$	$-3.79 \pm 0.04 \times 10^{4}$
-6.2ϵ	49.999 ± 0.004	$1.2018 \pm 0.0007 \times 10^{-6}$	$-4.35 \pm 0.03 \times 10^{4}$
-6.3ϵ	50.126 ± 0.008	$7.839 \pm 0.008 \times 10^{-7}$	$-9.8 \pm 0.7 \times 10^{3}$
-6.4ϵ	50.02 ± 0.01	$4.631 \pm 0.05 \times 10^{-7}$	$-2.69 \pm 0.09 \times 10^{4}$
-6.5ϵ	53.06 ± 0.05	$2.538 \pm 0.05 \times 10^{-7}$	$-2.1 \pm 0.2 \times 10^{4}$

Table C.1: Values obtained from fitting Equation 5.1 to the number of peptides in fibrils (N_{PiF}) for simulations with hydrogen bond energies between -4.9ϵ and -6.5ϵ.

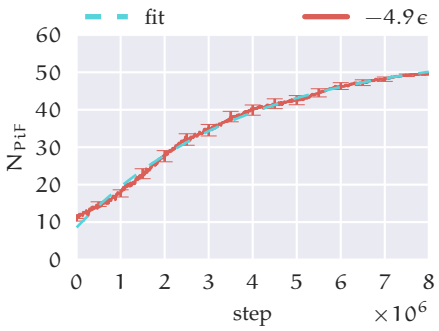

(a) −4.9ϵ

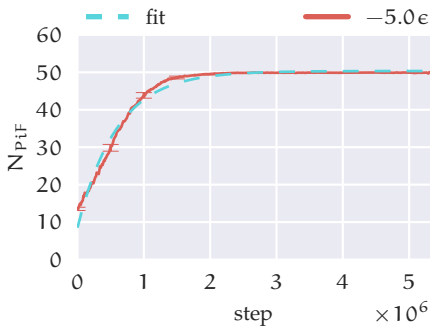

(b) −5.0ϵ

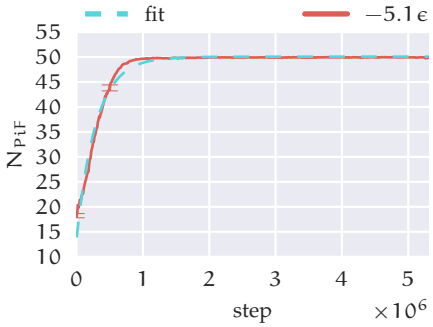

(c) −5.1ϵ

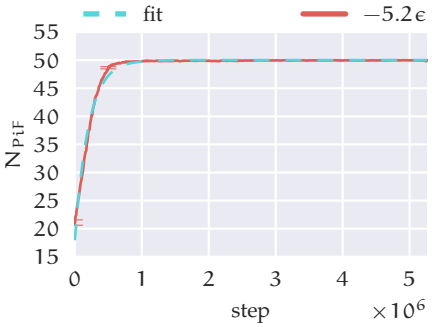

(d) −5.2ϵ

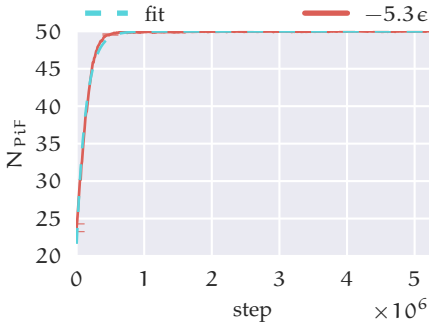

(e) −5.3ϵ

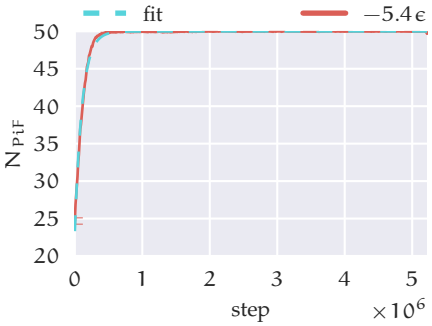

(f) −5.4ϵ

Figure C.1: Equation 5.1 fitted to N_{PiF} for different values of the hydrogen bond energies. *(continued on next page)*

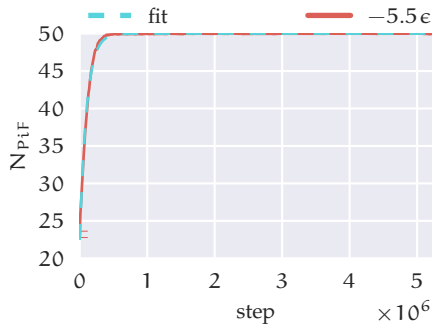

(a) −5.5ϵ

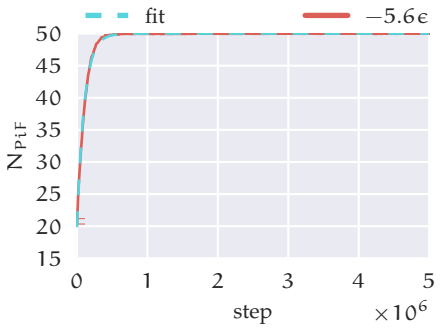

(b) −5.6ϵ

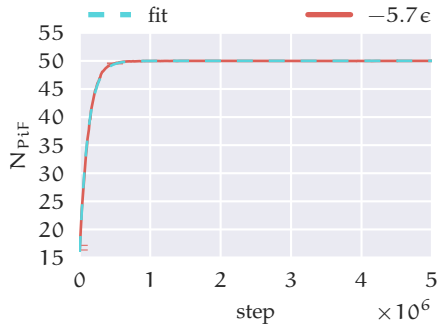

(c) −5.7ϵ

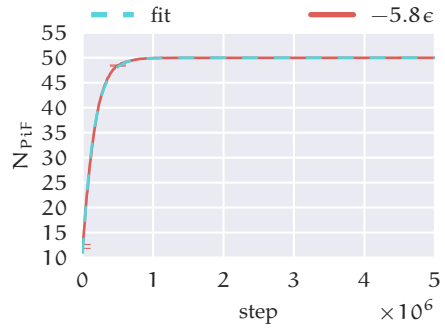

(d) −5.8ϵ

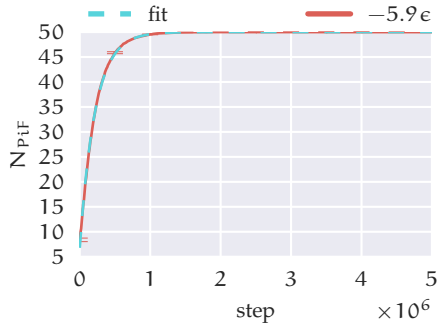

(e) −5.9ϵ

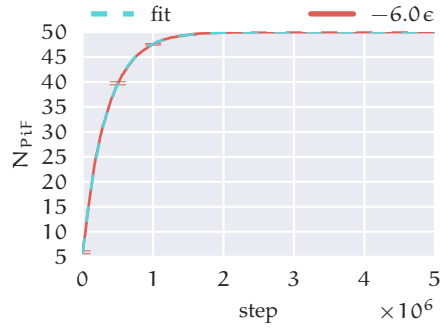

(f) −6.0ϵ

Figure C.2: Same as Figure C.1. *(continued on next page)*

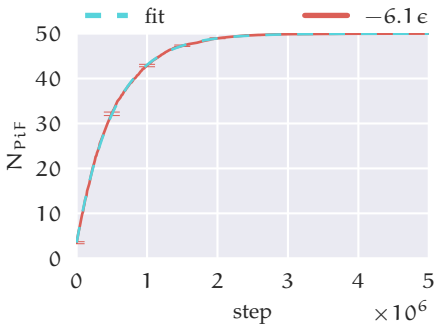

(a) −6.1ϵ

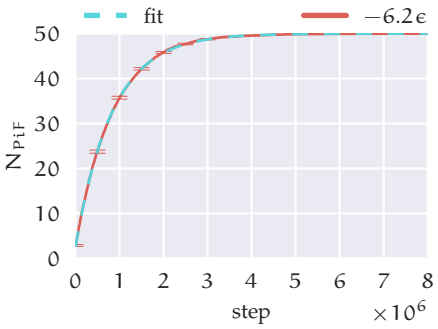

(b) −6.2ϵ

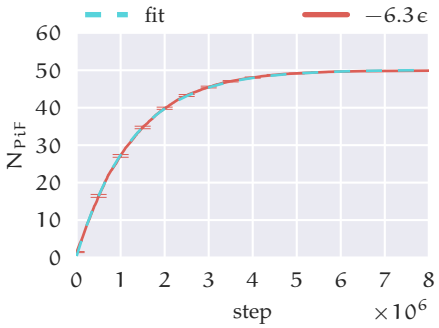

(c) −6.3ϵ

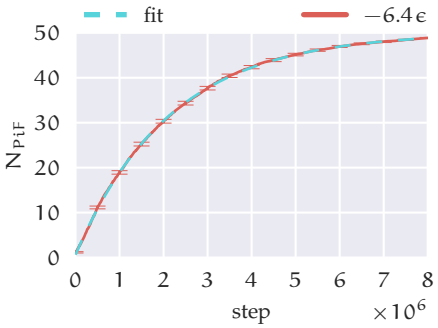

(d) −6.4ϵ

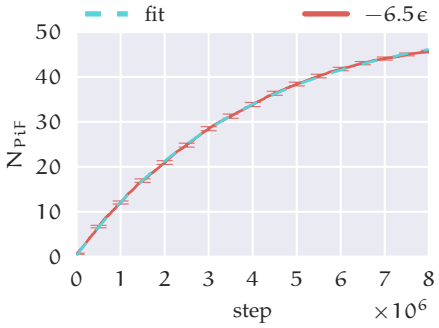

(e) −6.5ϵ

Figure C.3: Same as Figure C.1.

D

FIBRIL FORMATION IN THE PRESENCE OF MEMBRANES - IMAGES

In this appendix, the process of fibril formation in the presence of a membrane, shown in Section 6.3 with the membrane, is illustrated without the membrane visible and with coloured fibrils.

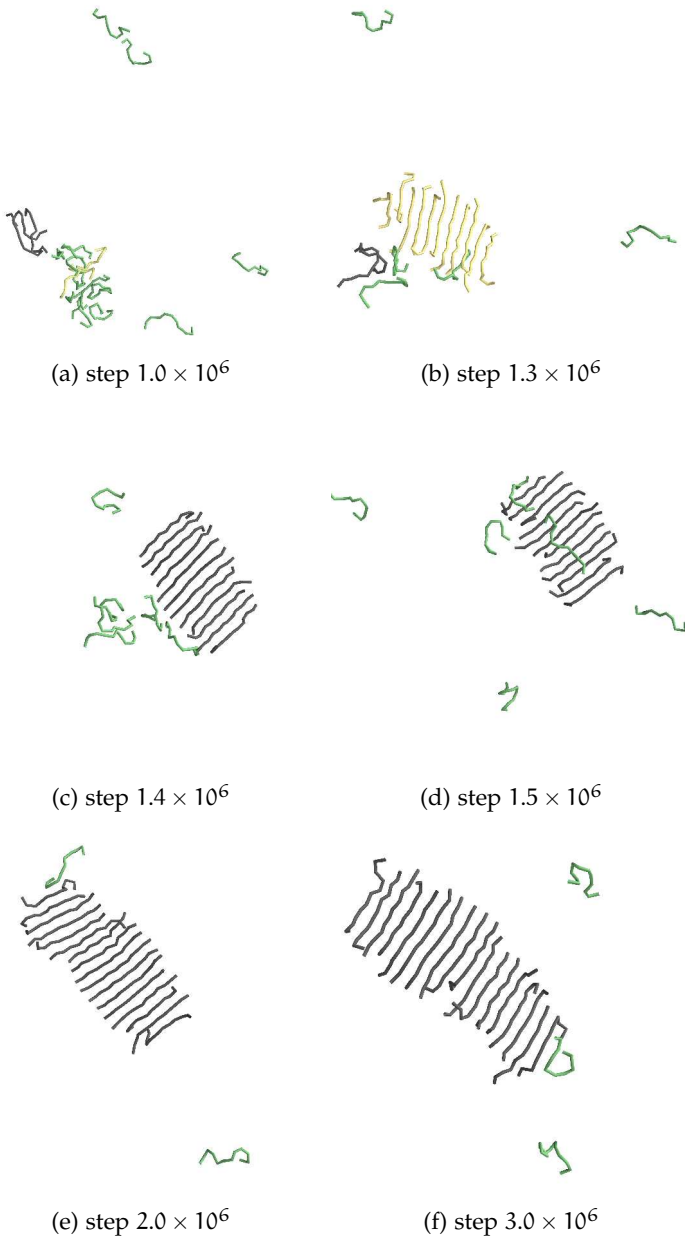

(a) step 1.0×10^6 (b) step 1.3×10^6

(c) step 1.4×10^6 (d) step 1.5×10^6

(e) step 2.0×10^6 (f) step 3.0×10^6

Figure D.1: Formation of a fibril in the presence of a membrane: Top view on the membrane in a simulation with $E_{HB,\,\text{cooperative}} = -1.0\epsilon$.

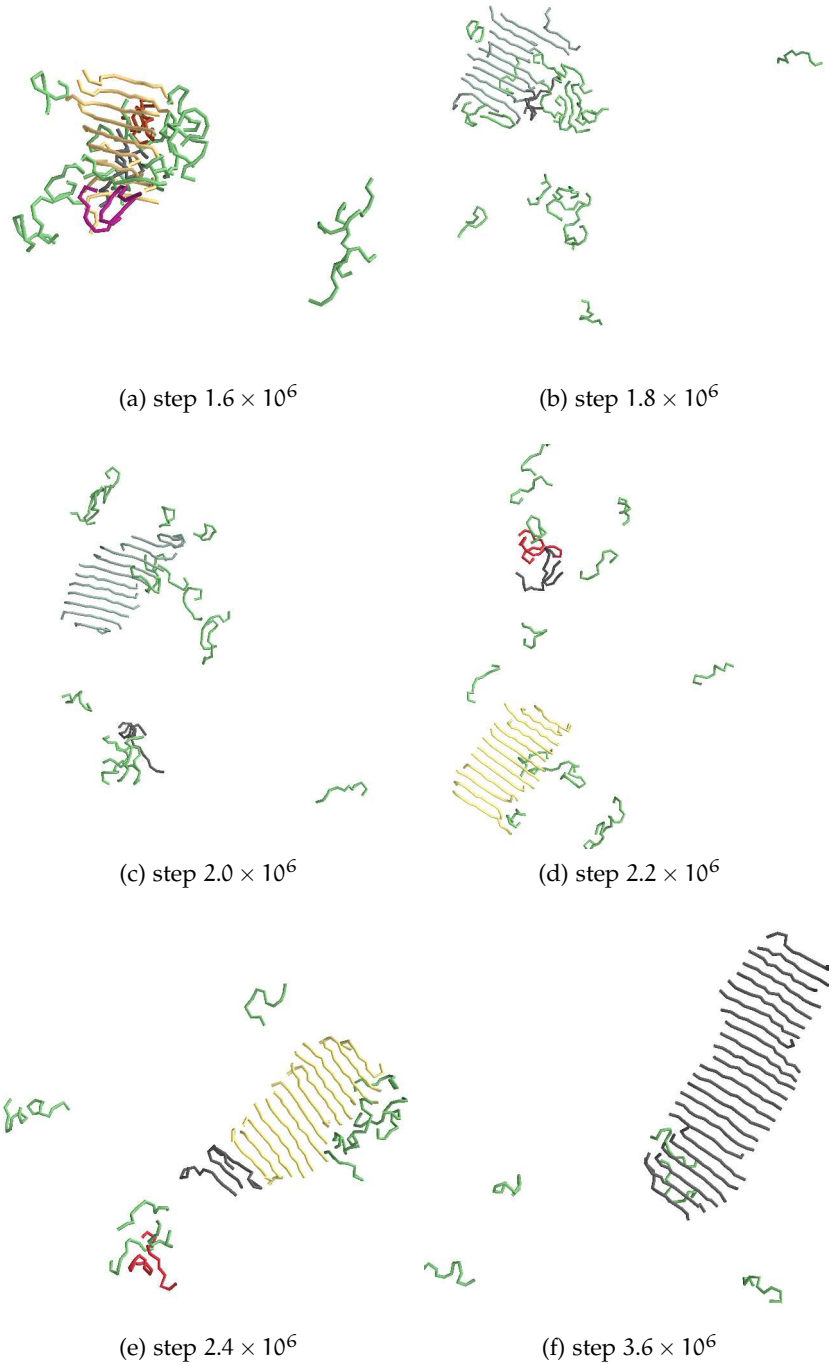

(a) step 1.6×10^6

(b) step 1.8×10^6

(c) step 2.0×10^6

(d) step 2.2×10^6

(e) step 2.4×10^6

(f) step 3.6×10^6

Figure D.2: Formation of a fibril in the presence of a membrane: Bottom view on the membrane in a simulation with $E_{HB,\,\text{cooperative}} = -1.0\epsilon$.

E

PARAMETERS USED FOR THE SIMULATIONS

parameter	value
temperature	1.1
pressure	2.0
solvent_diameter	1.1
lipid_Hbead_diameter	1.0
lipid_Tbead_diameter	1.0
peptide_bead_diameter	0.667
peptide_sequence	H-P
peptide_min_angle	1.431169987
peptide_max_angle	2.58308729
ba_epsilon	4.7
peptide_angle_thetao	2.0944
lipid_head_length	2
num_beads_per_lipid	6
num_beads_per_peptide	12
local_h_bond_min_length	0.783333
local_h_bond_max_length	0.933333
nonlocal_h_bond_min_length	0.683333
nonlocal_h_bond_max_length	0.883333
peptide_nonadjacent_distance	0.667
hh_epsilon	1.0
ht_epsilon	1.0
tt_epsilon	1.0
hs_epsilon	1.0
ts_epsilon	1.0
hh_sigma	1.0
ht_sigma	1.0
tt_sigma	1.0
hs_sigma	1.05
ts_sigma	1.05
hh_cutoff	1.0
ht_cutoff	1.0
tt_cutoff	2.0

Table E.1: Parameters, that do not change in our simulations. *(continued on next page)*

parameter	value
hs_cutoff	1.0
ts_cutoff	1.0
peptide_solvent_cutoff	1.0
lipid_bl_ro	0.7
lipid_bl_dr_cutoff	0.2
lipid_bl_epsilon	100
peptide_bl_ro	0.63333
peptide_bl_dr_cutoff	0.2
peptide_bl_epsilon	100
shear_y_x_move_freq	50
shear_z_x_move_freq	50
shear_z_x_move_freq	50
prerun_shear_y_x_move_freq	1
prerun_shear_z_x_move_freq	1
prerun_shear_z_x_move_freq	1
volume_x_move_freq	50
volume_y_move_freq	50
volume_z_move_freq	50
prerun_volume_x_move_freq	1
prerun_volume_y_move_freq	1
prerun_volume_z_move_freq	1
peptide_peptide_hydr_sigma_HH	0.75
peptide_peptide_hydr_cutoff_HH	2.0
peptide_peptide_hydr_epsilon_PP	1.0
peptide_peptide_hydr_sigma_PP	0.75
peptide_peptide_hydr_cutoff_PP	1.0
peptide_peptide_hydr_epsilon_HP	1.0
peptide_peptide_hydr_sigma_HP	0.75
peptide_peptide_hydr_cutoff_HP	1.0

Table E.1: Parameters, that do not change in our simulations.

SIMULATIONS IN CHAPTER 4

Simulations of a single peptide in a box with 1818 solvent beads and no lipids. In all simulations, peptide_peptide_hydr_epsilon_HH is changed between 0.1ϵ and 2.0ϵ.

Weak hydrogen bond energies

parameter	value	min	max	increment
nonlocal_bond_energy		-2.0ϵ	-12.0ϵ	0.2ϵ
local_bond_energy	-4.0ϵ			
cooperative_bond_energy	-1.2ϵ			
peptide_angle_ko	14.1006			

Table E.2: Simulations with varied non-local hydrogen bond energies.

parameter	value	min	max	increment
nonlocal_bond_energy	-2.8ϵ			
local_bond_energy		-2.0ϵ	-12.0ϵ	0.2ϵ
cooperative_bond_energy	-1.2ϵ			
peptide_angle_ko	14.1006			

Table E.3: Simulations with varied local hydrogen bond energies.

parameter	value	min	max	increment
nonlocal_bond_energy	-2.8ϵ			
local_bond_energy	-4.0ϵ			
cooperative_bond_energy		-0.2ϵ	-4.0ϵ	0.2ϵ
peptide_angle_ko	14.1006			

Table E.4: Simulations with varied cooperative hydrogen bond energies.

Normal hydrogen bond energies

parameter	value	min	max	increment
nonlocal_bond_energy		-2.0ϵ	-12.0ϵ	0.2ϵ
local_bond_energy	-5.5ϵ			
cooperative_bond_energy	-1.65ϵ			
peptide_angle_ko	19.3883			

Table E.5: Simulations with varied non-local hydrogen bond energies.

parameter	value	min	max	increment
nonlocal_bond_energy	-3.85ϵ			
local_bond_energy		-2.0ϵ	-12.0ϵ	0.2ϵ
cooperative_bond_energy	-1.65			
peptide_angle_ko	19.3883			

Table E.6: Simulations with varied local hydrogen bond energies.

parameter	value	min	max	increment
nonlocal_bond_energy	-3.85ϵ			
local_bond_energy	-5.5ϵ			
cooperative_bond_energy		-0.2ϵ	-4.0ϵ	0.2ϵ
peptide_angle_ko	19.3883			

Table E.7: Simulations with varied cooperative hydrogen bond energies.

Strong hydrogen bond energies

parameter	value	min	max	increment
nonlocal_bond_energy		-2.0ϵ	-12.0ϵ	0.2ϵ
local_bond_energy	-8.0ϵ			
cooperative_bond_energy	-2.4ϵ			
peptide_angle_ko	28.2011			

Table E.8: Simulations with varied non-local hydrogen bond energies.

parameter	value	min	max	increment
nonlocal_bond_energy	-5.6ϵ			
local_bond_energy		-2.0ϵ	-12.0ϵ	0.2ϵ
cooperative_bond_energy	-2.4ϵ			
peptide_angle_ko	28.2011			

Table E.9: Simulations with varied local hydrogen bond energies.

parameter	value	min	max	increment
nonlocal_bond_energy	-5.6ϵ			
local_bond_energy	-8.0ϵ			
cooperative_bond_energy		-0.2ϵ	-4.0ϵ	0.2ϵ
peptide_angle_ko	28.2011			

Table E.10: Simulations with varied cooperative hydrogen bond energies.

SIMULATIONS IN CHAPTER 5

Simulations of 50 peptides in a simulation box with 14544 solvent beads and no lipids. peptide_peptide_hydr_epsilon_HH is set to 0.6ϵ in all simulations.

Simulations with $\epsilon_{HB,\,cooperative}$ *between* -4.0ϵ *and* -4.8ϵ

$E_{HB,\,local}$	$E_{HB,\,non\text{-}local}$	$E_{HB,\,coop}$	k0
-4.00ϵ	-2.80ϵ	-1.2ϵ	14.1006
-4.10ϵ	-2.87ϵ	-1.23ϵ	14.4531
-4.20ϵ	-2.94ϵ	-1.26ϵ	14.8056
-4.30ϵ	-3.01ϵ	-1.29ϵ	15.1581
-4.40ϵ	-3.08ϵ	-1.32ϵ	15.5106
-4.50ϵ	-3.15ϵ	-1.35ϵ	15.8631
-4.60ϵ	-3.22ϵ	-1.38ϵ	16.2157
-4.70ϵ	-3.29ϵ	-1.41ϵ	16.5682
-4.80ϵ	-3.36ϵ	-1.44ϵ	16.9207

Table E.11: Simulations with varied hydrogen bond energies.

Simulations with $\epsilon_{HB,\,cooperative}$ *between* -4.9ϵ *and* -5.5ϵ

$E_{HB,\,local}$	$E_{HB,\,non\text{-}local}$	$E_{HB,\,coop}$	k0
-4.90ϵ	-3.43ϵ	-1.47ϵ	17.2732
-5.00ϵ	-3.50ϵ	-1.50ϵ	17.6257
-5.10ϵ	-3.57ϵ	-1.53ϵ	17.9782
-5.20ϵ	-3.64ϵ	-1.56ϵ	18.3307
-5.30ϵ	-3.71ϵ	-1.59ϵ	18.6833
-5.40ϵ	-3.78ϵ	-1.62ϵ	19.0358
-5.50ϵ	-3.55ϵ	-1.65ϵ	19.3883

Table E.12: Simulations with varied hydrogen bond energies.

Simulations with $\epsilon_{HB,\,cooperative}$ *between* -5.6ϵ *and* -8.0ϵ

$E_{HB,\,local}$	$E_{HB,\,non\text{-}local}$	$E_{HB,\,coop}$	k0
-5.60ϵ	-3.92ϵ	-1.68ϵ	19.7408
-5.70ϵ	-3.99ϵ	-1.71ϵ	20.0933
-5.80ϵ	-4.06ϵ	-1.74ϵ	20.4458

Table E.13: Simulations with varied cooperative hydrogen bond energies. *(continued on next page)*

$E_{HB,\,local}$	$E_{HB,\,non\text{-}local}$	$E_{HB,\,coop}$	k0
-5.90ϵ	-4.13ϵ	-1.77ϵ	20.7983
-6.00ϵ	-4.20ϵ	-1.80ϵ	21.1509
-6.10ϵ	-4.27ϵ	-1.83ϵ	21.5034
-6.20ϵ	-4.34ϵ	-1.86ϵ	21.8559
-6.30ϵ	-4.41ϵ	-1.89ϵ	22.2084
-6.40ϵ	-4.48ϵ	-1.92ϵ	22.5609
-6.50ϵ	-4.55ϵ	-1.95ϵ	22.9134

Table E.13: Simulations with varied cooperative hydrogen bond energies.

Controlling the fibril formation process

parameter	**value**	**min**	**max**	**increment**
nonlocal_bond_energy	-3.85ϵ			
local_bond_energy	-5.50ϵ			
cooperative_bond_energy		-0.50ϵ	-1.50ϵ	0.1ϵ
peptide_angle_ko	19.3883			

SIMULATIONS IN CHAPTER 6

Simulations of 50 peptides in a simulation box with 13000 solvent beads and a lipid membrane consisting of $2 \times 20 \times 30$ lipids.

Free energy of insertion for a single peptide

Umbrella sampling simulation of a single peptide in a simulation box with 3636 solvent beads and a membrane consisting of $2 \times 10 \times 10$ lipids. Like in Chapter 5, peptide_peptide_hydr_epsilon_HH is set to 0.6ϵ in all simulations.

parameter	**value**	**varied values**
nonlocal_bond_energy	-3.85ϵ	
local_bond_energy	-5.50ϵ	
cooperative_bond_energy	-1.10ϵ	
peptide_angle_ko	19.3883	
H_peptide_lipid_h_sigma	0.83333σ	
H_peptide_lipid_h_cutoff	1	
H_peptide_lipid_h_epsilon	1ϵ	
H_peptide_lipid_t_sigma	0.83333σ	
H_peptide_lipid_t_cutoff	2	
H_peptide_lipid_t_epsilon		0.3ϵ - 1.1ϵ increment 0.1ϵ & 0.75ϵ

Table E.15: Umbrella sampling simulations to determine the insertion free energy. *(continued on next page)*

parameter	value	varied values
P_peptide_lipid_h_sigma	0.83333σ	
P_peptide_lipid_h_cutoff	1	
P_peptide_lipid_h_epsilon	1ϵ	
P_peptide_lipid_t_sigma	0.83333σ	
P_peptide_lipid_t_cutoff	1	
P_peptide_lipid_t_epsilon	1ϵ	

Table E.15: Umbrella sampling simulations to determine the insertion free energy.

Varried cooperative hydrogen bond strength

parameter	value	min	max	increment
nonlocal_bond_energy	−3.85ϵ			
local_bond_energy	−5.50ϵ			
cooperative_bond_energy		−0.80ϵ	−1.10ϵ	0.1ϵ
peptide_angle_ko	19.3883			
H_peptide_lipid_h_sigma	0.83333σ			
H_peptide_lipid_h_cutoff	1			
H_peptide_lipid_h_epsilon	1ϵ			
H_peptide_lipid_t_sigma	0.83333σ			
H_peptide_lipid_t_cutoff	2			
H_peptide_lipid_t_epsilon	0.6ϵ			
P_peptide_lipid_h_sigma	0.83333σ			
P_peptide_lipid_h_cutoff	1			
P_peptide_lipid_h_epsilon	1ϵ			
P_peptide_lipid_t_sigma	0.83333σ			
P_peptide_lipid_t_cutoff	1			
P_peptide_lipid_t_epsilon	1ϵ			

Table E.16: Simulations with varied cooperative hydrogen bond energies.

Varying lipid-peptide interaction strength

a) Simulations with $\epsilon_{\mathrm{HB,\,cooperative}} = -1.1\epsilon$

parameter	value	min	max	increment
nonlocal_bond_energy	−3.85ϵ			
local_bond_energy	−5.50ϵ			

Table E.17: Simulations with $\epsilon_{\mathrm{HB,\,cooperative}} = -1.1\epsilon$ and varied lipid-peptide interaction strength. *(continued on next page)*

parameter	value	min	max	increment
cooperative_bond_energy	-1.10ϵ			
peptide_angle_ko	19.3883			
H_peptide_lipid_h_sigma	0.83333σ			
H_peptide_lipid_h_cutoff	1			
H_peptide_lipid_h_epsilon	1ϵ			
H_peptide_lipid_t_sigma	0.83333σ			
H_peptide_lipid_t_cutoff	2			
H_peptide_lipid_t_epsilon		0.3ϵ	1.1ϵ	0.1ϵ
P_peptide_lipid_h_sigma	0.83333σ			
P_peptide_lipid_h_cutoff	1			
P_peptide_lipid_h_epsilon	1ϵ			
P_peptide_lipid_t_sigma	0.83333σ			
P_peptide_lipid_t_cutoff	1			
P_peptide_lipid_t_epsilon	1ϵ			

Table E.17: Simulations with $\epsilon_{\mathrm{HB,\,cooperative}} = -1.1\epsilon$ and varied lipid-peptide interaction strength.

b) Simulations with $\epsilon_{\mathrm{HB,\,cooperative}} = -1.0\epsilon$

parameter	value	min	max	increment
nonlocal_bond_energy	-3.85ϵ			
local_bond_energy	-5.50ϵ			
cooperative_bond_energy	-1.00ϵ			
peptide_angle_ko	19.3883			
H_peptide_lipid_h_sigma	0.83333σ			
H_peptide_lipid_h_cutoff	1			
H_peptide_lipid_h_epsilon	1ϵ			
H_peptide_lipid_t_sigma	0.83333σ			
H_peptide_lipid_t_cutoff	2			
H_peptide_lipid_t_epsilon		0.3ϵ	1.0ϵ	0.1ϵ
P_peptide_lipid_h_sigma	0.83333σ			
P_peptide_lipid_h_cutoff	1			
P_peptide_lipid_h_epsilon	1ϵ			
P_peptide_lipid_t_sigma	0.83333σ			
P_peptide_lipid_t_cutoff	1			
P_peptide_lipid_t_epsilon	1ϵ			

Table E.18: Simulations with $\epsilon_{\mathrm{HB,\,cooperative}} = -1.0\epsilon$ and varied lipid-peptide interaction strength.

F

ENERGY COMPARISON FOR UMBRELLA SAMPLING SIMULATIONS

JACKKNIFE ALGORITHM

The Jackknife algorithm or Jackknife Approach is recommended as the standard method for error calculations [135]. It was developed in the 1950s [148, 149]. In the following we give a short introduction, for more details we refer to the afore mentioned resources.

For n independent samples $x_1, \ldots, x_n$, that are identically distributed, we can calculate the Jackknife estimator $\bar{f}^{JK}$ for a function $f(x)$ of x. First we calculate n Jackknife mean values:

$$x_i^{JK} = \frac{1}{n-1} \sum_{k \neq i}^{n} x_k \quad . \tag{F.1}$$

Using these values we calculate $\bar{f}^{JK}$:

$$\bar{f}^{JK} = \frac{1}{n} \sum_{i=1}^{n} f(x_i^{JK}) \quad . \tag{F.2}$$

The estimator for the variance $\sigma^2\left(\bar{f}^{JK}\right)$ is then:

$$\sigma^2\left(\bar{f}^{JK}\right) = \frac{n-1}{n} \sum_{i=}^{n} \left(f(x_i^{JK}) - \bar{f}^{JK}\right)^2 \quad . \tag{F.3}$$

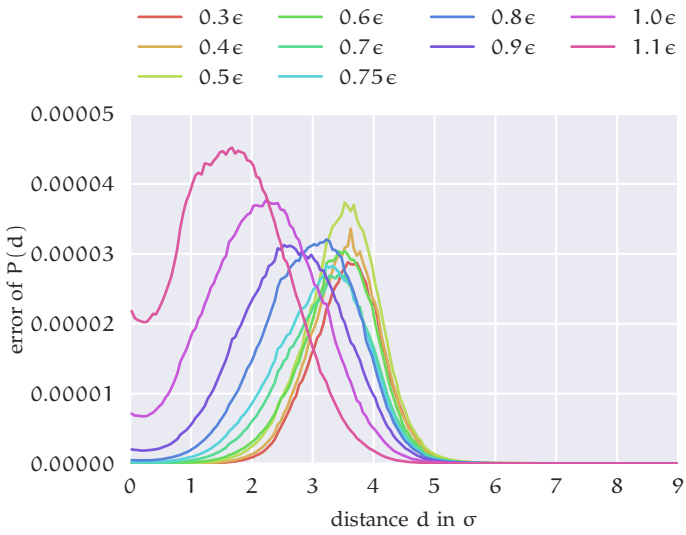

Figure F.1: Plot of the errors of probability density distribution $P(d)$, obtained using a Jackknife algorithm.

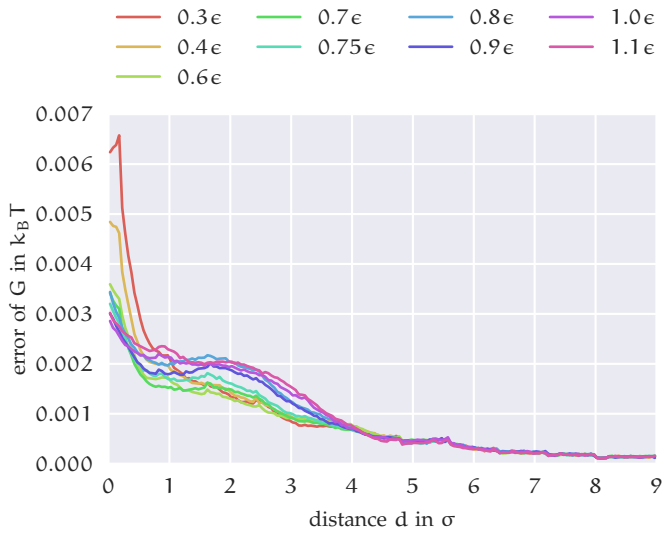

Figure F.2: Plot of the errors of the free energy G, obtained using a Jackknife algorithm.

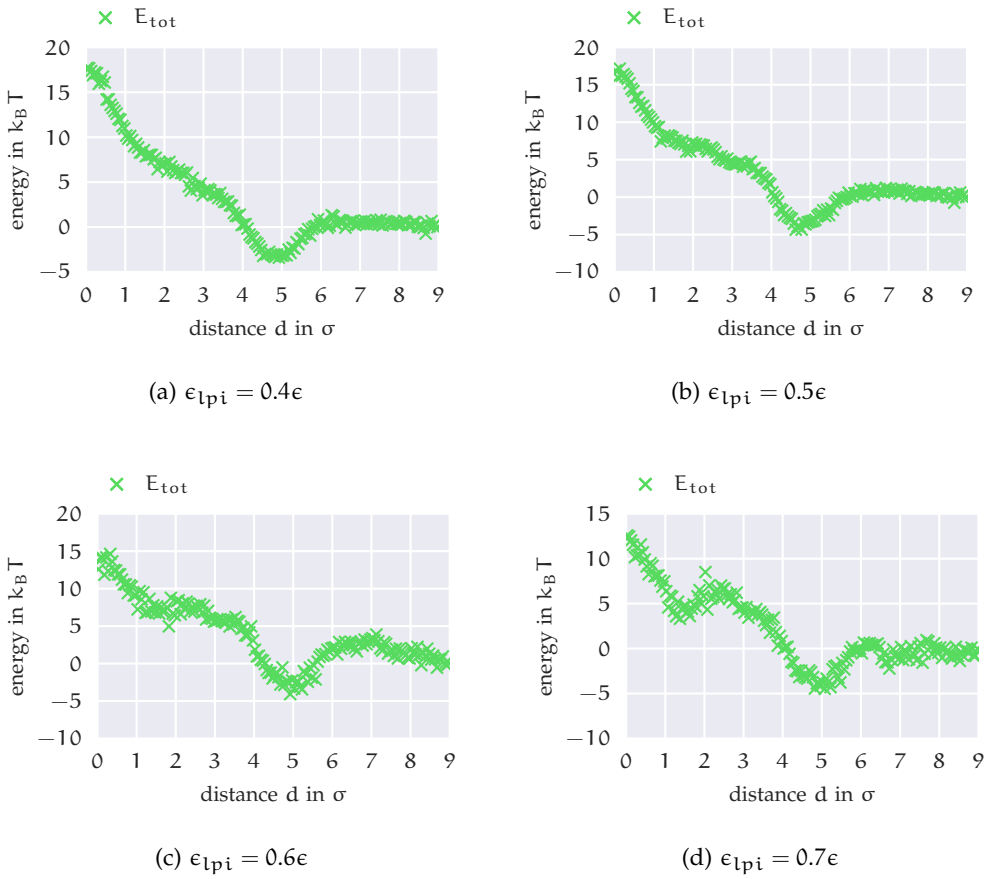

(a) $\epsilon_{lpi} = 0.4\epsilon$

(b) $\epsilon_{lpi} = 0.5\epsilon$

(c) $\epsilon_{lpi} = 0.6\epsilon$

(d) $\epsilon_{lpi} = 0.7\epsilon$

Figure F.3: Total energy for simulations with different values of ϵ_{lpi} as a function of the distance between the COM of the peptide and the COM of the lipid membrane. The plot for $\epsilon_{lpi} = 0.3\epsilon$ is given in Figure 6.6. Continued in Figure F.4.

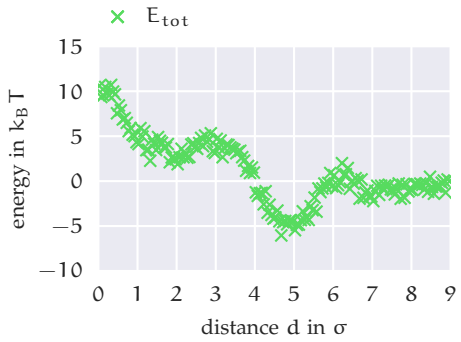

(a) $\epsilon_{lpi} = 0.75\epsilon$

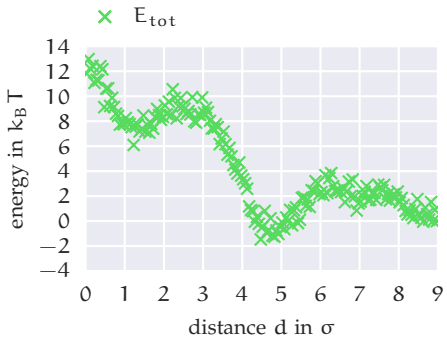

(b) $\epsilon_{lpi} = 0.8\epsilon$

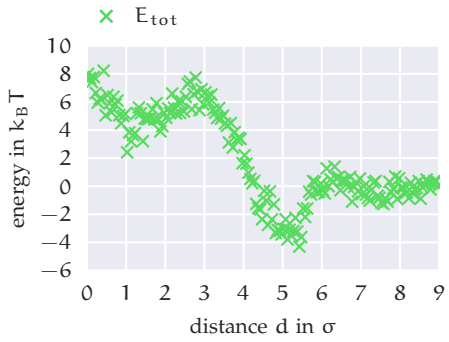

(c) $\epsilon_{lpi} = 0.9\epsilon$

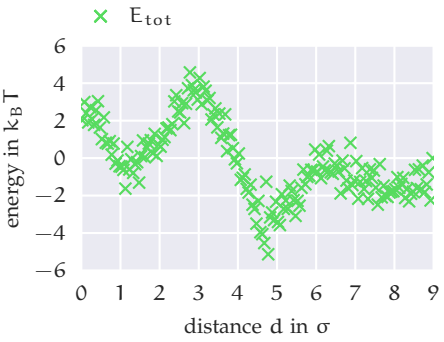

(d) $\epsilon_{lpi} = 1.0\epsilon$

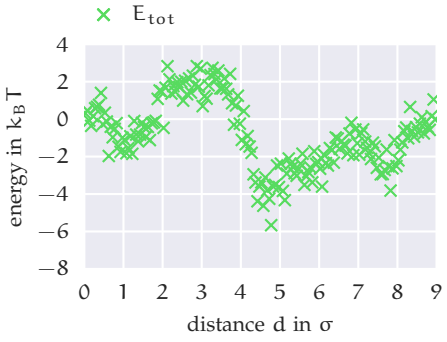

(e) $\epsilon_{lpi} = 1.1\epsilon$

Figure F.4: Same as Figure F.3.

G

IMAGES OF FIBRIL DOUBLE LAYERS ON MEMBRANE SURFACES

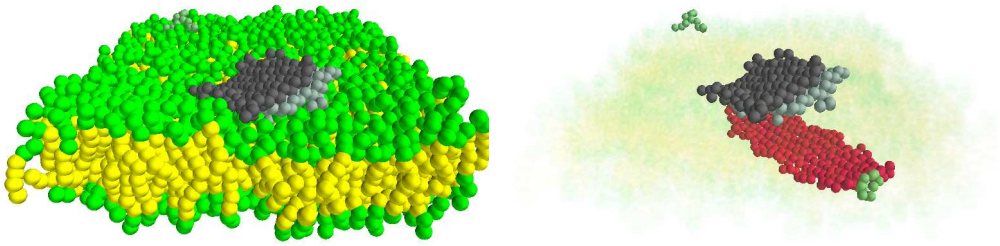

(a) (b)

Figure G.1: Snapshots taken from a simulation with $\epsilon_{lpi} = 0.4\epsilon$ and $\epsilon_{HB,\,\text{cooperative}} = -1.1\epsilon$, showing the layered fibrils on the membrane surface after five million steps. b) shows the same image with increased transparency of the lipid, to allow the peptides and fibrils, that formed on the opposite membrane surface to be visible. The red fibril consists of 25 peptides, the other two of 11 peptides each.

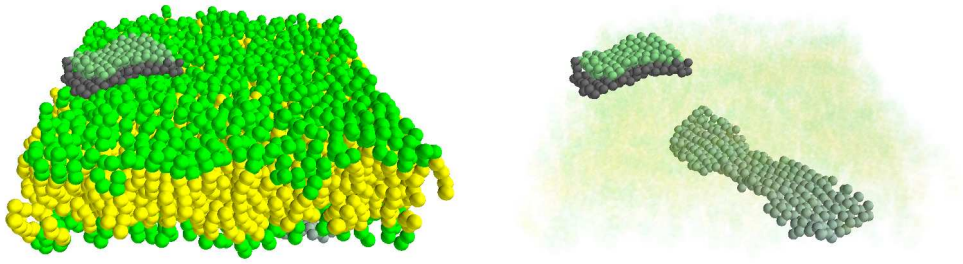

(a) (b)

Figure G.2: Same as Figure G.1 with $\epsilon_{lpi} = 0.5\epsilon$ and $\epsilon_{HB,\,\text{cooperative}} = -1.1\epsilon$. The green and black fibrils consist of 10 and 12 peptides, the grey fibril on the opposite membrane surface consists of 28 peptides.

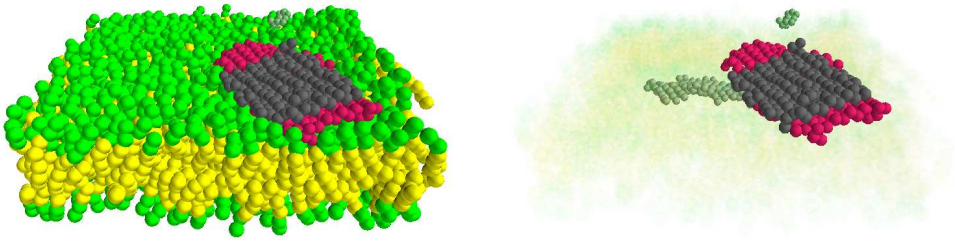

(a) (b)

Figure G.3: Same as Figure G.1 with $\epsilon_{lpi} = 0.6\epsilon$ and $\epsilon_{HB,\,cooperative} = -1.1\epsilon$ after eight million steps. The black fibril consists of 12 peptides, the red one of 19 peptides. The fibril on the opposite side consists of 18 peptides.

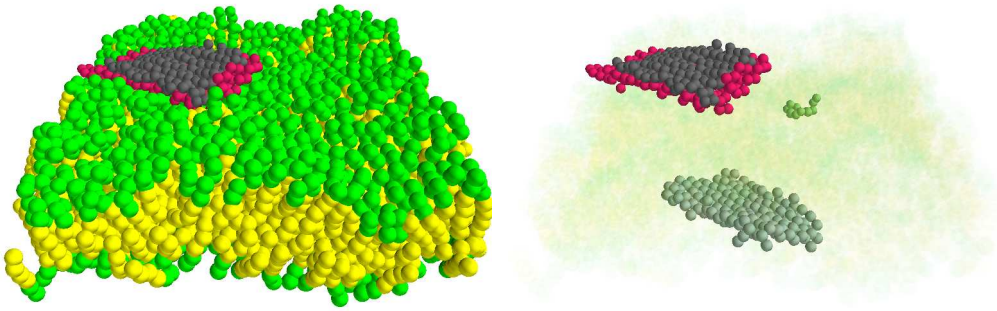

(a) (b)

Figure G.4: Same as Figure G.1 with $\epsilon_{lpi} = 0.7\epsilon$ and $\epsilon_{HB,\,cooperative} = -1.1\epsilon$. The red and black fibrils consist of 20 and 13 peptides, the grey one of 15.

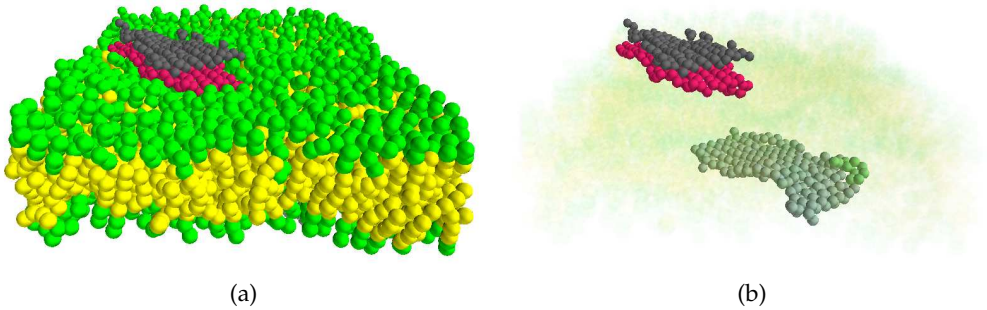

(a) (b)

Figure G.5: Same as Figure G.1 with $\epsilon_{lpi} = 0.8\epsilon$ and $\epsilon_{HB,\,cooperative} = -1.1\epsilon$. The red and black fibrils consist of 16 and 15 peptides, the grey one of 18.

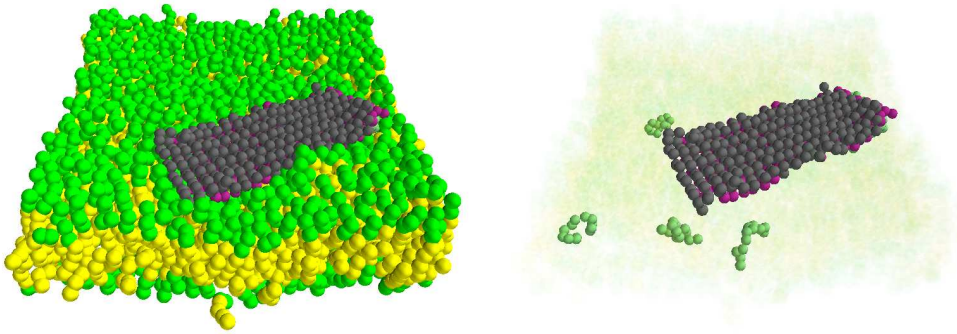

(a) (b)

Figure G.6: Same as Figure G.1 with $\epsilon_{lpi} = 0.9\epsilon$ and $\epsilon_{HB,\,cooperative} = -1.1\epsilon$. The purple fibril consists of 22, the black fibril of 21 peptides.

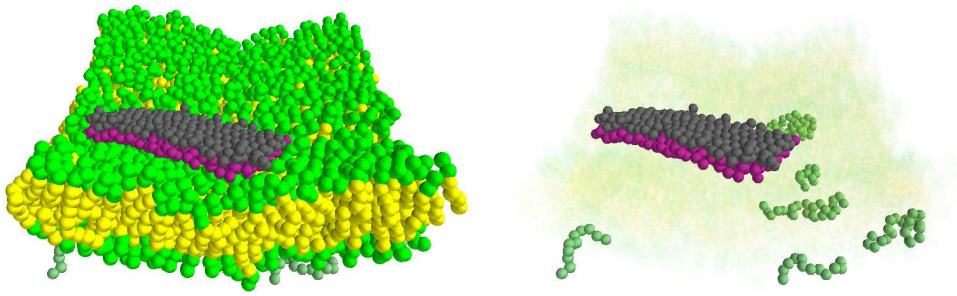

(a) (b)

Figure G.7: Same as Figure G.1 with $\epsilon_{lpi} = 0.3\epsilon$ and $\epsilon_{HB,\,cooperative} = -1.0\epsilon$. The purple fibril consists of 19, the black fibril of 20 peptides.

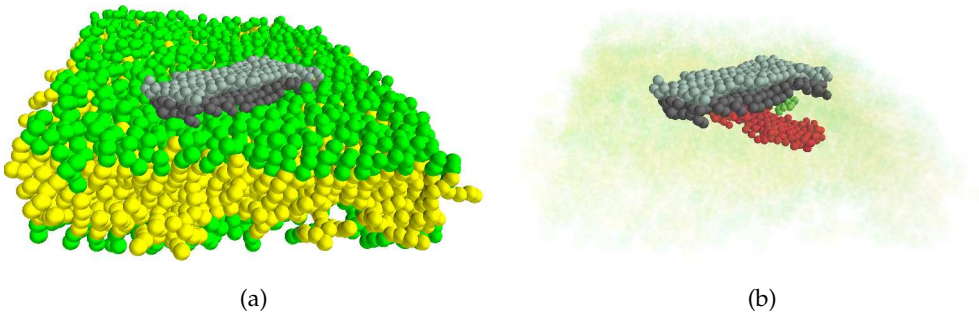

(a) (b)

Figure G.8: Same as Figure G.1 with $\epsilon_{lpi} = 0.4\epsilon$ and $\epsilon_{HB,\,cooperative} = -1.0\epsilon$. The grey fibril consists of 17, the black of 18 peptides. The red fibril on the opposite membrane surface consists of 14 peptides.

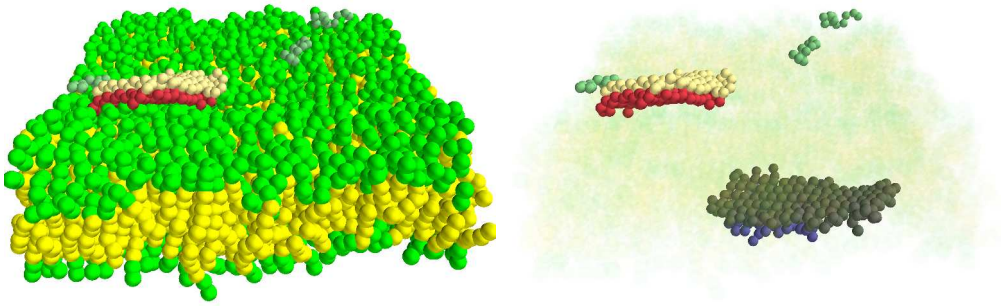

(a) (b)

Figure G.9: Same as Figure G.1 with $\epsilon_{lpi} = 0.5\epsilon$ and $\epsilon_{HB,\,cooperative} = -1.0\epsilon$. The yellow fibril consists of 11 peptides, the red fibril of 10. On the opposite side, also two layered fibrils formed, consisting of 9 (blue) and 17 (black) peptides.

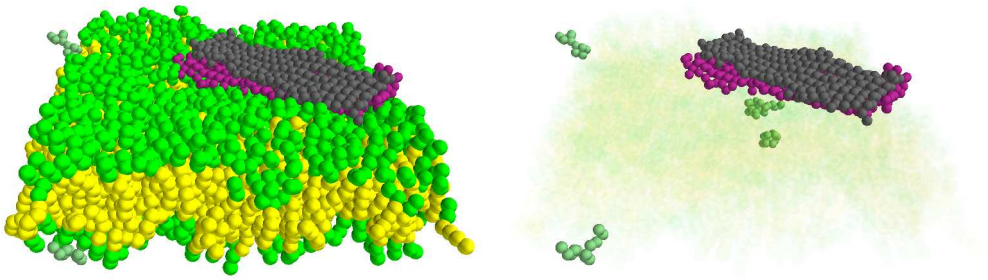

(a) (b)

Figure G.10: Same as Figure G.1 with $\epsilon_{lpi} = 0.6\epsilon$ and $\epsilon_{HB,\,cooperative} = -1.0\epsilon$. The purple fibril consists of 23, the black fibril of 22 peptides.

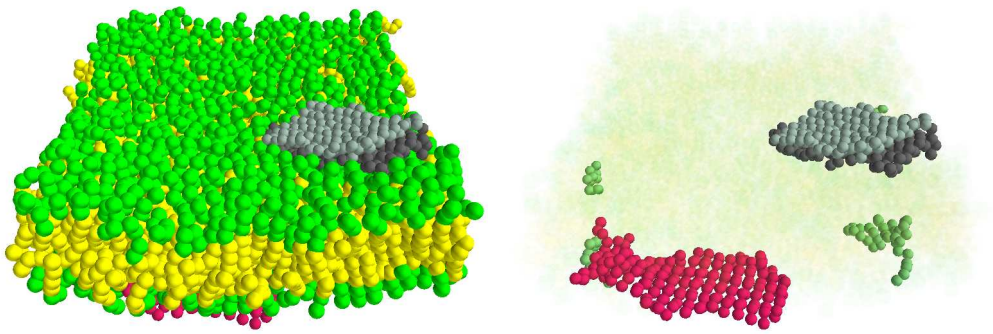

(a) (b)

Figure G.11: Same as Figure G.1 with $\epsilon_{lpi} = 0.7\epsilon$ and $\epsilon_{HB,\,cooperative} = -1.0\epsilon$. The grey fibril consists of 12, the black of 15 peptides. The red fibril on the opposite membrane surface consists of 17 peptides.

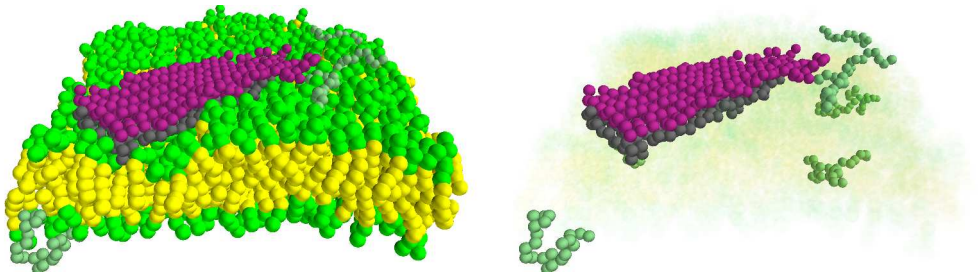

(a) (b)

Figure G.12: Same as Figure G.1 with $\epsilon_{\mathrm{lpi}} = 0.8\epsilon$ and $\epsilon_{\mathrm{HB,\,cooperative}} = -1.0\epsilon$. The purple fibril consists of 17, the black fibril of 20 peptides.

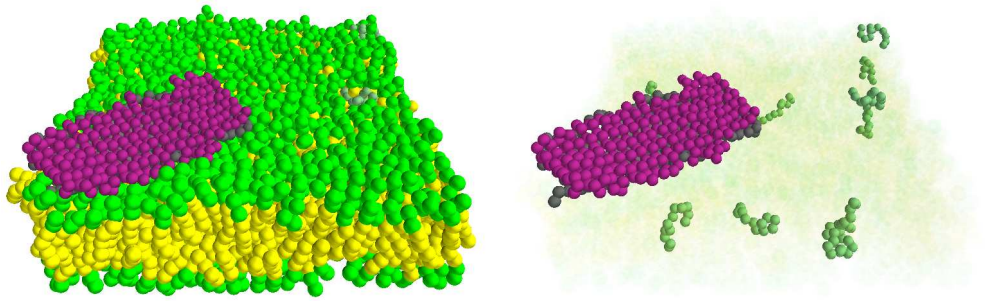

(a) (b)

Figure G.13: Same as Figure G.1 with $\epsilon_{\mathrm{lpi}} = 0.9\epsilon$ and $\epsilon_{\mathrm{HB,\,cooperative}} = -1.0\epsilon$. Both fibrils consist of 20 peptides.

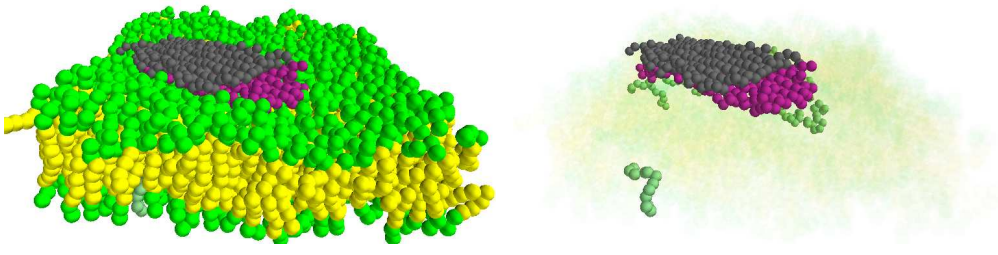

(a) (b)

Figure G.14: Same as Figure G.1 with $\epsilon_{\mathrm{lpi}} = 1.0\epsilon$ and $\epsilon_{\mathrm{HB,\,cooperative}} = -1.0\epsilon$. The purple fibril consists of 19, the black fibril of 23 peptides.

BIBLIOGRAPHY

[1] Bruce Alberts and John Howard Wilson. *Molecular biology of the cell*. 5. ed. New York, NY, 2008. ISBN: 0815341059.

[2] Gerrit Van Meer, Dennis R Voelker and Gerald W Feigenson. 'Membrane lipids: where they are and how they behave'. In: *Nature reviews Molecular cell biology* 9.2 (2008), pp. 112–124.

[3] Martin J Ruocco and G Graham Shipley. 'Characterization of the subtransition of hydrated dipalmitoylphosphatidylcholine bilayers. Kinetic, hydration and structural study'. In: *Biochimica et Biophysica Acta (BBA)-Biomembranes* 691.2 (1982), pp. 309–320.

[4] Helmut W Meyer, Konrad Semmler, Willi Rettig, Walter Pohle, Anne S Ulrich, Stephan Grage, Carsten Selle and Peter J Quinn. 'Hydration of DMPC and DPPC at 4 C produces a novel subgel phase with convex–concave bilayer curvatures'. In: *Chemistry and physics of lipids* 105.2 (2000), pp. 149–166.

[5] Rumiana Koynova and Martin Caffrey. 'Phases and phase transitions of the phosphatidylcholines'. In: *Biochimica et Biophysica Acta (BBA)-Reviews on Biomembranes* 1376.1 (1998), pp. 91–145.

[6] Á Csiszár, A Bóta, Cs Novák, E Klumpp and G Subklew. 'Changes in the thermotropic and the structural behaviour of 1, 2-dipalmitoyl-sn-glycero-3-phosphatidylcholine/water liposomes effected by 2, 4-dichlorphenol'. In: *Adsorption and Nanostructure*. Springer, 2001, pp. 145–152.

[7] Peter Nuhn and Ludger Wessjohann. *Naturstoffchemie: mikrobielle, pflanzliche und tierische Naturstoffe. Mit 80 Tabellen*. Hirzel, 2006.

[8] Peter C Heinrich, Matthias Müller and Lutz Graeve. *Löffler/Petrides Biochemie und Pathobiochemie*. Springer-Verlag, 2014.

[9] John J. Corrigan. 'D-Amino Acids in Animals'. In: *Science* 164.3876 (1969), pp. 142–149. DOI: 10.1126/science.164.3876.142. eprint: http://www.sciencemag.org/content/164/3876/142.full.pdf. URL: http://www.sciencemag.org/content/164/3876/142.short.

[10] A Meister et al. 'Biochemistry of the amino acids. Volume 2.' In: *Biochemistry of the amino acids. Volume 2.* 2 (1965), pp. xxiii+–593.

[11] Tadashi Ogawa, Mitsuru Fukuda and Kei Sasaoka. 'Occurrence of N-malonyl-D-alanine in pea seedlings'. In: *Biochimica et Biophysica Acta (BBA)-General Subjects* 297.1 (1973), pp. 60–69.

[12] John S Davies. 'Occurrence and biosynthesis of D-amino acids'. In: *Chemistry and biochemistry of amino acids, peptides and proteins. New York: Marcel Dekker inc* 4 (1977).

[13] William Ramsay Taylor. 'The classification of amino acid conservation'. In: *Journal of theoretical Biology* 119.2 (1986), pp. 205–218.

[14] Yan Zhang, Pavel V Baranov, John F Atkins and Vadim N Gladyshev. 'Pyrrolysine and selenocysteine use dissimilar decoding strategies'. In: *Journal of Biological Chemistry* (2005).

[15] H. Lodish, A. Berk, C.A. Kaiser, M. Krieger, A. Bretscher, H. Ploegh, A. Amon and K. Martin. *Molecular Cell Biology*. W. H. Freeman, 2016. ISBN: 9781464187490.

[16] Michael W Parker and Susanne C Feil. 'Pore-forming protein toxins: from structure to function'. In: *Progress in biophysics and molecular biology* 88.1 (2005), pp. 91–142.

[17] Kirsten Sandvig and Bo van Deurs. 'Membrane traffic exploited by protein toxins'. In: *Annual review of cell and developmental biology* 18.1 (2002), pp. 1–24.

[18] Claire Lesieur, Beatrix Vécsey-Semjén, Laurence Abrami, Marc Fivaz and F Gisou van der Goot. 'Membrane insertion: the strategies of toxins (review)'. In: *Molecular membrane biology* 14.2 (1997), pp. 45–64.

[19] Yasuo Yoshikuni, Thomas E Ferrin and Jay D Keasling. 'Designed divergent evolution of enzyme function'. In: *Nature* 440.7087 (2006), pp. 1078–1082.

[20] H Eldon Sutton and Robert P Wagner. 'Mutation and enzyme function in humans'. In: *Annual review of genetics* 9.1 (1975), pp. 187–212.

[21] EH Fischer, H Charbonneau and NK Tonks. 'Protein tyrosine phosphatases: a diverse family of intracellular and transmembrane enzymes'. In: American Association for the Advancement of Science. 1991.

[22] Susan S Taylor, Joseph A Buechler and Wes Yonemoto. 'cAMP-dependent protein kinase: framework for a diverse family of regulatory enzymes'. In: *Annual review of biochemistry* 59.1 (1990), pp. 971–1005.

[23] Wylie Vale, CATHERINE Rivier, AARON Hsueh, C Campen, H Meunier, T Bicsak, J Vaughan, A Corrigan, W Bardin, P Sawchenko et al. 'Chemical and biological characterization of the inhibin family of protein hormones'. In: *Laurentian Hormone Conference*. 2013, pp. 1–34.

[24] Keith W Kelley, Douglas A Weigent and Ron Kooijman. 'Protein hormones and immunity'. In: *Brain, behavior, and immunity* 21.4 (2007), pp. 384–392.

[25] Lawrence H Clouse and Philip C Comp. 'The regulation of hemostasis: the protein C system'. In: *New England Journal of Medicine* 314.20 (1986), pp. 1298–1304.

[26] DS Woulfe. 'REVIEW ARTICLES: Platelet G protein-coupled receptors in hemostasis and thrombosis'. In: *Journal of Thrombosis and Haemostasis* 3.10 (2005), pp. 2193–2200.

[27] Efrat Abramov, Iftach Dolev, Hilla Fogel, Giuseppe D Ciccotosto, Eyal Ruff and Inna Slutsky. 'Amyloid-β as a positive endogenous regulator of release probability at hippocampal synapses'. In: *Nature neuroscience* 12.12 (2009), pp. 1567–1576.

[28] M Franke. 'Statistische Untersuchungen über die senilen Drusen im menschlichen Gehirn'. In: *Diss. Prom. B. Akad. Ärztl. Fortbild.* (1975).

[29] World Health Organisation. *Dementia, WHO Fact sheet N°362*. Mar. 2015. URL: http://www.who.int/mediacentre/factsheets/fs362/en/.

[30] A Pick. 'Über die Beziehungen der senilen Hirnatrophie zur Aphasie'. In: *Prager Med Wochenschr* 17 (1892), pp. 165–167.

[31] Alois Alzheimer. 'Über eine eigenartige Erkrankung der Hirnrinde'. In: *Allgemeine Zeitschrift Psychiatrie* 64 (1907), pp. 146–148.

[32] Michael E Calhoun, Karl-Heinz Wiederhold, Dorothee Abramowski, Amie L Phinney, Alphonse Probst, Christine Sturchler-Pierrat, Matthias Staufenbiel, Bernd Sommer and Mathias Jucker. 'Neuron loss in APP transgenic mice'. In: *Nature* 395.6704 (1998), pp. 755–756.

[33] Joseph Rogers, Scott Webster, Lih-Fen Lue, Libuse Brachova, W Harold Civin, Mark Emmerling, Brenda Shivers, Douglas Walker and Patrick McGeer. 'Inflammation and Alzheimer's disease pathogenesis'. In: *Neurobiology of aging* 17.5 (1996), pp. 681–686.

[34] Lonneke ML de Lau and Monique MB Breteler. 'Epidemiology of Parkinson's disease'. In: *The Lancet Neurology* 5.6 (2006), pp. 525–535.

[35] Joseph Jankovic. 'Parkinson's disease: clinical features and diagnosis'. In: *Journal of Neurology, Neurosurgery & Psychiatry* 79.4 (2008), pp. 368–376.

[36] Joshua M Shulman, Philip L De Jager and Mel B Feany. 'Parkinson's disease: genetics and pathogenesis'. In: *Annual Review of Pathology: Mechanisms of Disease* 6 (2011), pp. 193–222.

[37] Mihael H Polymeropoulos, Christian Lavedan, Elisabeth Leroy, Susan E Ide, Anindya Dehejia, Amalia Dutra, Brian Pike, Holly Root, Jeffrey Rubenstein, Rebecca Boyer et al. 'Mutation in the α-synuclein gene identified in families with Parkinson's disease'. In: *science* 276.5321 (1997), pp. 2045–2047.

[38] Maria Grazia Spillantini, Marie Luise Schmidt, Virginia M-Y Lee, John Q Trojanowski, Ross Jakes and Michel Goedert. 'α-Synuclein in Lewy bodies'. In: *Nature* 388.6645 (1997), pp. 839–840.

[39] James Parkinson. 'An essay on the shaking palsy'. In: (1817). URL: http://www.gutenberg.org/files/23777/23777-h/23777-h.htm.

[40] Andrew J Lees. 'Unresolved issues relating to the shaking palsy on the celebration of James Parkinson's 250th birthday'. In: *Movement Disorders* 22.S17 (2007), S327–S334.

[41] Marcy E MacDonald, Christine M Ambrose, Mabel P Duyao, Richard H Myers, Carol Lin, Lakshmi Srinidhi, Glenn Barnes, Sherryl A Taylor, Marianne James, Nicolet Groot et al. 'A novel gene containing a trinucleotide repeat that is expanded and unstable on Huntington's disease chromosomes'. In: *Cell* 72.6 (1993), pp. 971–983.

[42] Christopher A Ross and Sarah J Tabrizi. 'Huntington's disease: from molecular pathogenesis to clinical treatment'. In: *The Lancet Neurology* 10.1 (2011), pp. 83–98.

[43] Stephen W Davies, Mark Turmaine, Barbara A Cozens, Marian DiFiglia, Alan H Sharp, Christopher A Ross, Eberhard Scherzinger, Erich E Wanker, Laura Mangiarini and Gillian P Bates. 'Formation of neuronal intranuclear inclusions underlies the neurological dysfunction in mice transgenic for the HD mutation'. In: *Cell* 90.3 (1997), pp. 537–548.

[44] Allan J Tobin and Ethan R Signer. 'Huntington's disease: the challenge for cell biologists'. In: *Trends in cell biology* 10.12 (2000), pp. 531–536.

[45] Francis O Walker. 'Huntington's disease'. In: *The Lancet* 369.9557 (2007), pp. 218–228.

[46] George Huntington. 'The medical and surgical reporter'. In: *Philadelphia, 13th April* (1872).

[47] G. Bates, S. Tabrizi and L. Jones. *Huntingtons Disease*. Oxford Monographs on Medical Genetics. Oxford University Press, 2014. ISBN: 978-019937047-4. URL: https://books.google.de/books?id=_if-AgAAQBAJ.

[48] Rakez Kayed, Yuri Sokolov, Brian Edmonds, Theresa M McIntire, Saskia C Milton, James E Hall and Charles G Glabe. 'Permeabilization of lipid bilayers is a common conformation-dependent activity of soluble amyloid oligomers in protein misfolding diseases'. In: *Journal of Biological Chemistry* 279.45 (2004), pp. 46363–46366.

[49] Arjan Quist, Ivo Doudevski, Hai Lin, Rushana Azimova, Douglas Ng, Blas Frangione, Bruce Kagan, Jorge Ghiso and Ratnesh Lal. 'Amyloid ion channels: a common structural link for protein-misfolding disease'. In: *Proceedings of the National Academy of Sciences of the United States of America* 102.30 (2005), pp. 10427–10432.

[50] Trinh Xuan Hoang, Antonio Trovato, Flavio Seno, Jayanth R Banavar and Amos Maritan. 'Geometry and symmetry presculpt the free-energy landscape of proteins'. In: *Proceedings of the National Academy of Sciences of the United States of America* 101.21 (2004), pp. 7960–7964.

[51] Trinh X Hoang, Luca Marsella, Antonio Trovato, Flavio Seno, Jayanth R Banavar and Amos Maritan. 'Common attributes of native-state structures of proteins, disordered proteins, and amyloid'. In: *Proceedings of the National Academy of Sciences* 103.18 (2006), pp. 6883–6888.

[52] Stefan Auer, CM Dobson and Michele Vendruscolo. 'Characterization of the nucleation barriers for protein aggregation and amyloid formation'. In: *HFSP journal* 1.2 (July 2007), pp. 137–146. ISSN: 1955-2068. DOI: 10.2976/1.2760023. URL: http://www.pubmedcentral.nih.gov/articlerender.fcgi?artid=2639838\&tool=pmcentrez\&rendertype=abstracthttp://www.tandfonline.com/doi/abs/10.2976/1.2760023.

[53] Stefan Auer, Filip Meersman, Christopher Dobson and Michele Vendruscolo. 'A generic mechanism of emergence of amyloid protofilaments from disordered oligomeric aggregates'. In: *PLoS Comput Biol* 4.11 (2008), e1000222.

[54] Stefan Auer and Dimo Kashchiev. 'Phase diagram of α-helical and β-sheet forming peptides'. In: *Physical review letters* 104.16 (2010), p. 168105.

[55] Olaf Lenz and Friederike Schmid. 'A simple computer model for liquid lipid bilayers'. In: *Journal of molecular liquids* 117.1 (2005), pp. 147–152.

[56] Olaf Lenz and Friederike Schmid. 'Structure of symmetric and asymmetric "ripple" phases in lipid bilayers'. In: *Physical review letters* 98.5 (2007), p. 058104.

[57] Beate West, Frank L H Brown and Friederike Schmid. 'Membrane-protein interactions in a generic coarse-grained model for lipid bilayers.' In: *Biophysical journal* 96.1 (2009), pp. 101–115. ISSN: 00063495. DOI: 10.1529/biophysj.108.138677. arXiv: 0809.1797. URL: http://dx.doi.org/10.1529/biophysj.108.138677.

[58] Jörg Neder, Beate West, Peter Nielaba and Friederike Schmid. 'Coarse-grained simulations of membranes under tension'. In: *The Journal of chemical physics* 132.11 (2010), p. 115101.

[59] Alex Morriss-Andrews and Joan-Emma Shea. 'Computational studies of protein aggregation: methods and applications'. In: *Annual review of physical chemistry* 66 (2015), pp. 643–666.

[60] Luca Monticelli, Senthil K Kandasamy, Xavier Periole, Ronald G Larson, D Peter Tieleman and Siewert-Jan Marrink. 'The MARTINI coarse-grained force field: extension to proteins'. In: *Journal of chemical theory and computation* 4.5 (2008), pp. 819–834.

[61] One-Sun Lee, Vince Cho and George C Schatz. 'Modeling the self-assembly of peptide amphiphiles into fibers using coarse-grained molecular dynamics'. In: *Nano letters* 12.9 (2012), pp. 4907–4913.

[62] Siewert J Marrink, H Jelger Risselada, Serge Yefimov, D Peter Tieleman and Alex H De Vries. 'The MARTINI force field: coarse grained model for biomolecular simulations'. In: *The journal of physical chemistry B* 111.27 (2007), pp. 7812–7824.

[63] Fabio Sterpone, Simone Melchionna, Pierre Tuffery, Samuela Pasquali, Normand Mousseau, Tristan Cragnolini, Yassmine Chebaro, Jean-Francois St-Pierre, Maria Kalimeri, Alessandro Barducci et al. 'The OPEP protein model: from single molecules, amyloid formation, crowding and hy-

drodynamics to DNA/RNA systems'. In: *Chemical Society reviews* 43.13 (2014), pp. 4871–4893.

[64] Scott P Carmichael and M Scott Shell. 'A new multiscale algorithm and its application to coarse-grained peptide models for self-assembly'. In: *The Journal of Physical Chemistry B* 116.29 (2012), pp. 8383–8393.

[65] M Scott Shell. 'The relative entropy is fundamental to multiscale and inverse thermodynamic problems'. In: *The Journal of chemical physics* 129.14 (2008), p. 144108.

[66] Gary S Ayton, Will G Noid and Gregory A Voth. 'Systematic coarse graining of biomolecular and soft-matter systems'. In: *Mrs Bulletin* 32.11 (2007), pp. 929–934.

[67] Noah S Bieler, Tuomas PJ Knowles, Daan Frenkel and Robert Vácha. 'Connecting macroscopic observables and microscopic assembly events in amyloid formation using coarse grained simulations'. In: *PLoS Comput Biol* 8.10 (2012), e1002692.

[68] Anders Irbäck, Niels Linnemann, Björn Linse, Stefan Wallin et al. 'Aggregate geometry in amyloid fibril nucleation'. In: *Physical review letters* 110.5 (2013), p. 058101.

[69] Giovanni Bellesia and Joan-Emma Shea. 'Self-assembly of β-sheet forming peptides into chiral fibrillar aggregates'. In: *The Journal of chemical physics* 126.24 (2007), 06B616.

[70] Ran Friedman and Amedeo Caflisch. 'Surfactant effects on amyloid aggregation kinetics'. In: *Journal of molecular biology* 414.2 (2011), pp. 303–312.

[71] F. Schmid, D. Duchs, O. Lenz and B. West. 'A generic model for lipid monolayers, bilayers, and membranes'. In: February (Aug. 2006), pp. 1–4. arXiv: 0608226 [physics]. URL: http://arxiv.org/abs/physics/0608226v1.

[72] Rudolf M Lequin. 'Enzyme immunoassay (EIA)/enzyme-linked immunosorbent assay (ELISA)'. In: *Clinical chemistry* 51.12 (2005), pp. 2415–2418.

[73] Charles G Glabe and Rakez Kayed. 'Common structure and toxic function of amyloid oligomers implies a common mechanism of pathogenesis'. In: *Neurology* 66.1 suppl 1 (2006), S74–S78.

[74] Jefferson D Knight and Andrew D Miranker. 'Phospholipid catalysis of diabetic amyloid assembly'. In: *Journal of molecular biology* 341.5 (2004), pp. 1175–1187.

[75] He-Jin Lee, Chan Choi and Seung-Jae Lee. 'Membrane-bound α-synuclein has a high aggregation propensity and the ability to seed the aggregation of the cytosolic form'. In: *Journal of Biological Chemistry* 277.1 (2002), pp. 671–678.

[76] Sajith A Jayasinghe and Ralf Langen. 'Lipid membranes modulate the structure of islet amyloid polypeptide'. In: *Biochemistry* 44.36 (2005), pp. 12113–12119.

[77] Candace M Pfefferkorn, Zhiping Jiang and Jennifer C Lee. 'Biophysics of α-synuclein membrane interactions'. In: *Biochimica et Biophysica Acta (BBA)-Biomembranes* 1818.2 (2012), pp. 162–171.

[78] Katsumi Matsuzaki. 'How do membranes initiate Alzheimer's Disease? Formation of toxic amyloid fibrils by the amyloid β-protein on ganglioside clusters'. In: *Accounts of chemical research* 47.8 (2014), pp. 2397–2404.

[79] Galyna P Gorbenko and Paavo KJ Kinnunen. 'The role of lipid–protein interactions in amyloid-type protein fibril formation'. In: *Chemistry and Physics of Lipids* 141.1 (2006), pp. 72–82.

[80] Galyna Gorbenko and Valeriya Trusova. 'Protein aggregation in a membrane environment'. In: *Adv Protein Chem Struct Biol* 84 (2011), pp. 113–42.

[81] Christopher M Dobson. 'Protein folding and misfolding'. In: *Nature* 426.6968 (2003), pp. 884–890.

[82] Fabrizio Chiti and Christopher M Dobson. 'Protein misfolding, functional amyloid, and human disease'. In: *Annu. Rev. Biochem.* 75 (2006), pp. 333–366.

[83] Sara M Butterfield and Hilal A Lashuel. 'Amyloidogenic protein–membrane interactions: mechanistic insight from model systems'. In: *Angewandte Chemie International Edition* 49.33 (2010), pp. 5628–5654.

[84] Thomas L Williams and Louise C Serpell. 'Membrane and surface interactions of Alzheimer's Aβ peptide–insights into the mechanism of cytotoxicity'. In: *Febs Journal* 278.20 (2011), pp. 3905–3917.

[85] Panchika Prangkio, Erik C Yusko, David Sept, Jerry Yang and Michael Mayer. 'Multivariate analyses of amyloid-beta oligomer populations indicate a connection between pore formation and cytotoxicity'. In: *PLoS One* 7.10 (2012), e47261.

[86] Patrick Walsh, Gillian Vanderlee, Jason Yau, Jody Campeau, Valerie L Sim, Christopher M Yip and Simon Sharpe. 'The mechanism of membrane disruption by cytotoxic amyloid oligomers formed by prion protein (106–126) is dependent on bilayer composition'. In: *Journal of Biological Chemistry* 289.15 (2014), pp. 10419–10430.

[87] Maarten FM Engel, Lucie Khemtémourian, Cécile C Kleijer, Hans JD Meeldijk, Jet Jacobs, Arie J Verkleij, Ben de Kruijff, J Antoinette Killian and Jo WM Höppener. 'Membrane damage by human islet amyloid polypeptide through fibril growth at the membrane'. In: *Proceedings of the National Academy of Sciences* 105.16 (2008), pp. 6033–6038.

[88] Lin Wai Hung, Giuseppe D Ciccotosto, Eleni Giannakis, Deborah J Tew, Keyla Perez, Colin L Masters, Roberto Cappai, John D Wade and Kevin J Barnham. 'Amyloid-β peptide (Aβ) neurotoxicity is modulated by the rate of peptide aggregation: Aβ dimers and trimers correlate with neurotoxicity'. In: *Journal of Neuroscience* 28.46 (2008), pp. 11950–11958.

[89] Sarah Henry, Helene Vignaud, Claude Bobo, Marion Decossas, Oliver Lambert, Etienne Harte, Isabel D Alves, Christophe Cullin and Sophie Lecomte. 'Interaction of Aβ1–42 Amyloids with Lipids Promotes "Off-Pathway" Oligomerization and Membrane Damage'. In: *Biomacromolecules* 16.3 (2015), pp. 944–950.

[90] Anna Kastorna, Valeriya Trusova, Galyna Gorbenko and Paavo Kinnunen. 'Membrane effects of lysozyme amyloid fibrils'. In: *Chemistry and physics of lipids* 165.3 (2012), pp. 331–337.

[91] Rachel AS Smith, Aleksey Nabok, Ben JF Blakeman, Wei-Feng Xue, Benjamin Abell and David P Smith. 'Analysis of toxic amyloid fibril interactions at natively derived membranes by ellipsometry'. In: *PloS one* 10.7 (2015), e0132309.

[92] Olaf Lenz. 'Computer Simulations of lipid bilayers'. PhD thesis. 2007.

[93] Andrey Milchev, Wolfgang Paul and Kurt Binder. 'Off-lattice Monte Carlo simulation of dilute and concentrated polymer solutions under theta conditions'. In: *The Journal of chemical physics* 99.6 (1993), pp. 4786–4798.

[94] K Kremer and GS Grest. 'Entanglement effects in polymer melts and networks'. In: *Monte Carlo and molecular dynamics simulations in polymer science*. Oxford University Press: New York, 1995, pp. 194–271.

[95] Stefan Auer, Antonio Trovato and Michele Vendruscolo. 'A condensation-ordering mechanism in nanoparticle-catalyzed peptide aggregation'. In: *PLoS Comput Biol* 5.8 (2009), e1000458.

[96] Stefan Auer, Christopher M Dobson, Michele Vendruscolo and Amos Maritan. 'Self-templated nucleation in peptide and protein aggregation'. In: *Physical review letters* 101.25 (2008), p. 258101.

[97] Huayu Xiong, Brian L Buckwalter, Hong-Ming Shieh and Michael H Hecht. 'Periodicity of polar and nonpolar amino acids is the major determinant of secondary structure in self-assembling oligomeric peptides'. In: *Proceedings of the National Academy of Sciences* 92.14 (1995), pp. 6349–6353.

[98] Alex Morriss-Andrews, Giovanni Bellesia and Joan Emma Shea. 'Effects of surface interactions on peptide aggregate morphology'. In: *Journal of Chemical Physics* 135.8 (Aug. 2011), p. 085102. ISSN: 1089-7690. DOI: 10.1063/1.3624929.

[99] Alex Morriss-Andrews and Joan Emma Shea. 'Kinetic pathways to peptide aggregation on surfaces: The effects of -sheet propensity and surface attraction'. In: *Journal of Chemical Physics* 136.6 (Feb. 2012), p. 065103. ISSN: 1089-7690. DOI: 10.1063/1.3682986. URL: http://www.ncbi.nlm.nih.gov/pubmed/22360223.

[100] Alex Morriss-Andrews, Frank L.H. Brown and Joan-Emma Shea. 'A Coarse-Grained Model for Peptide Aggregation on a Membrane Surface.' In: *Journal of Physical Chemistry B* (2014).

[101] William C Swope, Hans C Andersen, Peter H Berens and Kent R Wilson. 'A computer simulation method for the calculation of equilibrium constants for the formation of physical clusters of molecules: Application to small water clusters'. In: *The Journal of Chemical Physics* 76.1 (1982), pp. 637–649.

[102] HJC Berendsen and WF Van Gunsteren. 'Practical algorithms for dynamic simulations'. In: *Molecular-dynamics simulation of statistical-mechanical systems* (1986), pp. 43–65.

[103] Kurt Binder. *Monte Carlo and molecular dynamics simulations in polymer science*. Oxford University Press, 1995.

[104] J. M. Haile. *Molecular Dynamics Simulation: Elementary Methods*. A Wiley-Interscience publication. Wiley, 1997. ISBN: 9780471184393. URL: https://books.google.de/books?id=3Zq9IAlG7fkC.

[105] Daan Frenkel and Berend Smit. *Understanding molecular simulation, from algorithms to applications*. Elsevier, 2001.

[106] Michael P Allen. 'Introduction to molecular dynamics simulation'. In: *Computational soft matter: from synthetic polymers to proteins* 23 (2004), pp. 1–28.

[107] Dennis C Rapaport. *The art of molecular dynamics simulation*. Cambridge university press, 2004.

[108] NG Van Kampen. *Stochastic processes in physics and chemistry, (north-holland personal library)*. North Holland, 2007.

[109] Vasilios I. Manousiouthakis and Michael W. Deem. 'Strict Detailed Balance is Unnecessary in Monte Carlo Simulation'. In: 2753.1999 (1998), p. 8. ISSN: 00219606. DOI: 10.1063/1.477973. arXiv: 9809240 [cond-mat]. URL: http://arxiv.org/abs/cond-mat/9809240.

[110] Hidemaro Suwa and Synge Todo. 'Markov Chain Monte Carlo method without detailed balance'. In: *Physical Review Letters* 105.12 (2010), pp. 1–4. ISSN: 00319007. DOI: 10.1103/PhysRevLett.105.120603. arXiv: 1007.2262.

[111] Georges Louis Leclerc comte de Buffon. *Essai d'arithmétique morale*. Vol. 4. Supplément à l'Histoire Naturelle. 1777.

[112] Nicholas Metropolis and Stanislaw Ulam. 'The monte carlo method'. In: *Journal of the American statistical association* 44.247 (1949), pp. 335–341.

[113] Nicholas Metropolis, Arianna W. Rosenbluth, Marshall N. Rosenbluth, Augusta H. Teller and Edward Teller. 'Equation of State Calculations by Fast Computing Machines'. In: *The Journal of Chemical Physics* 21.6 (1953), pp. 1087–1092. ISSN: 00219606. DOI: doi:10.1063/1.1699114. arXiv: 5744249209. URL: http://jcp.aip.org/resource/1/jcpsa6/v21/i6/p1087_s1?bypassSSO=1.

[114] David P Landau and Kurt Binder. *A guide to Monte Carlo simulations in statistical physics*. Cambridge university press, 2014.

[115] Gareth O Roberts and Adrian FM Smith. 'Simple conditions for the convergence of the Gibbs sampler and Metropolis-Hastings algorithms'. In: *Stochastic processes and their applications* 49.2 (1994), pp. 207–216.

[116] Roy J Glauber. 'Time-dependent statistics of the Ising model'. In: *Journal of mathematical physics* 4.2 (1963), pp. 294–307.

[117] W. W. Wood. 'Monte Carlo Calculations for Hard Disks in the Isothermal-Isobaric Ensemble'. In: *The Journal of Chemical Physics* 48.1 (1968).

[118] I. R. McDonald. 'NpT-ensemble Monte Carlo calculations for binary liquid mixtures'. In: *Molecular Physics* 23.1 (1972), pp. 41–58. DOI: 10.1080/00268977200100031.

[119] R Martoňák, W Paul and K Binder. 'Monte Carlo simulation of crystalline polyethylene'. In: *Computer physics communications* 99.1 (1996), pp. 2–8.

[120] Nikos Ch Karayiannis, Vlasis G Mavrantzas and Doros N Theodorou. 'A novel Monte Carlo scheme for the rapid equilibration of atomistic model polymer systems of precisely defined molecular architecture'. In: *Physical review letters* 88.10 (2002), p. 105503.

[121] PV Krishna Pant and Doros N Theodorou. 'Variable connectivity method for the atomistic Monte Carlo simulation of polydisperse polymer melts'. In: *Macromolecules* 28.21 (1995), pp. 7224–7234.

[122] Stefan Geyler, Tadeusz Pakula and Johannes Reiter. 'Monte Carlo simulation of dense polymer systems on a lattice'. In: *The Journal of Chemical Physics* 92.4 (1990), pp. 2676–2680.

[123] Jörn Ilja Siepmann and Daan Frenkel. 'Configurational bias Monte Carlo: a new sampling scheme for flexible chains'. In: *Molecular Physics* 75.1 (1992), pp. 59–70.

[124] Alfred Uhlherr. 'Monte Carlo conformational sampling of the internal degrees of freedom of chain molecules'. In: *Macromolecules* 33.4 (2000), pp. 1351–1360.

[125] LR Dodd, TD Boone and DN Theodorou. 'A concerted rotation algorithm for atomistic Monte Carlo simulation of polymer melts and glasses'. In: *Molecular Physics* 78.4 (1993), pp. 961–996.

[126] Sebastian Meinhardt. 'Curvature induced nanoscale rafts in lipid membranes'. PhD thesis. 2013.

[127] C. Stadler. 'Monte Carlo-Simulationen von Langmuir-Monolagen'. PhD thesis. 1998.

[128] Davide Marenduzzo, Alessandro Flammini, Antonio Trovato, Jayanth R Banavar and Amos Maritan. 'Physics of thick polymers'. In: *Journal of Polymer Science Part B: Polymer Physics* 43.6 (2005), pp. 650–679.

[129] JR Banavar, A Flammini, D Marenduzzo, A Maritan and A Trovato. 'Tubes near the edge of compactness and folded protein structures'. In: *Journal of Physics: Condensed Matter* 15.18 (2003), S1787.

[130] Martin Ester, Hans-Peter Kriegel, Jörg Sander, Xiaowei Xu et al. 'A density-based algorithm for discovering clusters in large spatial databases with noise.' In: *Kdd*. Vol. 96. 34. 1996, pp. 226–231.

[131] Doros N Theodorou and Ulrich W Suter. 'Shape of unperturbed linear polymers: polypropylene'. In: *Macromolecules* 18.6 (1985), pp. 1206–1214.

[132] Peter Virnau and Marcus Müller. 'Calculation of free energy through successive umbrella sampling'. In: *The Journal of chemical physics* 120.23 (2004), pp. 10925–10930.

[133] Glenn M Torrie and John P Valleau. 'Nonphysical sampling distributions in Monte Carlo free-energy estimation: Umbrella sampling'. In: *Journal of Computational Physics* 23.2 (1977), pp. 187–199.

[134] Johannes Kästner. 'Umbrella sampling'. In: *Wiley Interdisciplinary Reviews: Computational Molecular Science* 1.6 (2011), pp. 932–942.

[135] Bernd A Berg and Alain Billoire. *Markov chain monte carlo simulations*. Wiley Online Library, 2008.

[136] Michelle A Poirier, Huilin Li, Jed Macosko, Shuowei Cai, Mario Amzel and Christopher A Ross. 'Huntingtin spheroids and protofibrils as precursors in polyglutamine fibrilization'. In: *Journal of Biological Chemistry* 277.43 (2002), pp. 41032–41037.

[137] Annalisa Relini, Silvia Torrassa, Ranieri Rolandi, Alessandra Gliozzi, Camillo Rosano, Claudio Canale, Martino Bolognesi, Georgia Plakoutsi, Monica Bucciantini, Fabrizio Chiti et al. 'Monitoring the process of HypF fibrillization and liposome permeabilization by protofibrils'. In: *Journal of molecular biology* 338.5 (2004), pp. 943–957.

[138] Massimo Stefani. 'Structural features and cytotoxicity of amyloid oligomers: implications in Alzheimer's disease and other diseases with amyloid deposits'. In: *Progress in neurobiology* 99.3 (2012), pp. 226–245.

[139] Monica Bucciantini, Stefania Rigacci and Massimo Stefani. 'Amyloid aggregation: Role of biological membranes and the aggregate–membrane system'. In: *J. Phys. Chem. Lett* 5.3 (2014), pp. 517–527.

[140] Ananthakrishnan Sethuraman and Georges Belfort. 'Protein structural perturbation and aggregation on homogeneous surfaces'. In: *Biophysical journal* 88.2 (2005), pp. 1322–1333.

[141] Xiaoxue Zhang, Johnna R St Clair, Erwin London and Daniel P Raleigh. 'Islet Amyloid Polypeptide Membrane Interactions: Effects of Membrane Composition'. In: *Biochemistry* (2017).

[142] Anja ND Stefanovic, Martin T Stöckl, Mireille MAE Claessens and Vinod Subramaniam. 'α-Synuclein oligomers distinctively permeabilize complex model membranes'. In: *FEBS journal* 281.12 (2014), pp. 2838–2850.

[143] Cara-Lynne Schengrund. 'Lipid rafts: keys to neurodegeneration'. In: *Brain research bulletin* 82.1 (2010), pp. 7–17.

[144] Narinder Sanghera, Bruno EFS Correia, Joana RS Correia, Christian Ludwig, Sonya Agarwal, Hironori K Nakamura, Kazuo Kuwata, Eric Samain, Andrew C Gill, Boyan B Bonev et al. 'Deciphering the molecular details for the binding of the prion protein to main ganglioside GM1 of neuronal membranes'. In: *Chemistry & biology* 18.11 (2011), pp. 1422–1431.

[145] Jorge Santos Da Silva, Takafumi Hasegawa, Taeko Miyagi, Carlos G Dotti and Jose Abad-Rodriguez. 'Asymmetric membrane ganglioside sialidase activity specifies axonal fate'. In: *Nature neuroscience* 8.5 (2005), pp. 606–615.

[146] Nelson Arispe and Michael Doh. 'Plasma membrane cholesterol controls the cytotoxicity of Alzheimer's disease AβP (1–40) and (1–42) peptides'. In: *The FASEB Journal* 16.12 (2002), pp. 1526–1536.

[147] Linge Bai and David Breen. 'Calculating center of mass in an unbounded 2D environment'. In: *Journal of Graphics, GPU, and Game Tools* 13.4 (2008), pp. 53–60.

[148] Maurice H Quenouille. 'Notes on bias in estimation'. In: *Biometrika* 43.3/4 (1956), pp. 353–360.

[149] John W Tukey. 'Bias and confidence in not-quite large samples'. In: *Annals of Mathematical Statistics*. Vol. 29. 2. 1958, pp. 614–614.